# On Structural Health Monitoring of Aircraft Adhesively Bonded Repairs


The University Of Sheffield.

A Thesis submitted to the University of Sheffield

for the degree of Doctor of Philosophy in the Faculty of Engineering

by

Sofia Pavlopoulou

Department of Mechanical Engineering

University of Sheffield

March 2013

# Acknowledgments

First of all I would like express my sincere gratitude to my supervisors Professor Costas Soutis and Professor Keith Worden for their excellent supervision without which this work would have been impossible. In particular, I would like to thank Professor Costas Soutis for his patience, his encouragement and for guiding me and advising me accordingly during these years, for which I am deeply grateful. Secondly I would like to thank Professor Keith Worden for his support and his assistance especially towards the last stages of my PhD and also for providing the necessary conditions that made the completion of this work possible. I am also grateful to Professor Wieslaw Staszewski who co-supervised my early PhD years. His contribution was critical for setting a strong basis for the continuation of my PhD.

I would like to express my gratitude to Dr Galal Mohamed for his assistance with numerical analysis and for all his valuable advices. Throughout these years I had the opportunity to collaborate with a number of people who critically contributed to this work. In particular I would like to acknowledge the help of Dr Miguel Angel Caminero Torija and Bjarni Nicolaisson. I would especially like to thank all the people who gave an opinion on my work and for all the stimulating discussions we had over my research, such as Professor Victor Giurgiutiu, Dr Paul Fromme, Sascha Duczek, Dr Sigrun Hirsekorn and her team in IZFP.

All my colleagues have provided the best possible working environment. Special thanks go to Ioannis, Alon, Steve, Yu Shi, Nikos, Ifigeneia, Charles, Pete and Tim for all their help and companionship. Moreover my sincere thanks go to Dr Lizzy Cross for her support and useful advices. The technicians and the workshop of the Mechanical Engineering department provided the necessary help that ensured

the successful completion of this work; special thanks to Michael Jackson and Les Morton.

My family and my friends have played a key role all these years with their encouragement and understanding. Sincere thanks go to my parents, my sister Niki and to Javier, for being there for me all these years, for sharing my joyful moments and for keeping me going when things went wrong.

In conclusion I would like to acknowledge the financial contribution of the EU IA-PETUS project and its partners for making this work possible.

# Abstract

The recent interest in life extension of ageing aircraft and the need to address the repair challenges in the new age composite ones, led to the investigation of new repair methodologies such as adhesively bonded repair patches. The present thesis focuses on structural health monitoring aspects of the repairs, evaluating their performance with guided ultrasonic waves aiming to develop a monitoring strategy which would eliminate unscheduled maintenance and unnecessary inspection costs. To address the complex nature of the wave propagation phenomena, a finite element based model identified the existing challenges by exploring the interaction of the excitation waves with different levels of damage. The damage sensitivity of the first antisymmetric mode was numerically investigated. An external bonded patch and a scarf repair, were further tested in static and dynamic loadings, and their performance was monitored with Lamb waves, excited by surface-bonded piezoelectric transducers. The response was processed by means of advanced pattern recognition and data dimension reduction techniques such as novelty detection and principal component analysis. An optimisation of these tools enabled an accurate damage detection under complex conditions. The phenomena of mode isolation and precise arrival time determination under a noisy environment and the problem of inadequate training data were investigated and solved through appropriate transducer arrangements and advanced signal processing respectively. The applicability of the established techniques was demonstrated on an aluminium repaired helicopter tail stabilizer. Each case study utilised alternative nondestructive techniques for validation such as 3D digital image correlation, X-ray radiography and thermography. Finally a feature selection strategy was developed through the analysis of the instantaneous properties of guided waves for damage detection purposes.

# Publications

## CONFERENCE PROCEEDINGS

**1. S. Pavlopoulou**, K. Worden, and C. Soutis, "Structural health monitoring and damage prognosis in composite repaired structures through the excitation of guided ultrasonic waves," Proc. SPIE, 11-14 March 2013, San Diego, California, USA.

**2. S. Pavlopoulou**, C. Soutis, and K. Worden, "Application of pattern recognition for damage classification in scarf repairs," *International Conference on Noise and Vibration Engineering (ISMA12)*, 17-19 September, 2012, Leuven, Belgium.

**3.** M. Caminero, **S. Pavlopoulou**, M. López-Pedrosa, B. Nicolaisson, C. Pinna, and C. Soutis, "Digital image correlation analysis applied to monitor damage evolution of composite plates with stress concentrations and bonded patch repairs," *Proceedings of the 15th European Conference on Composite Materials*, 2012, Venice, Italy.

**4. S. Pavlopoulou**, W. J. Staszewski, and C. Soutis, "A comparative study on novelty detection and frequency analysis of Lamb waves for the monitoring of metallic repaired structures," *5th International Conference on Emerging Technologies in Non-Destructive Testing (ETNDT5)*, 19-21 September, 2011, Ioannina, Greece.

**5. S. Pavlopoulou**, C. Soutis, and W. J. Staszewski, "Analysis of instantaneous characteristics of guided ultrasonic waves for composite cure monitoring," *5th EC-COMAS Thematic Conference on Smart Structures and Materials (SMART11)*, 6-8 July 2011, Saarland University, Saarbrücken, Germany.

**6. S. Pavlopoulou**, W. J. Staszewski, C. Soutis, and G. Manson, "Analysis of instantaneous characteristics of guided ultrasonic waves in metallic structures with aluminium repair patches", Proc. SPIE 7984, 79842Y, 6-8 March 2011, San Diego,

California, USA.

## JOURNAL PUBLICATIONS

**1. S. Pavlopoulou**, C. Soutis, and W. Staszewski, "Structural health monitoring of composite scarf repairs with guided waves," *Key Engineering Materials*, vol. 518, pp. 328–337, 2012.

**2.** M. Caminero, **S. Pavlopoulou**, M. López-Pedrosa, B. Nicolaisson, C. Pinna, and C. Soutis, "Analysis of adhesively bonded repairs in composites: Damage detection and prognosis," *Composite Structures*, vol. 95, pp. 500–517, 2013.

**3.** M. A. Caminero, **S. Pavlopoulou**, M. López-Pedrosa, B. G. Nicolaisson, C. Pinna, and C. Soutis, "Using digital image correlation techniques for damage detection on adhesively bonded composite repairs," *Advanced Composites Letters*, vol. 21, no. 2, pp. 51–57, 2012.

**4. S. Pavlopoulou**, W. J. Staszewski, and C. Soutis, "Evaluation of instantaneous characteristics of guided ultrasonic waves for structural quality and health monitoring," *Structural Control and Health Monitoring*, In press (Available online), 2012.

**5. S. Pavlopoulou**, C. Soutis, and W. J. Staszewski, "Cure monitoring through time-frequency analysis of guided ultrasonic waves," *Plastics, Rubber and Composites*, vol. 41, no. 4-5, pp. 180–186(7), 2012.

## PAPERS IN PREPARATION

**1. S. Pavlopoulou**, K. Worden, C. Soutis, "Novelty detection and dimension reduction on guided ultrasonic waves for the damage detection on scarf repairs," In preparation.

**2. S. Pavlopoulou**, K. Worden, C. Soutis, "On structural health monitoring of external patch repairs: numerical analysis and damage prognosis approaches," In preparation.

**3. S. Pavlopoulou**, K. Worden, C. Soutis, "Nondestructive evaluation of a repaired helicopter stabilizer through guided ultrasonic waves and lock-in thermography," In preparation.

# Nomenclature

**Acronyms**

AIC: Akaike information criterion
AR: Aspect ratio
BEM: Boundary element method
BVID: Barely visible impact damage
CC: Cross correlation
CCD: Charge couple device
CFRP: Carbon fibre reinforced polymer
CMI: Cure monitoring index
CNT: Carbon canotubes
CWT: Continuous wavelet transform
DIC: Digital image correlation
EEMD: Ensemble empirical mode decomposition
EMAT: Electro-magnetic acoustic transducer
EMD: Empirical mode decomposition
FDM: Finite difference method
FE: Finite elements
FEA: Finite element analysis
FEM: Finite element method
FT: Fourier transform
HHT: Hilbert-Huang transform
HT: Hilbert transform
IA: Instantaneous amplitude
IDT: Interdigital transducer

IF: Instantaneous frequency
IMF: Intrinsic mode function
IP: Instantaneous phase
IR: Infra red
IrT: Infrared thermography
LT: Lock-in thermography
MNI: Mean novelty index
MSD: Mahalanobis squared-distance
MSLM: Mass-spring lattice model
MT: Modulated thermography
NDT: Nondestructive techniques
NLPCA: Nonlinear principal component analysis
OA: Outlier analysis
PC: Principal component
PC: Pitch-catch
PCA: Principal component analysis
PE: Pulse-echo
PPT: Pulsed phased thermography
PT: Pulse thermography
PVDF: Polyvinylidene fluoride
PZT: Piezoelectric transducer
SDOF: Single degree of freedom
SEM: Spectral element method
SH: Shear horizontal
SHM: Structural health monitoring
SNR: Signal-to-noise ratio
SR: Stiffness ratio
SRM: Structural repair manual
SSD: Sum-squared difference
STFT: Short time Fourier transform
SV: Shear vertical
SVD: Singular value decomposition
TOF: Time of flight
WVD: Wigner-Viller distribution

# Table of Contents

# List of Figures

# List of Tables

# Chapter 1

# Introduction

This chapter provides a brief introduction to the objectives of this thesis. First the main industry area the thesis focused on is demonstrated, namely the repair of critical damage of primary structures in aerospace industry. Then the concept of *in-situ* monitoring is presented and the current challenges with respect to maintenance in aerospace industry are briefly explained. Finally an overview of the most representative nondestructive testing (NDT) techniques will be presented as well as the next step ahead of these techniques which is the use of structural health monitoring (SHM) strategies. At the end of the chapter, the motivation and main objectives of this work will be stated as well as a brief overview of the thesis.

## 1.1 Composite repairs in aerospace industry

The aerospace industry is currently required to deal with the problem of ageing aerostructures. Approximately 30% of the current world wide fleet is estimated to be over 15 years in age. These metallic structures mainly suffer from fatigue and corrosion damage. In addition, aerospace industry has recently moved towards the implementation of advanced polymer-based composite materials for the manufacturing of the new age commercial aircraft such as the Airbus 380 and Boeing 787 [1]. These are made of a high percentage of composite materials while the new Airbus 350 has primarily used carbon fibre reinforced polymer (CFRP) for both fuselage and wing structures. The composite materials in aerospace industry aim to create a

whole new era where the maximised stiffness-to-weight ratio and the fuel efficiency are the key requirements. Composite structures can exhibit damage mainly due to low velocity impact. In this case, damage can remain invisible and undetected, while its propagation can be catastrophic under certain loading conditions [1].

It is therefore clear that aerospace industry needs to address the demanding problem of repair and maintenance in order to prolong the life of the ageing aircraft and to address the repair challenges in the new composite ones through a reliable, robust and cost effective repair scenario. This work focuses on the proposed repair technique of adhesively bonded repair patches, mainly made of composites. This technology was first introduced to Australian military industry in the early 1970s and later in the USA in the early 1980s [2]. The considerable performance of the technique extended its application to civil industry. However, extensive research over the last years highlighted the technological challenges related to their design, manufacturing, application and in-service performance. The current thesis will investigate the monitoring of the in-service performance of this technology when subjected to a variety of representative loading scenarios in different applications and will address the key problems related to the efficient assessment of the repaired region. This is a very critical step towards the certification of the technique by the Civil Aviation Authorities, especially of primary carrying load structures [1].

## 1.2 The concept of in-situ monitoring

As stated in [3], the damage tolerance chain in aerospace industry is as strong as its weakest link (e.g. the inspection), which would lead to appropriate maintenance if needed, in order to prevent any failures. The cost of inspection though is a considerable aspect which spurred the interest in the utilisation of smart monitoring systems. The term *smart* refers to any system that can respond and adapt to changes in its environment. Studies performed in metal and composite aircraft structures showed that more than 40% of the inspection time and approximately 20% of the maintenance/inspection cost would be saved if a smart monitoring system was integrated [3]. Smart monitoring systems involve the implementation of a series of sensors, actuators, controllers and signal processors which would perform *in-situ*, on-line monitoring. This technology aims to provide extra performance reliability by offering certain implementation and sensitivity advantages over the conventional inspection

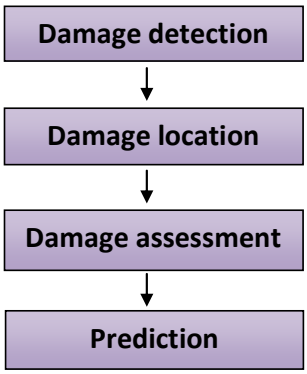


Figure 1.1: Rytter's hierarchy model. [4]

strategies while keeping the number of scheduled and unscheduled inspections low and the downtime of the aircraft to a minimum.

The continuous monitoring of a structure aims to provide information about the structural integrity of the monitored region and to predict its residual life following a hierarchical model as described by Rytter [4] (Figure 1.1). The first level of the hierarchy examines the presence of damage in the structure. The second level provides information about the possible location of the damage. In the third level an estimation of the extent or the type of the damage is performed. The fourth step predicts the residual life of the structure. It is sensible that each level is dependent on the previous one. The first level which is the most vital one for the damage identification is preferably implemented on-line and it might be successfully accomplished even if the physics of the damage are not known. However the fourth level cannot be implemented without the theoretical background of the structure and the damage. The current work mostly focused on the first step of Rytter's model, while in combination with more conventional off-line techniques, the second and third levels were performed.

This work focused on the application of the *in-situ* monitoring of the repaired area when a critical damaged area has been first removed and subsequently repaired by a composite adhesively bonded patch. Figure 1.2 illustrates the proposed monitoring scenario which is based on an active damage monitoring concept where the excitation of the system is required. First the system is excited with a suitable source, and as the induced energy (here in the form of stress waves) propagates through the system and through the region of interest such as the repaired region, the output response can be recorded, post-processed and further assessed in order to determine its residual life. This monitoring system can be continuous, monitoring the structure

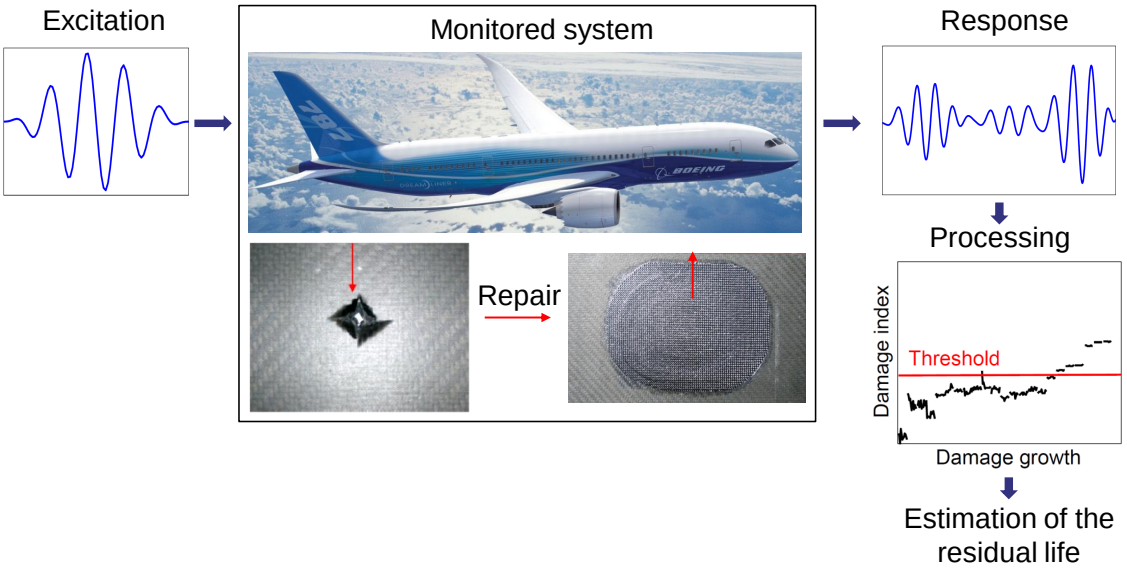


Figure 1.2: On-line monitoring scenario of repaired aerospace structures.

in an *in-situ* mode, and it can identify if patch debonding is happening during the real time health monitoring of the repaired region.

## 1.3 Nondestructive testing

A variety of conventional NDT methods have been used for years in several engineering disciplines in order to detect defects and evaluate structural integrity, with the most basic ones dating back to the mid-1960s. The technological advances in many fields of sciences have resulted in a significant progress in NDT technologies over the last few years. NDT technologies are required to reliably detect flaws over a critical size, to be least affected by local geometry and property variations and to operate fast with the least possible cost. Some of the most established techniques that are employed by the aircraft maintenance operators include: visual inspection, the eddy current technique, ultrasonic inspection and acoustic emission. Some background information will be provided for each of these methods while the reader can refer to the more extended work performed by Bar-Cohen [5], [6] and Staszewski et al. [3] for further details.

*Visual inspection* is one of the most widely used NDT techniques, for the evaluation of the structural integrity of metallic aircraft accounting for the detection of up to 80% of cracks. It provides immediate results with the least possible required

training but it is not recommended for composite structures since its efficiency is mostly restricted to surface or near surface damage, rather than internally, between plies.

The *Eddy current technique* monitors the change in the electromagnetic impedance due to damage. Closed loops of current are induced in the monitored structure by a coil [7]. All possible flaws in a conductor (inspected component/part) behave as an obstacle for these eddy currents, modify the magnetic field, and are eventually sensed by impedance change in the coil. The change of the impedance can be related to the depth, length and orientation of the defect. This technique has proved to be successful in detecting surface and subsurface damage (up to 6 mm depth). A requirement for its application is that the material is an electrical conductor. Its applicability is sometimes restricted due to the high power that is required and due to the difficulty in the data interpretation.

*Acoustic emission* is defined as the rapid release of elastic energy which could occur in composites due to a variety of failure modes such as fibre/resin cracking, fibre debonding or delaminations (ply separations). The released energy is captured in the form of an acoustic signal by appropriate sensors, bonded or embedded into the structure, such as accelerometers. Monitoring of discontinuities, fatigue failure, material flaws, welding flaws in metals and stress corrosion cracking has been successfully applied in many engineering areas. A limitation arises from the fact that this is a passive method, hence it requires loading of the inspected panel. As a consequence, the inspected part might fail to detect stabilised damage [8].

*Ultrasonic inspection* is probably the most established method for the inspection of both metallic and composite structures. Damage is located using the travel of ultrasonic waves within the material. The waves reflect and refract when they meet boundaries and the signal is received by sensors which are attached on the surface of the component. Ultrasonic waves can travel long distances (few metres long) in solid materials. When the waves travel through a damaged area, they are scattered or absorbed and the received signal is attenuated. A result of damage presence could be a change in velocity or amplitude or even conversion of modes.

Other conventional or emerging NDT methods and which have been used in the current work include: X-ray radiography, digital image correlation (DIC) and thermography. *Radiography* utilises gamma rays or X-rays and measures the degree of absorption from the inspected structure, which in turn indicates the presence of

defect or damage. The application of a penetrant solution is first required, therefore it can only detect open damage [9].

*Digital Image Correlation* is an optical method, which estimates the surface displacement and strain fields of an object when under loading in two possible patterns, 2-dimensional and 3-dimensional. The main principle of this method is to match the speckle pattern that covers the surface of the tested panel before and after the loading [10]. The speckle is created by applying a black and white paint on the examined surface. Then the estimation of the surface displacement vector is possible by means of sub-image correlations in the two pictures that are recorded by cameras [11]. The correlation of the sub-images is performed with certain softwares which are based on well established algorithms that utilise either subset-based cross correlation (CC) criteria or sum-squared difference (SSD) correlation criteria [12]. DIC can be performed on-line. More information can be found in Appendix A.

*Thermography* detects potential damage by collecting thermal images after thermal waves have been generated within the inspected material. Then the material emits thermal energy based on its thermal conductivity, its temperature and its emissivity of defects. Each time the generated energy meets a defect, it is reflected back and absorbed by a thermal camera [3]. Thermography can be performed on-line. More information can be found in Appendix B.

The aforementioned methods usually require an *a priori* knowledge of the presence of damage and its location, while the implementation of most of them is performed off-line in a local manner. The area to be inspected needs to be accessible and properly processed and sometimes expensive equipment needs to be utilised. A point to point measurement is usually performed which dramatically increases the cost and the duration of the inspections. In addition, some of these techniques require the removal of the tested component for an off-line inspection which increases the downtime of the structure. Finally their damage sensitivity is often reduced when complex structures are considered while the bulky transducers that are sometimes used can limit their efficiency and ease of application. Therefore the next step in damage detection moves towards the so called *structural health monitoring* area.

## 1.4 Structural health monitoring

*Structural health monitoring* (SHM) has shown considerable progress over the years with promising applications in aerospace, marine, automotive and civil industry. Research on SHM methods has proved their remarkable advantages over the traditionally used NDT due to the cost-effective and reliable damage detection abilities they provide. SHM is referred to as the process of implementing a damage identification strategy to aerospace, civil and mechanical infrastructure [13]. More generally, SHM systems have the ability to monitor the tested structures in a continuous and *in-situ* mode, to detect and interpret adverse changes and attribute those changes to critical damage. A robust SHM system can provide life-cycle health monitoring in order to avoid extended periods of inspections, reduce maintenance costs and avoid unexpected catastrophic failures. There are many categories in SHM testing which can be implemented on-line, among which perhaps the most common are vibration-based and wave propagation methods. This work focuses on the latter and more specifically on guided ultrasonic waves which will be discussed in detail. More detailed reviews can be found in literature [14], [3].

## 1.5 Motivation and objectives of the thesis

The main objective of this work is to set the basis for an on-line monitoring system that could be permanently installed in the repaired area and perform continuous monitoring. The author has identified the following main points which need to be addressed towards that direction.

**1)** Simulation and understanding of the underlying mechanisms of the Lamb wave propagation through metallic and polymer-based composite repaired structures with finite element analysis (FEA).

**2)** Study of the effect of different damage scenarios on the propagating waves and determination of damage indices which can identify critical damage and locations through FEA.

**3)** Experimental validation of the proposed monitoring technique on a variety of representative repairs, of different types, ranging from small scale to large scale industrial demonstrators and under aerospace typical loads, with additional support

from most established NDT methods for extra validation.

**4)** Establishment of advanced signal processing tools ranging from linear to non-linear statistical pattern recognition for damage assessment, and investigation of their performance and limitations for each experimental case study.

**5)** Exploration of potential solutions for the aforementioned limitations which aim to overcome problems related to undesirable noise and environmental effects or inadequate training data-sets.

**6)** Analysis of different ways of excitation of a pure Lamb wave mode based on simple and more elaborate excitation techniques and realisation of techniques to reliably determine the efficiency of the excitation methods through analysis of the obtained signals.

**7)** Investigation of the factors that could affect pattern recognition analysis such as the selection of features, and definition of alternative feature selection approaches through the definition of indices after the time-frequency analysis of the obtained signals.

## 1.6 Outline

**Chapter 1.** In this chapter the key points that motivated the current thesis are briefly introduced such as the need for a new repair methodology for the adhesively bonded composite patches in aircraft industry. Attention is focused on the need for on-line monitoring while its benefits are emphasised. A brief outline of the most representative NDT methods in aerospace industry is given and the advantages of the new SHM techniques are investigated. Finally the motivation and the objectives of the work are explained and an overview of the thesis is briefly presented.

**Chapter 2.** This chapter aims to address the most important characteristics of the technology of bonded repairs. First a general illustration of the application of this technology in aerospace industry is given and then the most critical design parameters are explained for the most representative types of repairs, namely the external patch and the scarf repairs. Finally the key problems related to this technology are demonstrated, justifying the need for SHM of the repaired area aiming towards a built-in monitoring system.

**Chapter 3.** A general background on the wave propagation theory in elastic solids is presented in this chapter, focusing on the bulk and guided waves and more specifically on the propagation of Lamb waves at isotropic and anisotropic plates. Finally the chapter demonstrates the fundamental theory regarding the generation and detection of Lamb waves and their applicability on nondestructive testing.

**Chapter 4.** A theoretical background and examples are presented in this chapter focusing on the pattern recognition and dimension reduction methods for high dimensional, multivariate data. A general introduction as well as a basic literature review are given aiming to explain the fundamental theory behind the outlier analysis, principal component analysis and nonlinear principal component analysis. The chapter also presents a brief literature review on the theory and the previously conducted work on various Fourier-based methods reaching the concepts of the instantaneous properties of nonstationary signals as well as some recent approaches for their estimation, such as the Hilbert-Huang transform. These methods were subsequently used for analysing data of specific applications.

**Chapter 5.** The complications that arise from inappropriate features are outlined in this chapter, and an alternative post-processing approach is proposed which would determine more reliable features, based on the time-frequency analysis of Lamb waves. An aluminium panel repaired with an aluminium, adhesively bonded patch was tested under fatigue. The proposed time-frequency analysis tools are evaluated first on simple Lamb wave responses and then a physical interpretation is attempted to be given on the basis of the effect of damage on the instantaneous properties of the acquired waves. Appropriate damage indices are defined and the performance of the selected features is assessed with respect to the developed damage.

**Chapter 6.** The aim of this chapter is the investigation of the effect of different kinds of damage on a simplified model of a repaired composite plate with a composite patch through modelling with finite elements. First the built model is presented and a validation study is performed. Then a study is demonstrated which focuses on the effect of different damage types on the first antisymmetric mode, namely debonding of different areas of the patch, degradation of the substrate and both types combined together.

**Chapter 7.** The objective here is to apply the outlier analysis and the linear and nonlinear principal component analysis, in experimental cases and to investigate the efficiency of each proposed method for the purpose of the successful damage clas-

sification under representative loading conditions. Two different repaired scenarios were considered, namely one scarf repair and one external patch repair, subjected to two different loading conditions, namely static and dynamic loading. Each repaired scenario investigates different pattern recognition concepts while the attempt of a pure mode excitation is performed at the external patch repair. The study deals with certain problems that can arise in realistic testing conditions such as noise and inadequate training data.

**Chapter 8.** This chapter presents the experimental testing of an aluminium helicopter stabilizer repaired with a composite patch under bending fatigue with the purpose of scaling up the previously investigated methods and determining the key challenges arising in real industrial applications. The chapter concludes on the performance of each processing method and establishes a benchmark for real industrial cases.

**Chapter 9.** The final chapter summarises the most important conclusions of the current work as well as the contribution to knowledge and presents some ideas regarding near future work.

# Chapter 2

# Bonded Repairs

Research on composite patches as a repair method has received considerable interest over the last years in many industries such as aerospace, automotive and marine. The big challenge of aircraft companies is to ensure operational life extension of ageing aircraft with the lowest possible maintenance cost [15]. Composite patch repair is a promising method which could meet the increasing aerospace industry demands for aircraft maintenance in an affordable, efficient and relatively easy to apply way [16]. SHM methods are an essential part for the design of a reliable and robust repair system. *In-situ* continuous damage assessment of the repaired region can provide information about the integrity of the repaired structure when it is subjected to mechanical and thermal loads. The 'smart' maintenance system will lead to the elimination of unscheduled maintenance after the implementation of the repair patch. A very good review of composite patches with applications in industry can be found in Baker's work [17], [18]. A brief literature review background will be outlined in this chapter concerning design and structural integrity monitoring aspects.

## 2.1 Composite repair patches

When metallic aircraft structures are subject to fatigue loads and corrosion, cracks might start propagating which can lead to unpredictable failures. These cracks can initiate in unexpected regions due to local stress concentration. This could be the

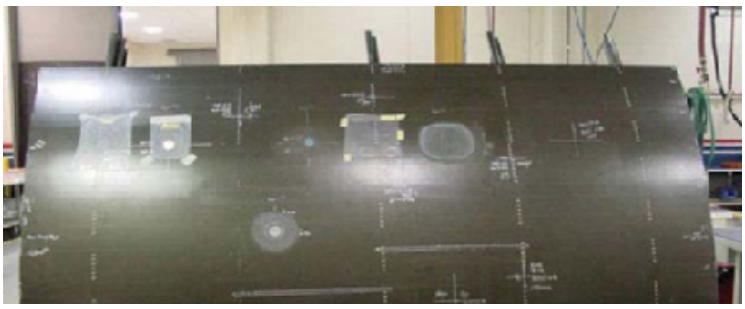

Figure 2.1: Panel with adhesively bonded composite patches [AMRC with Boeing research centre].

result of material defects, poor manufacturing procedures or in-service introduced damage. Traditional repair methods involved the disassembling of the damaged part and its repair with a mechanically fastened doubler. This approach leads to increased local overloads through the load transfer paths of the mechanical fasteners and results in high maintenance cost due to the required aircraft downtime [19]. The new age polymer-based composite aircraft are mostly susceptible to damage due to low velocity impact, the so-called barely visible impact damage (BVID). This type of damage can be the result of runaway debris, bird strikes or tool drop during manufacturing and can cause internal damage in the form of delamination or resin cracking which can lead to complete failure under loading. The traditional fastened doubler has no application on composite airframes, since mechanical fastening can cut fibres and cause further damage due to stress concentration. Representative external repairs performed on a fuselage-like structure are illustrated in Figure 2.1.

One of the most important advantages of composite repair patches is that they provide a lightweight solution, easy to design in order to address the shape and stiffness requirements of the repair, which is rather critical for aerospace structures. Compared to mechanical methods, adhesive bonding provides efficient load transfer paths and introduces less stress concentration into the structure [20]. Moreover, adhesive bonding seals the interface preventing in this way any possible fuel leakage and reduces the risk of fretting fatigue between the patch and the component. The application of the patch can be carried out *in-situ*, is suitable for emergency (field) cases and if performed carefully it can be considered as a permanent repair. It can either be pre-cured prior to its adhesion in the repaired region or co-cured. The damaged part is removed and the composite patch is adhesively bonded on the damaged region after the careful preparation of the surface [21]. The appropriate surface preparation specifically in the case of metallic substrates is of significant importance

in order to ensure a strong repair with long term environmental durability. Some of the most widely used methods include the grit blast/silane & primer (BR127) method, the phosphoric acid anodize surface preparation method (PACS) and the pasa-jell 105 surface preparation method. The surface preparation though, is more critical for cases where the patch aims to repair cracks. In this case, the surface treatment should be avoided in case the pre-existing crack propagates faster due to stress-corrosion. In such cases the phosphoric acid gel anodising surface treatment has shown better results [22], [23].

There is a variety of adhesively bonded repairs that are available depending on the severity of the damage. *Cosmetic repairs* refer to any type of damage that is structurally insignificant such as scratches or missing surface plies and only aims to restore the surface smoothness through the spread of a liquid adhesive or a resin compound into the damaged region, which then cures at room temperature. *Injection repairs* are used for minor disbonds or delaminations, in which case holes are drilled to the depth of the damage and filler resin is injected under pressure until the excess resin starts flowing out of them. A prior heating ensures the decrease in the resin's viscosity while the pressure ensures that the resin will fill any gaps in the repaired region. However when the severity of the damage is more critical, then other types of more elaborate repairs need to be employed such as *scarf repairs* and *external patch repairs* which are the focus of the current work [23].

### 2.1.1 External patch repairs

*External patch repair* is a type of repair that can be implemented following an easy procedure; it aims to provide a temporary restoration of the mechanical strength at regions that are not so critical in terms of structural performance. These repairs can be either one-sided or two-sided depending on the accessibility. This method usually follows the tapering design approach, according to which each repair ply overlaps the ply below in a way that it provides a straighter, stronger, load path, reducing the shear stresses that develop in the adhesive and the peel stresses that develop at the ends of the patch. There are certain design parameters which need to be considered before the application of an external patch. In Figure 2.2 a repaired configuration with a double external patch is illustrated. Here only a brief summary will be presented based on the results of a theoretical model by Hart-Smith [24], [25] and further developed by Hu and Soutis [21]. In this model, the repair is approached

as a single or double-lap joint on which a shear-lag model can be applied together with the maximum shear-strain criterion in the adhesive.

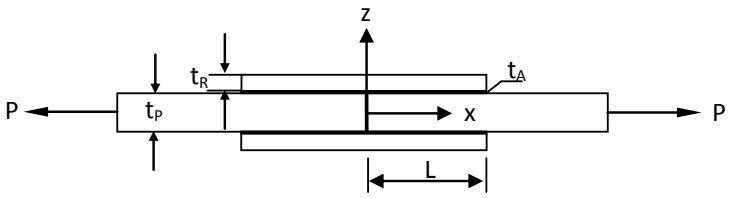


Figure 2.2: Double-lap joint [21].

The *optimum patch thickness* ($t_R$) is responsible for the overall strength of the joint and its selection is of critical importance. A thin patch or a patch with low elastic modulus leads to a repaired region of low strength. However, a patch that is overstiff might lead to increased weight and reduced strength due to higher shear stresses developed in the joint. In addition, as the thickness of the patch increases, then the through-thickness tensile stresses (peel stresses) can increase, potentially limiting the joint strength and causing failure in an adherent with a low through-thickness tensile strength. Therefore a good balance of membrane stiffness (i.e. the product of elastic modulus and thickness) should be kept between patches and the parent plate. If an appropriate stiffness ratio (SR) can be defined as the ratio of patch stiffness to skin stiffness, then the ideal SR value can be defined as 1. If the thickness of the patch is higher than the thickness of the substrate then bending moments could be introduced to the repaired region.

The *optimum overlap length* (L) is defined by the designer according to the mechanical conditions that the structure is expected to be subjected to and according to the various environmental conditions. Short overlap length leads to high shear stresses that can develop in the adhesive material. As the overlap length increases, the failure strength of the adhesive increases until the length reaches a critical point after which there is no considerable benefit. However the limiting overlap for current carbon fibre-epoxy systems is around $30t_R$, where $t_R$ is the repair patch thickness. The reason for that is that several factors should be taken into account such as imperfect bonding, patch delamination, environmental effects and a safety factor. In practice it is recommended that a patch length of 80–100 times the repair thickness be used.

The *adhesive thickness* ($t_A$) is perhaps the most important design parameter in repair patches since it carries most of the developed shear loads. Therefore an adhe-

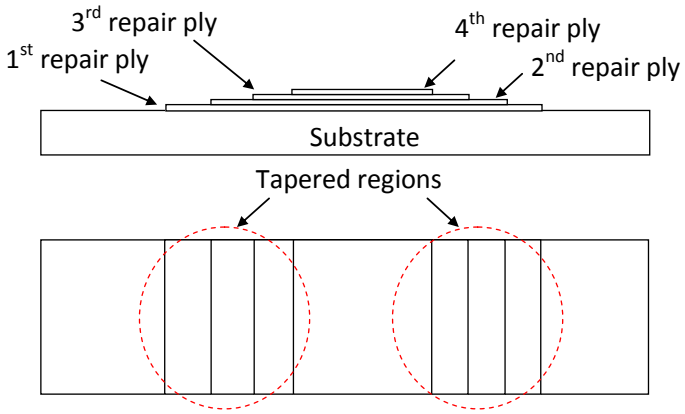


Figure 2.3: Illustration of the tapering manufacturing technique on a 4-plies external patch repair.

sive material with high shear properties is desirable. An important manufacturing characteristic that contributes to the reduction of the stress concentration in the adhesive layer is tapering of the patch (Figure 2.3). Based on this method, each repair ply overlaps the ply that it is repairing giving a straighter, stronger load path. This method will eventually reduce the developed peel stresses which are introduced at the ends of the patch [26]. Additionally the tip thickness is reduced and the adhesive layer at that region is deliberately increased in order to minimise the shear strain developed at the edges. However, thick bonds could be porous and weak. The selection of the adhesive relies on a variety of parameters such as its shear modulus, its performance in environmental conditions that the structure might be exposed to, cure temperatures and ease of application.

It has been widely accepted by many researchers that double-sided symmetric bonded repairs offer significant advantages over single-sided bonded composite repairs. The first category provides a significant reduction in the stress intensity of the repaired region and improves the structural behaviour under fatigue by increasing its fatigue life up to two times compared to the single-sided repair [27]. This is on one hand due to the double stress transfer in the double-sided configuration and on the other hand due to the eccentricity of the composite patch which avoids the development of the bending effect that can be observed in the single-sided patch. In addition, the stress distribution in the case of the symmetric repair is uniform. The stress intensity factor is reduced by up to 30% compared to single-sided repair. If the bending effect is considered on top of that, then the difference can reach the percentage of 40%. One of the significant disadvantages that needs to be taken into consideration

though is the fact that with double-sided repairs there is the risk of higher residual stress development due to the double adhesive curing. This can be a problem mainly when the repaired component is metallic. It is reported that the use of a circular shape of the patch can potentially reduce the intensity of the developed thermal residual stresses [27].

### 2.1.2 Scarf patch repairs

*Scarf patch repair* technology is performed when severe damage needs to be repaired and when the key requirements are the maintenance of the surface smoothness and of the aerodynamic properties of the repaired structure. Scarf repairs are also preferred when the component that has to be repaired is relatively thick, since a scarf does not add an excessive out-of-mould line thickness such as external patches do and it also offers higher peel and shear strengths [28]. Also scarf repairs are more flexible when different shapes have to be considered in order to match the geometry that has to be repaired.

This type of repair is implemented after the damaged region is removed and then the patch is implemented while matching ply to ply the original structure [21]. For the implementation, a careful preparation of the region is required (step sand) in order to obtain the correct scarf angle and dimensional tolerances while removing the damaged region. The tapered area is a function of the number of plies or structure thickness with most common taper ratios of length to thickness for thin structures being 50:1 and 30:1 for thicker structures. The ply orientation of the patch and the laminate should be the same. In commercial applications sometimes additional plies are required, overlapping the patch in order to protect the tip of the scarf patch and provide extra reinforcement by more effectively carrying the loads [29].

There are two main techniques for the manufacturing of the scarf repairs, namely the soft-patch and the hard-patch. The first involves the lay up of the plies in the scarf cavity and its subsequent curing on the plate, while the later involves the adhesive bonding of a pre-formed patch into the scarf cavity. In the second method the patch can either be manufactured in a mould (moulded approach) or machined from a composite panel following the geometry requirements of the scarf cavity [29]. The most commonly employed shape of the patch is a concentric ellipse since lower stresses develop.

There are certain disadvantages that have to be considered before the implementation of a scarf repair such as the design procedure. First of all, the manufacturing of a scarf repair requires a higher level of expertise than the other types. Moreover it results in the removal of an excessive amount of undamaged material for the achievement of an appropriate scarf angle, which has to be approximately 3° in order to ensure the stiffness and strength recovery [29]. This might reduce the buckling resistance of the repaired configuration when loaded under compression or bending.

## 2.2 Structural health monitoring of repair patches

In recent years, researchers have become increasingly interested in the problems related to repair patches that can emerge either from design issues or from extensive loading, such as the risk of debonding between the patch and the substrate [20]. That might occur if the ultimate shear strength of the adhesive is exceeded. Moreover, the rate at which the stress intensity factor of the crack tip increases under loading under the patch in metallic structures might exceed the threshold resulting in failure. In the same way, composite structures might develop resin microcracks around the removed damaged area which can propagate under the patch. In addition, failure might be caused by the peel stresses introduced at the ends of the patch. The thickness of the patch is of high importance since it can fail under bending stresses if it is too thin. Additionally the surface preparation prior to bonding can affect the effectiveness of the repair. Finally one of the most significant weaknesses of the application of composite patches like boron/epoxy and graphite/epoxy on metallic substrates is the development of residual tensile stresses due to the mismatch in the thermal expansion coefficients which occurs in the final stage of the curing process (cooling down). This in the end will introduce compressive or tensile strains which will affect the structural integrity of the repaired region [30].

An example that displays the necessity of monitoring of the repair can be seen in Figure 2.4. A composite plate, 250 mm long and 300 mm wide, is illustrated on which a pre-preg patch has been attached and cured. The patch was attached at the centre of the plate, and it consisted of 5 plies following a 20 mm step wise configuration. The overall size of the patch was 160 x 160 mm. Four areas of no adhesion were introduced between the substrate and the first patch layer (5 mm, 10 mm, 15 mm

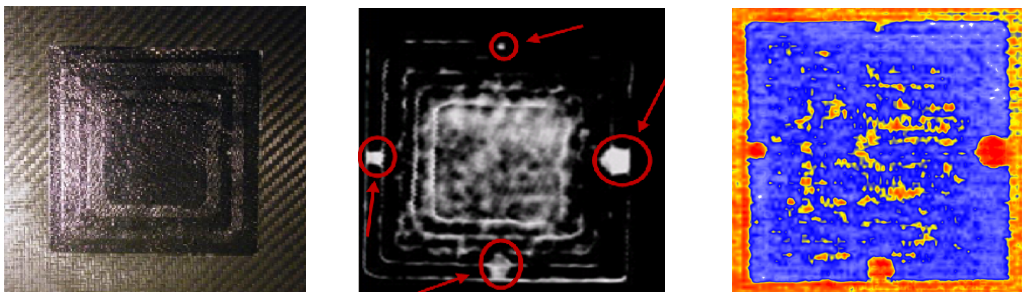

(a) External patch repair (b) C-scan (c) Sampling phased array

Figure 2.4: C-scan and sampling phased array scanning of an external composite patch with pre introduced defects (shown by arrows). [31]

and 20 mm). As is clearly observed from the picture of the repaired configuration in Figure 2.4(a), no visible damage can be detected. However, ultrasonic C-scan testing was performed which confirmed the extensive damaged areas underneath the surface (indicated in Figure 2.4(b) with red arrows). Additionally the result of an alternative NDT method is illustrated, namely sampling phased array, illustrated in Figure 2.4(c). This technique is a novel phased array technology developed in the Fraunhofer Institute for nondestructive testing, Germany (IZFP) and the test was conducted during the visit of the author to the institute. The technique aims to reconstruct the defects at high inspection speeds through the scanning of the tested panel with a single shot compared to the conventional phased array, providing higher sensitivity and resolution especially for anisotropic materials [32]. Both NDT techniques successfully identified the pre-introduced defects as well as possible voids in the repaired region.

Consequently, there are several critical reasons which make the design of a continuous monitoring system of high importance in order to ensure the high performance of the repaired components. Recent interest has been focused on the continuous life cycle health monitoring of the repaired site which will ensure the reliability of the repair and will avoid any unexpected failure [33]. The key point that makes such health monitoring systems necessary, is the increase of portability which will eliminate any restrictions like the removal of parts for lab testing. Baker [34] highlighted the importance of a smart patch to perform on-line structural health monitoring which will be necessary to get industrial approval for the wide application of repair patches as a repair method.

Built-in structural diagnosis is a concept which has relatively lately emerged and which is one of the most promising approaches related to patch repair monitoring.

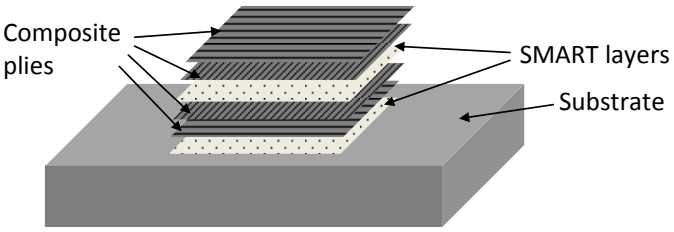


Figure 2.5: SMART layer inserted in the plies of a composite repair patch. [35]

SMART layers consist of a network of built-in sensors which can be inserted in the critical plies of the patch. These sensors can be piezoelectric sensor arrays, strain gauge-based techniques or optic fibres. Jones et al. demonstrated the effectiveness of an optical fibre sensor array in monitoring crack growth and delamination under a bonded repair [36]. In recent work by Soutis et al. two SMART layers with an embedded network of piezoelectric actuators/sensors were inserted into a boron/epoxy laminated patch at different ply-locations to successfully monitor crack growth via Lamb wave excitation [37]. A similar experimental set-up for SMART layer implementation in a composite repaired configuration which has been efficiently used for cure monitoring, bond evaluation and damage under fatigue detection [38] is illustrated in Figure 2.5. The vast majority of these techniques utilise Lamb waves which will be discussed in the next chapter.

## 2.3 Discussion

This chapter presented a brief introduction in the underlying concepts of repairs with a more specific focus on the composite adhesively bonded patch repair. Among the most common categories, two are the most commercially promising which will be the consideration of this work, namely external patch repairs and scarf patch repairs. Their main design features were discussed and the risks that make the need of continuous monitoring of their structural integrity were realised. The most recent approach is on-line monitoring with built-in diagnostics which is expected to help towards an industrial approval and certification. In the next chapter, ultrasonic waves, their propagation characteristics and properties are presented and discussed.

# Chapter 3

# Ultrasonic Waves

Techniques utilising ultrasonic waves have been extensively used in a wide range of fields with more significant applications in nondestructive testing and medical diagnosis. These fields have extensively taken advantage of the physical principles of the ultrasonic waves in order to describe the underlying mechanisms in each field. This chapter aims to provide a general background on the wave propagation theory in elastic solids, focusing on the different mechanisms that describe the bulk waves and the Lamb waves and to highlight important concepts such as the concept of dispersion and cut-off frequencies as well as the physical meaning of the propagation modes. More attention will be given on the propagation of Lamb waves in anisotropic elastic solids which is the primary case study of this thesis. Finally, the chapter will demonstrate the fundamental theory regarding the generation and detection of Lamb waves, analysis of signals and relation to damage, and their applicability in nondestructive testing.

## 3.1 Wave propagation in isotropic elastic solids

There is a variety of waves that can propagate in solids which primarily depends on the boundary conditions. The easier type of wave in terms of physical interpretation is the one that propagates through unbounded solids, namely the *bulk waves*. In this case, there are basically two types of waves, the *dilatational* and the *distorsional*. Each of these types can be explained by examining the particle's motion with re-

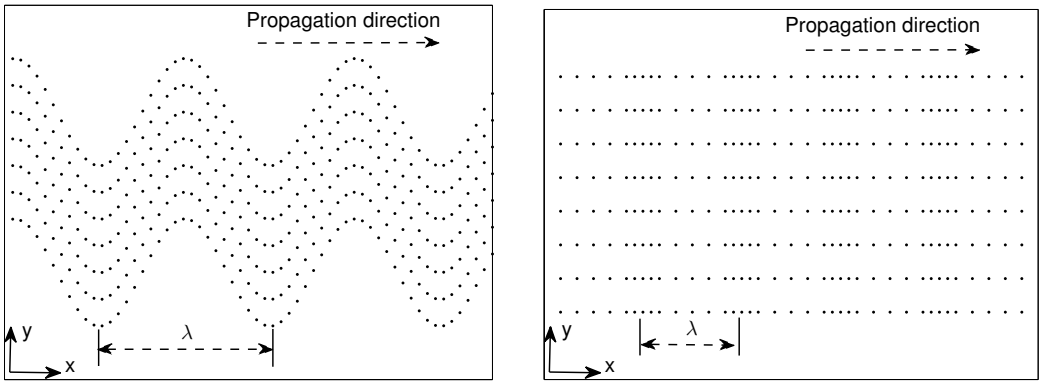


(a) Shear waves (b) Longitudinal waves

Figure 3.1: Particles motion with respect to the direction of the propagation for shear (a) and longitudinal (b) waves.

spect to the direction of propagation. More specifically, the first category, otherwise referred to as *longitudinal*, *pressure*, or *primary* (P) waves, describes a parallel particle's motion to the wave propagation direction. The second category, otherwise referred to as *transverse*, *shear* or *secondary* (S) waves, describes a transverse particle's motion to the wave propagation direction. In addition, the later category can be further divided into two sub-categories, based on the polarisation of the waves. Therefore if they are horizontally polarised, they are referred to as *shear horizontal waves* (SH), while if they are vertically polarised (z-axis) they are referred to as *shear vertical waves* (SV). Figures 3.1 and 3.2 illustrate the underlying differences.

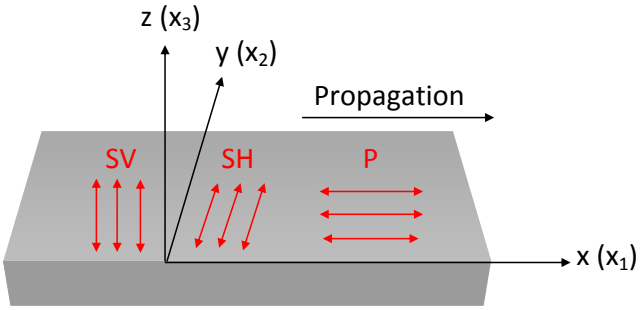


Figure 3.2: Types of bulk waves that can propagate in solids.

Wave propagation mechanisms become more complicated when a bounded media is considered where the propagating waves interact with the boundaries. In this case, the type of the wave is referred to as a *guided wave* as the wave is 'guided' by the boundaries of the media, the names of which have been given after the names of their investigators. Some examples of guided waves are the *Rayleigh waves* which

propagate on the surface of semi-infinite solids. This type of waves travels very close to the surface of the plate and decays in amplitude at a certain distance from the surface. Such waves are typically produced by earthquakes at the surface of the earth. In addition to Rayleigh waves, *Stonely waves* travel at the interface between two media. The amplitude of the wave is high when it travels close to the interface of the media while it decays as it travels away from it. *Lamb waves* is another category of guided waves, which are plane strain waves that occur in a free plate, exhibiting different propagation modes and depending upon the frequency of the wave and the thickness of the plate. The last category will be investigated in more detail in later section.

In principle, the equations that govern the bulk and the guided waves are similar, while the main difference lies in the fact that the equations that describe the latter should satisfy the boundary conditions which makes the solution of such equations a quite demanding task. In addition, there is an infinite number of modes that can occur in guided wave propagation in contrast to bulk waves where the number of modes is finite. In this chapter, a more detailed approach of the basic motion equations will be given with focus only on the bulk waves and the propagation of Lamb waves in isotropic media.

### 3.1.1 Bulk waves

The mathematical expression of the wave propagation as bulk waves that is presented in this section is based on the theoretical approaches demonstrated by Kolsky [39]. The equation of motion for an elastic media which is approached by the investigation of the stress variation across a small rectangular parallelepiped is derived from Newton's second law. If the body forces are neglected the equation can be expressed as:

$$\rho \frac{\partial^2 u_i}{\partial t^2} = \frac{\partial \sigma_{ij}}{\partial x_j} \tag{3.1}$$

where $i$, $j$=1, 2, 3, $u_i$ is the particle's displacement in the 1, 2, 3 or x, y, z directions, $\sigma_{ij}$ is the stress field tensor and $\rho$ is the density of the material. According to the generalised Hooke's law, the stress $\sigma_{ij}$ of a given isotropic elastic material is proportional to the stiffness tensor $C_{ijkl}$ and the strain $\epsilon_{ij}$:

$$\sigma_{ij} = C_{ijkl}\varepsilon_{kl} \tag{3.2}$$

where *i, j, k, l*=1, 2, 3 and the strain tensor $\epsilon_{ij}$ is linked to the displacement $u$ equations by:

$$\varepsilon_{ij} = \frac{1}{2}(\frac{\partial u_i}{\partial x_j} + \frac{\partial u_j}{\partial x_i}) \tag{3.3}$$

where *i, j*=1, 2, 3. Based on the stress symmetry $\sigma_{ij}$=$\sigma_{ji}$ and on the strain symmetry $\epsilon_{ij}$=$\epsilon_{ji}$, the stiffness tensor derives the following symmetry expressions: $C_{ijkl}$=$C_{jikl}$ and $C_{ijkl}$=$C_{ijlk}$ respectively. In addition, if the following matrix notation is defined:

$$[\sigma] = \begin{bmatrix} \sigma_{11} \\ \sigma_{22} \\ \sigma_{33} \\ \sigma_{23} \\ \sigma_{31} \\ \sigma_{12} \end{bmatrix} \equiv \begin{bmatrix} \sigma_1 \\ \sigma_2 \\ \sigma_3 \\ \sigma_4 \\ \sigma_5 \\ \sigma_6 \end{bmatrix} ; \; [\varepsilon] = \begin{bmatrix} \varepsilon_{11} \\ \varepsilon_{22} \\ \varepsilon_{33} \\ 2\varepsilon_{23} \\ 2\varepsilon_{31} \\ 2\varepsilon_{12} \end{bmatrix} \equiv \begin{bmatrix} \varepsilon_1 \\ \varepsilon_2 \\ \varepsilon_3 \\ \varepsilon_4 \\ \varepsilon_5 \\ \varepsilon_6 \end{bmatrix} \tag{3.4}$$

then the stiffness tensor can be analytically expressed as:

$$\begin{bmatrix} C_{11} & C_{12} & C_{13} & C_{14} & C_{15} & C_{16} \\ .. & C_{22} & C_{23} & C_{24} & C_{25} & C_{26} \\ .. & .. & C_{33} & C_{34} & C_{35} & C_{36} \\ .. & .. & .. & C_{44} & C_{45} & C_{46} \\ .. & .. & .. & .. & C_{55} & C_{56} \\ .. & .. & .. & .. & .. & C_{66} \end{bmatrix} \tag{3.5}$$

Hooke's law can also be written as:

$$\sigma_{ij} = \lambda \delta_{ij} \varepsilon_{kk} + 2\mu \varepsilon_{ij} \tag{3.6}$$

where $\delta$ is the Kronecker delta and $\lambda$, $\mu$ are the Lamé constants which describe the only non-zero elastic coefficients of an isotropic material and they are sufficient for describing its elastic behaviour:

$$C_{12} = C_{13} = C_{21} = C_{23} = C_{31} = C_{32} = \lambda \tag{3.7}$$

$$C_{44} = C_{55} = C_{66} = \mu \tag{3.8}$$

$$C_{11} = C_{22} = C_{33} = \lambda + 2\mu \tag{3.9}$$

The Lamé constants can also be expressed in terms of the Young's modulus $E$, Poisson's ratio $\nu$ and bulk modulus $\mu$, for more practical convenience. These expressions

are based on the definition of $E$ as the ratio between the applied stress and fractional extension when an uniform stress is applied to the plane ends of an unconstrained cylindrical or prismatic specimen, and on the definition of $\nu$ as the ratio between the lateral contraction and longitudinal extension of the specimen:

$$E = \frac{\mu(3\lambda + 2\mu)}{\lambda + \mu} \tag{3.10}$$

$$\nu = \frac{\lambda}{2(\lambda + \mu)} \tag{3.11}$$

Taking into consideration the expressions above, equation (3.1) (Navier equation), can be rewritten as:

$$\rho \frac{\partial^2 u_i}{\partial t^2} = (\lambda + \mu) \frac{\partial \triangle}{\partial x_i} + \mu \bigtriangledown^2 u_i \tag{3.12}$$

where $i$, $j$=1, 2, 3; $\triangle$=$\varepsilon_{11}$+$\varepsilon_{22}$+$\varepsilon_{33}$, which represents the change in the volume of a unit cube, is referred to as dilatation, and the operator $\bigtriangledown^2$ is defined to be equal to $\partial^2/\partial {x_1}^2$+$\partial^2/\partial {x_2}^2$+$\partial^2/\partial {x_3}^2$. If equation (3.12) is further processed, then it can be proved that two different velocities propagate in the interior of the medium. These two velocities correspond to the previously mentioned longitudinal and shear waves, among which the first represents motion where no rotation takes place and the second represents motion where no dilatation occurs. The Lamé constants can be expressed as:

$$\lambda = \rho c_L^2 - 2\mu \tag{3.13}$$

$$\mu = \rho c_T^2 \tag{3.14}$$

where $c_L$ represents the longitudinal propagation velocity and $c_T$ represents the transverse propagation velocity, hence enabling the separate representation of the two propagation modes as demonstrated below for the longitudinal and the shear waves.

$$\frac{\partial^2 u_i}{\partial t^2} = c_L^2 \bigtriangledown^2 u_i \tag{3.15}$$

$$\frac{\partial^2 u_i}{\partial t^2} = c_T^2 \bigtriangledown^2 u_i \tag{3.16}$$

Based on Helmholtz's theorem, the displacement vector $u$ can be decomposed into a scalar potential $\phi$ and a vector potential $\psi$ as:

$$u = \bigtriangledown \phi + \bigtriangledown \times \psi \tag{3.17}$$

If this equation is substituted into the Navier equation (3.12), one obtains the following:

$$\bigtriangledown\left[(\lambda+2\mu)\bigtriangledown^2\phi-\rho(\frac{\partial^2\phi}{\partial t^2})\right]+\bigtriangledown\times\left[\mu\bigtriangleup^2\psi-\varrho\frac{\partial^2\psi}{\partial t^2}\right]=0 \tag{3.18}$$

This equation requires that both terms are zero, which eventually leads to the wave equations that describe each mode (longitudinal and shear) as:

$$\bigtriangledown^2\phi=\frac{1}{c_L^2}\frac{\partial^2\phi}{\partial t^2} \tag{3.19}$$

$$\bigtriangledown^2\psi=\frac{1}{c_T^2}\frac{\partial^2\psi}{\partial t^2} \tag{3.20}$$

The resulting equations are uncoupled. The physical meaning of the scalar potential $\phi$ is associated with the dilatation and the vector potential $\psi$ is associated with the rotation enabling the effect of each mode on the media's motion. Finally from equations (3.13) and (3.14) the general expression for the longitudinal ($x_1$) and the transverse ($x_3$) propagation velocities for the infinite isotropic medium can be given respectively as:

$$c_L=\sqrt{\frac{(\lambda+2\mu)}{\rho}},\quad c_T=\sqrt{\frac{\mu}{\rho}} \tag{3.21}$$

while the respective wavelengths can be defined as:

$$\lambda_L=\frac{c_L}{f}=\frac{2\pi c_L}{\omega}=\frac{2\pi}{k_L},\quad \lambda_T=\frac{c_T}{f}=\frac{2\pi c_T}{\omega}=\frac{2\pi}{k_T} \tag{3.22}$$

where $k_L$ and $k_T$ are the respective wave numbers, $\omega$ is the circular frequency and $f$ is the temporal frequency.

### 3.1.2 Lamb waves

Lamb waves were first proposed by Horace Lamb in 1917 and since then a remarkable progress has been made in understanding their complicated mechanisms. The model that describes the basic approach of the governing equations that will be given here, is based on the free plate problem as described in [40] which is illustrated in Figure 3.3. This is a infinite plate with thickness d=2h.

When an elastic perturbation occurs at the plate, then the particles of the material propagate both in a parallel and perpendicular direction to the propagation. It needs

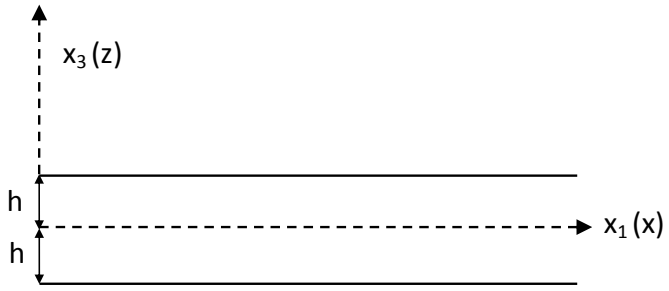


Figure 3.3: Free plate of thickness d=2h for the estimation of Lamb wave equations for isotropic materials.

to be reminded at this point, that shear waves can propagate in two polarisation modes, creating a series of SH and SV modes. If we assume that the propagation occurs at direction $x_1$, and only plane strain is considered ($\partial/\partial x_2$=0 $u_2$=0), then based on the Helmholtz decomposition, the longitudinal and shear wave equations are given respectively as:

$$\frac{\partial^2\phi}{\partial x_1^2}+\frac{\partial^2\phi}{\partial x_3^2}=\frac{1}{c_L^2}\frac{\partial^2\phi}{\partial t^2} \tag{3.23}$$

$$\frac{\partial^2\psi}{\partial x_1^2}+\frac{\partial^2\psi}{\partial x_3^2}=\frac{1}{c_T^2}\frac{\partial^2\psi}{\partial t^2} \tag{3.24}$$

and the resulting displacements and stresses can be obtained as:

$$u_1=\frac{\partial\phi}{\partial x_1}+\frac{\partial\psi}{\partial x_3} \tag{3.25}$$

$$u_3=\frac{\partial\phi}{\partial x_3}-\frac{\partial\psi}{\partial x_1} \tag{3.26}$$

$$\sigma_{31}=\mu(\frac{\partial u_3}{\partial x_1}+\frac{\partial u_1}{\partial x_3})=\mu(\frac{\partial^2\phi}{\partial x_1\partial x_3}-\frac{\partial^2\psi}{\partial x_1^2}+\frac{\partial^2\psi}{\partial x_3^2}) \tag{3.27}$$

$$\sigma_{33}=\lambda(\frac{\partial u_1}{\partial x_1}+\frac{\partial u_3}{\partial x_3})+2\mu\frac{\partial u_3}{\partial x_3}=\lambda(\frac{\partial^2\phi}{\partial x_1^2}+\frac{\partial^2\phi}{\partial x_3^2})+2\mu(\frac{\partial^2\phi}{\partial x_3^2}-\frac{\partial^2\psi}{\partial x_1\partial x_3}) \tag{3.28}$$

In order to solve equations (3.23) and (3.24), a solution has been proposed which as described in [41], represents travelling waves in the $x_1$ direction and standing waves in the $x_3$ direction. This suggested solution is called *transverse resonance* and it represents only waves that travel along the direction of the plate while the distributions in the transverse direction are assumed to be fixed. This can be understood from the fact that only the variable $x_1$ is contained in the complex exponential term

in the following equations.

$$\phi = \Phi(x_3)\exp[i(kx_1 - \omega t)] \tag{3.29}$$

$$\psi = \Psi(x_3)\exp[i(kx_1 - \omega t)] \tag{3.30}$$

If these equations are substituted into equations (3.23) and (3.24) aiming to express the unknown functions $\Phi$ and $\Psi$, then the following expressions can be obtained:

$$\Phi(x_3) = B_1\sin(px_3) + B_2\cos(px_3) \tag{3.31}$$

$$\Psi(x_3) = C_1\sin(qx_3) + C_2\cos(qx_3) \tag{3.32}$$

where $B_1$, $B_2$, $C_1$ and $C_2$ are arbitrary constants, $k$ is the Lamb wave number, $\omega$=$2\pi f$ and

$$p^2 = \frac{\omega^2}{c_L^2} - k^2 \quad \text{and} \quad q^2 = \frac{\omega^2}{c_T^2} - k^2 \tag{3.33}$$

Substitution of equations (3.29) and (3.30) into the obtained equations for the displacements (3.25), (3.26) and the stresses (3.27), (3.28) and if the term $exp[i(kx_1\text{-}\omega t)]$ is omitted from the resulting equations, then the following expressions are obtained:

$$u_1 = [ik\Phi(x_3) + \frac{d\Psi(x_3)}{dx_3}] \tag{3.34}$$

$$u_3 = [\frac{d\Phi(x_3)}{dx_3} - ik\Psi(x_3)] \tag{3.35}$$

$$\sigma_{33} = [\lambda(-k^2\Phi(x_3) + \frac{d^2\Phi(x_3)}{dx_3^2}) + 2\mu(\frac{d^2\Phi(x_3)}{dx_3^2} - ik\frac{d\Psi(x_3)}{dx_3})] \tag{3.36}$$

$$\sigma_{31} = \mu(2ik\frac{d\Phi(x_3)}{dx_3} + k^2\Psi(x_3) + \frac{d^2\Psi(x_3)}{dx_3^2}) \tag{3.37}$$

### 3.1.3 Propagation modes

What is clear from equations (3.31), (3.32), (3.36) and (3.37), is that the obtained expressions involve symmetric and antisymmetric modes, which are represented with the sines and cosines functions which are odd and even about $x_3$=0 respectively. This enables the separation of two solutions, each one governing each mode. Displacements in direction $x_1$ are assumed to be symmetric when the respective displacement $u_1$ contains only cosines and antisymmetric when it contains only sines. The opposite

happens with the displacements in direction $x_3$.

First the equations for the symmetric modes will be demonstrated. Therefore we assume that the constants $B_1$, $C_2$ which are associated with the antisymmetric modes are zero. If equations (3.31), (3.32), (3.36) and (3.37) are combined, the following expressions regarding the displacements and stresses of the symmetric modes can be obtained.

$$u_1 = ikB_2 \cos(px_3) + qC_1 \cos(qx_3) \tag{3.38}$$

$$u_3 = -pB_2 \sin(px_3) - ikC_1 \sin(qx_3) \tag{3.39}$$

$$\sigma_{31} = \mu[-2ikpB_2 \sin(px_3) + (k^2 - q^2)C_1 \sin(qx_3)] \tag{3.40}$$

$$\sigma_{33} = -\lambda(k^2 + p^2)B_2 \cos(px_3) - 2\mu[p^2 B_2 \cos(px_3) + ikqC_1 \cos(qx_3)] \tag{3.41}$$

The displacements in direction along the propagation are symmetric with respect to the mid-plane of the plate and the displacements in the direction vertical to the propagation are antisymmetric. This property is very important and it will be later exploited for verifying the isolation of specific modes for finite elements analysis by monitoring the displacements at the middle plane of the tested plates. If the plane strain traction-free boundary conditions that have been assumed for the plate model are considered ($\sigma_{31}$=$\sigma_{33}\equiv 0$ at $x_3$=$\pm d/2$= $\pm h$), then the unknown constants $B_2$, $C_1$ can be defined. This can be done if the determinant of the coefficient matrix of the homogeneous system that will result from the equations that define the constants is zero, in order to ensure solutions other than trivial one. This would lead to the following expression:

$$\begin{bmatrix} -2ikp\sin(ph) & (k^2 - q^2)\sin(qh) \\ -(\lambda k^2 + \lambda p^2 + 2\mu p^2)\cos(ph) & -2\mu ikq\cos(qh) \end{bmatrix} \cdot \begin{bmatrix} B_2 \\ C_1 \end{bmatrix} = \begin{bmatrix} \sigma_{11} \\ \sigma_{31} \end{bmatrix} = 0 \tag{3.42}$$

After some manipulation of the equation above, the following expression is obtained.

$$\frac{\tan(qh)}{\tan(ph)} = \frac{4k^2 qp\mu}{(\lambda k^2 + \lambda p^2 + 2\mu p^2)(k^2 - q^2)} \tag{3.43}$$

If the expression above is further simplified by assuming the expressions defined for the longitudinal $c_L$ and the transverse $c_T$ velocities in equation (3.21), then the final equation, often referred to as *Rayleigh-Lamb frequency relation*, for the symmetric mode is derived:

$$\frac{\tan(qh)}{\tan(ph)} = -\frac{4k^2 pq}{(q^2 - k^2)^2} \tag{3.44}$$

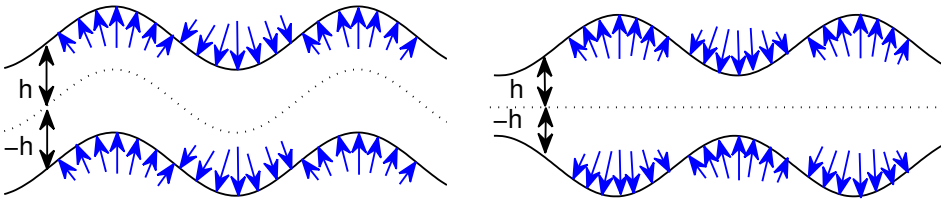


(a) Antisymmetric mode (b) Symmetric mode

Figure 3.4: Illustration of the antisymmetric (a) and symmetric (b) Lamb wave modes.

In the same way the respective equations for the antisymmetric modes can be determined if the constants $B_2$, $C_1$ which are associated with the symmetric modes are zero.

$$u_1 = ikB_1 \sin(px_3) - qC_2 \sin(qx_3) \tag{3.45}$$

$$u_3 = pB_1 \cos(px_3) - ikC_2 \cos(qx_3) \tag{3.46}$$

$$\sigma_{31} = \mu[2ikpB_1 \cos(px_3) + (k^2 - q^2)C_2 \cos(qx_3)] \tag{3.47}$$

$$\sigma_{33} = -\lambda(k^2 + p^2)B_1 \sin(px_3) - 2\mu[p^2 B_1 \sin(px_3) - ikqC_2 \sin(qx_3)] \tag{3.48}$$

Similarly, the nature of the propagation for the antisymmetric modes across the thickness, is symmetric at a vertical direction to the propagation and antisymmetric at a parallel direction to the propagation. Then following the same procedure as with the symmetric modes, the Rayleigh-Lamb frequency relations can be obtained for the antisymmetric modes as below:

$$\frac{\tan(qh)}{\tan(ph)} = -\frac{(q^2 - k^2)^2}{4k^2pq} \tag{3.49}$$

It should be reminded that, $k$ is the Lamb wave number and is equal to $\omega/c_p$, where $c_p$ is the *phase velocity* of the Lamb wave mode and $\omega$ is the circular frequency.

The illustration of the two Lamb wave modes is presented in Figure 3.4. The Rayleigh-Lamb frequency equations were derived following the method of potentials as proposed by Achenbach [42]. It is clear however, that this approach can only be valid for isotropic materials; yet it is considered a fundamental interpretation of the basic equations that govern Lamb waves. An alternative approach proposed by Solie

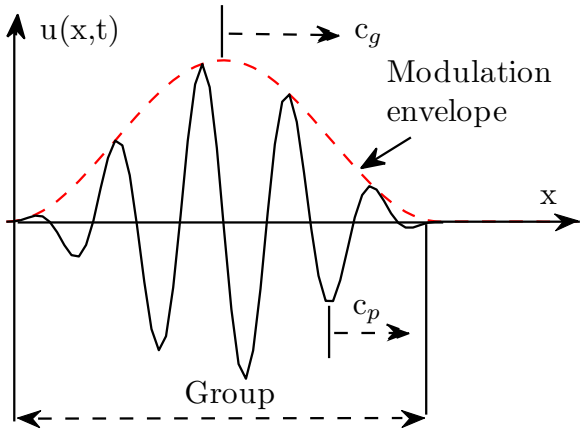


Figure 3.5: Phase ($c_p$) and group velocities ($c_{gr}$) of a pulse.

and Auld [43] attempts to derive the Lamb wave equations through the partial wave technique which aims to include the case of wave propagation in anisotropic media. This approach will be discussed later. The solution of the Rayleigh-Lamb equations can be a quite demanding task, often requiring advanced numerical methods.

### 3.1.4 Phase and group velocities

Two of the most important aspects of Lamb waves that determine their behaviour are the *phase velocity* ($c_p$) and *group velocity* ($c_{gr}$). The phase velocity of the Lamb wave mode has been previously introduced as equal to $\omega/k$. The phase velocity is associated with the velocity of the phase of a wave mode at a given frequency. However, in cases where wave packages form, such as in the propagation of Lamb waves, the introduction of the concept of group velocity is necessary. Therefore as group velocity one could define the velocity at which a group of waves propagates, which can be lower than the phase velocity as a wave package advances through a group and it decays as it approaches its interior limit (Figure 3.5). A brief explanation of how the group velocity of the Lamb waves is derived will be given in this section as explained in the work of Stokes [44] and Graff [45].

If two propagating harmonic waves are considered which have equal amplitude but different frequencies, $\omega_1$ and $\omega_2$, then the displacement formula will be given as:

$$u = A\cos(k_1 x - \omega_1 t) + A\cos(k_2 x - \omega_2 t) \tag{3.50}$$

where $k_1$=$\omega_1/c_1$ and $k_2$=$\omega_2/c_2$. Based on the following trigonometric identity:

$$A(\cos\alpha + \cos\beta) = 2A[\cos(\frac{\alpha-\beta}{2}) \cdot \cos(\frac{\alpha+\beta}{2})] \tag{3.51}$$

then:

$$u = 2A\cos[\frac{1}{2}(k_2-k_1)x - \frac{1}{2}(\omega_2-\omega_1)t] \cdot \cos[\frac{1}{2}(k_2+k_1)x - \frac{1}{2}(\omega_2+\omega_1)t] \tag{3.52}$$

where the following can be defined:

$$\omega_2 - \omega_1 = \Delta\omega \tag{3.53}$$

$$k_2 - k_1 = \Delta k \tag{3.54}$$

and the average circular frequency and the wave number are defined as:

$$\bar{\omega} = \frac{1}{2}(\omega_1 + \omega_2) \tag{3.55}$$

$$\bar{k} = \frac{1}{2}(k_1 + k_2) \tag{3.56}$$

and then the representation of equation (3.52) is possible as:

$$u = 2A\cos[\frac{1}{2}\Delta kx - \frac{1}{2}\Delta\omega t] \cdot \cos(\bar{k}x - \bar{\omega}t) \tag{3.57}$$

The first term of the expression above is a low-frequency term which enables the definition of the group velocity as:

$$c_g = \frac{\Delta\omega}{\Delta k} \tag{3.58}$$

which is otherwise represented with the differential operator $d$ as:

$$c_g = \frac{d\omega}{dk} \tag{3.59}$$

If the equation $k$=$\omega/c_p$=$2\pi f/c_p$ is substituted into equation (3.59) then the general expression of the group velocity of a Lamb wave mode is given as:

$$c_g = c_p^2[c_p - (fd)\frac{dc_p}{d(fd)}]^{-1} \tag{3.60}$$

It can be noted that both the group and phase velocities of each Lamb wave mode,

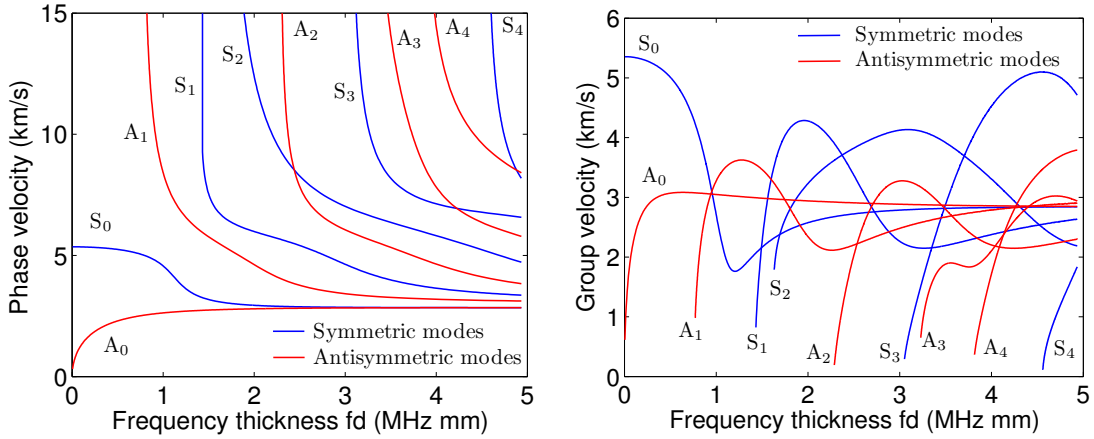


(a) Phase velocity (b) Group velocity

Figure 3.6: Dispersion curves diagrams of an Aluminium plate (thickness=2mm).[46]

depend upon the frequency-thickness product ($fd$). This property is often referred to as *dispersion*. The understanding of the dispersive nature of the Lamb waves is essential for the understanding of the physics when a wave propagates through a plate. Dispersion is often undesirable in practical applications such as nondestructive testing, due to the difficulty in the data interpretation. Information about the relationships between the wave velocities, the wavelength and the frequency for a given material and thickness, can be estimated through *dispersion curves*.

The calculation of the dispersion curves is a relatively straightforward task for isotropic materials but it exhibits a certain level of complexity in the case of anisotropic materials. Commercially available programmes can provide fast and reliable solutions for the dispersion curves of plates. *Vallen dispersion* [46], is a freeware which was used in the current study for the estimation of the dispersion curves for single layered isotropic solids such as the one illustrated in Figure 3.6. *Disperse* [47] has been widely used in order to obtain the dispersion curves of isotropic and anisotropic, layered materials and cylindrical structures or structures immersed in a fluid or embedded in a solid. For the purposes of the current study, the semi-analytical finite element (SAFE) method was employed for the calculation of the dispersion curves of the anisotropic plates as can be found in the previous work carried out by Ahmad [48]. This approach is expected to overcome the restrictions met with the finite element method (FEM) for Lamb wave propagation analysis, since it reduces the required computational time by performing discretisation only to the plate cross section and by employing an exponential function in the wave propagation direction [49].

### 3.1.5 Mode cut-off frequencies

*Cut-off frequencies* are those points on the dispersion curves, that only exist at $fd$ values for modes higher than the fundamental $S_0$ and $A_0$ symmetric and anti-symmetric modes, respectively. At these values, the phase velocities tend to the infinite while the group velocities tend to zero. Another explanation of the physical meaning of these frequencies as proposed by Rose [41] is that at these values only standing longitudinal and shear waves are present at a given thickness of the plate. The mathematical expression of these values will be here demonstrated as presented in Rose [41], after assuming that the wave number approaches zero $k \to 0$. If this is substituted to the Rayleigh-Lamb equation (3.44) that describes the symmetric modes, then the following expression is obtained:

$$\sin(qh)\cos(ph) = 0 \tag{3.61}$$

Assuming that $qh = n\pi$ and $ph = n(\pi/2)$ while $n = 0,1,2,..$ then with some simple manipulations the following expressions are derived:

$$qh = \frac{\omega}{c_T}\frac{d}{2} = \frac{2\pi}{c_T}\frac{fd}{2} = n\pi \quad \text{or} \quad fd = nc_T \tag{3.62}$$

$$ph = \frac{\omega}{c_L}\frac{d}{2} = \frac{2\pi}{c_L}\frac{fd}{2} = \frac{n\pi}{2} \quad \text{or} \quad fd = \frac{nc_L}{2} \tag{3.63}$$

This leads to the general $fd$ values that are given by the following expressions:

$$fd = \{c_T, 2c_T, 3c_T, ..\} \tag{3.64}$$

$$fd = \left\{\frac{c_L}{2}, \frac{3c_L}{2}, \frac{5c_L}{2}, ...\right\} \tag{3.65}$$

In a similar way and after the same manipulations, the respective expressions for the frequency-thickness of the antisymmetric modes are given below.

$$fd = \{c_L, 2c_L, 3c_L, ..\} \tag{3.66}$$

$$fd = \left\{\frac{c_T}{2}, \frac{3c_T}{2}, \frac{5c_T}{2}, ...\right\} \tag{3.67}$$

The estimation of the cut-off frequencies for a given plate and at a given thickness ($d$), has proved to be a valuable tool in nondestructive testing applications. The

estimation of the first cut-off frequency enables the determination of the excitation frequency, in such a way that only the two fundamental symmetric and antisymmetric modes propagate. This significantly simplifies the problem of data interpretation, hence signal processing and computational power required.

## 3.2 Lamb waves in anisotropic elastic solids

The propagation of Lamb waves in anisotropic solids has recently attracted a lot of interest due to the wide application of composite materials in most of the prevailing industries. However due to the anisotropy in the materials' properties the understanding of the physical mechanisms is more demanding compared to the isotropic materials. This lies in the fact that in the case of the anisotropic materials, several phenomena occur that are not observed in the isotropic, such as three different wave speeds, wave skewing, differences in the group and phase velocities and others. Although there has been an extensive effort lately to solve the Lamb wave governing equations for anisotropic materials, no established theoretical background is available yet. This section will present the most prevailing theories, omitting elaborate mathematical formulae due to space restrictions.

Recalling from equations, (3.1), (3.2) and (3.3), the equation of motion assuming zero body forces for an anisotropic material, is expressed as:

$$\rho \frac{\partial^2 u_i}{\partial t^2} = C_{ijkl} \frac{\partial^2 u_k}{\partial x_j \partial x_l} \tag{3.68}$$

So it is clear that the case of anisotropic solids becomes more difficult since the number of the elastic constants in the stiffness matrix increases considerably depending on the material. In the case of an orthotropic anisotropic material, which has at least two orthogonal planes of symmetry, the stiffness matrix can be written as:

$$\begin{bmatrix} C_{11} & C_{12} & C_{13} & 0 & 0 & 0 \\ & C_{22} & C_{23} & 0 & 0 & 0 \\ & & C_{33} & 0 & 0 & 0 \\ & & & C_{44} & 0 & 0 \\ & & & & C_{55} & 0 \\ & & & & & C_{66} \end{bmatrix} \tag{3.69}$$

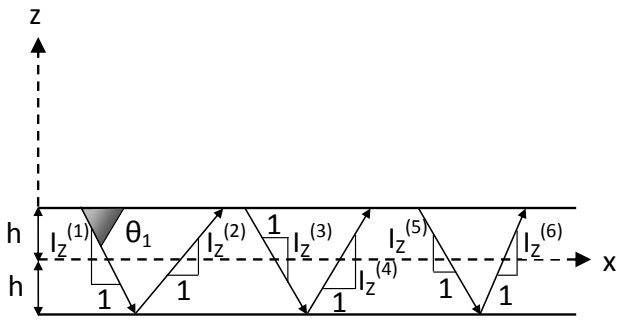


Figure 3.7: Six partial waves considered for the demonstration of Lamb wave propagation in isotropic plates through the partial wave technique.

These can be further simplified in case the material is transversely isotropic, where $C_{44}$=$C_{55}$ and $C_{66}$=($C_{11}$-$C_{12}$)/2. In the more complicated orthotropic case, the equations of wave motion for a plain strain problem for a propagation in the direction of the material's symmetry, would be given as:

$$\rho\frac{\partial^2 u_1}{\partial t^2} = C_{11}\frac{\partial^2 u_1}{\partial x_1^2} + C_{13}\frac{\partial^2 u_3}{\partial x_1 \partial x_3} + C_{55}\left(\frac{\partial^2 u_1}{\partial x_3^2} + \frac{\partial^2 u_3}{\partial x_1 \partial x_3}\right) \tag{3.70}$$

$$\rho\frac{\partial^2 u_3}{\partial t^2} = C_{33}\frac{\partial^2 u_3}{\partial x_3^2} + C_{13}\frac{\partial^2 u_1}{\partial x_1 \partial x_3} + C_{55}\left(\frac{\partial^2 u_1}{\partial x_1 \partial x_3} + \frac{\partial^2 u_3}{\partial x_1^2}\right) \tag{3.71}$$

As mentioned before the problem of Lamb wave propagation in anisotropic materials can only be approached with partial wave techniques, which aim to solve the governing equations based on the boundary conditions by assuming that three upward and three downward waves superimpose each other when travelling in the considered anisotropic layer [41], each of which is referred to as a partial wave while they all contribute to the formation of a single Lamb wave mode (Figure 3.7). Each of these waves is assumed to obey the following type of solution:

$$u_i = \alpha_i \exp[ik(x + \mathrm{I}_z z)] \exp(-i\omega t) \tag{3.72}$$

where $\mathrm{I}_z$ is the angle of each propagation wave with respect to the layer surfaces and $\mathrm{I}_z$=tan($\theta_i$)=$k_z/k_x$. If equation (3.72) is substituted into (3.68) then the following expression is derived.

$$\left[C_{ijkl}k_j k_l - \rho\omega^2\delta_{ik}\right]\alpha_k = 0 \tag{3.73}$$

and the general displacement field of each Lamb wave mode in the anisotropic layer

can be obtained from the following:

$$u_i(x,z,t) = \xi_i(z)e^{ik(x-ct)} \tag{3.74}$$

where $k$ is assumed to be the wave number of the general mode after the superimposition of the partial waves, which are assumed to have equal $k$ in the $x$ component. The component $\xi_i(z)$ represents the variation of the displacements with respect to the depth $z$ of the layer. In addition the phase velocity will be $c{=}c_p{=}\omega/k$. A possible solution of the equation above can be obtained if the determinant of the left hand side in equation (3.73) is set to zero in an attempt to find non-trivial solutions.

$$\det\left[C_{ijkl}k_jk_l - \rho\omega^2\delta_{ik}\right] = 0 \tag{3.75}$$

If a linear combination of the six different partial waves is considered as:

$$u_j = \sum_{1}^{6} C_n\alpha_j^n \exp[ik(x + \mathrm{I}_z^n z)] \tag{3.76}$$

and through the boundary conditions which assume zero traction on the upper and lower surfaces of the model layer ($T_{xz}{=}T_{yz}{=}T_{zz}{=}0$) the traction components can be calculated based on the generalised Hooke's law,

$$T_{ij} = C_{ijkl}\varepsilon_{kl} \tag{3.77}$$

on equation (3.3) and on the symmetrical property of the elastic constant tensors $\mathrm{C}_{ijkl}{=}\mathrm{C}_{ijlk}$ as:

$$T_{xz} = T_{13} = C_{13kl}\frac{\partial u_k}{\partial x_l} \tag{3.78}$$

$$T_{yz} = T_{23} = C_{23kl}\frac{\partial u_k}{\partial x_l} \tag{3.79}$$

$$T_{zz} = T_{33} = C_{33kl}\frac{\partial u_k}{\partial x_l} \tag{3.80}$$

The resulting set of equations will have the form:

$$B_{ij}(\rho, C_{ijkl}, hk)C_j = 0 \tag{3.81}$$

where $C_j$ are the six amplitudes of the partial waves and the matrix $[B]$ is determined through the density, the elastic properties, the thickness of the layer and the assigned $x$ component for the wavenumber $k$. Non-trivial solution of the equation above,

requires that the determinant of the matrix $[B]$ is zero, and this finally derives the dispersion equation for the anisotropic layer.

$$\det[B(\rho, C_{ijkl}, hk, \omega)] = 0 \tag{3.82}$$

## 3.3 Lamb waves in media with varying thickness

The majority of the previous studies that have exploited Lamb waves for nondestructive testing have only focused on case studies which employed media of uniform thickness ($d$). However in many practical applications, the problem of varying thickness is inevitable. One significant example in aerospace industry is the lap joints on the aircraft fuselage or wings. In such cases the skin is thicker near the root and gets thinner near the wing tip. In addition, apart from the initial design characteristics of the system, variations in thickness can occur when the surface is subjected to a corrosive environment or when actual damage takes place in the form of cracks and holes.

The variation in the thickness imposes a significant difficulty factor in the understanding of the propagation mechanisms, since it will lead to multiple mode conversions. This means that when a mode propagates through a media and meets a thickness variation, it will convert into another mode which will be very different from the incident mode with respect to phase, group velocity, amplitude and sensitivity. The mode conversion can be easier understood if a dispersion curve diagram is analysed. Even though the excitation mode ensures the propagation of only the two fundamental symmetric ($S_0$) and antisymmetric ($A_0$) modes, the increase in the thickness can be such that the working points on the curves can move to a frequency-thickness product where more modes might appear. Only very few studies have explored the phenomenon of mode conversion in systems with varying thickness.

Cho [50] employed the hybrid boundary element method in order to investigate the mode conversion phenomena caused by a waveguide thickness variation in different symmetric and antisymmetric configurations reaching the conclusion that in working areas before a new mode appears, the symmetric configurations cause mode conversion only within the same mode families as with the incident wave, while in the antisymmetric configuration, there can be mode conversion from symmetric to

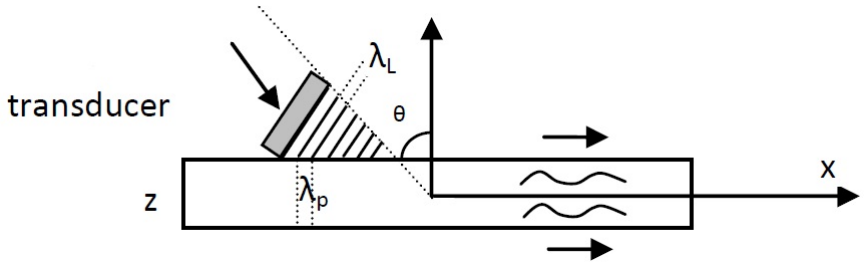


Figure 3.8: Wedge transducer's operation.

antisymmetric and vice versa. On the other hand, the work performed by Alleyne et al. [51] focused on the study of Lamb wave propagation in plates containing a variety of defects in the form of notches with finite elements and proved that the mode conversions due to the thickness variation can provide an advantage for non-destructive testing. This conclusion relies on the fact that when a pure mode is excited it only generates additional modes when a discontinuity (or defect) exists.

## 3.4 Generation and detection of Lamb waves

The widespread application of Lamb waves over the last years imposed the need for development of necessary generation and detection transducers. The substantial materials' progress over the last years led to a number of generation and detection techniques that are available depending on the application and the required cost. These techniques can be divided into five general categories based on the physical principles employed. These are: ultrasonic probes, piezoelectric wafers and piezo-composite transducers, laser-based ultrasonics, interdigital transducers (IDTs) and fibre optic sensors [52]. This section will briefly present the most basic techniques that exist among these categories, while extra attention will be drawn to the piezo-electric transducers which were utilised within the frame of the current work.

Among the ultrasonic probes, the most popular transducers which have been employed for Lamb wave problems are the angle transducers such as the wedge and the comb transducers and the non-contact electro-magnetic acoustic transducers (EMATs). The angle of the wedge and the comb transducers can be appropriately tuned in order to activate a specific Lamb wave mode by exciting the desired wavelength of a given velocity and excitation frequency [53]. This is performed through

Snell's law (Figure 3.8):

$$\sin\theta = \frac{\lambda_L}{\lambda_P} = \frac{c_L}{c_P} \tag{3.83}$$

The EMATs were primarily introduced in order to provide a non-contact source of excitation aiming to avoid all problems related to coupling conditions [54]. The required mode is excited through the spacing of the coil limbs of a wire which is placed close to the monitored surface and a magnet, where the geometry of the coil can favour specific wave propagations. Non-contact probes enable the excitation and generation of Lamb waves in complex geometries. However, complications might arise when the precision is minimum due to potential acoustic mismatch between the air/fluid and the monitored surface. In addition, their use is restricted to metallic objects since electrical conductivity is necessary.

Laser-based generation and detection of Lamb waves has relatively lately emerged following the advances in the technology of 3-D laser interferometers where the generation of the waves is usually performed through the monitoring of out-of-plane displacements [55]. The laser source can excite specific modes of Lamb waves in cases where the approach is restricted or in irregular surfaces where the coupling of a transducer would be impossible. However the significant cost, size as well as safety issues of the adopted equipment are significant limitation factors for practical applications.

IDTs use the widely commercially available piezoelectric material polyvinylidene fluoride (PVDF) and they consist of a number of electrodes which are connected alternately to two electrode strips on a piezoelectric substrate. These transducers take advantage of the piezoelectric effect in order to convert a periodic introduced electric field to periodic mechanic stress waves on the monitored surface. The spacing between the electrodes can tune the required wavelength. This type is suitable for cases where the key requirement is the impedance of the transducers within the layers of a composite laminate or when a permanent attachment is necessary. They are cheap and easy to manufacture, although their operation frequencies are limited to be within the range of 0.5–4 MHz [56].

### 3.4.1 Fundamentals on the piezoelectric transducers

The generation and detection of Lamb waves in this work was performed with piezoelectric transducers (PZT). These exploit the piezoelectric effect in order to convert


(a) Planar resonance mode (b) Thickness resonance mode

Figure 3.9: Resonance modes of circular piezoelectric transducers.

electric energy into mechanical strains and vice versa. The piezoelectric effect was first discovered by the Curie brothers and the word *piezo* was given after the Greek word *piezen* which means press. This effect can be found in natural crystals (quartz) and artificially polarised ceramics and polymers such as polyvinylidene flouride. According to this effect, when stress is applied on a crystalline material, it generates electric charge. This phenomenon is reversible, namely when voltage is applied on the crystal, then mechanical strains are produced. The current technology of piezoelectric transducers, exploits several electrodes that can be placed on the crystal, one pair of which is used to generate voltage to the crystal and the other pair to receive charge as a result of developed strain.

The crystallites or crystal cells operate as electric dipoles. These exist in some natural crystals in which these cells have a specific orientation along the crystal axes, naturally enabling the aforementioned voltage-strain conversion. However in artificially polarised materials, the dipoles follow a random orientation and therefore there is need for the material to be polarised. The most common technique used for this process involves the following steps [57]. First the crystalline material is exposed to temperatures slightly below its Curie temperature in order to enable an easier orientation of the dipoles in the desirable direction. Then an electric field $E$ is applied on the material, where the dipoles align along the field lines, after which the material is allowed to cool down under the electric field. Finally the electric field is removed. The polarisation is maintained for as long as the materials are exposed to temperatures lower than the Curie temperatures. In the current study, the Curie temperature of the piezoelectric transducers used was 340$^{o}$C.

The use of piezoelectric transducers for nondestructive testing has attracted significant attention over the last years; probably the most comprehensive analysis in this field has been carried out by Giurgiutiu [58]. PZTs offer a low-cost and low-weight and size means of generation and detection of Lamb waves, they can be surface-

mounted or inserted between layers of lap joints or of composites where they are non-intrusive and they can operate over a wide range of frequencies. In this work, circular piezoelectric transducers were used for the excitation and detection of Lamb waves in an attempt to minimise the resonance modes. The circular transducers have two main resonance modes; the radial or planar resonance mode and the thickness resonance mode (Figure 3.9). A limitation of this type of transducers is that they unavoidably excite multiple wave modes compared to wedge transducers.

## 3.5 Nondestructive testing with Lamb waves

Inspection with Lamb waves is currently considered to be the most promising SHM technique for aluminium and composite structures. The whole thickness of the structure can be excited by small and conformable transducers which require little power. Those can be wireless, targeting an on-line continuous health monitoring. There are two basic modes for the configuration of the sensors: the pulse-echo mode and the pitch-catch mode. These will be further explained later. When Lamb waves interact with discontinuities, then changes occur in the form of attenuation, scattering, modes conversion, reflection or refraction.

*Attenuation* refers to the drop of the pulse amplitude as a result of energy absorption when the wave interacts with a defect or even with geometrical features. *Scattering* is defined as the combined drop in the magnitude and the pulse spreading. This phenomenon can occur when the wave meets a flaw or any kind of obstacle. *Mode conversion* is generally caused by the local reduction of the thickness due to a geometrical feature or due to a defect such as a crack or corrosion. *Reflection and refraction* can occur at boundaries (either of the tested structure or of defects) and they refer to the turning back of a wave when it interacts with a boundary or its passing through the interface respectively. Finally a significant property of Lamb waves is their dispersive nature. The effect of dispersion is that the duration of the wave packet propagating through the structure will increase and its amplitude will decrease. These two phenomena will eventually lead to the loss of resolution and in the decrease in the sensitivity of the testing system [59].

### 3.5.1 Excitation signal and modes selection

The selection of the appropriate excitation signal in order to excite Lamb waves is a challenging task due to their dispersive nature. This is further complicated due to the propagation of a number of different symmetric and antisymmetric modes as previously explained. Therefore the selection of the excitation signal is of high importance for NDT applications in order to ensure that the obtained response signals are easy to interpret.

First of all, the dispersive nature of the Lamb waves can be minimised through the limitation of the bandwidth of the excitation signal, an operation called *windowing*. The most common window that is selected is the *Hanning window* whose effect can be visualised in Figure 3.10. A 5-cycle tone pulse is selected and its frequency response after windowing is clearly more preferable since the magnitude of the undesired side lobes has been largely minimised, resulting in a strong main carrier lobe. This is expected to minimise the dispersive nature of Lamb waves. A higher number of cycles would further minimise the dispersion effect and it would increase the signal-to-noise ratio. However, it would lead to undesirable overlapping of the reflected echoes at closely spaced features in the monitored structure [53]. The amplitude of the pulse affects the magnitude of the Lamb wave strain introduced to the monitored structure. Higher amplitude helps in minimising the captured noise; however, it can increase the drift in the signal leading to lower resolution [60].

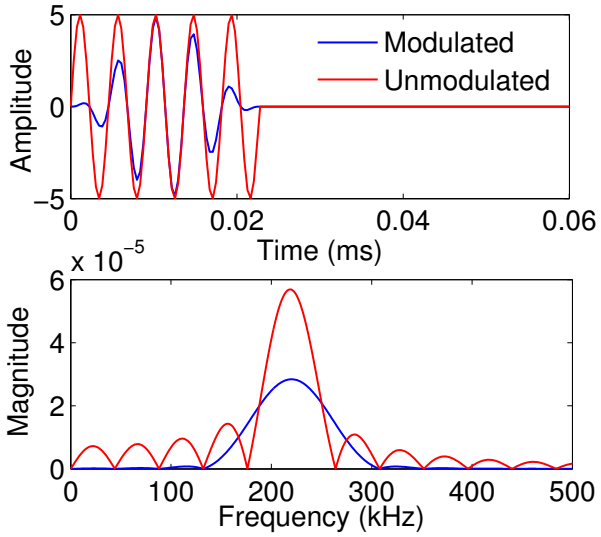


Figure 3.10: The effect of windowing on the excitation pulse for Lamb waves and on its frequency content.

Furthermore, the isolation of a pure mode in complex structures and more specifically in anisotropic materials, is considered to be a quite challenging task which requires a very good prior understanding of the dispersion mechanisms of the tested material. Therefore the plot of the dispersion curves is the first step, which will reduce the number of the excited modes to only the first two by focusing on a specific frequency range, namely below the first cut-off frequency. As previously illustrated, the circular piezoelectric transducers have two resonance modes, hence two resonance frequencies. The transducers maximise the output energy when driven close to or at these frequencies. These though can significantly change due to the damping effect of the adhesive used to bond them on the tested surface as well as the material of the structure. In addition, based on the dispersion properties of the material, these frequencies might not be suitable for the isolation of a pure mode.

Moreover, the excited mode and frequency will finally determine the wavelength. The size of the wavelength is critical for the nondestructive testing applications, since it basically determines the minimum size of the discontinuity that can be detected. More specifically, studies suggest that the minimum size that can be detected by ultrasonic nondestructive testing, is associated with the *diffraction limit*, which is half the wavelength $\lambda$. According to this suggestion, only two scatterers that are separated by more than the diffraction limit can be detected [61]. It is therefore obvious that the smaller the wavelength the higher the damage sensitivity. This directly means that at a given velocity $c$, higher frequency ($f$) Lamb waves can potentially provide higher damage sensitivity ($\lambda{=}c/f$). Some studies have shown that the detectability of defects is possible even below the diffraction limit. Alleyne et al. [51] showed that notches could be detected with Lamb waves when the wavelength-to-notch depth ratio was of the order of 40 and when the notch width was small with respect to the wavelength. Also it was highlighted that although higher frequency-thickness products provide higher damage sensitivity, yet other parameters like the appropriate mode selection could be more critical. However, problems that are related to higher frequencies are the high sensitivity to undesirable material features which will inevitably lead to high noise [61]. It is therefore clear that monitoring with Lamb waves is a rather demanding technique, the efficiency of which depends upon several factors. More explicit mode excitation scenarios will be demonstrated in the practical case studies in the next chapters.

The selection of the fundamental mode ($S_0$ or $A_0$) relies on the matching of the resolution of each mode with the application. Due to the fact that the $S_0$ mode

travels faster than the $A_0$, the $A_0$ mode is usually preferable since the corresponding wavelength is shorter, hence it can detect smaller defect sizes. However, the $A_0$ mode exhibits a considerable dispersive behaviour at low frequencies which results in an energy leakage. In terms of modelling, the simulation of the $A_0$ propagation can also be more demanding due to the short wavelength which in turn requires fine meshing and hence high computational power [62]. On the other hand, the $S_0$ mode travels faster than the $A_0$, leading to lower damage sensitivity. However, the resulting mode shapes are simpler and it exhibits a more uniform distribution of stresses through the thickness of the plate, with potential good sensitivity to defects that can occur at any depth [63].

## 3.6 Modelling methods for Lamb waves

Analytical solution of guided wave propagation problems in complex structures is a very demanding task due to the complicated mechanisms that take place during the interaction of the waves with the material and discontinuities' boundaries. The excitation of multiple propagating modes and the dispersive nature of the waves make the modelling aspects of Lamb waves even more challenging. One more parameter that needs to be considered is that the actual wave propagation in composite materials is by itself complex due to the anisotropy of the microscopic structure. Therefore numerical solutions have been extensively investigated by many researchers since they provide quick and efficient solutions under various conditions as long as the operating parameters are carefully selected.

The most popular methods that have been used to address the Lamb waves propagation problem are the *finite difference method* (FDM) [64] and the *finite elements method* (FEM) [65]. There are various methods that have been used in the past that are either FEM-based or FDM-based. The *boundary element method* (BEM) is a popular method that was implemented by Cho and Rose [66] for inspection with Lamb waves and it is FEM-based. The basic concept of the method is that it simulates the integrated numerical equations by converting the volume integrals to surface integrals through the Green's functions [67]. The BEM has computational advantage over FEM when simple geometries are considered. However, when the analysed geometry is complex, the BEM is less efficient than FEM or FDM. The *spectral element method* (SEM) has lately attracted the attention of researchers for

the numerical simulation of guided waves [68]. SEM is a FEM-based technique which utilises the finite element concepts, but also takes advantage of spectral method accuracy. Its basic difference though is that it provides a global simulation of the partial differential equations in contrast to FEM and FDM which are only local. This means that it approximates functions as a sum of smooth basis functions that are non-zero over the solution domain and not only on local subdomains [69]. One more FDM-based numerical modelling method for wave propagation that has been developed is the *mass-spring lattice model* (MSLM). This model simulates the tested structure by means of mass points interconnected to each other with linear and rotational spring elements which represent the stiffness whose behaviour is described by finite difference equations [70]. The advantage of MSLM over the FDM is the simulation of discontinuities with spring disconnections [71].

The current work will focus on the investigation of the propagation of Lamb waves through the numerical simulation with FEM and more specifically with the commercially available package ABAQUS [72]. For the sake of completeness a brief literature review of the work carried out so far in the field of numerical analysis of Lamb wave propagation in aluminium and composite materials will be given here. Fromme et al. [73] explored the scattering behaviour of the $A_0$ Lamb wave mode in Aluminium plates containing partially through and through-thickness cracks while he developed a sensitivity prediction hybrid model for the detection of defects at potential locations and orientations. Wilcox [74] performed a detailed analysis on the excitation methods of Lamb and shear horizontal waves by point and line sources in isotropic plates, demonstrating the effect of each method on the excitability functions. Yang et al. [75] developed models of surface-bonded PZT discs in order to investigate aspects of the Lamb wave propagation in composite materials using 3D solid/shell elements. Diamanti et al. [76] simulated the $A_0$ mode at low frequencies in order to successfully detect and locate low velocity impact damage in composite laminates and in stiffened panels, mainly by exploiting the time of flight (TOF) concept. This concept in a plate excited with pitch-catch mode, is given as $x{=}L{\cdot}\Delta_{td}/\mathrm{TOF}$, where $x$ is the location of the defect, $\Delta_{td}$ is the time difference between the reflection from the damage and the excitation pulse, and TOF is the time difference between the excitation pulse and the reflection from the boundary.

Although extensive work has been focused on isotropic and anisotropic plates of uniform thickness, little effort has been made in simulating and understanding the propagating mechanisms of Lamb waves in anisotropic panels of varying thickness

such as the repairs investigated in the current work. Among the very few works that can be found in literature, the most notable was performed by Diamanti et al. [77] where the excitation of $A_0$ mode was performed at low frequencies in sandwiches and composite single and double-lap repairs in order to detect impact damage. The FEM model was approached with shell elements and debonding between the patch and the substrate was modelled by means of node release. The debonded area was detected in the captured waveforms through the analysis of the TOF. Koh et al. [78] demonstrated the disbond growth beneath a composite repair patch through FEM and detected the initiation of the disbond through the power transmitted between a pair of surface mounted PZTs. These cases can be complex in terms of interpretation, since the nature of the waves that propagate in this type of structures, can be considerably affected by their interaction with the multiple interfaces, and could lead to other types of waves, such as Stoneley waves. These waves propagate along interfaces (solid-fluid or solid-solid) as previously explored.

## 3.7 Discussion

This chapter presented an introduction to the theory of wave propagation in solids in order to explain the field of interest, namely the propagation of Lamb waves in isotropic and anisotropic plates. The basic concepts were explained and the characteristic equations were derived. The chapter demonstrated the basic background on significant aspects related to Lamb waves such as the generation and detection methods, excitation concepts and numerical modelling. The nature of the Lamb waves was evaluated in order to highlight the complications as well as the benefits that emerge from their application in nondestructive testing studies. In the next chapter, the signal processing techniques employed in this work are illustrated, namely pattern recognition-dimensional reduction techniques and time-frequency analysis approaches.

# Chapter 4

# Signal Processing Techniques

This chapter attempts to investigate and analyse the signal processing approaches that fall into the category of pattern recognition, dimension reduction analysis for high-dimensional, multivariate data and time-frequency analysis for nonstationary signals. It aims to give some background information that is required for a general understanding of the employed methods, with extra focus on the techniques of outlier analysis, linear and nonlinear principal component analysis, the Hilbert transform and the Hilbert-Huang transform. All necessary mathematical concepts related to these techniques will be briefly explained with given examples where applicable.

## 4.1 Pattern recognition and dimensional reduction

### 4.1.1 Outlier analysis

*Outlier analysis* (OA) is a pattern recognition technique which can be in general defined as the process of statistical determination of the class of a set of data. This is an approach that applies to the general novelty detection tools and deals with two general classes: 'normal' or 'damaged'. Being an unsupervised learning method, it only requires data from the normal condition and not from all damage classes, enabling the implementation of a fast and reliable algorithm that performs a first

assessment of the structural integrity of the tested system and provides a visually friendly result that can be easily interpreted. This tool is applicable to systems that involve both univariate (consisting of one variable or else consisting of a single scalar component) and multivariate (consisting of more than one variables at each sampling point) data although the current analysis will focus only on multivariate.

The aim of the method is to detect *outliers* among a set of given data. As an outlier, one would define any value that comes from the recorded data and which seems to follow a different behaviour than the rest. As a result it is assumed that it reflects the value that makes the monitored system deviate from the normal condition. It is important to mention at this point, that this deviation might refer to any possible parameter that could affect the recorded signals including damage, environmental and coupling conditions among others. The current work focused on experimental conditions where any other potential effect than the damage (such as temperature variation or mounting conditions) was kept constant. The deviation is estimated on the basis that the normal condition data follow a Gaussian distribution.

Outlier Analysis has been investigated by some researchers for damage detection applications. Worden et al. [79] have performed damage detection using outlier analysis on four engineering case studies with successful results, although assumptions such as, the normal condition set follows a Gaussian distribution are highlighted. Worden et al. [80] performed novelty detection analysis on two composite plates using outlier analysis, an auto-associative neural network and kernel density estimation to detect the effect of delamination with Lamb waves. Outlier analysis proved to be the fastest technique, however the weakness of the assumption of Gaussian statistics is not present in the other methods. Finally, Pavlopoulou et al. [31] performed outlier analysis in order to detect the crack propagation and the debonding of an external patch in an Aluminium repaired structure, with significant success. However the Mahalanobis squared-distance exhibited a slight drop in cases where damage kept increasing, a complication which will be further examined in this work.

### 4.1.2 Outlier analysis in multivariate data

The steps that are followed for the application of outlier analysis on multivariate data can be illustrated in Figure 4.1. The *discordancy value* in the case of multivariate data is called the *Mahalanobis squared-distance* and it can be estimated through the

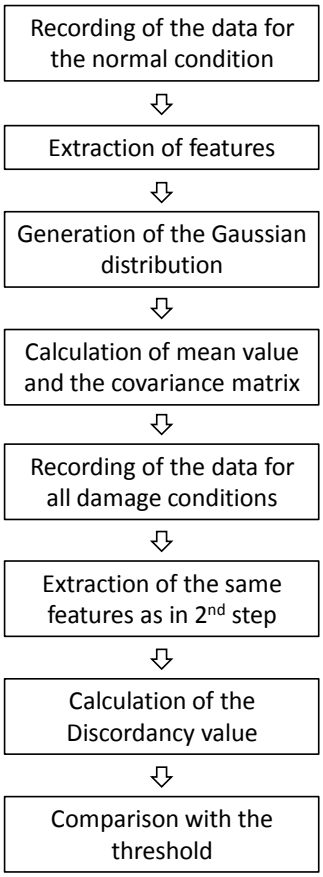


Figure 4.1: Outlier analysis steps.

following equation:

$$D_\zeta = (\{x_\zeta\} - \{\bar{x}\})^T [S]^{-1} (\{x_\zeta\} - \{\bar{x}\}) \tag{4.1}$$

where, $\{x_\zeta\}$ is the potential outlier and $\{\overline{x}\}$ and $S$ are the mean value and the covariance matrix of the training data, respectively. $T$ indicates transpose and the notation $\{\}$ indicates vector. The estimation of the assigned threshold in the final step, is performed through the employment of a Monte Carlo approach and by taking into consideration the dimensions of the extracted features for the monitored system. Any observation that lies above the threshold is classified as an outlier. The followed steps can be briefly summarised below as suggested in previous work [79].

• **Step 1**: Generation of a $p$ x $n$ matrix of random numbers which follow a Gaussian distribution and whose dimensions match the dimensions of the extracted features ($p$ - observations, $n$ - dimensions).

• **Step 2**: Application of equation (4.1) for all of the observations and storing of

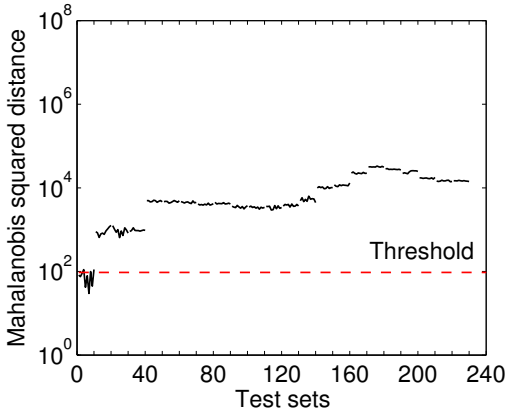


Figure 4.2: Example of outlier analysis.

the largest value.

• **Step 3**: Repetition of Steps 1 and 2 for a large number of trials and ordering of the largest values in terms of magnitude.

• **Step 4**: The threshold is assigned as a percentage of the resulting array in Step 3. In the current work a 99 % confidence threshold was utilised, which means that any values above that threshold have less than 1 % probability of occurring as extracted from the random variation of the normal condition set.

An example of the performed algorithm on a panel which was loaded under fatigue, is illustrated in Figure 4.2. Details on the monitored system are later explained in Section 8. Here the figure is only given as an example of how the approach works. The data set (isolated features) was 50-dimensional while the training set consisted of 100 observations and each subsequent set consisted of 10 observations. The threshold was estimated based on the Monte Carlo approach by taking into consideration the dimensions of the tested features. Then the Mahalanobis squared-distance was measured and the values were plotted with respect to the test sets. Each test set corresponds to the observations of a specific structural condition of the monitored system (10 observations for each condition). The higher the test set number, the higher loads the monitored system was subjected to. Test sets 0-10 correspond to the normal condition (usually before any loading takes place), which also functions as a baseline reference condition. These observations are usually obtained from the training data in order to validate the performance of the algorithm, hence they are not considered for its training. Figure 4.2 demonstrates that the normal condition is successfully identified as unfaulted (e.g. below the assigned threshold) while the rest of the structural conditions gradually exhibit a certain deviation from the normal

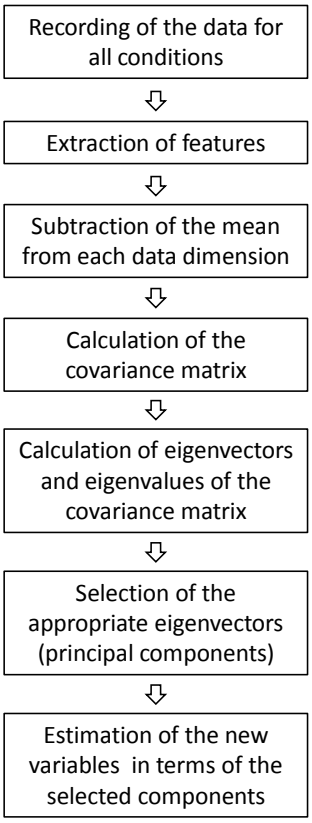


Figure 4.3: Principal component analysis steps.

condition and the threshold, hence identifying the presence of damage.

### 4.1.3 Linear principal component analysis

In the case of multivariate sets of data, it is often essential to represent the required information in a reduced-dimensional space for purposes of easier interpretation. One very common technique for implementing that is *principal component analysis*. This technique projects the data into a lower-dimensional space (e.g. a new set of axes) through orthogonal linear transformations in such a way that each new variable is a linear combination of the original variables. The values of the new variables are estimated on the basis of coordinates of each projected observation on each orthogonal axis. The resulting axes are called *principal components* and the new variables are called *principal component scores*. Every new variable that is estimated after the transformation, accounts for a certain percentage of the total variance of the data. Therefore, the first new variable accounts for the maximum variance in the data, the second new variable accounts for the maximum variance

that has not been accounted for by the first variable; the $p^{\text{th}}$ new variable accounts for the variance that has not been accounted for by the $p$-1 variables. The resulting variables are uncorrelated to each other. For the purpose of the current work, the concept of principal component analysis was further developed for nonlinear cases, therefore the standard principal component analysis is referred here as *linear principal component analysis* (PCA). The general theoretical steps that are followed for the application of PCA on multivariate data are illustrated in Figure 4.3. In the current work PCA was estimated through the application of the *singular value decomposition* (SVD).

Principal component analysis is a rather useful tool in pattern recognition problems for damage detection applications, since it can provide information about the separation between the clusters of each data set and it enables the understanding of their behaviour with respect to damage growth. Two-dimensional and three-dimensional representations are preferable in terms of visual illustration, while at the same time the selection of the first two or three principal components has to ensure that most of the system's information is maintained and hence accurately represented. The loss of information can be estimated via the components that were not selected. At these first stages of damage detection analyses, the efficiency of the selected feature can be evaluated on the basis of how clear separation between the data clusters of the different damage sets is obtained.

PCA has been used as a tool for damage detection purposes in the past. Chetwynd et al. [81] identified optimal Lamb wave propagation paths for detection of damage that was introduced in a curved aluminium plate in the form of drilled holes and saw cuts. The investigation was performed through the post-processing of the signals with OA after the application of PCA to ensure the appropriate selection of the tested features. Yan et al. [82] used a PCA-based approach in order to discriminate between damage and environmental effects for vibration features in a bridge model. In the present work, PCA has only been used as a tool for setting the basis of understanding damage detection problems and for further development of more advanced damage prognosis tools.

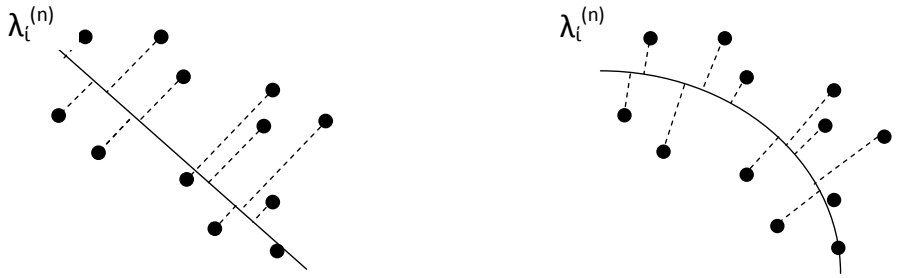


(a) Principal component analysis (b) Nonlinear principal component analysis

Figure 4.4: Schematic illustration of the data projection nature for the linear (a) and nonlinear (b) principal component analysis (arc length $\lambda$).

### 4.1.4 Nonlinear principal component analysis

Principal component analysis only extracts linear relationships in order to project the data on the principal components. In simple words, this means that the sets of the analysed data are projected into lines. This limitation led to the establishment of a more generalised concept, namely *nonlinear principal component analysis* (NLPCA). This approach extracts both linear and nonlinear relationships such as higher-order statistics, and enables the projection of the data into curves or surfaces instead of lines or planes in such a manner that the length of the orthogonal projections from the data points to the curve is minimised. Figure 4.4 graphically indicates the basic difference between the two methods. NLPCA is a technique which can further reduce the dimensions in an accurate way for damage detection problems where high-dimensional sets of data are acquired. However it has not been systematically exploited for such applications yet. Among the very few applications, Worden et al. [83] performed NLPCA on Lamb waves obtained from a composite plate exposed to temperature variation in order to achieve data compression. The work demonstrated that the NLPCA scores exhibited a monotonic behaviour with respect to the increasing temperature hence making Lamb waves a temperature sensor. Hsu et al. [84] performed NLPCA using an auto-associative neural network in order to extract the environmental factors and estimated the damage extent by carrying out modal analysis in a road bridge subject to varying environmental conditions.

### Implementation algorithm

Several algorithms have been proposed for the estimation of the principal curves but that proposed by Hastie and Stuetzle [85] is the one that was implemented in this work. This algorithm starts with a prior line which is usually the first principal component. For the current study, a FORTRAN programme [83] was used, which can be briefly summarised in the following two steps.

Each curve is parametrised by its arc length $\lambda$ (Figure 4.4). The arc length is translated as the scores which are the coordinates of the projections of the data into the new axis. There are two basic steps which alternate for each iteration until the mean orthogonal distance between the data points and the curve is minimised. This is achieved when the relative change in the mean distance between the iterations is below a threshold. The data points here are expressed as $x_i$ and the resulting curve after each iteration is expressed as $f_i$. As span here one would define the number of points in the neighbourhood of the respective $\lambda_i$. This is a user-defined parameter and its function is to control the smoothness of the curve.

**Step 1 (Projection):** Each $x_i$ is projected on the curve $f_i$ and the coordinates of the projection on the closest point of the curve are estimated along with the arc length $\lambda_i$. The arc length of each point is defined from the end point of the curve denoted as $\lambda_1$=0. Then the points are reordered in order of increasing $\lambda$ and the arc lengths are recalculated. The algorithm starts with a prior line which is the first linear principal component.

**Step 2 (Conditional - expectation):** For each point of the curve $f_i$, the span is defined. Next, for all the points $x_j$ associated with $\lambda_j$ within this span, a weighted regression line is fitted coordinate wise to the pairs ($\lambda_j$, $x_j$) and the new values of $f_i$ are defined as the evaluated linear curve-fits $\lambda_i$.

### Demonstration of the algorithm

A schematic illustration of how the algorithm works can be seen in Figure 4.5. As explained before, the algorithm defines as a starting point the first linear principal component whose arc length is denoted here as $\lambda_0$. As illustrated, this line does not perfectly fit the data set, which can be evaluated through the estimation of the mean orthogonal distance between the points and the curve. This is clearly not the

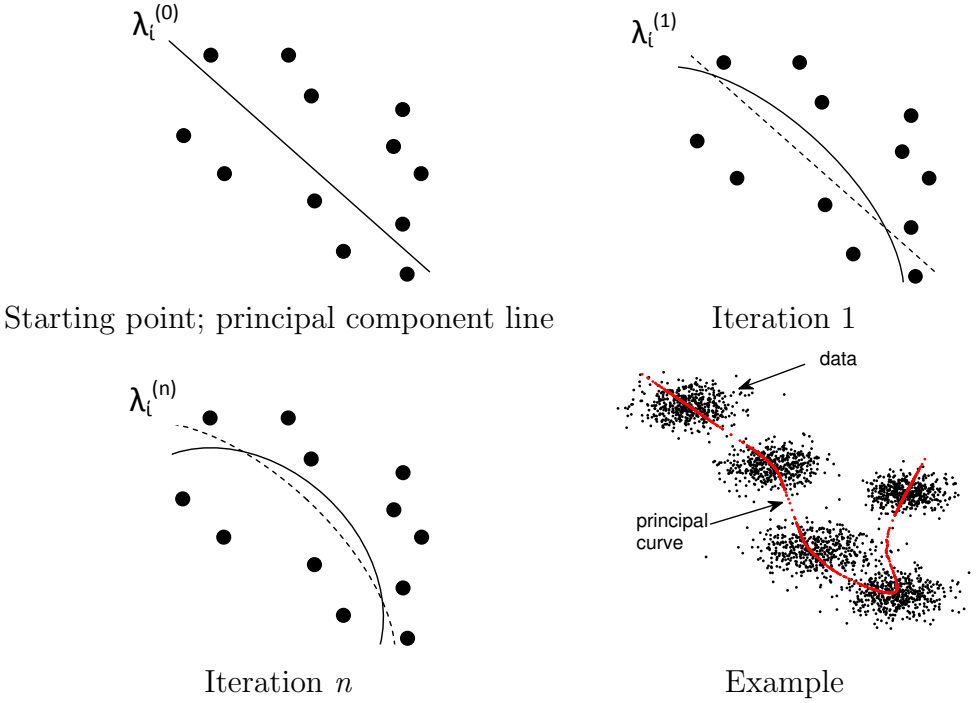


Figure 4.5: Schematic illustration of the iterative nature of the algorithm and an example of its final result on a set of data.

minimum possible. The curve in the first iteration is a function of the obtained $\lambda^{(0)}$ from the previous step and the new $\lambda^{(1)}$ are estimated through the projection of the data to the new curve. This procedure is repeated for $n$ iterations after which the curve has bent to the optimum shape. The successive bending of the starting line, is achieved through the fact that the same data point is not projected into the same point of the curve at each iteration. Finally an example is presented here, illustrating a principal curve fitted to a set of Gaussian distributions. The curve has bent to obtain the required shape.

## 4.2 Time-frequency analysis of nonstationary signals

### 4.2.1 Classical frequency analysis concepts: Fourier-based methods

There are several approaches that have been employed in the past which look at the representation of the spectrum of time signals in order to extract useful information. Some of the most representative ones are discussed here. The *Fourier transform* (FT) is a very well established method and has been extensively used in the past as a feature selection approach for SHM problems with Lamb waves. This approach is based on the decomposition of any periodic function $x(t)$ into a sum of simple oscillating functions, sines and cosines (or complex exponentials), the so called *Fourier series*. The Fourier representation of a function $x(t)$ defined on the interval [-$\tau$/2,$\tau$/2] is:

$$x(t) = \alpha_0 + \sum_{n=1}^{\infty} a_n \cos(n\omega t) + \sum_{n=1}^{\infty} b_n \sin(n\omega t) \tag{4.2}$$

where $\omega$=2$\pi/\tau$ and the period $\tau$ and the amplitudes $a_n$ and $b_n$ are associated with each of the decomposed oscillating functions.

If the Moivre's theorem is applied, then one obtains:

$$\cos(n\omega t) = \frac{1}{2}(e^{in\omega t} + e^{-in\omega t}) \tag{4.3}$$

$$\sin(n\omega t) = \frac{1}{2i}(e^{in\omega t} - e^{-in\omega t}) \tag{4.4}$$

Following the equations (4.3), (4.4), the Fourier series can be written in the following form:

$$x(t) = \sum_{n=-\infty}^{\infty} c_n e^{in\omega t} \tag{4.5}$$

where

$$c_n = \begin{cases} (a_n - ib_n)/2 \text{ if } n > 0 \\ (a_n + ib_n)/2 \text{ if } n < 0 \\ a_0 \text{ if } n = 0 \end{cases} \tag{4.6}$$

The orthogonality relation,

$$\int_{-\frac{\tau}{2}}^{\frac{\tau}{2}} e^{in\omega t} e^{-im\omega t} dt = \tau \delta_{mn} \tag{4.7}$$

allows the exponential representation of $c_n$ as:

$$c_n = \frac{1}{\tau} \int_{-\frac{\tau}{2}}^{\frac{\tau}{2}} x(t) e^{-in\omega t} dt \tag{4.8}$$

If equations (4.5) and (4.8) are combined, and if $\tau \to \infty$, and $\omega_k$=kd$\omega$ for the $k_{th}$ spectral line, then in the limit, the following expression is obtained:

$$x(t) = \frac{1}{2\pi} \int_{-\infty}^{\infty} \left\{ \int_{-\infty}^{\infty} x(t') e^{-i\omega t'} dt' \right\} e^{i\omega t} dt \tag{4.9}$$

From equation (4.9) the Fourier transform (FT) can be derived as following:

$$F[x(t)] = X(\omega) = \int_{-\infty}^{\infty} x(t) e^{-i\omega t} dt \tag{4.10}$$

which represents the spectral content of the time signal in terms of frequency $\omega$ and of magnitude $X(\omega)$. Although the FT provides a useful tool that easily manipulates the analysed signals, it cannot represent the spectrum of the signal with respect to its time-varying behaviour, namely it cannot interrogate nonstationary signals. This means that it fails to identify when each frequency component of the same magnitude occurs. This poses a significant limitation since most signals that are dealt with in real problems are nonlinear and nonstationary.

Since this limitation proved to be crucial for certain signal processing analyses, the *short time Fourier transform* (STFT) approach attempted to make up for the shortcomings of the FT by introducing a sliding window to the decomposed signal which extracts small portions of the signal which in turn is considered as stationary if the window is sufficiently narrow and then the FT can be performed.

$$STFT[x(t)] = X(\tau, \omega) = \int_{-\infty}^{\infty} x(t) w(t - \tau) e^{-i\omega t} dt \tag{4.11}$$

where $w(t\text{-}\tau)$ is the selected time window that provides a time resolution equal to the defined coefficient $\tau$. STFT highly depends on the size and shape of the selected time window. A short time window leads to high time resolution and poor frequency

resolution and vice versa. The degree of overlapping between the selected windows is also of significant importance, since non-zero overlap provides good results but high computational time while a certain degree of overlap can affect the accuracy of the resulting spectrum [86].

Another significant approach to the time-variant interpretation of the spectrum, also based on the FT, is the *continuous wavelet transform* (CWT) [87] which aims to overcome the limitations of STFT by building a window function that can be adjusted according to the changing of the signal and which can be defined as:

$$WT[x(t)] = X(a,b) = \int_{-\infty}^{\infty} x(t)w(\frac{t-a}{b})dt \tag{4.12}$$

where the decomposition depends on the so-called *wavelets* $w(\frac{t-a}{b})$ instead of infinitely long harmonic functions. Coefficient $\alpha$ indicates the translation of the wavelet while $b$ indicates a scaling factor which corresponds to the inverse of the frequency. This approach has been investigated by many researchers for SHM problems with a considerable degree of success. However, the disadvantage of the method lies in the fact that the resolution of CWT depends on the selection of the basic wavelet function and only provides a non-locally adaptive approach. This means that the wavelet base is constant during the processing and cannot change which can lead to energy leakage in certain frequency regions [88].

Another popular method for time-varying signals representation is *Wigner-Ville distribution* (WVD). This is based on the FT of the central covariance function of the signal. If the central covariance of a signal $x(t)$ is:

$$C_c(\tau,t) = x(t-\frac{1}{2}\tau)x^*(t+\frac{1}{2}\tau) \tag{4.13}$$

then its Wigner-Ville distribution is defined as:

$$V(\omega,t) = \int_{-\infty}^{\infty} C_c(\tau,t)e^{-i\omega t}d\tau \tag{4.14}$$

The reader is referred to further explanation if needed [89]. One of the most significant limitations of this method is that it fails to deal with the existence of negative power for some frequency ranges. It is therefore clear that new approaches needed to be employed for the accurate representation of nonstationary signals that would enable the appropriate feature selection of the obtained signals in the current work,

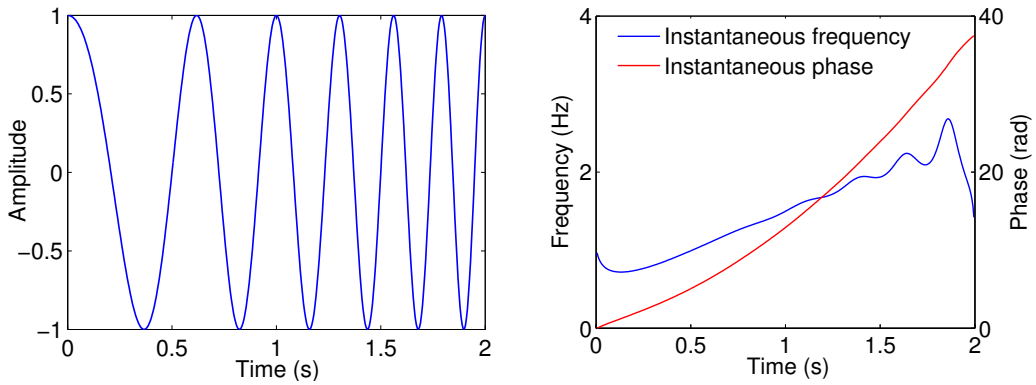


(a) Time signal (b) Instantaneous frequency and phase

Figure 4.6: The instantaneous properties of a chirp signal.

which are by definition transient signals, hence nonstationary and nonlinear.

### 4.2.2 The concept of instantaneous properties

The concept of the instantaneous properties (frequency and phase) emerged from the need to represent the spectrum of nonstationary signals. Nonstationary signals are defined as those signals whose statistic characteristics vary with time. According to its classical definition, frequency is defined as the number of cycles that take place during one unit of time when a body performs an oscillatory (periodic) motion. This means that if the body does not perform a full circle then the frequency cannot be defined. This definition does not provide any finer temporal information of the frequency and it can only be established for *multi-component signals*, namely signals which can be decomposed into more frequency components. However when the signal is *mono-component*, namely signal whose energy distribution spreads around a single frequency or a narrow range of frequencies, then the *instantaneous frequency* (IF) can be estimated for each sampling point of the signal. A general definition for the IF is that it is a time-varying parameter which provides information about the location of the signal's spectral peak as it varies with time. Accordingly the *instantaneous phase* (IP) can be extracted. Further details can be found in the work of Boashash [90],[91] and Huang et al. [92]. As an illustration of the aforementioned concept, a nonlinear and nonstationary signal was selected, namely a chirp signal. Its instantaneous properties were extracted through a Hilbert transform which will be discussed later. The results are displayed in Figure 4.6. It is clear that both properties vary with time.

### 4.2.3 Instantaneous frequency through the Hilbert transform

Among the most popular definitions of instantaneous frequency is the one proposed by Gabor [93] and Ville [94] which will be investigated in the current study and which is based on the *Hilbert transform* (HT). According to these definitions, the analytical signal associated with the real signal $x(t)$ is first defined as:

$$z(t) = A(t)\exp[i\varphi(t)] = x(t) + iH[x(t)] \tag{4.15}$$

The HT of a real-valued function $x(t)$ can be defined through the convolution theorem as:

$$\widehat{x(t)} = H[x(t)] = \frac{1}{\pi}\int_{-\infty}^{\infty} x(t)\frac{1}{t-\tau}d\tau \tag{4.16}$$

and $A(t)$ is the time-varying amplitude of the envelope of $z(t)$, also defined as *instantaneous amplitude* (IA) which is given by:

$$A(t) = |x(t) + iH[x(t)]| \tag{4.17}$$

The phase of $z(t)$, $\phi(t)$ is defined as the IP:

$$\phi(t) = \tan^{-1}\frac{H[x(t)]}{x(t)} \tag{4.18}$$

Finally the IF $\omega(t)$ can be obtained through $\phi(t)$ and can be expressed as:

$$\omega(t) = \frac{1}{2\pi}\cdot\frac{d\phi(t)}{dt} \tag{4.19}$$

From equation (4.16), three properties of the HT can be derived. First of all, the HT preserves the domain in which the signal is defined; this is necessary since the analytical signal that is defined through the HT maintains its time domain nature. Secondly, the HT shifts the phase of a signal by 90°. Positive frequency components are shifted by -90° and negative frequency components are shifted by +90°. Finally the analytical signal which is composed by the real signal and its HT has a spectrum which exists only in the positive frequency domain. This is based on the fact that the imaginary part that is added to the signal is equivalent to the suppression of the negative frequencies and the magnification (x2) of the positive frequencies in order

to preserve the total energy of the original signal [94] as illustrated in Figure 4.7.

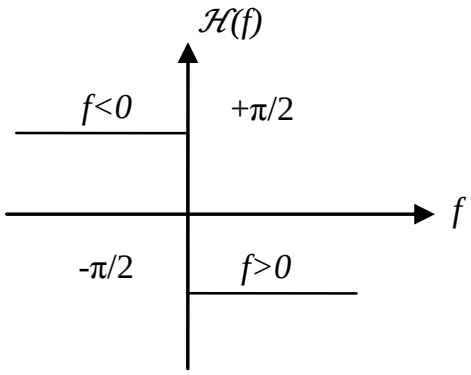


Figure 4.7: Phase shift property of the Hilbert transform. [93]

The definition of the IF through the HT requires a prior decomposition of the analysed signal since it is only meaningful for mono-component signals, which also poses one of its limitations. In addition, the definition of the analytical signal through which the IF can be obtained, cannot be defined for some signals. In these cases, the original and analytical signals might have different spectra or the analytical signal that will be constructed might not be unique for a specific time signal [95]. Nevertheless, the interpretation of the IF is a promising signal processing tool that can reveal important information hidden in the obtained signals which can be exploited for SHM purposes.

Several multi-component signal decomposition methods have been proposed in the past. However, the current study focuses on the most recent ones, namely the *empirical mode decomposition* (EMD) [96] and the *ensemble empirical mode decomposition* (EEMD) [97]. The main principal of these methods is the decomposition of the time signal into signals that admit a well behaved HT, namely mono-component signals. Each of these signals is called an *intrinsic mode function* (IMF).

### 4.2.4 The intrinsic mode function

The demodulation approach followed in the current study, is based on the decomposition of a time signal $x(t)$ into its IMFs. An IMF is a narrow-band signal that should fulfil the two following principles. If these two principles are followed, then the decomposed signal is assumed to consist only of those fundamental components [96]:

• **Principle 1**: Its number of extrema $N_e$ (minima and maxima) and the number of zero crossings $N_z$ should either be equal or differ at most by one over its entire length.

$$(N_z - 1) \leq N_e \leq (N_z + 1) \tag{4.20}$$

• **Principle 2**: The mean value of the envelope of the signal defined by the local maxima $e_{\max}$ and the envelope of the local minima $e_{\min}$ should be zero at any point $t_i$ in order to ensure that the IMF will be locally symmetric.

$$\frac{|f_{\max}(t_i) + f_{\min}(t_i)|}{2} = 0 \tag{4.21}$$

When the IMF is properly defined, then the decomposition of the time signal can be performed by means of a sifting process as described in the following sections.

### 4.2.5 Empirical mode decomposition

Huang et al. [96] developed the EMD which employs a sifting procedure in order to decompose a nonstationary signal into its IMFs. The steps followed for the decomposition of a time signal $x(t)$ into its IMFs, are summarised below:

• **Step 1**: Identification of the local maxima and minima of the time signal $x(t)$.

• **Step 2**: Generation of upper $e_{\max}(t)$ and lower $e_{\min}(t)$ envelopes by initialising the method of cubic spline interpolation.

• **Step 3**: Calculation of the mean $m_1(t)$ from the upper and lower envelope.

$$m_1(t) = \frac{e_{\min}(t) + e_{\max}(t)}{2} \tag{4.22}$$

• **Step 4**: Subtraction of the mean $m_1(t)$ from the signal and calculation of the difference $d_1(t)$ between $x(t)$ and $m_1(t)$:

$$d_1(t) = x(t) - m_1(t) \tag{4.23}$$

Then $d_1(t)$ is tested whether it satisfies the principles of the IMFs or not. If the principles are not satisfied then $x(t)$ is replaced by $d_2(t)$ and the procedure is repeated.

$$d_2(t) = d_1(t) - m_2(t) \tag{4.24}$$

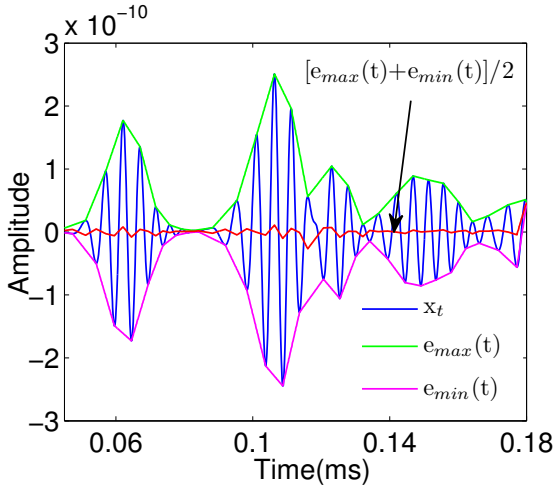


Figure 4.8: Illustration of the sifting procedure during the EMD.

The procedure is repeated from 1 to $k$ times until an IMF is found, in which case a stopping criterion is fulfilled and $d_k(t)$ is denoted as the first IMF, $c_1(t)$.

• **Step 5**: The residue $r_1(t)$ is estimated by subtracting $c_1(t)$ from the initial time signal $x(t)$. This is treated as new data.

$$r_1(t) = x(t) - c_1(t) \tag{4.25}$$

Steps 1-5 are repeated until the $n^{\text{th}}$ residual $r_n(t)$ after the $n$ trial is a monotonic function or constant, hence no more IMFs can be extracted. Then the original decomposed signal $x(t)$ can be reconstructed through the sum of all IMFs.

$$x(t) = \sum_{i=1}^{n} c_i(t) + r_n(t) \tag{4.26}$$

This sifting procedure produces IMFs with decreasing frequency content as the algorithm iterates. An illustration of the sifting procedure is graphically shown in Figure 4.8 where a representative Lamb wave response is used. The maximum and minimum envelopes ($e_{\max}(t)$, $e_{\min}(t)$) are first estimated as well as their mean value and then the mean is subtracted from the original signal $x(t)$ and the result is treated as the new signal. After the decomposition of the original time signal, the HT can be performed on its IMFs in a method named after Huang as the *Hilbert-Huang transform* (HHT).

Even though this approach seems to be a very straightforward decomposition method, yet it has certain drawbacks. First of all a considerable limitation is the absence of

strong mathematical background, hence its empirical nature cannot guarantee that all signals can be analysed. Secondly, the decomposition into the IMFs in some cases might fail to separate signals with very close frequencies, while the IMFs themselves do not have a specific physical meaning. In addition, the effect of the utilised spline fitting algorithm and the selection of the stopping criterion on the efficiency of the decomposition need to be further explored. Finally, two problems related to the EMD are the end effect and the mode mixing. In the first case, the application of spline fitting for the estimation of the envelopes could possibly lead to large swings in its envelope which could propagate inwards and corrupt the signal. This problem has been addressed by Rilling et al. [98] through the mirroring of the extrema close to the edges. In the second case, the resulting IMFs after the decomposition, could either involve a single IMF component which comprises of signals with different scales, or a signal of similar scale residing in different IMF components.

Other user-defined options that can affect the efficiency of the algorithm are the selection of the stopping criteria as well as the maximum number of sifting iterations for the computation of each mode. In the current work, the criteria proposed by Rilling et al. [98] as well as the freeware codes developed for this work were used. According to those, a stopping criterion was defined, based on two thresholds, namely $\theta_1$ and $\theta_2$. These thresholds would ensure globally small fluctuations in the mean and locally large excursions. Then a *mode amplitude* is defined as $\alpha=(e_{\max}(t)$-$e_{\min}(t))/2$ and an *evaluation function* as $\sigma=|m(t)/\alpha(t)|$. Then the iteration process progresses until $\sigma(t)<\theta_1$ for a prescribed function (1-$\alpha$) of the total duration while $\sigma(t)<\theta_2$ for the remaining fraction. In the employed algorithm, these parameters were set as $\alpha\approx0.05$, $\theta_1\approx0.05$ and $\theta_2\approx10\theta_1$. Finally the default maximum number of sifting iteration for each mode in this study was 2,000 [98].

### 4.2.6 Ensemble empirical mode decomposition

The *ensemble empirical mode decomposition* (EEMD) is a noise-assisted method which was suggested by Wu et al. [97] with the aim of overcoming the problems related to the EMD which were briefly described in Section 4.2.5. This is mainly accomplished through the addition of white noise to the original time signal. This solves the problem of mode mixing by the projection of parts of the signal on proper scales of reference established by the white noise, which effectively occupies the entire time-frequency space [99]. After the extraction of the IMFs, the added noise is

removed by a timespace ensemble mean. The steps of the procedure are summarised below [97]:

• **Step I**: Set the number of ensembles $N_E$ and the amplitude of the added white noise $A_n$.

• **Step II**: Generation and addition of white noise $n_m(t)$. The new time signal is then defined as the sum of the original time signal $x(t)$ and the defined noise as:

$$x_m(t) = x(t) + n_m(t) \tag{4.27}$$

The same sifting procedure is performed for the decomposition of the new signal into its IMFs as described in Steps 1-5 in Section 4.2.5 until the $i^{\text{th}}$ IMF, $c_{i,m}$ is extracted and the residual $r_m(t)$ after the $m$ trial is a monotonic function or constant, hence no more IMFs can be extracted. If the trial number $m$ is smaller than the number of the defined ensemble $N_E$, $m<N_E$, then the algorithm goes back to Step II and defines $m=m+1$. In this way the algorithm generates new white noise and the procedure is repeated again.

• **Step III**: Calculation of the ensemble mean of the corresponding IMFs of the decomposition $c_i(t)$ as well as the corresponding residue $r_i(t)$

$$\bar{c_i}(t) = \frac{1}{N_E}\sum_{m=1}^{N_E} c_{i,m}(t) \tag{4.28}$$

$$\bar{r_i}(t) = \frac{1}{N_E}\sum_{m=1}^{N_E} r_m(t) \tag{4.29}$$

There are two user-defined parameters in the specific algorithm, namely the number in the ensemble and the amplitude of the added white noise. The selection of the ensemble number in general followed the rule $\epsilon_n=\epsilon/\sqrt{N}$, where $N$ is the number in the ensemble, $\epsilon$ the amplitude of the white noise and $\epsilon_n$ is the standard deviation of the error that represents the difference between the input signal and the IMFs. In addition the amplitude of the added white noise will not have any effect on the decomposition if too small or it will complicate the analysis if too big. The current analysis followed the general suggestion by Wu et al. [100], that it should be about 0.2–0.4 of the standard deviation of the amplitude of the raw data.

## 4.3 Discussion

The pattern recognition and data dimensions reduction techniques that were demonstrated in this chapter, aim to set a basis for the subsequent damage monitoring analysis of the current work. The selection of these tools was performed on the basis of novelty and on ease of application in the field of damage detection, where the main objective is the expression of a set of obtained signals in a way that can be readily attributed to the structural integrity state of the monitored system. Outlier analysis has been used so far for simple idealised damage detection case studies when there was an *a priori* knowledge of damage. Principal component analysis is a well established method leading to nonlinear principal component analysis which as an advanced method has not been systematically established yet for damage detection purposes.

A brief but fundamental illustration of the theoretical background around the Hilbert-Huang transform was also presented in this chapter while its advantages and disadvantages compared to previously employed methods were identified and discussed. In terms of SHM applications, this method provides certain advantages over the more traditional time-frequency approaches since it is an adaptive method with no need for an *a priori* defined basis, which reduces the energy leakage problem and provides higher accuracy for nonlinear and nonstationary signals. Several studies previously performed, have attempted to evaluate structural integrity problems on simple structures while the gap in the physical interpretation of the obtained result is prominent. The next chapter demonstrates an application of Lamb wave propagation on an Aluminium repaired plate, processed through the aforementioned concepts of time-frequency analysis.

# Chapter 5

# Time-Frequency Analysis of Lamb Waves for Feature Selection

Time-frequency analysis has been a powerful tool for nondestructive testing, widely used in the past by many researchers. Most of the studies aim to employ a feature selection process through relevant time-frequency analysis algorithms, that would provide potential features with damage detection capabilities. This chapter aims to exploit the time-frequency analysis methods demonstrated in Chapter 4 in order to extract appropriate features from an aluminium panel which is repaired with an aluminium patch. The repaired panel was interrogated with Lamb waves. The proposed time-frequency analysis tools are evaluated first on simple Lamb wave responses and then a physical interpretation is attempted on the basis of the effect of damage on the instantaneous properties of the acquired waves. Finally, the selected features are assessed and compared with respect to the damage development and relevant conclusions are derived. This study deals with a simple system, namely an aluminium flat plate, which exhibits a much more expected failure mode than a composite repaired panel, in order to better illustrate the proposed feature selection strategy. This work has already been published in [101].

## 5.1 Feature selection strategies

In pattern recognition the analysis of the obtained signals is performed after the selection of appropriate features. Such a selection is usually performed on the basis of separate modes, wave packages that interact with the region of interest or moving windows over the time waveform. All these methods, could be categorised as *amplitude-based* methods. This means that these methods utilise amplitude monitoring of the acquired signals including attenuation and/or mode conversion, and compare any observed changes with a baseline reference set of data i.e. data representing a pristine condition. However, there are several factors that could influence the amplitude of the acquired signal and which could consequently distort the obtained signals and lead to false alarms or undetected critical defects. These factors can be noise, variation in the environmental conditions, specimen mounting conditions or poor coupling between the transducer and the tested surface. Environmental changes could involve unmeasured temperature and moisture variation especially in systems that are exposed to such extreme conditions such as in aerospace industry. In addition, in the case of complex systems, such as systems with variable thickness, the extraction and isolation of specific modes requires a very good understanding of the wave propagation mechanisms so that the appropriate excitation scenario and the transducers arrangement are selected. If those parameters are not properly selected, then complications like mixed wave packages or extensive wave attenuation over large inspected distances, might lead to the misinterpretation of the amplitude-based analysis. Moreover, when all the above complications apply to the baseline reference, then the reliability of the monitoring analysis becomes weaker from the very early stages. It is therefore reasonable that a more advanced approach for the feature selection needs to be employed, in such a way that more repeatable features of the signal can be isolated.

## 5.2 Damage detection based on the Hilbert-Huang transform

The concept of the estimation of the instantaneous properties through the HHT in the SHM field has recently emerged and been tested for various applications. Some of the most notable work will be presented here. Ghazalli et al. [102] estimated

the instantaneous phase and frequency signals obtained by pressure transducers through the HT and HHT in order to detect leaks and pipe ends. Yan et al. [103] used the HHT for analysing transient vibration signals of a bearing test bed in order to effectively detect the deterioration of a test bearing. Liu et al. [104] employed the EMD and HT in order to perform localised gearbox fault diagnosis in a gearbox with a tooth crack highlighting the advantages over wavelet transform. Chen et al. [105] developed an optimal sensor placement procedure using genetic algorithms and a finite element analysis technique and then they successfully used the HHT for damage detection on a composite wingbox while they introduced axis symmetry signal extension in order to solve the end effect of the EMD. Quek et al. [106] investigated the effect of the HHT for locating anomalies in the form of cracks, delaminations, stiffness loss or boundaries in beams and plates with a considerable level of success. Although many of the aforementioned studies have managed to effectively correlate the instantaneous properties of the obtained signals with the developed damage, yet very little effort has been made in terms of understanding of the physical mechanisms that lead to the observed changes in the indices. In addition, there is little work on Lamb waves to the knowledge of the author.

## 5.3 Experiment

The experimental set up and the obtained signals have been previously used by the author in [9]. However a brief explanation of the experimental procedure is considered important for the understanding of the underlying mechanisms. For the purpose of the experimental demonstration, a typical aerospace aluminium-2024 plate of 2 mm thickness was employed, while an artificially introduced damage in the form of a 10 mm hole was introduced into it. Two notches of 2 mm were introduced at either side of the hole for the faster initiation of the fatigue cracks. The bonding of the transducers and of the patch was carefully performed since the aluminium can develop severe deformations under fatigue which can have an immediate effect on the bonding quality. Therefore the surface was prior processed by means of sanding with a fine 180-grit sandpaper and was afterwards cleaned by acetone. The patch which was made out of the same material as the substrate and of the same thickness, was bonded with epoxy adhesive (Araldite 2015 provided by Huntsman) which was then left to cure at room temperature. The set up is displayed in Figure 5.1.

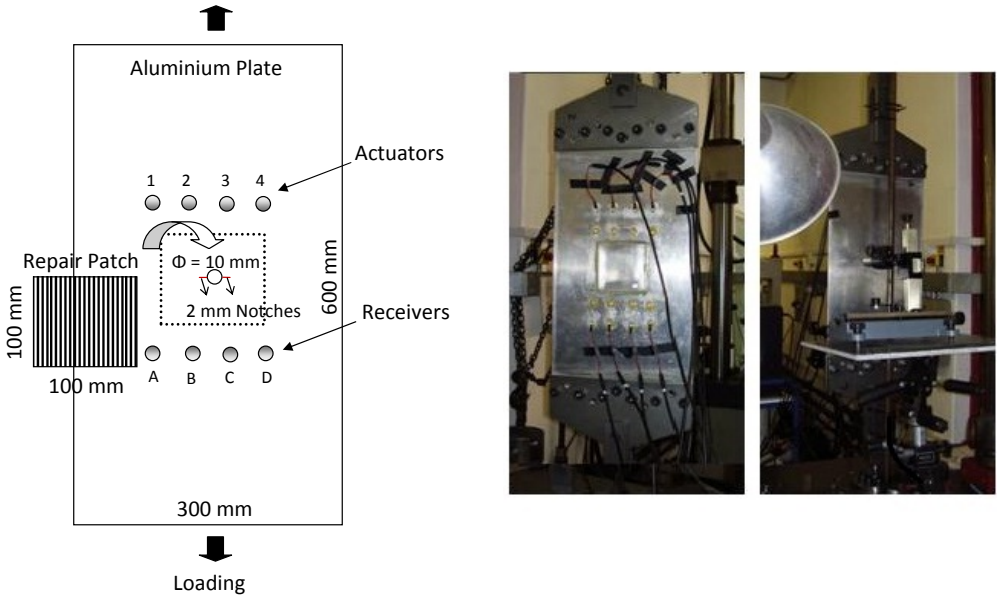


(a) Schematic illustration (b) Front (left) and rear (right) side

Figure 5.1: Experimental set up.

The metallic panel was subjected to cyclic loading between 10–70 kN which corresponds to approximately 7–50 % of the panel's strength at a 3 Hz frequency. Two types of damage were expected to initiate and simultaneously propagate in the repaired region during cycling. First was the propagation of two cracks in the aluminium plate, initiating at the tips of the notches. A microscope was employed for the monitoring of the cracks at the reverse side of the plate where there is no patch. Second was the debonding of the patch as a result of crack initiation in the adhesive when the ultimate shear strain of the adhesive would be exceeded under loading. The debonding of the patch was verified with visual inspection. Cycling was stopped every 5,000–10,000 cycles (starting after 15,000 cycles) at a pre-tension (40 kN) at which stage signals were recorded. This ensured the least interference of the obtained signals with the machine while the pre-tension would help with the damage detection by keeping the cracks open. The experiment was stopped after 70,655 cycles, a step at which the panel had developed a substantial level of damage. Also the temperature conditions in the laboratory facilities were considered to be relatively unchanged during the performance of the experiment. The developed damage is illustrated in the crack propagation curves in Figure 5.2.

For the monitoring of the panel, eight PZT transducers were surface-bonded with the same type of glue that was used for the patch. Four operated as actuators and four

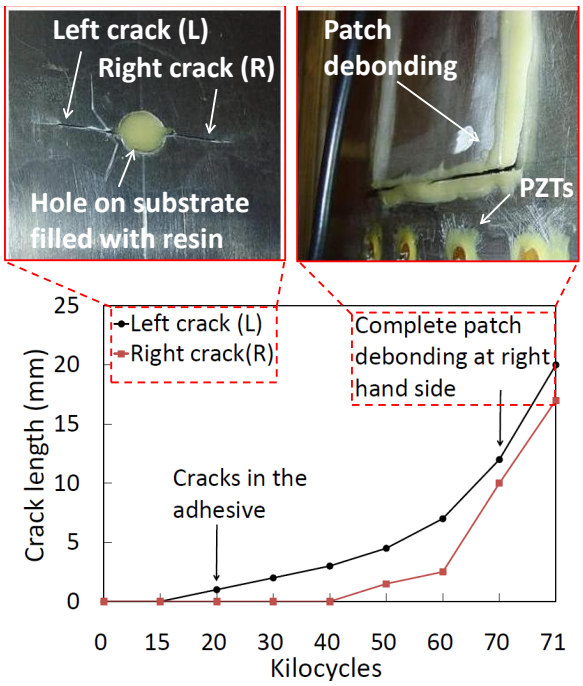


Figure 5.2: Developed damage in the form of cracks propagation in the substrate and patch debonding; crack propagation curves.

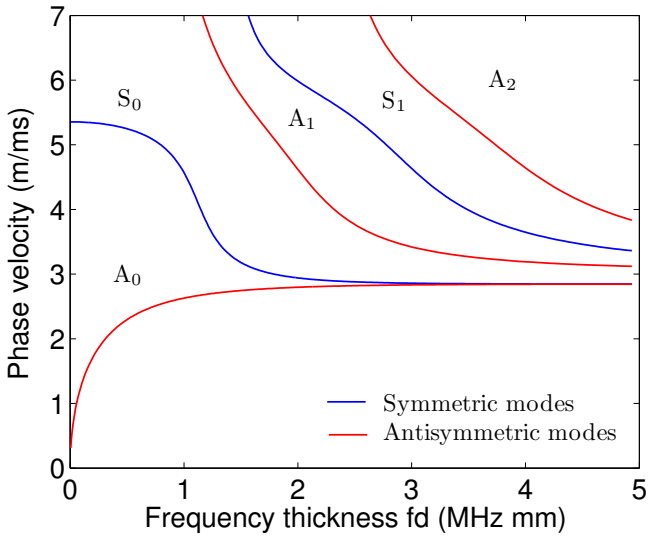


Figure 5.3: Dispersion curves for the Aluminium substrate (thickness=2 mm). [46]

as receivers, forming in total 16 propagation paths. The excitation signal was a five-cycle sine pulse enclosed in a Hanning window of a 10-Volt peak-to-peak amplitude generated by a TTi TGA1230 30 MHz wave generator. The data acquisition was performed at a 10 MHz sampling rate by a LeCroy LT224 oscilloscope and the excitation frequency was 240 kHz. At this frequency, only the two fundamental

$A_0$ and $S_0$ modes were excited as illustrated in the dispersion curves (Figure 5.3). This frequency was selected on the basis of an observed maximum energy for all propagation paths.

## 5.4 Instantaneous frequency of guided waves

The instantaneous frequency (IF) represents the energy content of nonstationary signals such as transient signals. Therefore this tool is employed in this study in an attempt to isolate damage sensitive features which would focus on more fundamental characteristics of the obtained signals rather than on amplitude-based tools. A preliminary investigation of the instantaneous frequency as extracted from the guided waves was essential in order to understand its behaviour. Due to space restrictions, only one propagation path was selected for benchmarking of the approach, namely propagation path 3-B. This path is considered to directly propagate through the monitored region of interest. In Figure 5.4 the IF of a response from the aluminium substrate prior to the patch bonding is illustrated along with the original time waveform. The method that was followed for the estimation of the following indices is explained in Section 4.2.2.

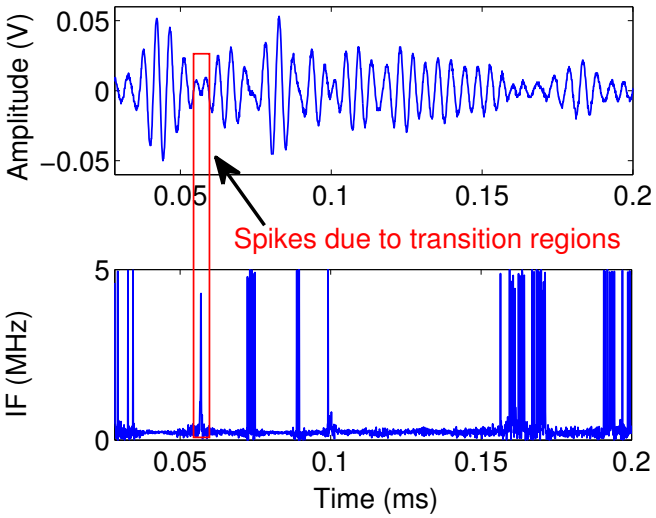


Figure 5.4: Instantaneous frequency of a time signal obtained from the aluminium substrate prior to patch bonding.

As illustrated, the trace exhibits several 'spikes' at specific time intervals of the time signal. These spikes are observed in areas with low amplitude. Low amplitude regions are present in guided waves in the beginning of the waveform or in

the transition areas between the wave packets. Since the IF is obtained after the differentiation of the IP, then it is possible that these spikes are the result of the amplification of the noise that is more prominent in the low amplitude regions of the original time signal. This means that for the subsequent feature selection, specific regions of the resulting IF traces need to be selected. The following sections will focus on the exploitation of the signal decomposition as a means of minimizing the spikes by converting the multi-component guided wave into a mono-component one and on a strategy for feature selection. Finally the correlation of the selected features with the developed damage will be displayed.

## 5.5 Empirical mode decomposition and ensemble empirical mode decomposition as noise filtering tools

Multi-component waves can be defined as waves that at any given time, involve more than one oscillatory mode. When guided ultrasonic waves propagate through a bounded media, then two basic modes coexist, namely the symmetric and the anti-symmetric; as they interact with the boundaries of the plate or with the defects, they undergo reflection, refraction and mode conversion which can result in the superposition of certain wave packages. Therefore, decomposition of the guided waves would be essential in this case in order to obtain mono-component signals before the application of the HT. In addition, the hypothesis that motivated this work supported the idea that the decomposition would effectively filter the high-frequency regions observed in Figure 5.4 and would produce signals that are easier to interpret.

Figure 5.5 displays a time signal obtained after the panel was cycled for 20,000 cycles. This signal exhibits areas of very low amplitude, in which the first wave packages have been considerably attenuated while the amplitude of subsequent wave packages has been magnified, due to the complex mechanisms during the interaction of the wave with the boundaries of the patch, the substrate, the hole and the developed cracks. The resulting IF prior to decomposition, contains a considerable level of noise. Decomposition of the time signal was performed with the EMD and the EEMD and the IF of some of the most representative IMFs were further plotted

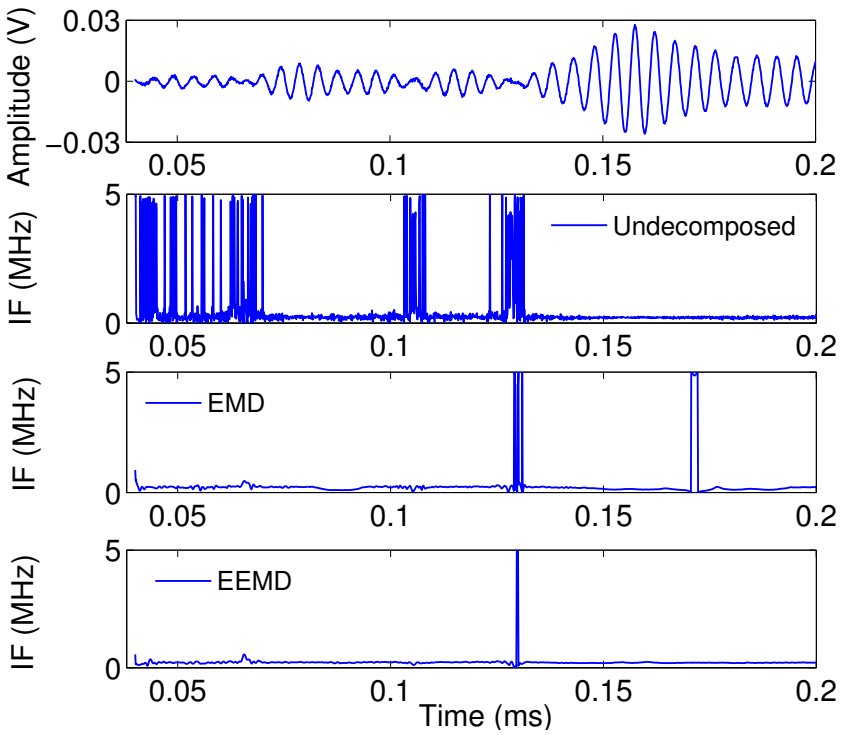


Figure 5.5: Behaviour of the instantaneous frequency of the time signal obtained after 20,000 cycles before and after its decomposition.

as illustrated in Figure 5.5. The most representative IMFs were selected after the high-frequency IMFs were removed, namely the first IMF for EMD and the first two for EEMD, and the remaining IMFs were added. The sum of the low-frequency IMFs was considered to be the new decomposed time signal as reconstructed by its IMFs; its IF was estimated through the HT.

The analysis was performed with an ensemble of $N$=100, and the ratio of the standard deviation of the added white noise and that of the original time signal was 0.1. These parameters were maintained for the rest of the analysis. The results demonstrate that both decomposition methods filter out almost all of the noise, highlighting the advantage of the EEMD over the EMD with respect to the percentage of filtered noise. Therefore the EEMD was considered as the optimum decomposition method for the rest of the analysis.

In Figure 5.6, the IMF components obtained by the EEMD method are illustrated for the time signal investigated in Figure 5.5 for comparable reasons. The time signal was decomposed into nine IMFs among which the first two are in the high-frequency region exhibiting a significant level of noise. The rest of the IMFs are in the low-frequency region. The corresponding residue is clearly monotonic.

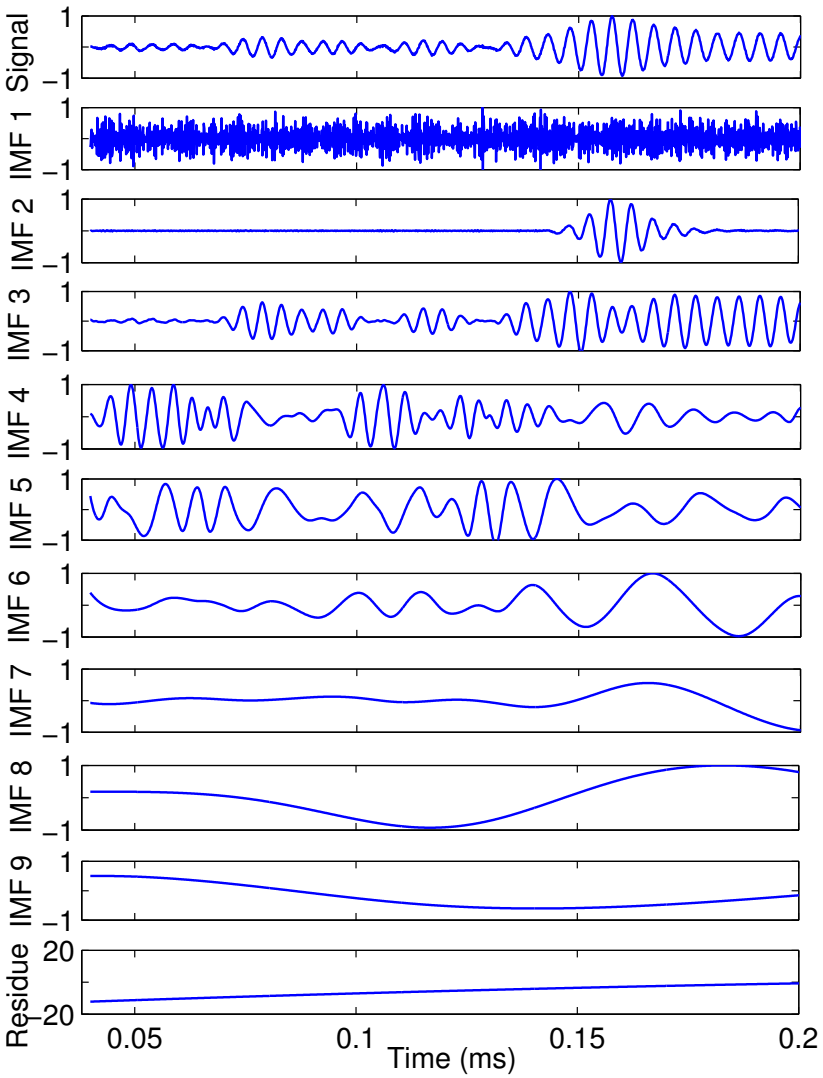


Figure 5.6: EEMD analysis of the time signal obtained after 20,000 cycles (normalised amplitudes).

## 5.6 The effect of damage on the instantaneous frequency of Lamb waves

This section investigates the effect of damage on the instantaneous frequency of the obtained signals and attempts to conclude on a sensible damage index for assessing the developed damage. For the understanding of the physical mechanism of the effect of damage on the behaviour of instantaneous frequency, a simple analytic simulation was conducted. Figure 5.7 illustrates the IF and the frequency content of the time signal that was presented in Figure 5.4. The IF curve is focused on the interesting

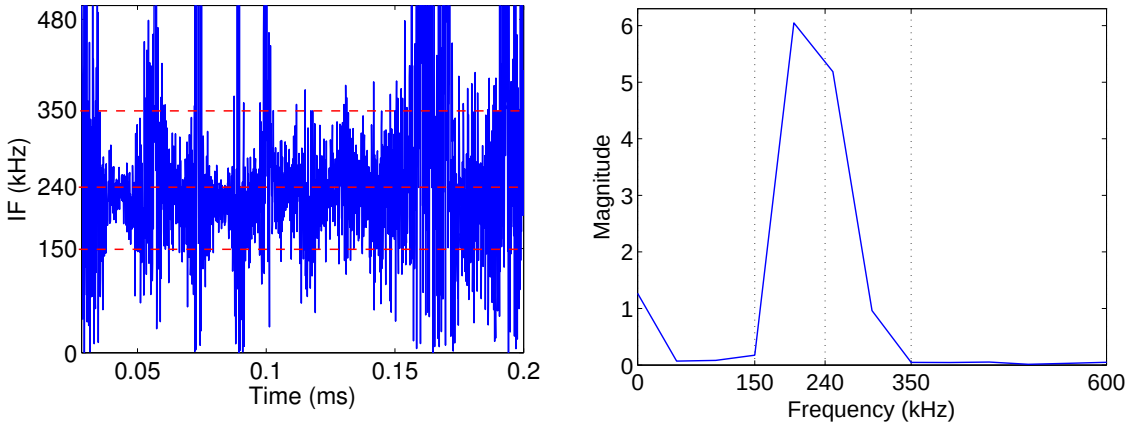


(a) Instantaneous frequency (b) Frequency content

Figure 5.7: Instantaneous frequency and Fourier transform of the time signal in Figure 5.4; the dotted lines (a) correspond to the average IF value together the upper and lower boundaries.

region (0–480 kHz) in order to visually isolate the observed spikes. Dashed lines have been added to both plots in order to display the observed phenomenon, according to which, the obtained frequency oscillates around a mean value that corresponds to the excitation frequency (i.e. 240 kHz) while its maximum and minimum values correspond to 350 kHz and 150 kHz respectively. The frequency content of the same signal exhibits a peak that agrees with the excitation frequency while the boundaries of the lobe expand at frequency values that agree with the maximum/minimum values of the IF oscillation.

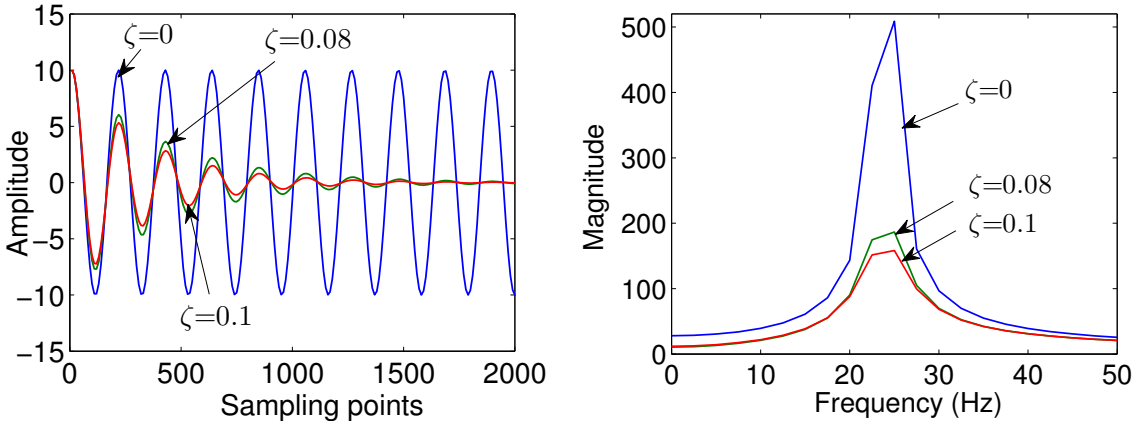


(a) Time domain (b) Frequency domain

Figure 5.8: Undamped and damped single degree of freedom system.

Figure 5.8 demonstrates the behaviour of a single degree of freedom (SDOF) oscil-

latory system when the damping coefficient factor is artificially increased. The time signals have an initial displacement equal to 10 at a sampling rate of 500 Hz, while the natural frequency was 15 rad/s. Its frequency spectra shows that as damping increases, then the main peak slightly moves towards lower frequency values and the sides of the main lobe expand significantly towards lower minimum and higher maximum frequency values, while the magnitude of the main lobe drops. This observation is better illustrated in Figure 5.9 where the normalised behaviour of the frequency domain curves are plotted. In the same figure the IF of the signals shows that although the dominant phenomenon is the amplification of noise when the amplitude drops, yet the variance of the curves increases as the damping coefficient factor increases.

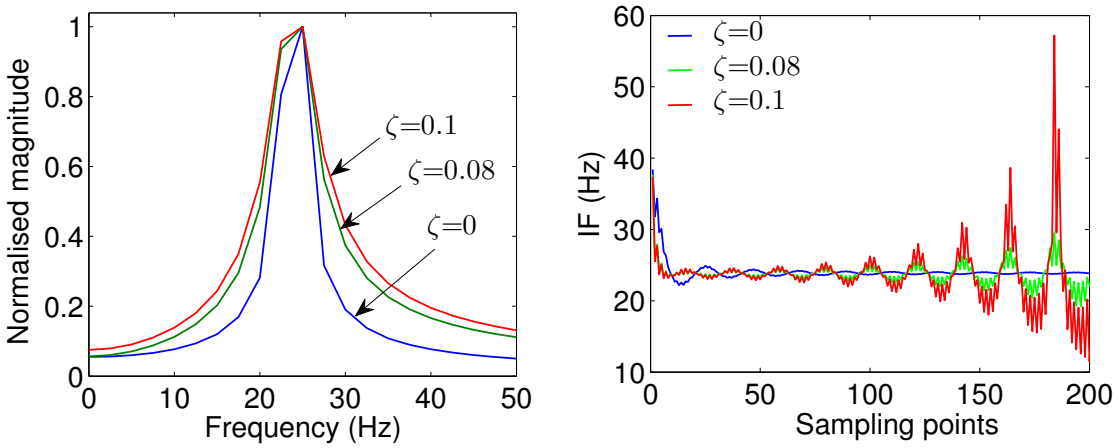


(a) Normalised Fourier content (b) Instantaneous frequency

Figure 5.9: Normalised Fourier spectrum (a) and behaviour of the IF (b) for a single degree of freedom system under varying damping.

Although it can not be claimed that the response of such a complex system like the tested panel of the current work can be described by a SDOF system, the demonstrated physical interpretation can explain the underlying mechanism of the effect of damage on the behaviour of the instantaneous frequency. As damage grows, namely as damping increases, then the peak-to-peak amplitude of the instantaneous frequency is expected to increase since the change of the mean value is considered to be negligible compared to the change of the maximum and minimum values.

The physical explanation is ultimately verified through the study of the experimental response. Figure 5.10 displays the IF traces for two different damage levels as obtained for propagation path 3-B, namely 20,000 and 70,000 cycles. The tested time interval is 135–204 $\mu$s in order to better visualise the phenomenon. The hy-

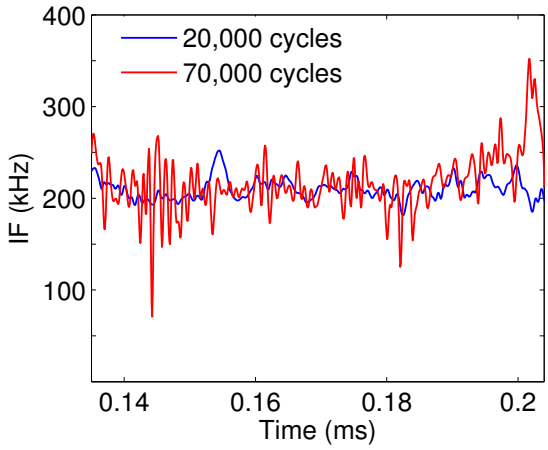


Figure 5.10: Instantaneous frequency compared for two damage cases (20,000 and 70,000 cycles) for propagation path 3-B and for time interval (135–204 $\mu$s).

pothesis is that the propagation paths that are mostly affected by the damage will exhibit a more distinctive effect on the resulting IF. Path 3-B is considered to propagate directly through the damaged region, hence it interacts with the damage more intensively than the rest. As illustrated, the IF traces oscillate around a mean value that corresponds to the excitation frequency (240 kHz). However, as damage grows with respect to the cycles, then the IF exhibits an increasing behaviour reaching higher peak-to-peak amplitudes.

In order to evaluate the developed damage and test the sensitivity level of the investigated tools, a prior feature selection had to be performed. Therefore all resulting signals from all propagation paths, were first pre-processed by means of the EEMD decomposition and IF estimation and then appropriate time intervals were selected on the basis of the waveform regions that exhibited areas with no noise. IF was performed on the reconstructed signal from the IMFs. In order to select which IMFs would be further used for the signal reconstruction, the power spectrum of each one of them was estimated, and only the ones whose spectral density gave results that were closer to the original time signal (i.e. peak) were selected and added. These IMFs were IMF 4–IMF 8. In addition, the illustrated results are limited only up to 60,000 cycles, because after that stage, the patch was debonded and the interference of the propagating waves with the structure's boundaries resulted in high attenuation, hence significant areas of noise in the IF curves were apparent. The selected time intervals for each propagation path are summarised in Table 5.1.

| Path | dt(1)($\mu$s) | dt(2)($\mu$s) | dt(3)($\mu$s) | dt(4)($\mu$s) |
|---|---|---|---|---|
| 3–B | 71–101 | 105–112 | 115–123 | 139–203 |
| 2–C | 82–87 | 111–121 | 122–136 | 154–157 |
| 4–D | 73–85 | 87–149 | 159–171 | 179–209 |
| 1–A | 56–61 | 69–99 | 158–163 | 179–209 |

Table 5.1: Time intervals for the estimation of the instantaneous frequency.

After the selection of the tested features, an appropriate damage index DI(IF) had to be established in order to assess the features with respect to damage, as following:

$$\mathrm{DI(IF)} = \Delta \mathrm{F} = [\mathrm{IF}(t)_{\max} - \mathrm{IF}(t)_{\min})]_{t_2}^{t_1} \tag{5.1}$$

where $dt$=$t_2$-$t_1$ is the tested time interval for each IF curve (Table 5.1). Figure 5.11 displays the results for the damage indices for all the propagation paths and for all the considered time intervals. The crack propagation curves have been also displayed for comparison reasons. The figure has been divided in two phases based on the extent of the developed damage as extracted from the crack propagation curves. The dominant characteristic of phase I is that damage is negligible in contrast to phase II where damage accumulated in the panel in the form of cracks on the substrate and patch debonding.

In the same figure, the defined threshold represents the average amplitude of the traces that were captured in phase I where no damage was apparent, and it is the same for all paths and equal to 124 kHz. As can be deduced from Figure 5.1, the propagation paths that interact with the repaired region where the damage is developed are the paths 3-B and 2-C, while paths 4-D and 1-A propagate outside the critical region. This is effectively reflected at the behaviour of the resulting DI which showed good sensitivity with the developed damage for paths 3-B and 2-C. The DI exhibits no significant deviation from the defined threshold in phase I where no damage is present, whereas in phase II, the DI clearly deviated from the threshold. On the other hand, propagation paths 1-A and 4-D show little sensitivity at the developed damage for both phases, with insignificant change in the employed DI. These observations suggest that the employed damage index could provide a potential tool that could distinguish between critical regions in complex SHM problems like the current one, exhibiting substantial damage sensitivity.

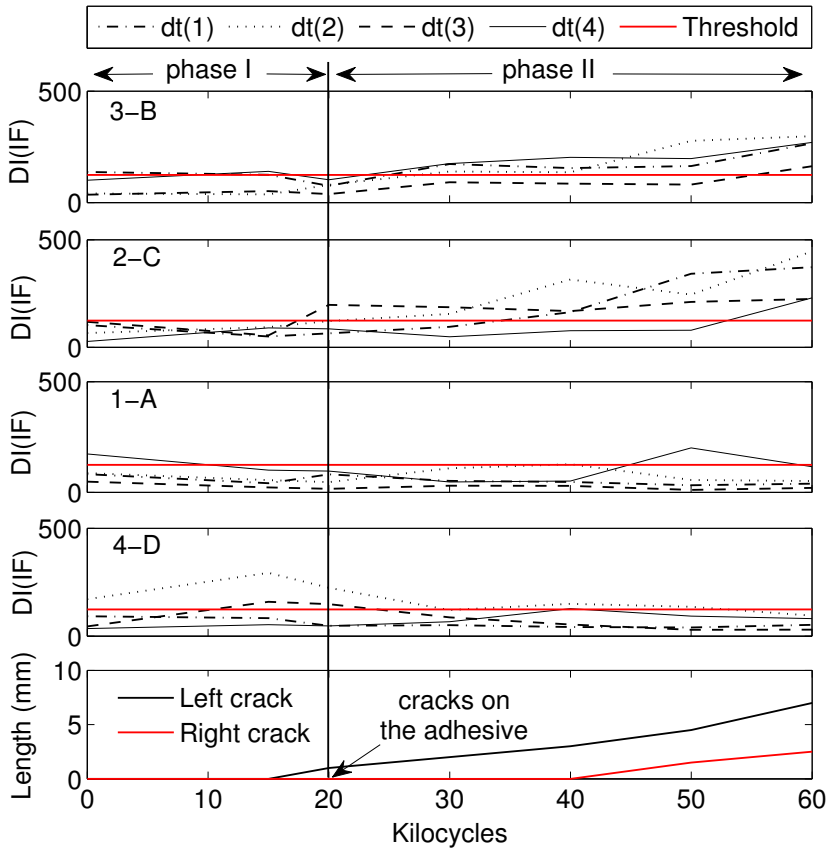


Figure 5.11: Damage index DI(IF) for four propagation paths in different considered time intervals (units in kHz).

## 5.7 The effect of damage on the instantaneous phase

The next step was the interpretation of the instantaneous phase as a consequence of the increasing level of damage. The hypothesis is obviously that the IP increases with respect to damage exhibiting a similar behaviour as the IF. Figure 5.12 displays the estimated IP traces for propagation path 3-B, prior to the signal decomposition. The respective damage index ID(IP) that was defined for the damage assessment is expressed with the following equation:

$$\mathrm{DI(IP)} = \Delta \mathrm{P} = [\mathrm{IP}(t)_{\max} - \mathrm{IP}(t)_{\min}]_{t_1}^{t_2} \tag{5.2}$$

where $t_1$=0 and $t_2$=240 $\mu$s for all propagation paths. The results are displayed in Figure 5.13 for the investigated propagation paths and up to 60,000 cycles. Two

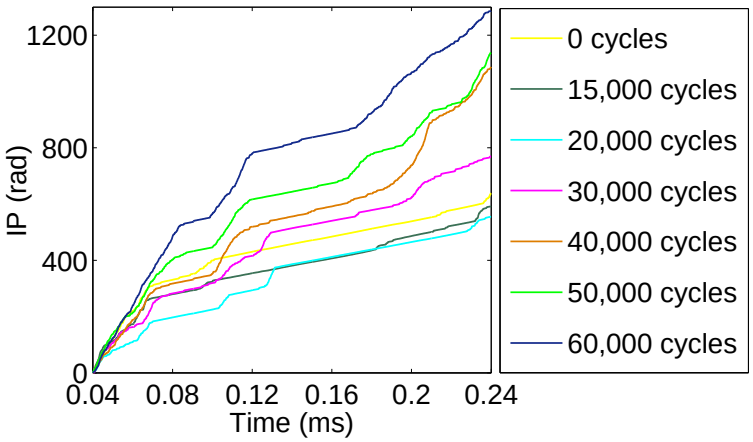


Figure 5.12: Instantaneous phase for propagation path 3-B for all damage cases.

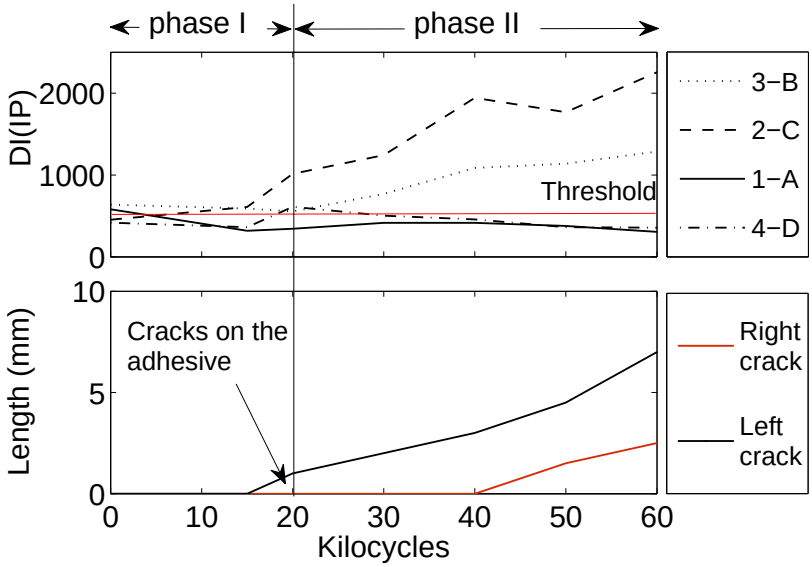


Figure 5.13: Damage index DI(IP) for four propagation paths.

phases are illustrated in a similar mode as in Figure 5.11 based on the degree of measured damage. The DI(IP) exhibits a similar behaviour with the DI(IF). In a similar way, a threshold that expresses the average values of the DI amplitude for phase I was defined and which is equal to 522 rad. Phase I shows no remarkable change of the DI with respect to the damage while in phase II the DI of the critical paths (3-B and 2-C) is estimated to be above the threshold while exhibiting an increasing mode with respect to the cycles. On the other hand, paths 1-A and 4-D show no considerable variation over phase II.

This short study indicates that the IP exhibits same damage sensitivity as the IF. The resulting damage index is only affected when estimated for propagation paths

that are mostly affected by the developed damage, hence providing a tool that could potentially distinguish critical areas for further damage assessment cases. In contrast to the features extracted from the IF, the respective IP traces do not need any prior processing or filtering which is quite an important advantage.

## 5.8 Discussion

In this chapter, an effort was made to understand the effect of the HHT on Lamb waves and to extract features that could provide some damage diagnostic capabilities. An Aluminium panel was tested under fatigue and the obtained signals were subsequently assessed through the concepts of the HT and the HHT. The resulting IF traces exhibited big artefacts as a consequence of the amplification of noise during the differentiation of the IP in order to obtain the IF. The EEMD was then employed in an attempt to remove most of these undesirable artefacts through a clean-up process, which removed most of the 'spikes'. This decomposition, enabled the isolation of certain parts of the waveforms, to be studied as potential features for damage detection. However, the level of artefacts was still high enough, especially as we moved towards higher damage levels. This fact poses a certain degree of limitation with respect to the efficiency of the analysis, since only four very small time intervals could be isolated, with the risk of masking important information hidden in other parts of the waveform. The effect of damage on the IF traces, was interpreted through the analysis of a single degree of freedom oscillatory system, which showed that the peak to peak amplitude of the IF is possibly increasing with respect to the increasing damping (e.g. increasing level of damage). This physical phenomenon was represented by most of the isolated features in the experimental study. Finally, simple damage indices derived from the IF and IP traces exhibited a relatively good agreement with the level of damage and a potential sensitivity with respect to wave paths that propagated through the most critical regions.

This study showed some relatively good results that provided an insight into time-frequency analysis tools which has not been so widely explored yet and which offer the advantage of an adaptive nature compared to other time-frequency approaches. This is considered to be a very preliminary stage of analysis, with results that on one hand provide certain damage diagnostic potentials, but on the other hand the damage sensitivity might not be at the necessary level that is required for the study

of complex structures such as repaired composite ones. From the experimental point of view, the effect of the interruption of the fatigue loading for the data acquisition, as well as the environmental variations need to be further investigated. Moreover the effect of structural features such as the boundaries of the patch or of the adhesive itself should be analysed in order to gain more confidence as to what causes the sensitivity in the paths that directly propagate through the critical region of the repair. Finally further tests should take into consideration more tested time intervals and more measurement points for a more reliable validation of the results. Overall, the most important limitation of the explored tools, is the lack of physical meaning of the resulting indices, which prohibits the association of the acquired features with the required damage sensitivity level. Therefore the author decided not to proceed with these tools for the rest of this work, as a result of their limited performance. Future work that could probably enhance the confidence these tools provide is essential. The numerical simulation of Lamb wave propagation in patch repair configurations is explored in the next chapter.

# Chapter 6

# Numerical Analysis of Lamb Wave Propagation

The objective of the current chapter is to investigate the physics of the wave propagation mechanisms that take place in composite repaired structures with numerical techniques, to analyse the effect of the developed damage and to conclude in terms of the efficiency and applicability of the physics-based processing approach as well as to locate the existing challenges in terms of modelling. The analysis focused on different types of damage based on a simple external patch repair. These types involve the debonding of the patch at representative locations, the degradation of the substrate and the simultaneous effect of both. The input files of the ABAQUS models can be found in Appendix C.

## 6.1 Introduction in explicit finite elements analysis

The general equation of motion in matrix form for linear structural dynamics, is given by:

$$M\ddot{u} + C\dot{u} + Ku = R \tag{6.1}$$

where $M$ is the structural mass matrix, $C$ is the structural damping matrix, $K$ is the structural stiffness matrix, $R$ is the vector of the applied loads, and $u$, $\dot{u}$ and $\ddot{u}$

are the displacement vector and its first two time derivatives, respectively.

In the current work, only the explicit dynamic analysis was selected since it is an ideal tool for high speed dynamic events, providing a computationally efficient solution for the analysis of large models with relatively short dynamic response times [107]. The explicit central difference integration rule is given as described below:

$$\dot{u}^{(i+\frac{1}{2})} = \dot{u}^{(i-\frac{1}{2})} + \frac{\Delta t^{(i+1)} + \Delta t^{(i)}}{2}\ddot{u}^{(i)} \tag{6.2}$$

$$u^{(i+1)} = u^{(i)} + \Delta t^{(i+1)}\dot{u}^{(i+\frac{1}{2})} \tag{6.3}$$

where $i$ refers to the increment number in an explicit dynamic step and $i$-$\frac{1}{2}$ and $i$+$\frac{1}{2}$ refer to mid-increment values. The kinematic state is advanced in each increment by considering the values of $\dot{u}^{(i-\frac{1}{2})}$ and $\ddot{u}^{(i)}$ at the last increment. The advantage of the computational efficiency of the explicit analysis lies in the use of diagonal or 'lumped' element mass matrices since the inversion of the mass matrix that is used in the computation for the accelerations at the beginning of each increments is trivial. The accelerations are described as:

$$\ddot{u}^{(i)} = M^{(-1)} \cdot (F^{(i)} - I^{(i)}) \tag{6.4}$$

where $M$ is the diagonal lumped mass matrix, $F$ is the applied load and $I$ is the internal force. No iterations and no tangent stiffness matrix is required for each time increment. The mean velocities $\dot{u}^{(i+\frac{1}{2})}$ and $\dot{u}^{(i-\frac{1}{2})}$ should be specially treated since the state velocities for each increment are defined as linear interpolations of the mean velocities:

$$\dot{u}^{(i+1)} = \dot{u}^{(i+\frac{1}{2})} + \frac{1}{2}\Delta t^{(i+1)}\ddot{u}^{(i+1)} \tag{6.5}$$

For the integration procedure to advance, the mean velocity $\dot{u}^{(-\frac{1}{2})}$ needs to be defined. At time $t = 0$, the default values of the velocity and the acceleration are zero if not otherwise used-defined. This would lead to the following definition for $\dot{u}^{(-\frac{1}{2})}$.

$$\dot{u}^{(-\frac{1}{2})} = \dot{u}^{(0)} - \frac{\Delta t^{(0)}}{2}\ddot{u}^{(0)} \tag{6.6}$$

| $\mathbf{E}_1$ | $\mathbf{E}_2$ | $\mathbf{E}_3$ | $\mathbf{G}_{12}$ | $\mathbf{G}_{13}$ |
|---|---|---|---|---|
| 153 GPa | 10.3 GPa | 10.3 GPa | 6 GPa | 6 GPa |
| $\mathbf{G}_{23}$ | $\mathbf{v}_{12}$ | $\mathbf{v}_{13}$ | $\mathbf{v}_{23}$ | $\rho$ |
| 3.7 GPa | 0.3 | 0.3 | 0.4 | 1600 kg/m$^3$ |

Table 6.1: Material properties of HTS40/977-2 (UD).

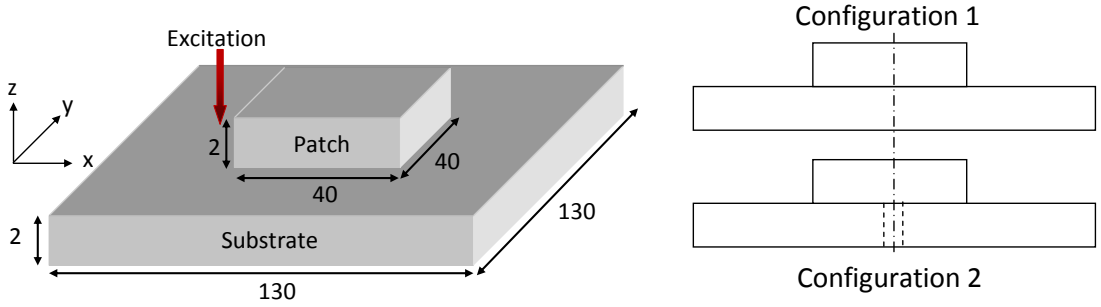


(a) Model (b) Studied cases

Figure 6.1: Schematic illustration of FEA model; dimensions in mm.

## 6.2 Model

For the purposes of the current analysis an adhesively bonded patch attached to a composite substrate was considered (single-lap repair). Each part was made of 8 plies from carbon fibre/epoxy resin pre-preg with a stacking ply sequence $[(0/90)s]_2$. The pre-preg was made from continuous unidirectional high tensile strength carbon fibres (Tenax HTS40 12 K 300) impregnated with a typical high temperature curing aerospace grade system Cycom 977-2 epoxy resin the properties of which are summarised in Table 6.1. The substrate was 130 x 130 mm and the patch 40 x 40 mm while the thickness of both was 2 mm. No tapering was considered, Figure 6.1(a).

The substrate's dimensions were symmetric in order to avoid undesirable reflections from the edges and to favour the propagation of the wave in the required direction. The patch was attached at the centre of the substrate, it had the same stacking ply sequence with the substrate, and it was made out of the same material. In real applications, the substrate has a hole underneath the patch, which represents the removed damaged area but usually filled with a plug made of the same material. Therefore two configurations were considered for the substrate, namely one with a hole of 6 mm and one without a hole, in order to investigate the effect of the hole on the behaviour of the propagating Lamb waves as illustrated in Figure 6.1(b). The

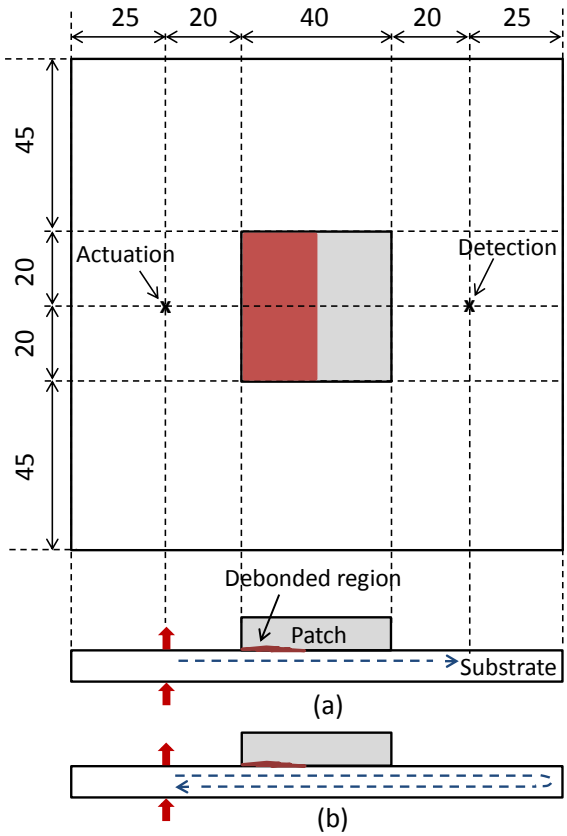


Figure 6.2: Schematic illustration of the model and the wave propagation modes (a) pitch-catch mode (b) pulse-echo mode (dimensions in mm).

aforementioned details comply with the general design characteristics represented in Chapter 2. The stiffness ratio of the patch to the structure should be equal to 1. This can be defined as:

$$S = \frac{E_R \cdot t_R}{E_S \cdot t_S} \tag{6.7}$$

where $E_R$ and $E_S$ are the Young's moduli of the patch and the substrate, respectively while $t_R$ and $t_S$ are the thicknesses of the patch and the substrate. In addition, the limiting overlap for current carbon fibre-epoxy systems is around $30t_R$, where $t_R$ is the patch thickness. For the current study, the aim was the demonstration of the wave propagation mechanisms based on artificially introduced damage, so the overlap length was not of critical importance since the panel would not be subjected to real loading.

Two cases were considered for the excitation and detection of Lamb waves, namely pitch-catch mode and pulse-echo mode (Figure 6.2). In both cases, two sets of actuating points were defined at the top and at the bottom surface of the substrate

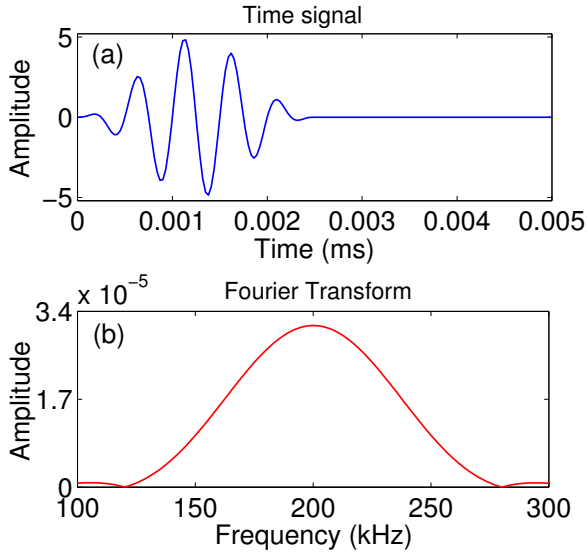


Figure 6.3: (a) Excitation time signal (b) Fourier transform.

exciting the plate with displacements that correspond to the actuating pulse. In the first case a sensing point defined at the other side of the patch was set to capture the response signals and in the second case the same points at which the excitation was induced, operated as sensing points after the wave had interacted with the discontinuities and the boundaries of the plate. The actuating and sensing points were defined at a distance 20 mm from the left and the right edge of the patch, respectively. The excitation signal is a five cycles pulse enclosed in a Hanning window (Figure 6.3). Figure 6.4 illustrates the dispersion curves for the current material and for the given thickness of the substrate [48].

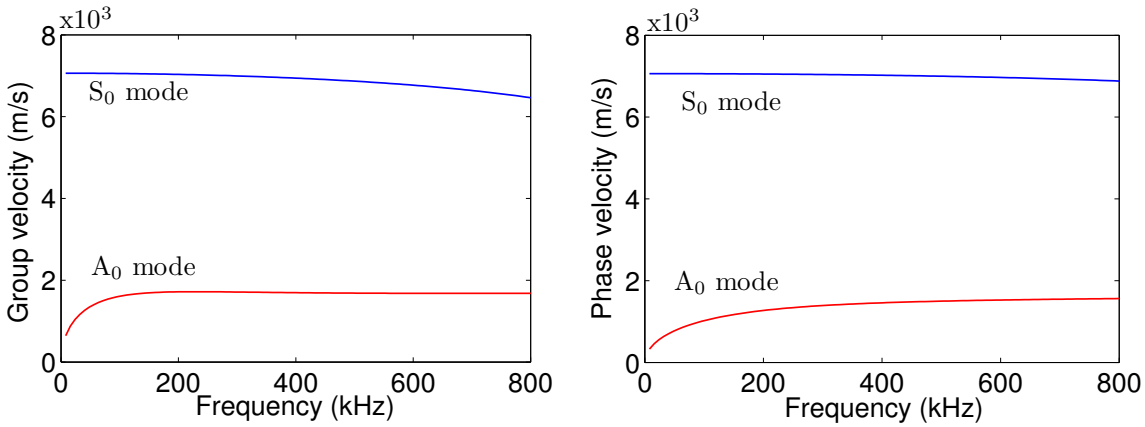


(a) Group velocity (b) Phase velocity

Figure 6.4: Dispersion curves for a $[(0/90)s]_2$ laminate of 2 mm thickness. [48]

The selection of the desired Lamb wave mode was decided on the basis of the most widely employed mode for composite testing in the previous literature review, which is the $A_0$ mode. First of all as it can be observed from the dispersion curves, the $A_0$ mode has a sufficiently shorter wavelength ($\lambda = c_g/f$) at a given frequency which can provide a monitoring system with higher resolution, offering the potential of capturing smaller sizes of damage. Secondly, the $A_0$ mode produces a more uniform shear stress distribution through the thickness of the tested composite laminates than the $S_0$ which indicates that it would be more appropriate for debonding detection. Finally, in composite materials, below the cut-off frequency, there are more than one symmetric modes that could propagate, namely the Lamb waves $S_0$ modes and shear horizontal $SH_0$ modes. It is therefore suggested that the analysis would provide sufficiently easier to interpret results when only a pure mode is excited.

The model was built with the Abaqus CAE pre-processing package and it was solved using Abaqus (version 6-10.2) explicit analysis which utilises an explicit integration based on the central difference method. The temporal and spatial resolutions are of significant importance since they both highly affect the stability of the numerical solution [108]. The definition of the size of the finite element $L_e$, depends on the wavelength of interest, hence on the required damage sensitivity of the model. A general criterion that has been proposed is the assignment of 10 or 20 nodes per wavelength [109]. For the current study 10 nodes per wavelength proved to ensure the required resolution. This condition can be expressed as:

$$L_e = \lambda_{\min}/10 \tag{6.8}$$

As far as the time step is concerned, a stability limit is recommended by ABAQUS Explicit for the integration time step $\delta t$ in cases of wave propagation in the longitudinal direction across the element:

$$\Delta t = L_{\min}/c_L \tag{6.9}$$

where $L_{\min}$ is the smallest dimension of the smallest finite element of the model and $c_L$ is the bulk longitudinal wave velocity through the material. However best resolution is achieved when the criterion is adjusted to the studied dynamic problem. In this case, certain studies suggest that at least 20 points need to be used for each cycle at the highest frequency $f_{\max}$ of the problem [110]. This can be expressed as:

$$\Delta t = 1/(20 f_{\max}) \tag{6.10}$$

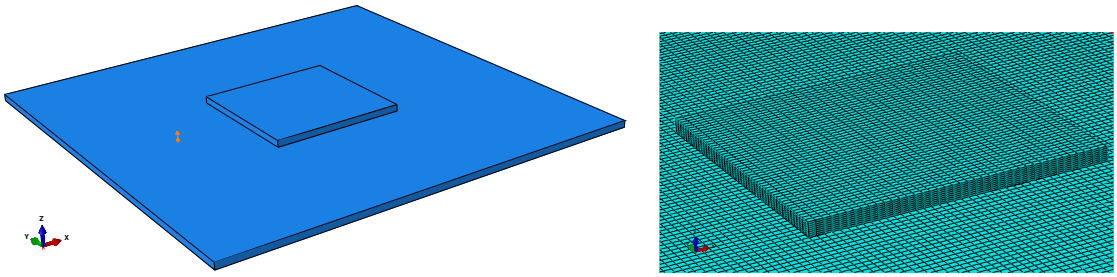

(a) ABAQUS model (b) Mesh

Figure 6.5: Model and meshing realisation for the patch repaired plate.

The element type employed in this model was a general purpose C3D8R element (3D-solids, 8-node linear brick of reduced integration) since it has been extensively used in the past with successful results. The mesh was uniform, consisting of square elements in order to avoid any reflections occurring from the differences in the mesh and to favour similar wave propagation in all directions as illustrated in Figure 6.5. The current study focused on point force excitation for the purpose of simplicity. Based on this approach, the effect of the transducers on the parent plate, was modelled as a pair of in-phase forces applied on nodes on the upper and lower surface of the plate and which corresponded to the centre of a real PZT sensor of a diameter equal to 10 mm. The in-phase force excitation would ensure the excitation of a pure $A_0$ mode. These forces were given an amplitude that followed the excitation signal in Figure 6.3. The model assumed perfect bonding between the patch and the substrate assuming that the effect of the adhesive on the propagating signals was negligible. Figure 6.2 displays the in-phase assignment of the displacements at the actuating points, in order to excite the $A_0$ mode. This is the effect that a pair of real transducers would have when operating out-of-phase.

As previously mentioned, in modelling applications of wave propagation with finite elements (FE), it is required that an appropriate mesh will be used and which would enable the uniform propagation of the wave in all directions. Therefore an appropriate meshing approximation had to be employed in terms of modelling the hole at the substrate. As illustrated in Figure 6.6, the square mesh elements were employed by approximating the shape and size of the hole through a Cartesian approach. The nodes were selected in such a way that they lay either on the radius of the circular hole or at the closest inside point, assuming that if the grid size is sufficiently small compared to the hole radius and the smallest wavelength, then no considerable deviation would be observed in the analysis [111].

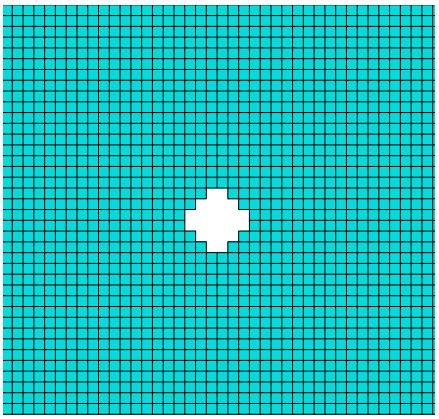

Figure 6.6: Meshing approach for the modelling of the hole.

Additional parameters that were investigated were the effect of the aspect ratio (AR) and the effect of the contact interaction on the response signals. Normally the aspect ratio of the mesh should be close to unity for the achievement of maximum accuracy with an unavoidable trade off with respect to the computational time. A mesh convergence study between AR=2 and AR=4 was conducted without any effect on the acquired waveforms but with significant increase in the computational time for the first case. Therefore an AR=4 was considered in the current study. Furthermore, a brief analysis showed that the assignment of contact interaction between the debonded surfaces of the patch and the substrate resulted in more accurate results compared to models where the surfaces were allowed to penetrate each other. The excitation frequency was selected to be below the cut-off frequency

| Wavelength ($\lambda$) | Excitation frequency ($f$) | Time step ($dt$) | Element size ($L_e$) |
|---|---|---|---|
| 10 mm | 200 kHz | $10^{-7}$ s | 1 mm |

Table 6.2: Model characteristics.

(200 kHz) in order to avoid the excitation of the $A_1$ mode, and in addition it was ensured to be high enough in order to allow a short wavelength (10 mm), hence a high resolution analysis. Table 6.2 summarises the modelling parameters considered for this model after appropriate estimations based on the dispersion curves and the aforementioned criteria.

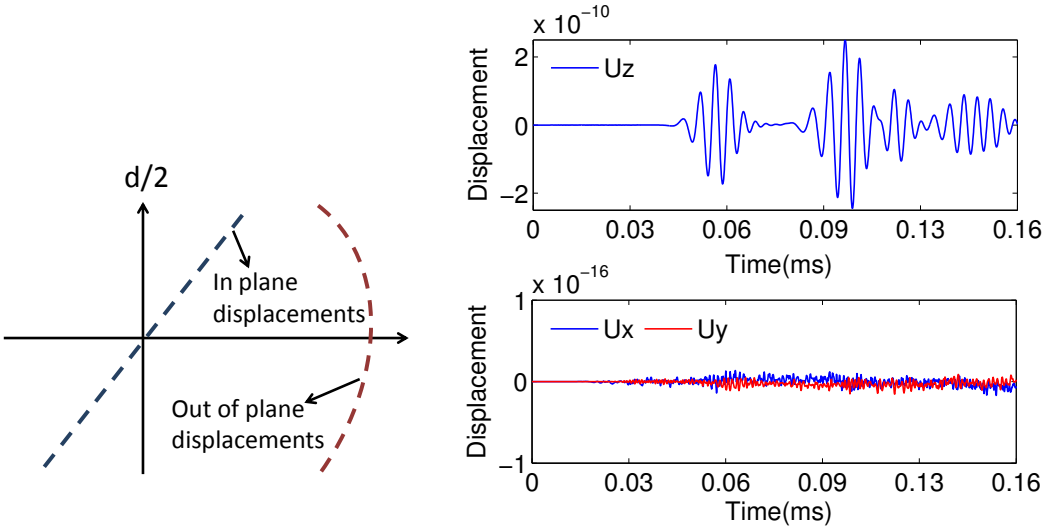


(a) Theoretical displacements in the middle plane

(b) In-plane and out-of-plane displacements in the middle plane of the model

Figure 6.7: Validation of the antisymmetric mode through the middle plane displacements.

## 6.3 Verification and validation of the model

For the theoretical verification of the model, two approaches were employed, one qualitative and one quantitative, respectively. It needs to be highlighted at this point that any theoretical verification could only be conducted for the substrate without the hole, since the hole would lead to mode conversion. The first was the investigation of the behaviour of the middle plane of the built model. As illustrated in Figure 6.7, when a plate is excited with an antisymmetric mode, then the in-plane displacements in the middle plane (half thickness plane) are zero. The respective signals were recorded at the middle plane of the substrate, namely the in-plane and out-of-plane displacements, and the in-plane proved to be negligible compared to the out-of-plane, verifying the excitation of a pure antisymmetric mode.

For a more quantitative verification, the theoretical and the numerical group velocities of the substrate were compared. The numerical group velocity was estimated for the given distance between the actuating and the sensing point (as defined in the pulse-echo mode), and by measuring the arrival time of the response signals for a wide range of frequencies (50 kHz–200 kHz). The arrival time was visually selected in this case since there was no noise present and this task was straightforward. However, the application of a more elaborate algorithm has been explored in

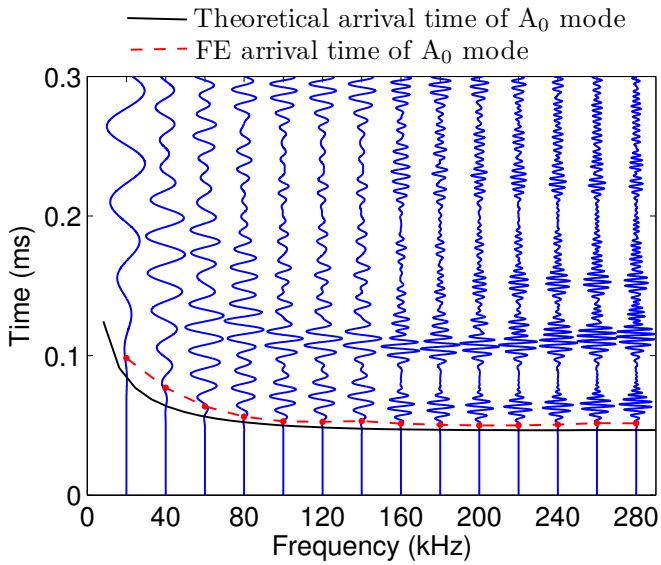


Figure 6.8: Theoretical and numerical arrival time for the first antisymmetric mode.

this work for the identification of the accurate arrival time, where the arrival time in experimental cases was 'buried' in noise. Figure 6.8 shows the numerical and the theoretical group velocity. The numerical and theoretical results show a remarkable agreement.

Different failure modes will be further considered for the current analysis. However the most common failure mode under loading, involves the debonding of the patch as a first level of damage and then when the patch can no longer carry the loads, the plate starts failing around the hole. As a result, for the experimental validation of the model, only the debonding of the patch was primarily considered in a numerical and experimental level as visually illustrated in Figure 6.2.

The plates were manufactured in accordance to the characteristics described in Section 6.2. Three PZT transducers were surface bonded with instant glue on the pre-defined locations (Figure 6.2), while the distance of their centres was equal to 40 mm from the centre of the plate and 20 mm from the edges of the patch hence forming a 80 mm propagation path for the pitch-catch mode. The third PZT transducer was surface-bonded at the bottom side of the substrate in order to approximate the interrogation of the panel with pulse-echo mode. The wave generator that was used was a TTi TGA 1230 30 MHz model exciting the panels with the pre-defined excitation signal (Figure 6.3) and the data acquisition was performed by a LeCroy LT224 oscilloscope. The patch was attached at the centre of the plate using rapid Araldite after the cleaning of the surface with acetone. The amount of glue was as

little as it was required for the patch to effectively bond while the adhesive would form a very thin almost negligible layer in order to avoid any deviations from the employed FE model. Two levels of debonding were simulated for the validation of the model, namely 1/4 of the patch and 1/2. This was achieved through the use of PTFE coated fibreglass sheets cut at the dimensions of the debonded area. The debonded area was all the way across the width of the bonding line between the patch and the substrate.

As previously investigated, the excitation of a single Lamb wave mode with PZTs can be a quite demanding task. Giurgiutiu [112] has developed a model using the space domain Fourier transform, based on which the tuning of certain modes at specific frequencies is possible for the excitation and detection with PZT transducers. This concept is based on the fact that Lamb wave mode wavelengths vary with frequency. He then performed an experimental validation on aluminium plate and derived appropriate tuning curves which showed that the $A_0$ mode is preferably excited at lower frequencies than the $S_0$ mode.

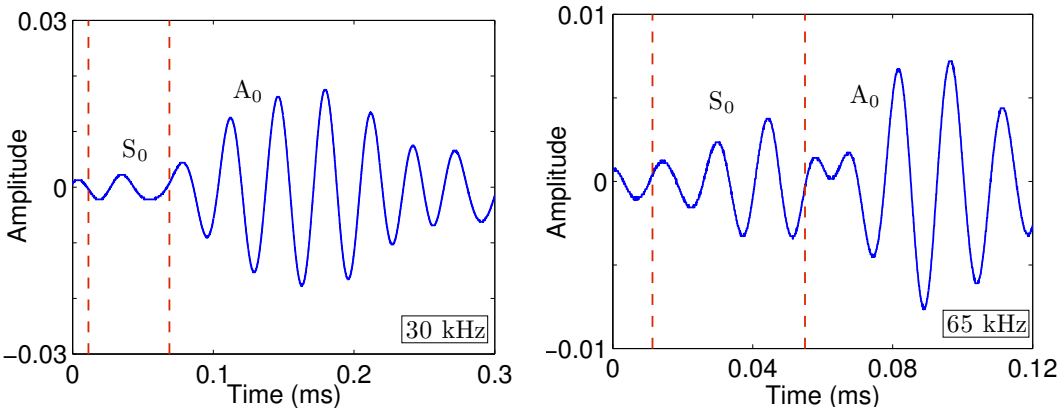


(a) Excitation frequency=30 kHz (b) Excitation frequency=65 kHz

Figure 6.9: Modes tuning result for excitation frequencies 30 kHz (a) and 65 kHz (b).

In a similar way, PZT transducers were used in this study for the experimental validation of the FE model and their tuning was performed experimentally after exciting the substrate (without the hole) at a number of frequencies belonging to the range that is found to be below the cut-off frequency. This would ensure only the excitation of the two fundamental $A_0$ and $S_0$ modes. Then the estimation of the theoretical arrival time of each mode was carried out through the dispersion curves, and the characterisation of the response signals was performed in an attempt to identify which mode is excited at each frequency. It was found that a relatively pure

$A_0$ mode could only exist at 30 kHz or below as shown in Figure 6.9(a), while after that frequency, a perturbation started propagating at the region of the $S_0$ mode which started getting stronger at 65 kHz, Figure 6.9(b). Therefore the validation of the model was performed at 30 kHz.

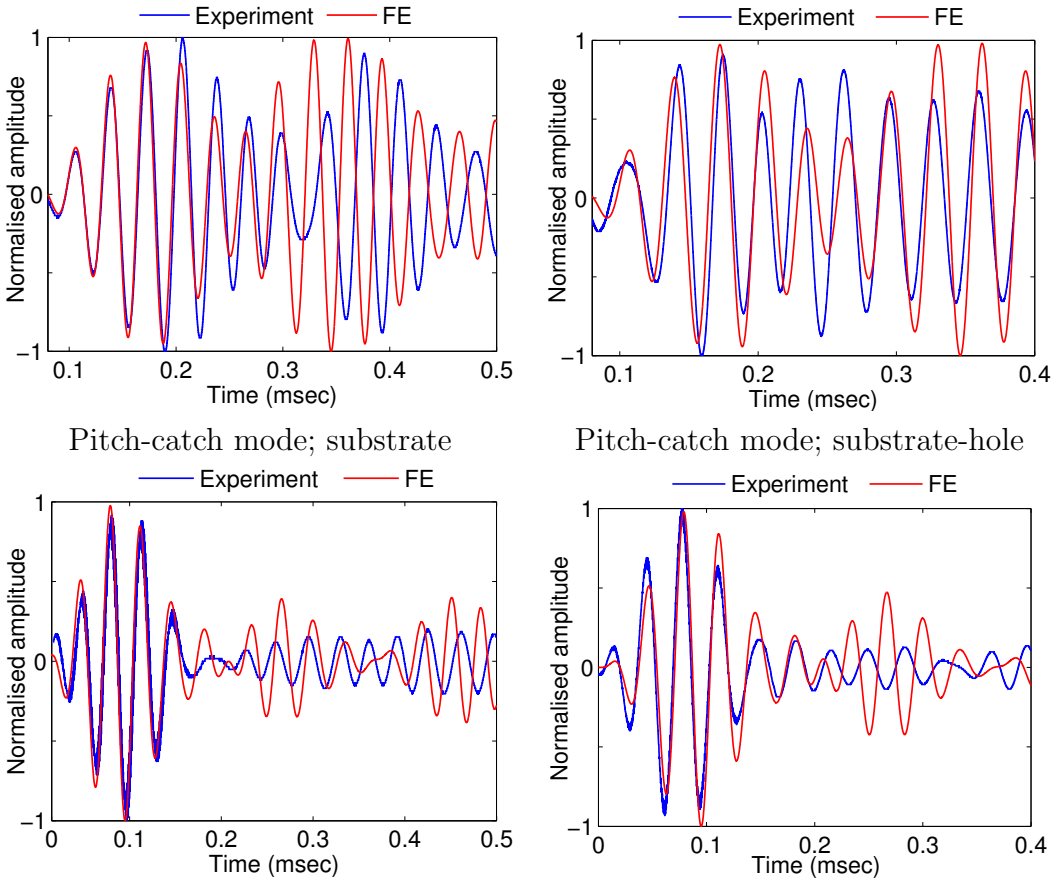


Figure 6.10: Validation of the FE model for the substrates of both configurations.

First the validation of the response signals for both configurations (with and without hole) and for both actuation modes (pitch-catch and pulse-echo) had to be validated before the bonding of the patch (Figure 6.10). As illustrated, the experimental and the FE signals exhibit a good agreement which is more profound for the first wave packages in both pitch-catch and pulse-echo modes. The model accurately simulated the developed phenomena during the reception of the incident signal as well as the reflected packages from the boundaries. Slight disagreement can be observed at the arrival time of the reflections for the pitch-catch mode and at the amplitude of the reflections at the pulse-echo modes as a result of the material imperfections, the modelling approximation with respect to the excitation method and the Cartesian

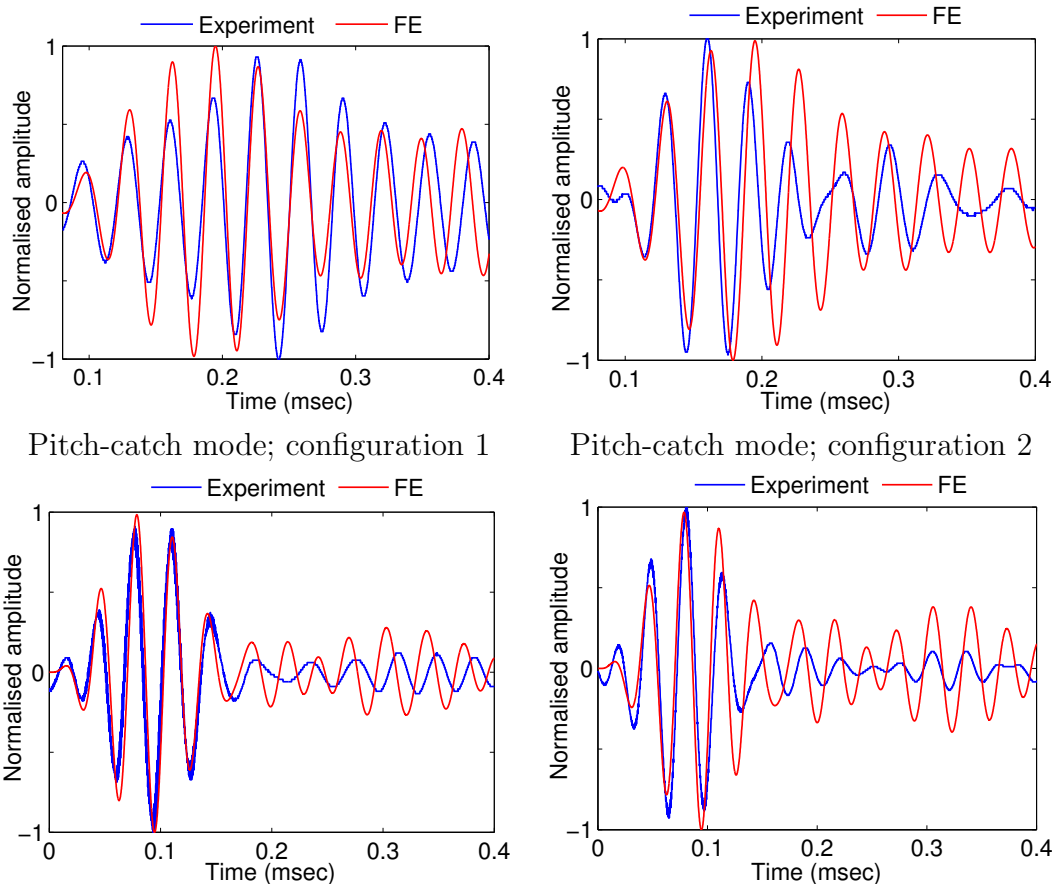


Pitch-catch mode; configuration 1 Pitch-catch mode; configuration 2

Pulse-echo mode; configuration 1 Pulse-echo mode; configuration 2

Figure 6.11: Validation of the FE model for the repaired plate without debonding of both configurations.

simulation of the hole. Also the adhesive of the PZT transducers might affect the accuracy of the acquired signals.

Approximately the same results can be observed in Figures 6.11, 6.12 and 6.13 when the patch bonding took place. For the case that no debonding took place, the model can accurately capture the arrival times for both excitation modes, however the boundary reflections in the experimental set up, exhibit a significant attenuation especially for the configuration 2 (substrate with hole). This could be attributed to the effect of the energy scattering over the adhesive which significantly attenuates the reflections from the boundaries of the patch, while those in the case of the model are superimposed with the reflections of the substrate's boundaries resulting in stronger wave packets after the first incident wave. Similar observations can be extracted from the considered cases of the debonded patch at different levels. It needs to be highlighted that any differences between the incident waves for the pulse-echo mode

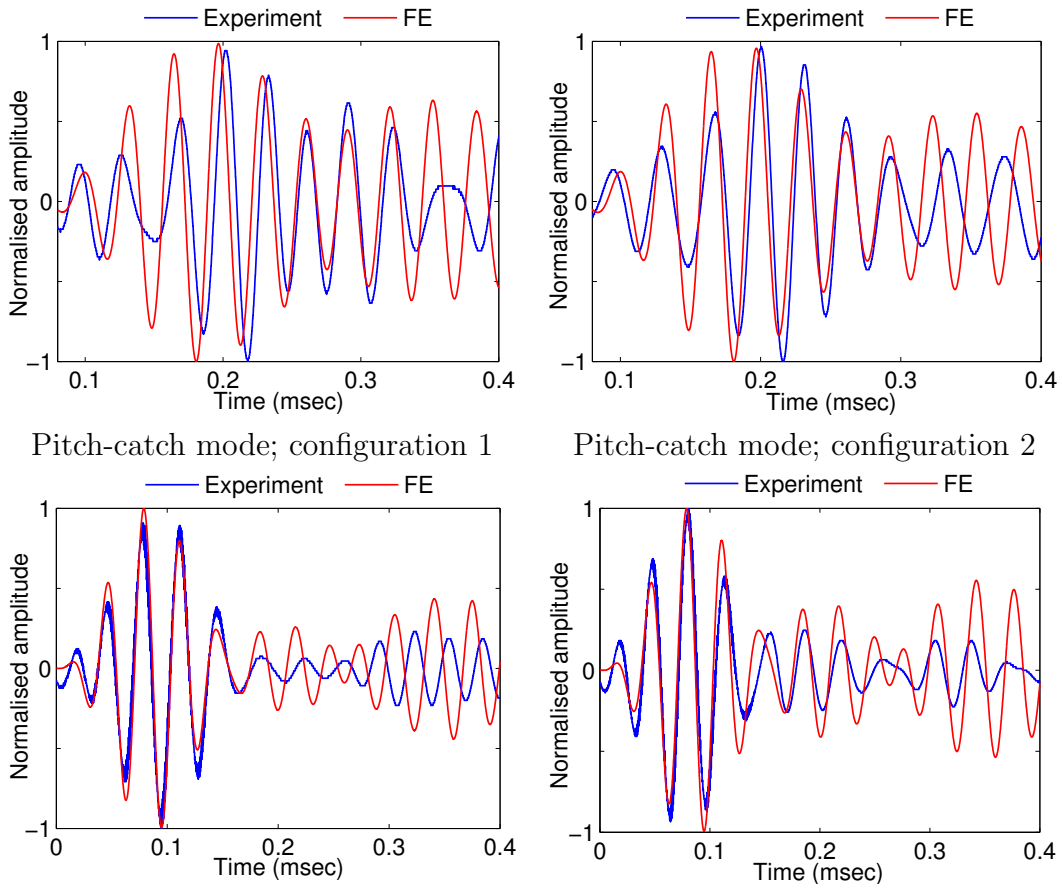


Figure 6.12: Validation of the FE model for the repaired plate of both configurations for the case of patch debonding equal to 1/4 of its total bonding area.

lie in the fact that different plates were manufactured for each bonding scenario resulting in possible slightly different alignment of the PZT transducers or different material imperfections. Overall the level of agreement is considered to be sufficient, which gives confidence that the model can successfully represent the underlying mechanisms during the wave propagation in bonded and debonded repaired plates.

## 6.4 Propagation mechanisms

The propagation mechanisms that take place during the testing of a composite repaired panel with Lamb waves are the scope of the current section. Figure 6.14 illustrates contour plots of the field output at representative time instants. These results only refer to the pristine condition of configuration 1. As shown, the substrate

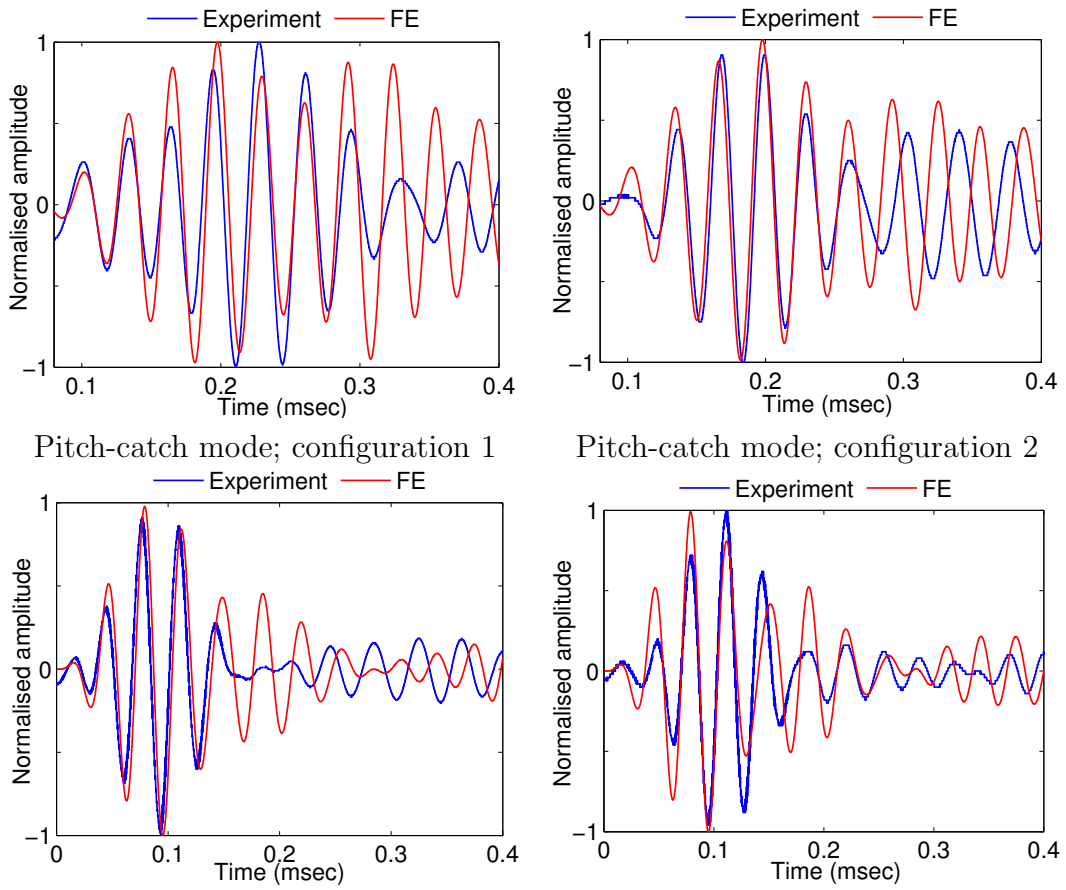


Figure 6.13: Validation of the FE model for the repaired plate of both configurations for the case of patch debonding equal to 1/2 of its total bonding area.

is excited with the excitation signal and the waves propagate around the excitation point uniformly. At $t_1$=24 $\mu$s the incident wave interacts with the left boundary of the patch and with the left boundary of the substrate. The interaction with the substrate's boundary is expected to cause reflection while the interaction with the boundary of the patch will cause a portion of the signal to be transmitted through the repaired area and another portion to be reflected as illustrated at $t_2$=34 $\mu$s. In addition, the increase in the panel's thickness at this stage will cause mode conversion.

The same mechanisms of reflection, mode conversion and transmission take place every time any wave package meets the boundaries of the substrate or of the patch. Needless to say, the same mechanisms take place for any wave packet which is the result of the same mechanisms occurred at a prior time instant. An example is illustrated at $t_3$=48 $\mu$s and at $t_4$=64 $\mu$s. At these time instants, the wave propagates

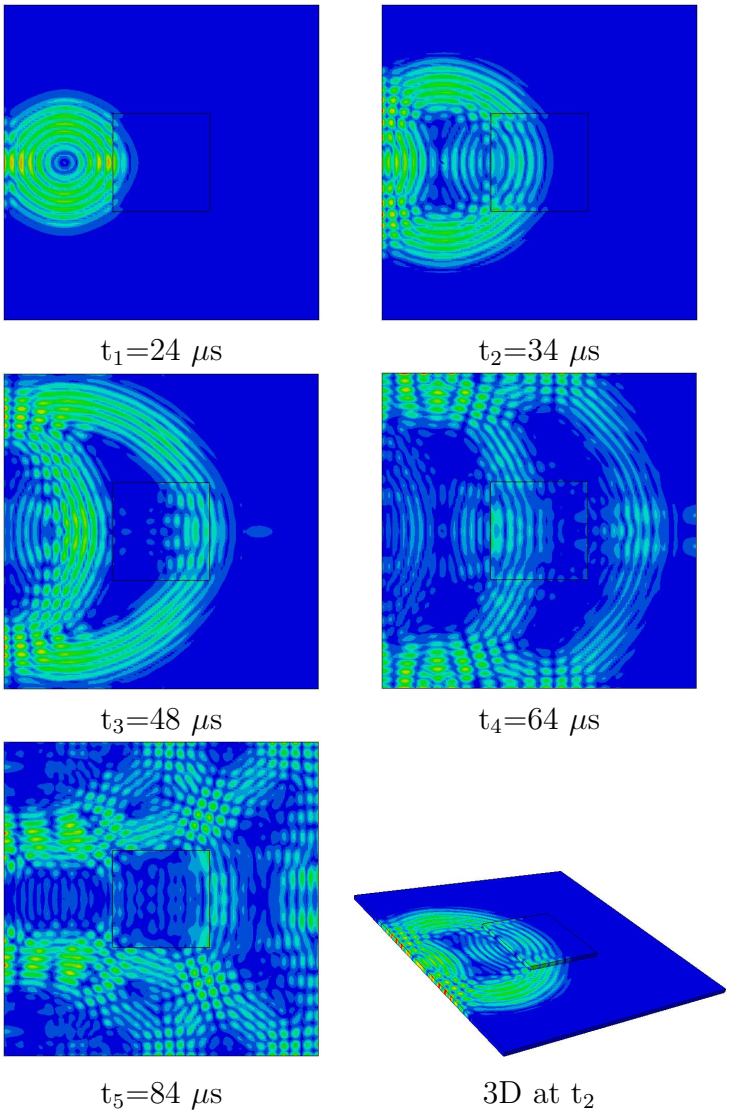


Figure 6.14: Field output results of configuration 1 (substrate without hole) for the pristine condition at representative time instants.

through the repaired area, it reaches the sensor assigned for the pitch-catch mode while it also interacts with the right boundary of the patch. In addition the reflected waves are reflected again at the boundaries of the left side of the panel. Finally at $t_4$=84 $\mu$s several wave packages superimpose each other, forming mixed packages, as a result of the multiple reflections. Another significant parameter that complicates the propagation mechanisms is the presence of hole at configuration 2. It is expected that the hole will lead to further mode conversions and it will substantially distort the propagating signals. As illustrated in the contour plot captured at the back of the repaired panel at $t$=35.5 $\mu$s, (Figure 6.15), the hole causes a certain degree of reflections at its boundaries when the incident wave first reaches the hole.

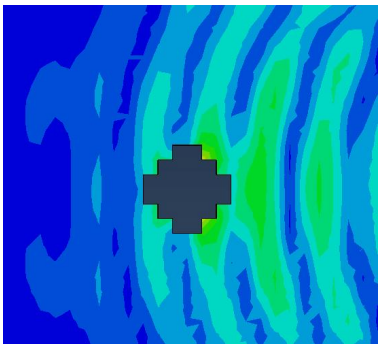

Figure 6.15: Propagation of $A_0$ mode through the hole of the substrate at t=35.5 $\mu$s.

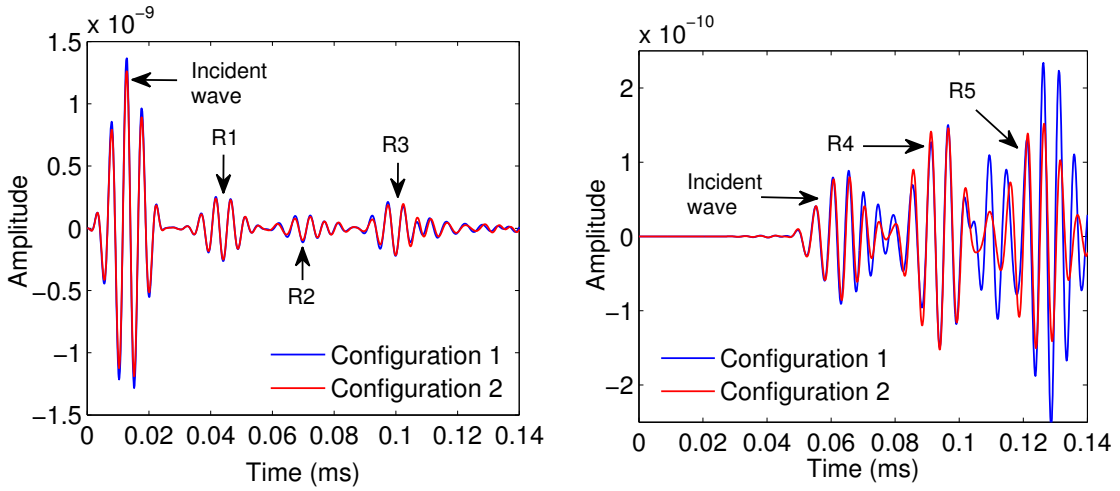


(a) Pulse-echo mode (b) Pitch-catch mode

Figure 6.16: History output results of configurations 1 and 2 for the pristine condition.

Therefore as observed, reflections can occur at all possible structural features and boundaries, each of which will eventually lead to mode conversions. Figure 6.16 illustrates the results obtained for the two configurations at the pristine condition. Each wave packet is denoted accordingly at both excitation modes, while the response signals for the two configurations are overlaid for comparison purposes. The first wave to arrive is the incident wave for both pitch-catch and pulse-echo modes (Figure 6.14, $t_1$=24 $\mu$s, $t_4$=64 $\mu$s). R1 represents the wave packet which is the result of the reflection of the incident wave at the left edge of the patch superimposed with the reflection of the incident wave at the left edge of the substrate (Figure 6.14, $t_2$=34 $\mu$s). The considerably attenuated wave package R2 was formed when the reflections of the wave package produced at R1 at the left edge of the substrate and at the left edge of the patch were superimposed (Figure 6.14, $t_4$=64 $\mu$s). R3 is the

result of multiple reflections at the boundaries of the patch and the substrate. R4 represents the backscattering of the incident wave at the right edge of the substrate and it is the second wave packet to arrive after the incident wave for the pitch-catch mode. It is assumed that this wave packet is superimposed with the package that occurred after the incident wave was reflected at the left boundary of the substrate (Figure 6.14, $t_5$=84 $\mu$s). Finally R5 is caused due to multiple reflections at the boundaries of the patch and the substrate. The comparison between the response signals for the two configurations (substrate with and without hole) shows no considerable differences for the pulse-echo mode, while for the pitch-catch mode, the signal obtained from the configuration 2 shows a drop in amplitude and a distortion in the wave shape as a consequence of energy scattering over the hole.

## 6.5 Failure modes and their effect on the propagating waves

There are several types of damage that can occur when a repaired configuration like the one of the current model is subjected to mechanical loads. The most representative ones involve:

**Damage mode 1:** Debonding of the patch initiated at the edges due to loads most commonly occurred at a perpendicular direction to the orientation of the debonding. The damage propagates towards the centre of the repair until the patch is completely debonded.

**Damage mode 2:** Debonding of the patch at the centre and propagation towards the edges until the patch is completely debonded. This type of damage usually occurs at the location above the hole (e.g. removed damage) or at other features that might be present such as rivets as it will be experimentally shown later.

**Damage mode 3:** Damage initiation at the substrate, most commonly met around the repaired region (e.g. around the hole) and propagation at the substrate. This type of damage can be more common when the debonding of the patch has reached a certain level at which the load transfer paths can no longer carry the asserted loads and the substrate is subjected to them, with the most critical area being the one around the removed damage. This damage mode is more prominent when the patch is used to repair cracks.

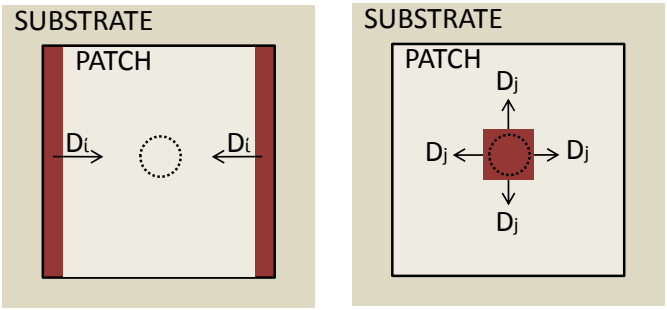


Damage scenario 1 Damage scenario 2

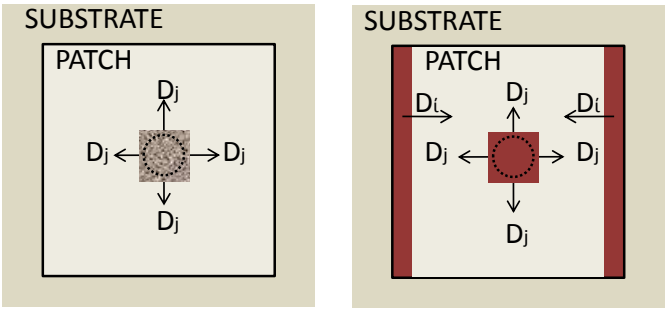


Damage scenario 3 Damage scenario 4

Figure 6.17: Schematic illustration of the damage scenarios.

**Damage mode 4:** It is rather uncommon that only one damage mode will be present. In most cases, a combination of damage modes takes place, resulting in complex failure mode mechanisms.

The purpose of the current section is to study the effect of each damage mode on the $A_0$ mode and to investigate its damage sensitivity for the two excitation modes and the two configurations. Figure 6.17 illustrates the damage scenarios that were considered and Table 6.3 summarises the details needed for the understanding of each damage step. Damage scenario 1 represents damage mode 1. Two debonded areas were first assigned after the appropriate partitioning of the model. One at the left and one at the right edge of the patch. The debonding was modelled by releasing the nodes at the interphase between the patch and the substrate, while surface properties were introduced to the debonded areas, in order to avoid any penetration of the one surface to the other during the wave propagation. The level of debonding is denoted here as $D_i$ where $i$=0,...,9. Equal length of debonding is assumed at both sides at each damage step for simplification. Damage scenario 2 represents damage mode 2. A debonded area was assigned at the centre of the patch with the same method as in damage scenario 1. The length of each side of the area is denoted as $D_j$ where $i$=0,...,9. The damage scenario assumes a uniform propagation

| | **Damage scenario 1** | **Damage scenario 2** | **Damage scenario 3** | **Damage scenario 4** |
|---|---|---|---|---|
| **D0** | 0 mm | 0 mm | 0 mm | $D_i$=$D_j$=0 mm |
| **D1** | 2 mm | 3 mm | 3 mm | $D_i$=2 mm,$D_j$=3 mm |
| **D2** | 4 mm | 5 mm | 5 mm | $D_i$=4 mm,$D_j$=5 mm |
| **D3** | 6 mm | 7 mm | 7 mm | $D_i$=6 mm,$D_j$=7 mm |
| **D4** | 8 mm | 9 mm | 9 mm | $D_i$=8 mm,$D_j$=9 mm |
| **D5** | 10 mm | 11 mm | 11 mm | $D_i$=10 mm,$D_j$=11 mm |
| **D6** | 12 mm | 13 mm | 13 mm | $D_i$=12 mm,$D_j$=13 mm |
| **D7** | 14 mm | 15 mm | 15 mm | $D_i$=14 mm,$D_j$=15 mm |
| **D8** | 16 mm | 17 mm | 17 mm | $D_i$=16 mm,$D_j$=17 mm |
| **D9** | 18 mm | 19 mm | 19 mm | $D_i$=18 mm,$D_j$=19 mm |

Table 6.3: Damage scenarios.

of the debonding, with the smallest debonding level being ($D_1$=3 mm), enough to cover the hole and the biggest ($D_9$=19 mm), resulting to an almost complete debonding of the patch. Damage scenario 3 represents damage mode 3. An area was isolated at the centre of the substrate whose properties were 10% lower. This area represented the degradation of the properties when naturally damage develops. The degraded area is denoted as $D_j$ where $i$=0,...,9. The propagation of the damage on the substrate is uniform starting at the location that corresponds to the edges of the hole and propagating towards the edges of the patch. Finally damage scenario 4, assumes a combination of the aforementioned damage modes.

The effect of each damage scenario on the response signals is illustrated in Figures 6.18–6.21. In Figure 6.18 (damage scenario 1), the pitch-catch mode exhibits a time delay with respect to damage which is more evident in configuration 2. In addition, a drop in amplitude indicates the energy dissipation over the debonded edges of the patch. The pitch-catch mode exhibits only very small differences while the responses for both configurations are identical since the waves have not interacted with the hole yet. In Figure 6.19 (damage scenario 2), the time delay in the pitch-catch mode is more obvious in this case accounting for a phase shift of almost half a cycle for both configurations while the pulse-echo mode shows almost no differences. This was somehow expected since the wave packages are a product of superimposed reflections that do not interfere with the centre of the patch.

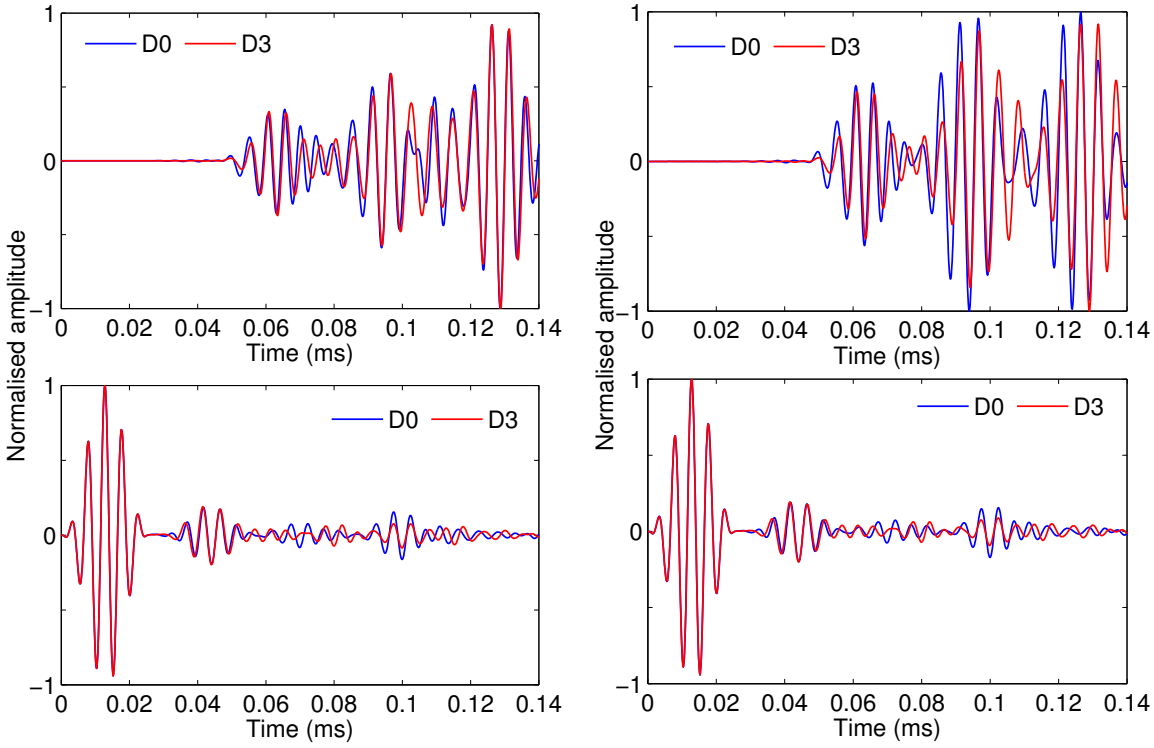


(a) Configuration 1 (b) Configuration 2

Figure 6.18: Response for pitch-catch mode (above) and pulse-echo mode (below) at steps D0 and D3 for damage scenario 1.

In Figure 6.20 (damage scenario 3), the pitch-catch mode does not show a significant damage sensitivity for configuration 1, while configuration 2 exhibits a distinctive amplitude drop. The pulse-echo mode shows no change for the same reason why damage scenario 2 shows little damage sensitivity in the pulse-echo mode. Finally in Figure 6.21 (damage scenario 4), the effect of multiple damage modes on the propagating waves is much more distinctive in this case, with extensive time delay and superimposition of wave packages in the pitch-catch mode, for both configurations. The pulse-echo mode on the other hand, shows a certain level of damage sensitivity compared to the other damage scenarios.

In order to evaluate the effect of all damage conditions, a damage index was defined, namely the *correlation coefficient*. This damage index can estimate the level of correlation between two variables based on the assumption of a linear dependence. The cross correlation coefficient $R$ for the two variables $x$ and $y$ is given below:

$$R(x,y) = \frac{\mathrm{cov}(x,y)}{\sigma_x \sigma_y} \tag{6.11}$$

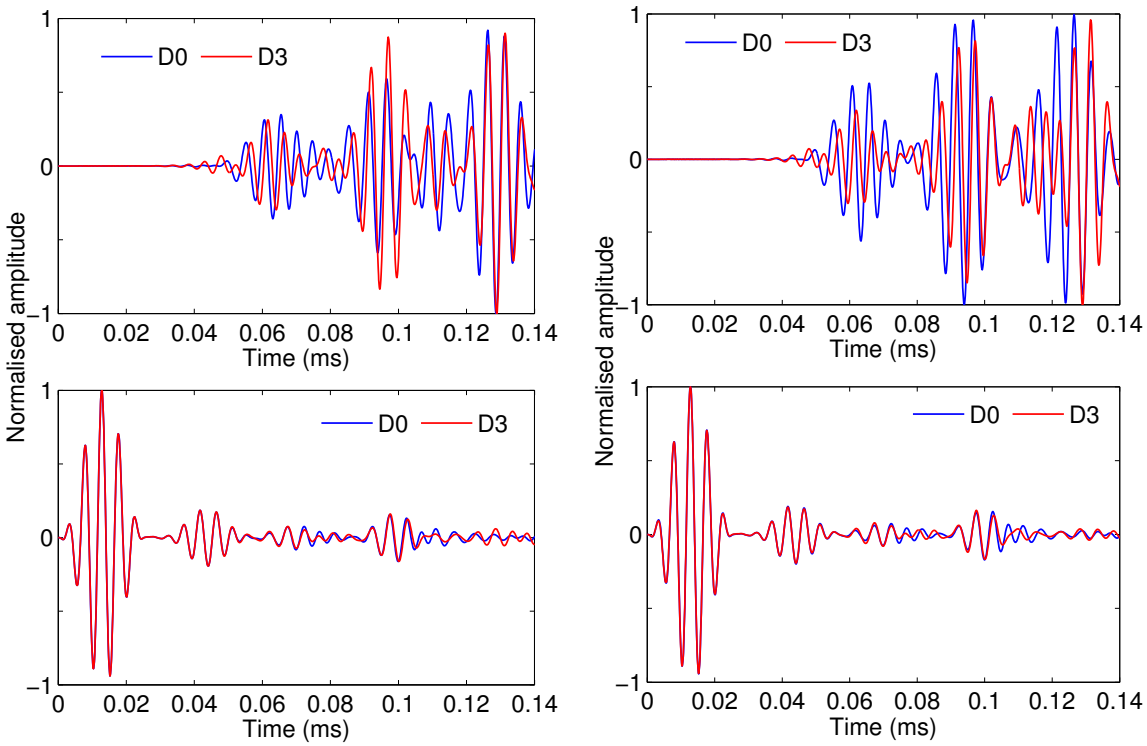


(a) Configuration 1 (b) Configuration 2

Figure 6.19: Response for pitch-catch mode (above) and pulse-echo mode (below) at steps D0 and D3 for damage scenario 2.

$$R(x,y) = \frac{\text{cov}(x,y)}{\sqrt{\text{cov}(x,x)\text{cov}(y,y)}} \tag{6.12}$$

where cov represents the covariance, and $\sigma$ represents the standard deviation. The two variables $x$ and $y$ represent the response time signals for the pristine condition and damage stages $\text{D}_i$, $\text{D}_j$ respectively. The correlation coefficient can also be written in the following form.

$$R(x,y) = \frac{E[(x-\bar{x})(y-\bar{y})]}{\sigma_x \sigma_y} \tag{6.13}$$

where $\bar{x}$ and $\bar{y}$ represent the mean values.

This coefficient can take values between +1 and -1 inclusive. If the coefficient is equal to +1, then this means that the two variables lie on a line which perfectly fits them, and if the one variable increases then the other variable also increases. If the coefficient is -1 then this can be interpreted by picturing the two variables lying on

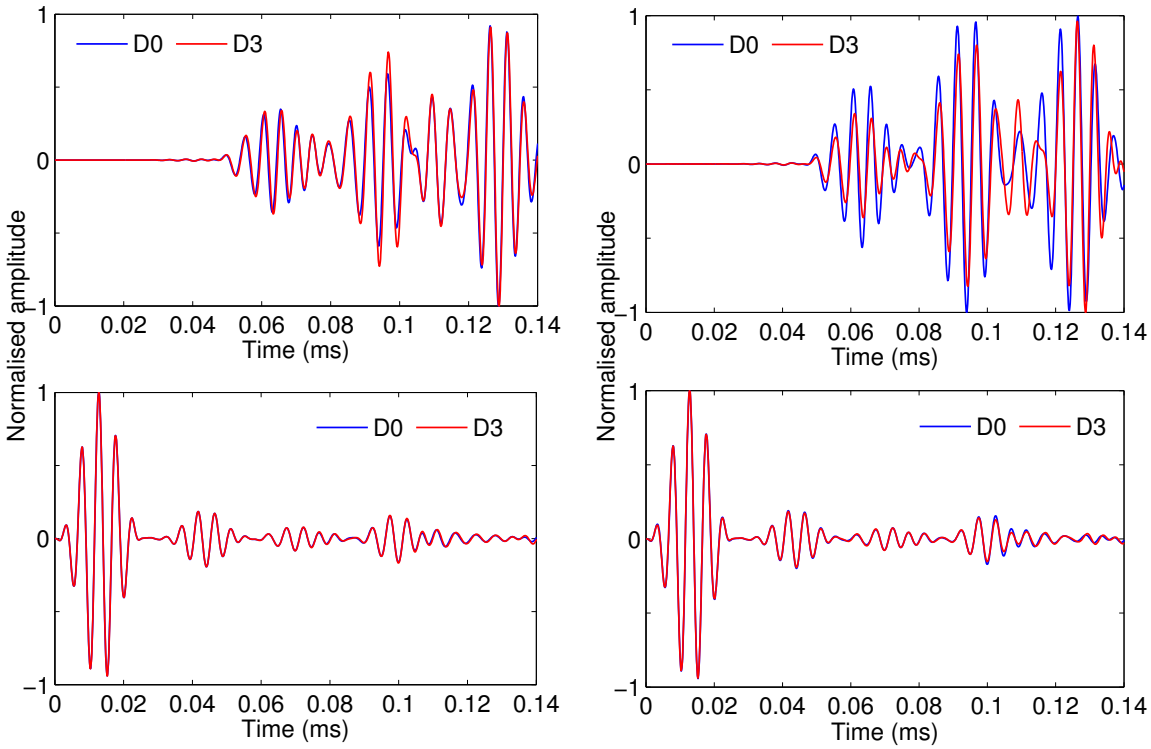


(a) Configuration 1 (b) Configuration 2

Figure 6.20: Response for pitch-catch mode (above) and pulse-echo mode (below) at steps D0 and D3 for damage scenario 3.

a line, but as the one variable increases, the other one decreases. If the coefficient is 0 then there is no correlation between the two variables.

Figure 6.22 displays the corresponding results of the correlation coefficient for the two excitation modes, pulse-echo (PE) and pitch-catch (PC), and for the two configurations, 1 (C1) and 2 (C2). The y-axis is scaled in the same way for all subplots, for comparison purposes. The pulse-echo mode for both configurations is very close to unity for all damage scenarios, hence underlying the fact that the pulse-echo mode does not exhibit a significant damage sensitivity for the considered damage scenarios. This is due to the fact that the waves are significantly attenuated after the multiple reflections at the substrate and at the patch before they even propagate through the critical region (e.g. the repaired region). However it would be possible to achieve a better damage sensitivity if a specific feature was to be selected, and not the whole waveform. This feature would better represent the effect of specific location such as the edges of the patch. In this case a single wavepackage could be isolated. However it is obvious that the determination and isolation of such a package can be very demanding in more complex configurations.

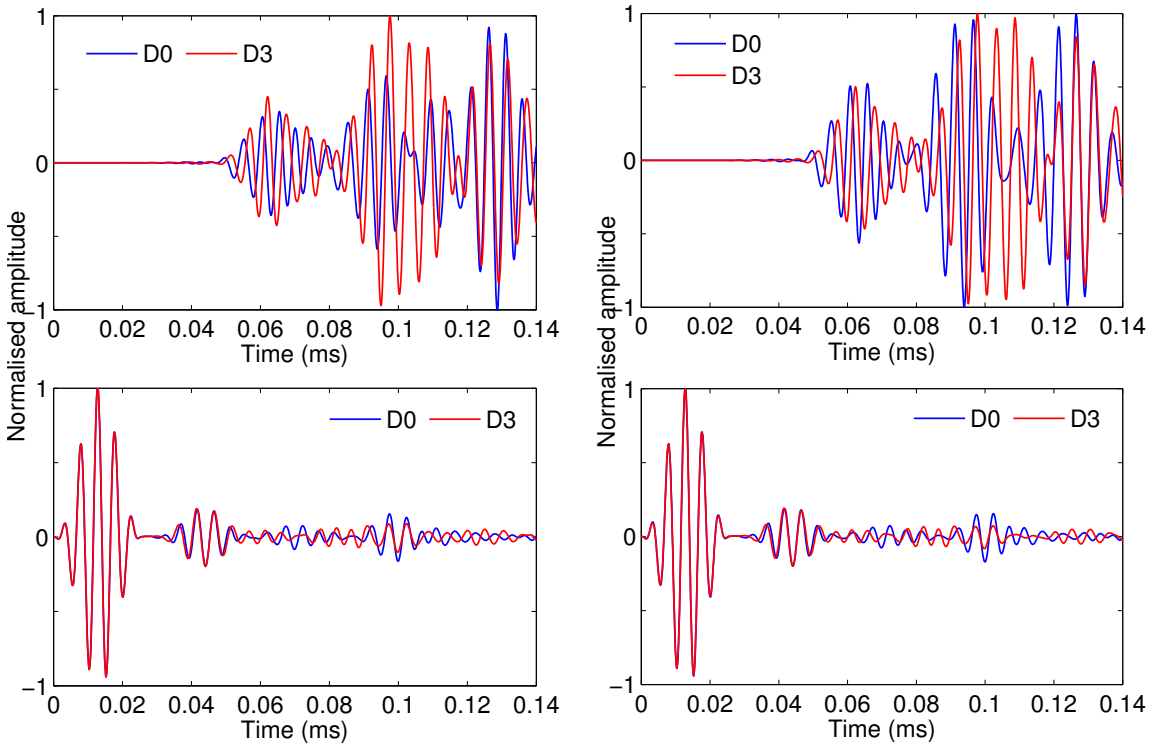


(a) Configuration 1 (b) Configuration 2

Figure 6.21: Response for pitch-catch mode (above) and pulse-echo mode (below) at steps D0 and D3 for damage scenario 4.

The pitch-catch mode for both configurations exhibits a monotonic behaviour for all damage scenarios except for the first. This might be due to the fact that as the waves interact with the debonded surfaces of the patch, they are reflected and refracted in such a way that in some cases they form superimposed packages and they lead to multiple mode conversions. Damage scenario 4 as expected shows the lower correlation coefficient while in general the correlation drops with respect to the damage. Damage scenario 3 indicates very low damage sensitivity compared to the rest. This might be due to the fact that the level of damage (10 % properties reduction at the substrate) is not readily comparable with the effect of debonding. In addition the damage on the substrate usually comprises cracks initiating around the repaired hole, which would under normal conditions have a more considerable effect on the waves.

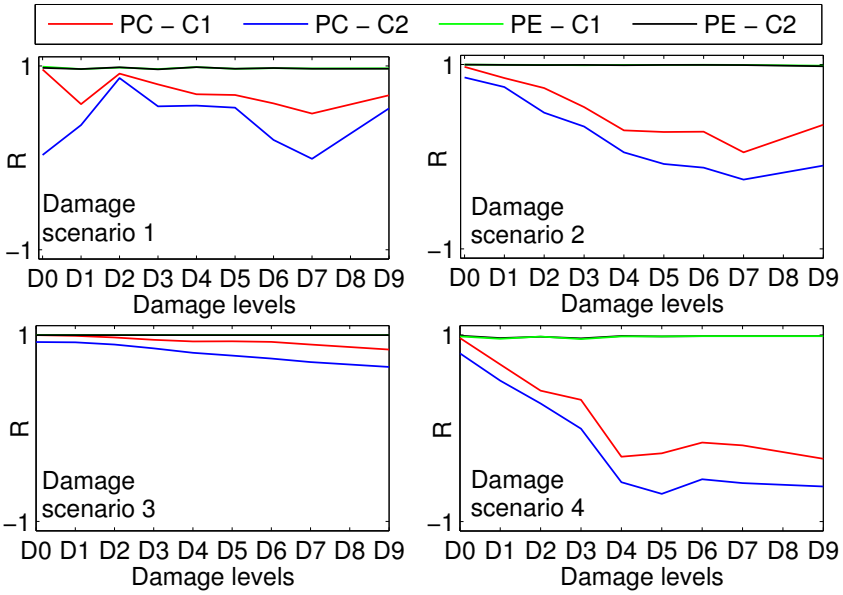


Figure 6.22: Correlation coefficient (R) for pitch-catch (PC) mode and pulse-echo (PE) mode for both configurations 1 and 2 (C1, C2 respectively) at all considered damage scenarios.

## 6.6 Discussion

This work illustrated step by step the methodology for the built model with ABAQUS whose verification and validation was performed through theory and experiment respectively. The propagation mechanisms of Lamb waves in repaired structures were evaluated in all possible configurations and excitations modes, while the damage sensitivity of the first antisymmetric mode $A_0$ was evaluated at the most representative damage modes that can occur at composite plates with adhesively bonded repairs.

The results indicate that the presence of the hole at the substrate significantly complicates the propagation phenomena. In addition the pitch-catch mode exhibits considerable damage sensitivity for the damage scenarios while the pulse-echo mode is less sensitive due to the multiple reflections that occur at the waves before they propagate through the repaired region. However, the pulse-echo mode can be potentially used for assessing the debonding of the patch mostly at the side which is closer to the actuating/sensing points since then the effect of the substrate hole could be isolated.

Overall this study aims to identify the key challenges in terms of physics-based

interpretation of the Lamb wave propagation in composite repaired structures. The model is a simplified model assuming that there are no other features that could interact with the propagating waves. However in real applications these phenomena are not straightforward since these mechanisms can be far more complicated with the presence of extra features such as rivets or stringers. The rest of the work focuses on feature selection strategies and follows a signal processing-based approach in order to identify the presence of damage.

# Chapter 7

# Damage Detection in Composite Repaired Structures

The objective of the current chapter is to apply the methods presented in section 4.1 to certain experimental set ups and to investigate the efficiency of each proposed method for the purpose of the successful damage classification under representative loading conditions. Two different repaired scenarios were considered, namely one scarf repair and one external patch repair, covering the most common repair methodologies. Also two different loading scenarios were employed for exploring all possible loading conditions that can occur in real applications, namely static and dynamic loading. In both cases alternative monitoring methods were implemented in order to validate the extent of the developed damage. The signal post-processing techniques focused on the extraction of the appropriate testing features, on the application of the pattern recognition and dimension reduction algorithms and on their subsequent correlation with the developed damage.

## 7.1 Scarf patch repair

### 7.1.1 Specimen geometry

The repaired plate was made out of woven carbon fibre (HTA) with toughened epoxy resin system (M21) which was supplied by Hexcel Composites and moulded

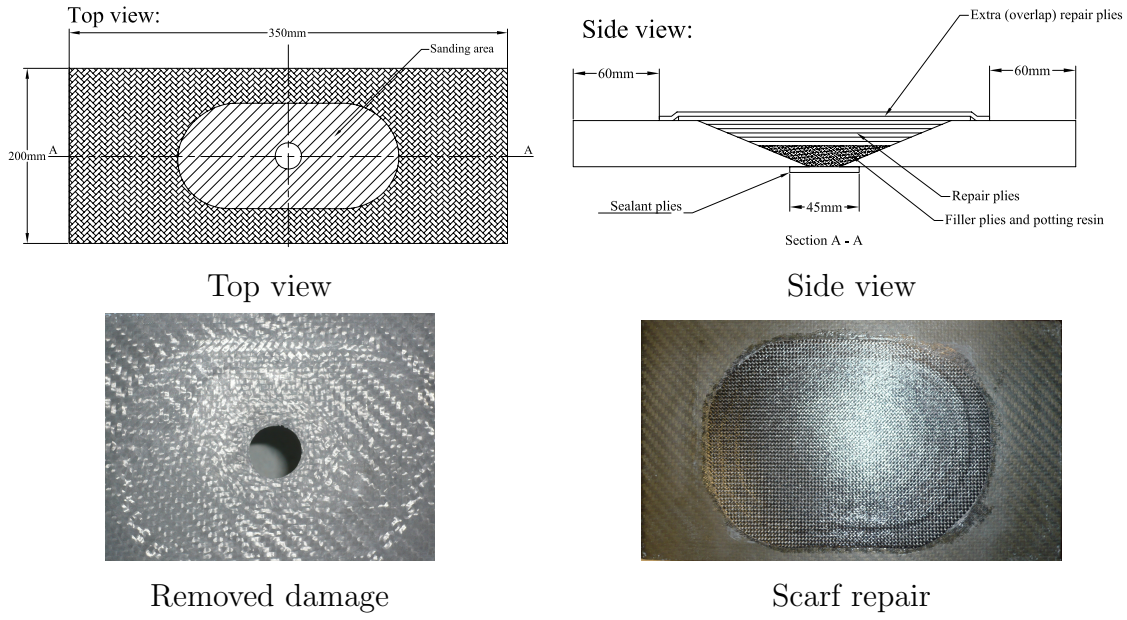


Figure 7.1: Illustration of the repaired plate and the implemented scarf repair.

by Hurel-Hispano UK at a 58 % fibre volume fraction. The panel's total thickness was 2.8 mm and its lay-up was $[0/90/\pm45/0/90]_{3T}$. After the manufacturing of the panel, an impact test was performed and the damaged area was removed. The impact height was 0.5 m and produced an impact velocity of 3 m/s. This panel was obtained from previous work [113]. Then the surface was properly processed and the scarf repair was implemented following the Boeing 767 structural repair manual (SRM) [114]. The scarf repair was made out of an aerospace qualified material and it was accomplished at the composite shop facility of Icelandair technical services (ITS) at Keflavik airport, Iceland for the purpose of previous work [115]. The damaged and the repaired plate are illustrated in Figure 7.1. The panel was mounted in a SCHENK hydraulic testing machine and was loaded in quasi-static tension.

### 7.1.2 Digital image correlation & Lamb wave experimental set up

Two techniques were employed for the monitoring of the panel during the tensile testing, 3D digital image correlation (DIC) and Lamb wave testing. DIC was used in order to provide full-field strain measurements from the surface of the tested panel during loading, which were further correlated with the results obtained from Lamb waves (Figure 7.2). More information on DIC can be found in Appendix A.

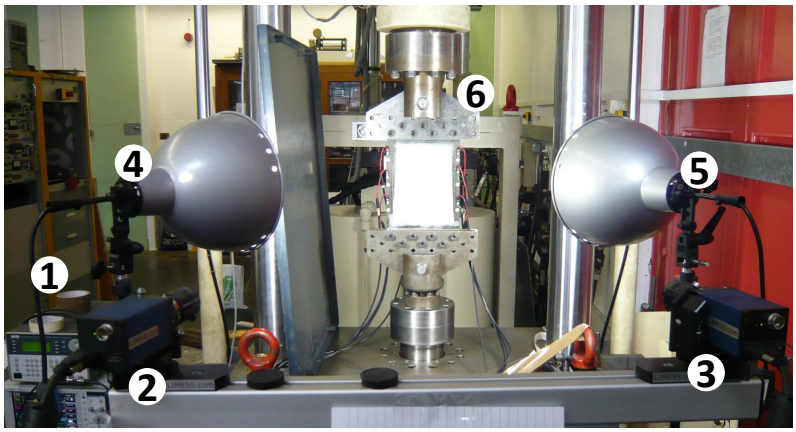


Figure 7.2: Experimental set up; ① Lamb wave testing equipment, ②,③ DIC digital cameras, ④, ⑤ lights, ⑥ scarf patch repair mounted on the testing machine.

For the first method, the surface was cleaned by acetone, a speckle pattern was applied on the surface of interest and two cameras were calibrated in order to take images during the testing. The images used in the 3D-DIC analysis were obtained by two digital cameras with a CCD matrix of more than five million pixels, model DCP 5.0 of LIMESS Messtechnik & Software GmbH. Schneider-Kreuznach Xenoplan 2.8/50 mm lens were mounted in the cameras and they were positioned symmetrically about the specimen in order to keep the magnification level consistent.

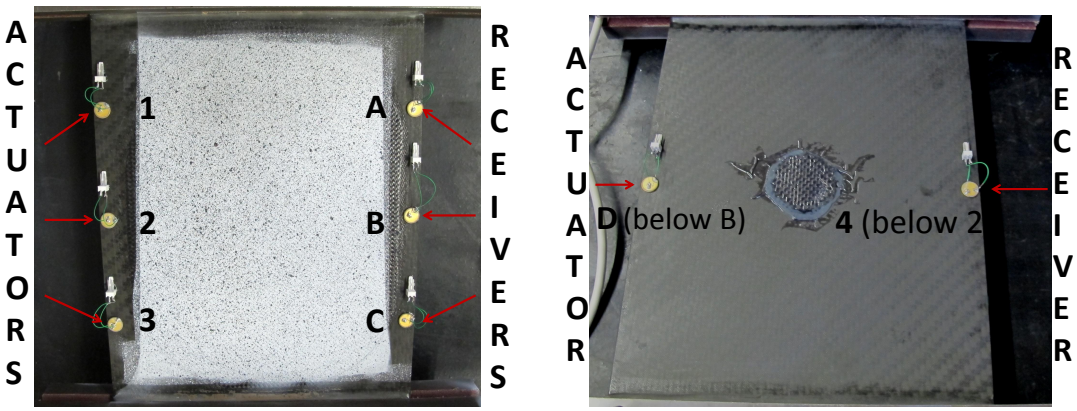


(a) Front side (b) Rear side

Figure 7.3: PZT arrangement for Lamb wave testing (1– 4: Actuators, A– D: Receivers).

In addition, eight PZTs of thickness 1 mm and diameter 10 mm supplied by CeramTec AG were surface bonded with instant glue on the repaired plate as shown in Figure 7.3, in order to avoid any possible transducer contact loss as a consequence of the patch debonding during the test, which was the first failure mode to be ex-

pected. Four of these transducers operated as actuators (1, 2, 3, 4) and the rest operated as receivers (A, B, C, D) functioning in a pitch-catch mode, forming 16 wave propagation paths in total and covering all critical areas. The excitation signal was a 10-Volt peak-to-peak amplitude, 5-cycle sine pulse modulated by a Hanning window and the excitation frequency was 225 kHz. The excitation frequency was selected in such a way that it provided maximum response signal power for all of the propagation paths. The wave generator that was used was a TTi TGA 1230 30 MHz model and the data acquisition was performed by a LeCroy LT224 oscilloscope at a 50 MHz sampling rate. DIC images and Lamb waves were recorded at approximate intervals of 10–20 kN until the final failure of the panel. The test was performed on the same day so the laboratory environmental conditions were considered to be constant. The specimen was illuminated by ordinary white light during the experiment.

Lamb wave signals and DIC images were successfully recorded up to 170 kN. At this load, the panel failed prematurely due to cracks that initiated around the holes that were drilled for gripping the specimen. This is a common complication in composite testing since composites exhibit relatively brittle behaviour, hence they cannot undergo plastic flow to relieve the local stresses that initiate around the holes. The failure might also be the result to some extent, of internally developed resin cracks and delaminations. As a result manufacturing characteristics such as specimen gripping and specimen design should follow appropriate specifications for successful testing under static or dynamic loads; the specimen end-tab should be of an appropriate size in relation to the gauge length in order to achieve valid failures.

### 7.1.3 Test results

Preliminary tensile tests that were performed on notched and unnotched specimens made of the same material as the repaired plate and with the same stacking ply sequence, along with the calculation of the locally developed stresses that were obtained from the DIC images, allowed an approximate estimation of the level of the internally developed damage [115]. In Table 7.1 the tensile strength of the unnotched and the notched specimens is illustrated as well as the estimated ultimate strength of the repaired plate. The size of the unnotched and notched panels was 175 x 50 mm and the hole was 5 mm. The tensile strength of the scarf patch repair is expected to be between the tensile strength of the unnotched and the notched

| **Material** | **Panel** | **Ultimate strength ($\sigma_f$)** |
|---|---|---|
| | Unnotched | 585 MPa |
| HTA/M21 | Notched | 379 MPa |
| $[0/90/\pm45/0/90]_{3T}$ | Scarf repair | 70–80 % of the $\sigma_f$(unnotched)=409–468 MPa |

Table 7.1: Tensile strength of notched, unnotched and repaired panels.

sample. However for precision purposes, it is well accepted that the optimum patch configuration can recover 70–80 % of the undamaged laminates strength. Therefore the tensile strength of the scarf repair can be estimated to be approximately between 409–468 MPa. In addition there are several factors that can lead to lower strength such as the defects and other imperfections introduced during the manufacturing process. According to the estimation of the maximum stress that developed at 160 kN locally around the hole, the stress was 415 MPa which is close to the failure stress of the repaired panel. This value was measured through the strain analysis of the DIC figures at an applied load of 160 kN. The current analysis concludes that it is possible that even though the load did not reach the ultimate strength of the scarf repair due to the premature grip failure, yet local internal damage is expected to develop. This assumption is well supported both from the DIC figures and the Lamb wave analysis as is later discussed.

In Figure 7.4 the results obtained from the DIC analysis are illustrated for all load levels. These images were processed with Vic-3D software from Correlated Solutions, Inc. The subset size was selected large enough to ensure that there is a sufficiently distinctive pattern contained in the area used for correlation. The surface strains that were obtained from the DIC analysis enabled the definition of 4 levels for the subsequent wave propagation paths of interest (Figure 7.3), each of which corresponded to groups of load levels that exhibited similar strain intensity. These levels are displayed in Table 7.2. Level 1 corresponds to normal and near normal condition (20 kN) where no substantial change has been introduced to the system (low applied strains). Level 2 which involves slightly different damage levels for the two paths, starts at 40 kN and is the stage at which the first noticeable change in the developed surface deformations can be observed from the DIC images. Level 3 starts at 80 kN for path 2A and at 100 kN for path 2C and it stops at 120 kN. At this stage DIC images show a more distinctive distribution of the strains depending on the most critical areas of the repaired panel; these are around the hole in the centre of the panel and at the tips of the patch where debonding of the outer plies was expected to initiate due to high interlaminar normal and shear stresses.

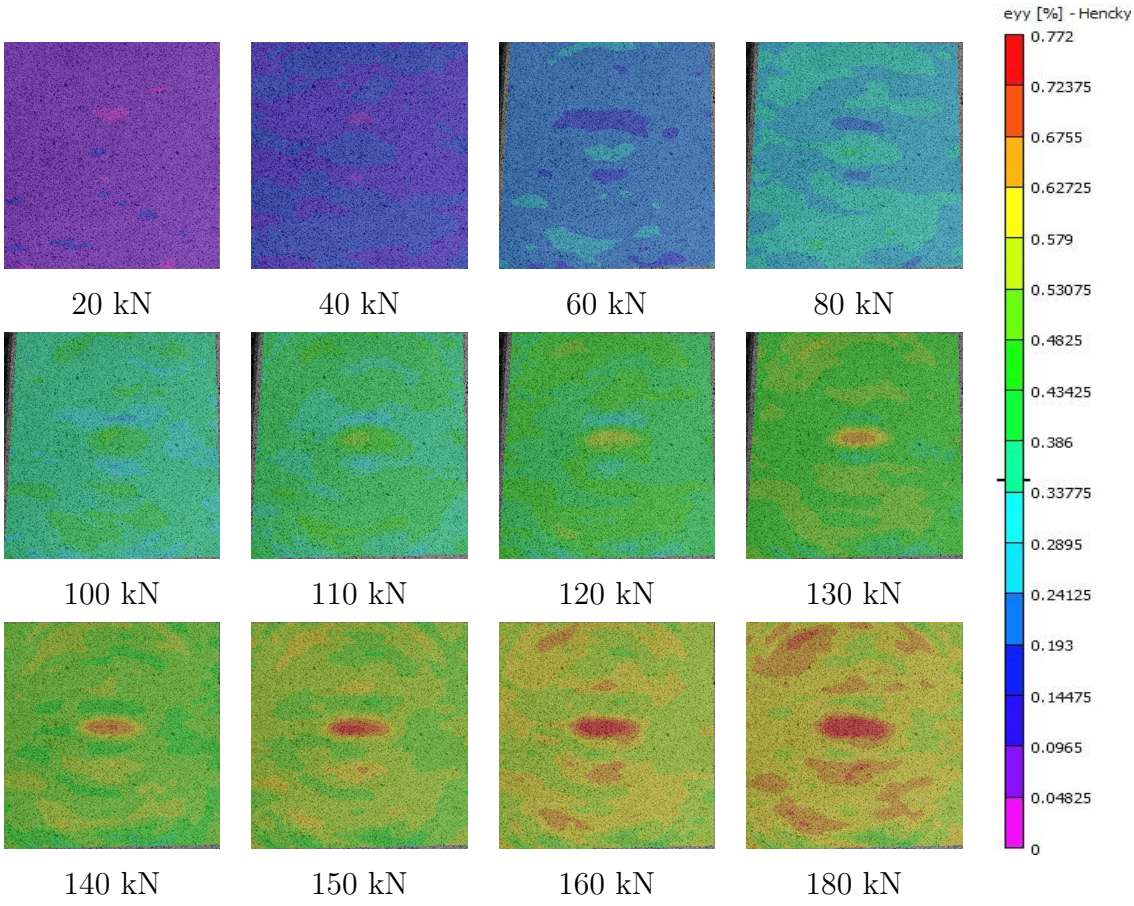


Figure 7.4: 2D Digital image correlation images (yy strains).

| **Levels** | **Load sets (kN)** | |
|---|---|---|
| | **Propagation path 2A** | **Propagation path 2C** |
| **1st Level** | 0–20 | 0–20 |
| **2nd Level** | 40–60 | 40–80 |
| **3rd Level** | 80–120 | 100–120 |
| **4th Level** | 130–160 | 130–160 |

Table 7.2: Damage levels as obtained from DIC strains for paths 2A and 2C.

### 7.1.4 Feature selection and pre-processing

As explained in the introduction, the focus of this part of the work in terms of pre-processing is based on the selection of appropriate features and their subsequent analysis for the reduction of the data dimensions and for their correlation with the internally developed damage. What this study aims to prove is that the employed analysis techniques can provide a fast and easy interpretation of the structural integrity of the tested component with the least possible required dimensions. The

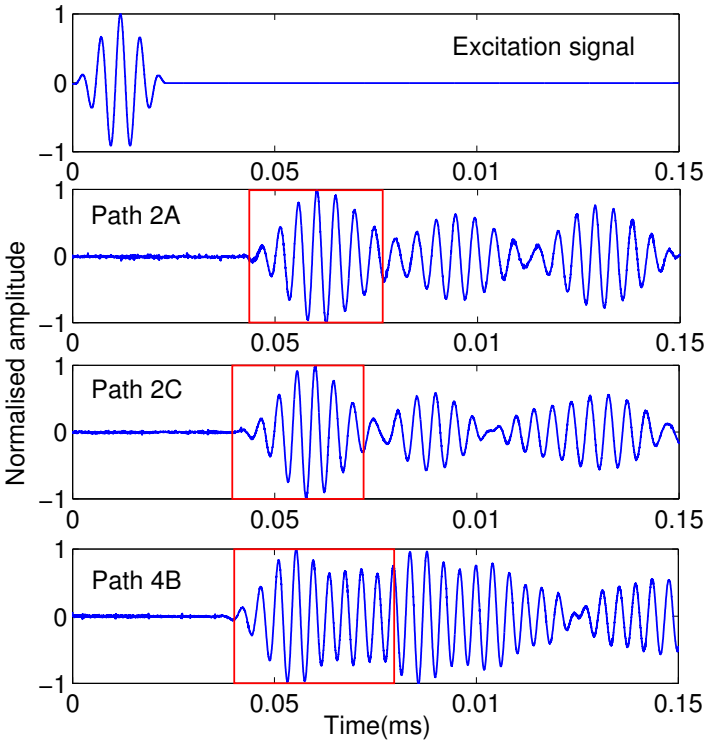


Figure 7.5: Response signals for paths 2A, 2C and 4B for the unloaded condition; selected features.

current work will only investigate these parameters on selected wave propagation paths due to size limitation. These paths are assumed to propagate through the most critical areas, covering the edges of the patch and the hole where damage was expected to be more severe even from the early stages of loading.

As a first step, all obtained signals were filtered with a lowpass filter in order to eliminate the noise. Then all signals were evaluated and the ones that were obtained from sensor 1 after 130 kN, were discarded since their peak-to-peak amplitude dropped by such an unexpected extent that it was assumed that the sensor lost perfect contact with the tested panel. Moreover, some waveforms exhibited a slight DC offset which was removed. In Figure 7.5 the excitation signal and the time signals recorded for the unloaded condition and for the propagation paths of interest are illustrated. It is interesting to note that the arrival time of each signal varies according to the distance of the actuator from the respective sensor. At this frequency, only the first two fundamental modes ($S_0$ and $A_0$) are expected to propagate in thin plates made of standard CFRP materials. However, as previously shown, these wave packets cannot be attributed to specific modes, since a single and pure Lamb wave mode can generate a variety of other modes when it interacts with defects that can be

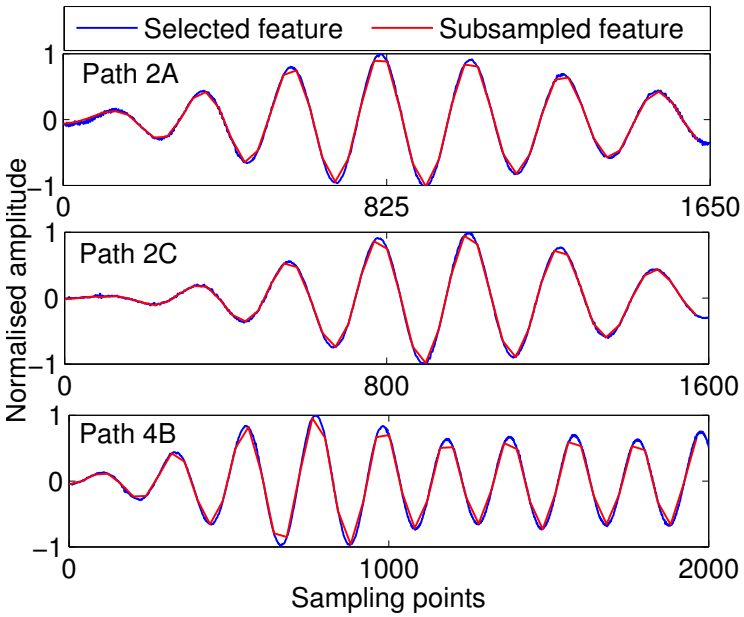


Figure 7.6: Response signals for paths 2A, 2C and 4B for the unloaded condition; selected features.

introduced during manufacturing of the laminate or with the different boundaries between the repaired plate and the implemented scarf patch repair. Therefore the recording of a baseline reference signal was essential in this case which corresponded to the unloaded condition.

The recorded figures show a distinctive first wave package for most of the propagation paths (path 2A and path 2C). In these cases this package was selected as the feature for further analysis due to its immediate interaction with the developed damage and in an attempt to avoid the signal's interference with the plate's boundaries. In some other cases though, like in path 4B, the selection of the feature was not straightforward, due to the observed mixed waves packages. In this case, the selected feature was selected to be a bit bigger than the previous ones in order to take into consideration the activity of the mixed wave packages and identify how this would affect the subsequent analysis. The selected features are illustrated in Figure 7.5. For further reduction of the dimensions, each feature was subsampled in order to finally get a 50-dimensional feature. The effect of this procedure on the final obtained features is illustrated in Figure 7.6. The dimensions are reduced without any considerable loss of information.

In order to construct a suitable mean vector and a covariance matrix for the normal condition, the selected features that served as the baseline reference (unloaded

| Test sets | Load levels (kN) |
|---|---|
| 1-200 | 0 |
| 201-700 | 20 |
| 701-1200 | 40 |
| 1201-1700 | 60 |
| 1701-2200 | 80 |
| 2201-2700 | 100 |
| 2701-3200 | 110 |
| 3201-3700 | 120 |
| 3701-4200 | 130 |
| 4201-4700 | 140 |
| 4701-5200 | 150 |
| 5201-5700 | 160 |

Table 7.3: Test set numbers and load sets for OA.

condition) were copied 1,000 times and each copy was subsequently corrupted with different Gaussian noise of signal-to-noise ratio (SNR) equal to 30. This SNR is considered to be representative of experimental noise levels. Each testing data set was copied 500 times and corrupted with the same noise level. The total testing data set consisted of 6,500 observations. It needs to be noted though that in real applications ideally a full set of signals needs to be recorded for a more efficient training of the employed algorithms. In this case, this was not possible due to equipment restrictions. In Table 7.3 the test sets and the load levels they correspond to are summarised. These test sets will be used to distinguish between each class in the following analysis.

### 7.1.5 Damage classification through principal component analysis and outlier analysis

After the pre-processing of the obtained signals, OA and PCA were performed in a comparative way in order to identify the agreement between the two methods and in order to explain the behaviour of the OA classes based on the orientation of the respective clusters in a 2-dimensional subspace. For the illustration of the PCA results, only the first two principal components were considered, since they accounted for the highest percentage of variance. For the purpose of the OA, the 1 % exclusive threshold value for novelty for a 1,000-observation, 50-dimensional problem was estimated after 1,000 trials which was found to be approximately the

same for all paths, namely 110. The first 800 observations of the unloaded condition were used as a training set in order to train the algorithm, and the remaining 200 observations were used as a validation set in order to evaluate how effectively the algorithm can identify the normal condition.

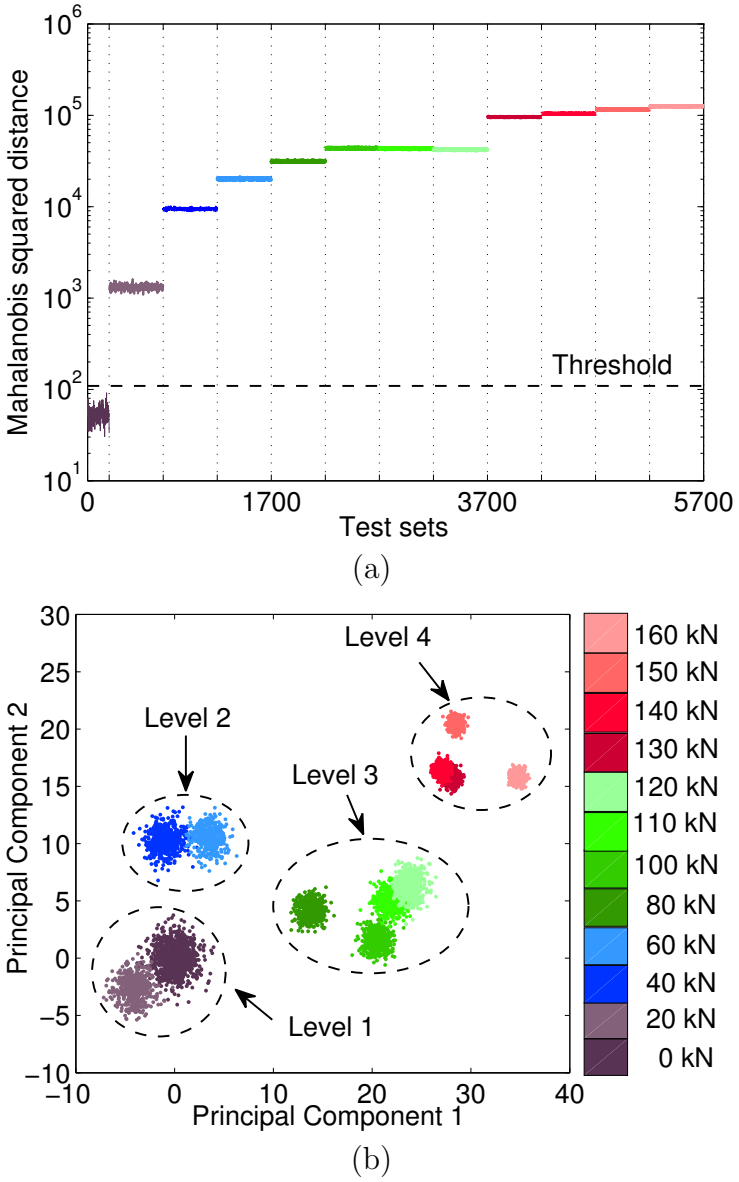


Figure 7.7: Outlier analysis (a) and principal component analysis (b) for path 2A.

In Figure 7.7, the results obtained from both processing methods are illustrated for wave propagation path 2A. All of the set that corresponds to the unloaded condition is successfully labelled as an 'inlier', positioned below the threshold which indicates that the training of the algorithm was accurate and that the observations obtained for the normal condition followed a Gaussian distribution as first assumed. OA shows

that as soon as damage started accumulating in the specimen, the sets are labelled as 'outliers', exhibiting a clear deviation from the normal condition while being flagged well above the assigned threshold. As load levels increase, the deviation level also increases, following a specific pattern which was further analysed through the PCA.

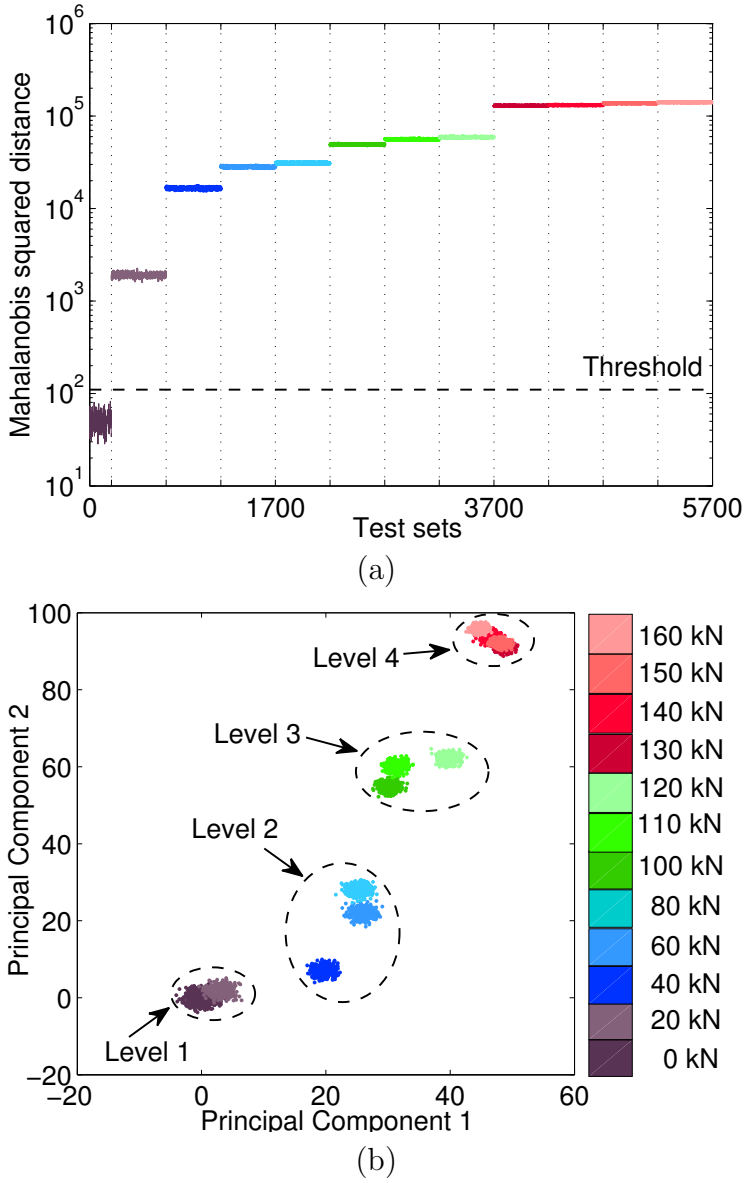


Figure 7.8: Outlier analysis (a) and principal component analysis (b) for path 2C.

The results obtained from PCA, resulted in significantly distinctive clusters, whose position in the 2-dimensional space changes with respect to the load level. This behaviour proves that the application of the novelty detection analysis is well supported in this case. The resulting clusters, can be visually further grouped into more precise categories as illustrated in Figure 7.7 with the circles and the same

colour notation. These categories agree with the assigned damage levels that are summarised in Table 7.2. In an attempt to comparatively assess the methods, one can observe that clusters that belong to the same level in PCA, exhibit equal values of Mahalanobis distance, an observation which highlights the agreement of the employed methods.

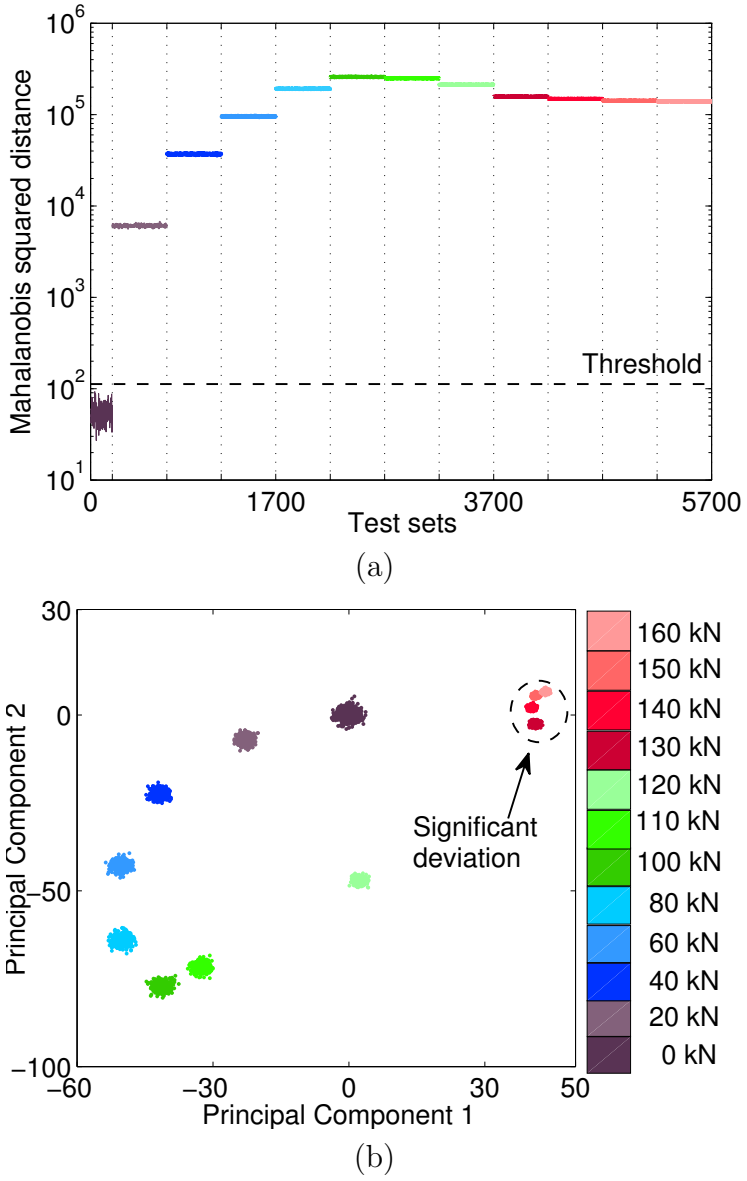


Figure 7.9: Outlier analysis (a) and principal component analysis (b) for path 4B.

Figure 7.8 illustrates the same results for the second wave propagation path of interest, path 2C. The path exhibits the same behaviour following an increasing deviation from the normal condition and from the threshold as loading increases, in a pattern that agrees with the orientation of the respective clusters in the 2-

dimensional space. In a similar way, the PCA clusters are grouped in categories that agree with the assigned damage levels for the specific path.

Figure 7.9 illustrates the PCA as well as the OA results for wave propagation path 4B. The reason why this path was selected among others is because it shows a different behaviour which was considered to be important to discuss. PCA exhibits very well separated data clusters which correspond to the increasing levels of loading. However, after 120 kN the recorded data exhibit a significant deviation from the normal condition in such a manner that the clusters move closer to the cluster that corresponds to the normal condition (0 kN) as it is illustrated in the same figure. This phenomenon has an immediate effect on the resulting OA results. Even though all the load sets are labelled as 'outliers' exhibiting increasing deviation from 0kN, the Mahalanobis squared-distance after 130 kN, drops to lower values than the previous loads. This is attributed to the significant deviation of the system in such an extent that the algorithm classifies these data as closer to the normal condition, as justified from the PCA results. This phenomenon could be a limitation in the application of outlier analysis in specific cases where significant damage scenarios might be labelled as 'inliers'. However in the specific study, the resulting indices were labelled well above the assigned threshold, hence successfully indicating damage.

Final step of the current analysis is the investigation of the sensitivity of the employed processing tool when compared with the results obtained from the DIC analysis for each path. The defined damage index in this case is expressed in equation (7.1), where MNI stands for mean novelty index and MSD stands for Mahalanobis squared-distance.

$$\mathrm{MNI} = \frac{1}{2}[(\mathrm{MSD})_{\max} + (\mathrm{MSD})_{\min}] \tag{7.1}$$

Therefore, here a representative value that corresponds to the previous analysis is assigned for each path and for each corresponding load level and the results are plotted against the load levels.

The results are illustrated in Figure 7.10. The figure is divided in four plots; each of which corresponds to a different actuator and includes all sensors. The y-axis has the same scale for all four plots for comparison reasons, and the Monte Carlo threshold is defined for all plots to be equal to 110. The plot for actuator 1 involves less analysed load levels, due to the debonding of the respective transducer after

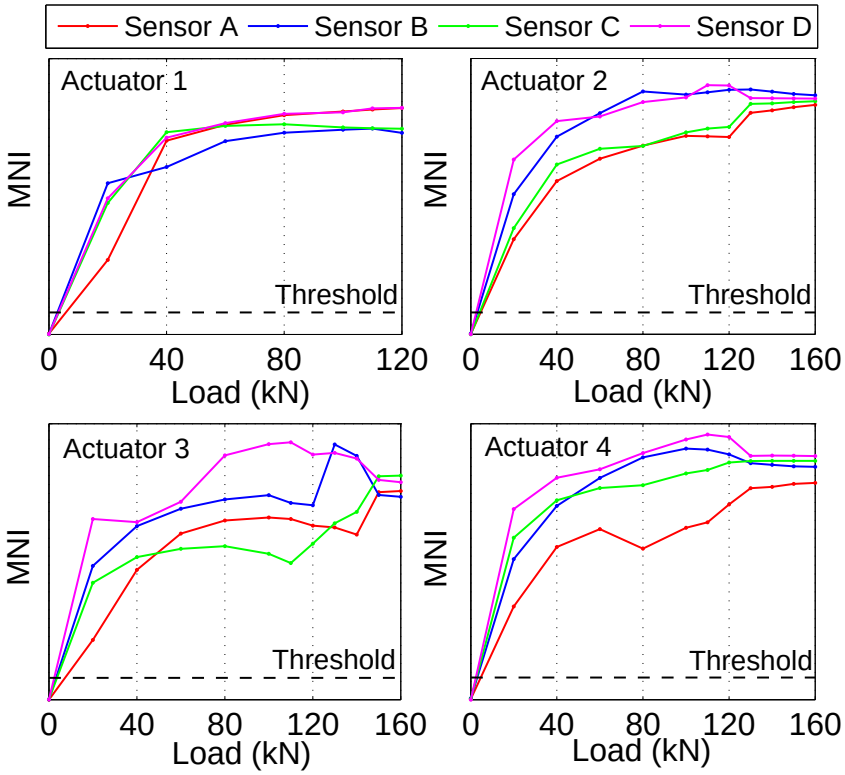


Figure 7.10: Mean novelty index (MNI) for all wave propagation paths.

130 kN as previously mentioned. The main damage mechanism that is investigate here, is the common failure mode under which repair patches fail, which is first debonding of edges of the upper plies of the repair, followed by a propagation of the debonding towards the centre of the repair until the plies can no longer carry the applied loads and the plate fails around the removed damaged area of the substrate. The main paths that represent these mechanisms in the current work, are paths 2B, 4B, 2D and 4D which directly propagate through the removed damaged area (hole), paths 1A and 3C which propagate through the regions where the first ply debonding was expected to initiate, and paths 3B, 3D, 1B, 1D, which propagate through the regions where the repair debonding would further propagate until it reached the hole. It needs to be mentioned at this point, that in reality Lamb waves propagate through bounded media and as they interact with the different boundaries, one can not easily attribute a specific propagation path to a precise region of the tested system. However, in this case the selected feature is the first wave package which is the direct response the sensor receives before the wave meets any other boundaries or interphases. The results show that all paths that are associated with the patch debonding seem to have a similar behaviour with the paths that are associated with

the damage initiating around the hole at the early stages of loading. This behaviour changes as the load levels increase, and the paths that propagate through the hole exhibit higher damage index from the rest of the paths, possibly indicating that the damage around the hole was becoming more intense.

### 7.1.6 Dimensions reduction through the fitting of principal curves

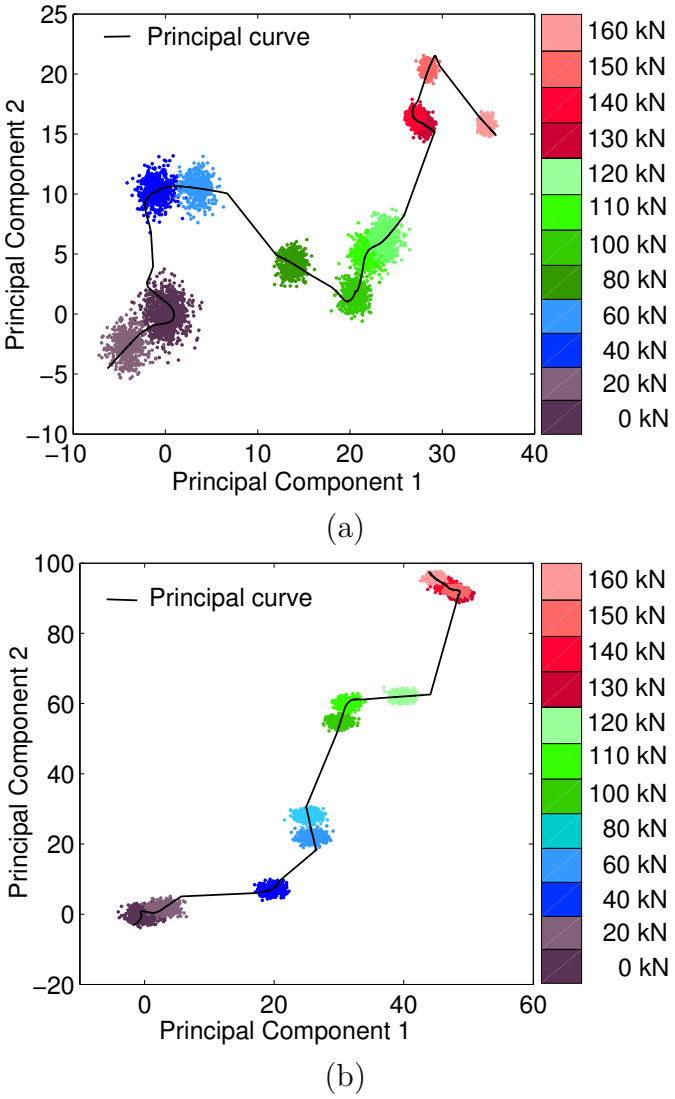


Figure 7.11: NLPCA for wave propagation paths 2A (a) and 2C (b).

An investigation into further dimensional reduction of the post-processing analysis was performed through the application of the NLPCA and the fitting of the principal

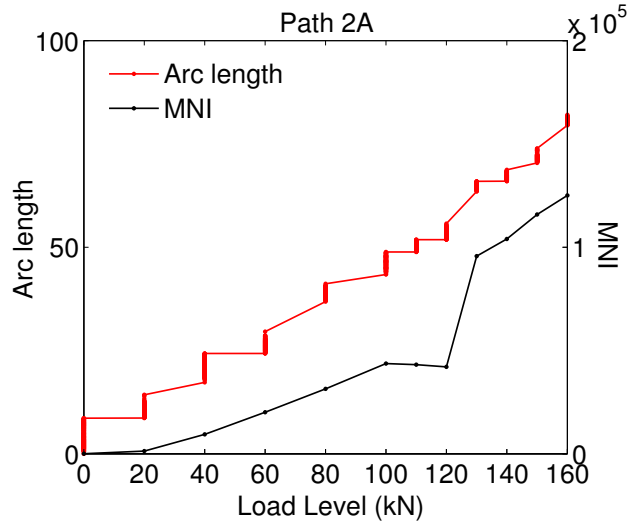


(a)

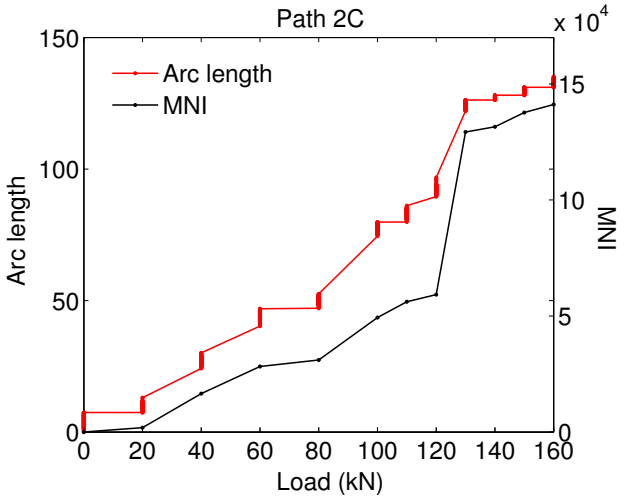


(b)

Figure 7.12: Comparative study between MNI and arc length for wave propagation paths 2A (a) and 2C (b).

curves. The principal curves were applied to the results of the previously analysed PCA, namely the data clusters. The algorithm started with a prior line which was the first linear principal component and it bent in order to obtain the optimum shape following successively the steps that were described in Section 4.1.

There were certain user-specified parameters in the applied algorithm such as the threshold for the relative change in the mean orthogonal distance which was defined to be 0.01. Also the initial span was defined to be 0.6 times the number of points. The span was reduced by a factor 5/6 per iteration. A brief convergence study showed that the optimum number of iterations was 10. The arc length was

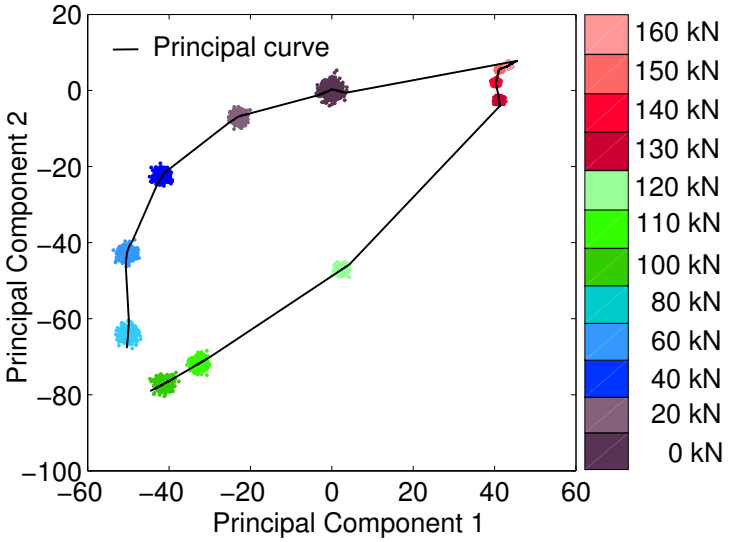


Figure 7.13: NLPCA for wave propagation path 4B.

interpreted as the NLPCA score and it was plotted with respect to the increasing loading.

Figure 7.11 exhibits the results after the application of the principal curves on the clusters that were previously obtained from the linear PCA. The curve is initially specified as the first linear principal component between the clusters and then bends until it fits the illustrated data points. The curve starts from the normal-early stage damage (Level 1) and then connects the clusters that correspond to increasing loads until it stops at 160kN which is identified as the last point. The curve represents the variation of the data-clusters with only a one dimensional curve, hence leading to a significant reduction in the dimensions of the data.

For the validation of the current results, the interpretation of the arc length of the curve was performed with respect to the load levels. The hypothesis was that the arc length increases according to the increase in the load level since all other parameters that can affect the signal's behaviour such as environmental conditions were kept under control. This variation is believed to be caused by the accumulating damage that develops within the repaired region of the tested panel. Figure 7.12 illustrates the resulting variations for both wave propagation paths 2A and 2C. For the purpose of connecting the current approach with the previously investigated MNI, both curves were included in the same plot for each path. MNI in this case is plotted on a linear scale for comparison reasons. The results show that the variation of the arc length depicts the increase in the MNI quite accurately, while at the same

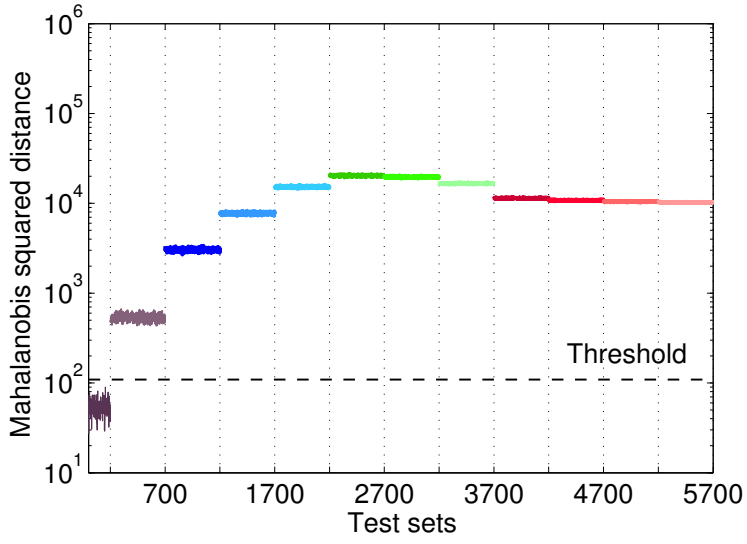


(a)

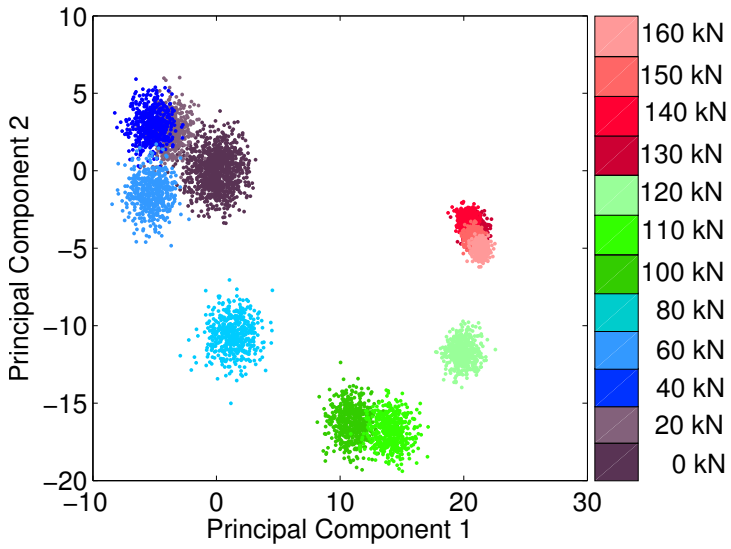


(b)

Figure 7.14: Outlier analysis (a) and principal component analysis (b) for path 4B with signal-to-noise ratio equal to 19.

time it shows approximately the same sensitivity as the MNI does for the different load increments between the two paths, hence reflecting the damage accumulation mode that was previously analysed. This conclusion is rather important since the same results were obtained from a very simple data manipulation that resulted in just a one dimensional curve.

One limitation of the NLPCA is graphically illustrated in Figure 7.13. The principal curve here is fitted in the clusters obtained for the wave propagation path 4B. As

observed, the principal curve identifies as a starting point the 80 kN and ends at 100 kN. This means that the curve does not successively connect clusters that correspond to increasing levels of load. Therefore the correlation of the arc length with the increasing damage would not be reliable in this case. Reordering is a potential solution to this problem which is proposed as a future work step since it is not within the scope of the current work.

### 7.1.7 Effect of noise

Noise in aerospace industry can occur due to various operational conditions such as the normal operation of rotors, propellers, engine drive shafts and transmissions. This could reduce the sensitivity of the previously investigated methods and impose a limitation to the efficiency in the structural monitoring of the aircraft's critical areas. Since the signal-to-noise ratio (SNR) that was considered in this chapter was artificially introduced based on previous experimental work, there was a need to investigate how the employed methods would be affected by higher noise levels.

In order to demonstrate the aforementioned study, a brief analysis is presented here after the original data were corrupted with a noise of a SNR equal to 19. It has to be noted that this is the level of noise at which PCA started showing different behaviour. In Figure 7.14, the results from the implementation of OA and PCA are demonstrated for propagation path 4B for comparison reasons. As illustrated, OA exhibits similar behaviour with the original results in Figure 7.9, only in this case, the values of discordancy are lower as an immediate effect of the high SNR. However, the damage cases are still flagged as outliers and the method seems to provide reliable results. On the other hand, the same results for PCA exhibit clusters that can not easily be distinguished from each other and hence be attributed to the different damage levels. This means that the proposed damage prognosis tool based on the principal curves would not be reliably applied in this case. Nevertheless, the considered level of noise is too high for normal operational conditions, which makes the proposed post-processing tools a strong candidate for a robust analysis in complex structures, although some further refinement may be required.

## 7.2 External patch repair

### 7.2.1 Experiment

This section focuses on a different type of repair namely an external bonded patch repair, in order to cover all representative configurations. A composite plate was used, repaired with an external composite patch provided by TECNALIA (San Sebastian, Spain). The substrate and the patch were made out of 2 x 2 Twill woven fabric pre-preg (MTM56/CF0300) provided by ACG, UK with area weight equal to 200 g/m$^2$. The properties of the material are illustrated in Table 7.4.

| $E_1$ | $E_2$ | $G_{12}$ | $v_{12}$ | $v_{13}$ | $\rho$ |
|---|---|---|---|---|---|
| 65 GPa | 65 GPa | 4.24 GPa | 0.04 | 0.04 | 1524 kg/m$^3$ |

Table 7.4: Material properties of MTM56/HTA5131 Fabric/CF0304 (normalised to 55 % $V_f$).

The substrate consisted of 300 mm length by 50 mm width made of 8 layers with a stacking ply sequence $[0/90]_{8T}$, whose thickness was 1.6 mm. A hole of 5 mm was introduced in the centre of the substrate in order to simulate the removed amount of material in the repaired region that the patch would cover. The patch consisted of 4 layers of the same material following a step wise configuration as illustrated in Figure 7.15; the size of the first ply was 120 x 50 mm while the total thickness of the patch was 0.4 mm. The subsequent curing took place under pressure of 6.2 bar. The temperature was increased up to 120°C at a rate of 3°/min. Both pressure and temperature were held for 10 min until the laminate was allowed to cool under pressure down to 80°C at a rate of 3°/min, after which the pressure was released.

GFRP tabs of 60 mm length and 50 mm width were bonded on the panel for gripping purposes after the surface was properly processed with sand blasting. A tension-tension fatigue was performed with cyclic frequency f=5 Hz and stress ratio R=0.1. The mechanical loading started from low levels and increased until it reached 95 % of the ultimate strength of the laminate which according to the manufacturer's technical specifications was 600 MPa. The number of cycles was also increasing with respect to the level of loading, starting from 500 cycles and ending up at 10,000 cycles per step. For better understanding of the effect of the damage propagation on the

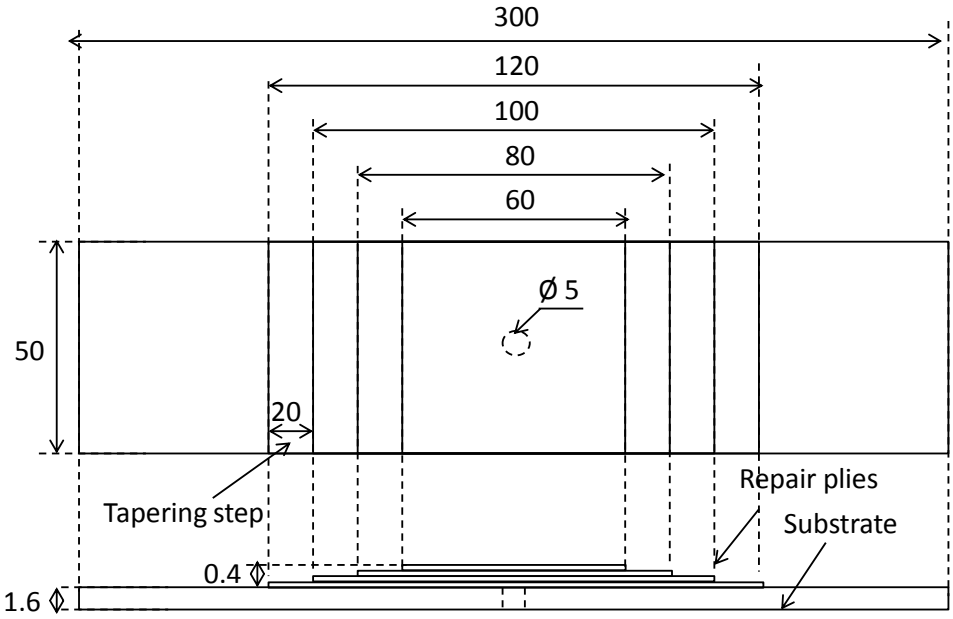


Figure 7.15: Schematic illustration of the tested external patch repair; dimensions in mm.

| Load | Number of cycles | Phase |
|---|---|---|
| 31 $\%\sigma_f$ | 0–500 | Phase I |
| 31 $\%\sigma_f$ | 500–1,500 | |
| 31 $\%\sigma_f$ | 1,500–2,500 | |
| 31 $\%\sigma_f$ | 2,500–4,500 | |
| 31 $\%\sigma_f$ | 4,500–6,500 | Phase II |
| 62 $\%\sigma_f$ | 6,500–7,500 | |
| 80 $\%\sigma_f$ | 7,500–9,500 | Phase III |
| 80 $\%\sigma_f$ | 9,500–11,500 | |
| 80 $\%\sigma_f$ | 11,500–16,500 | |
| 90 $\%\sigma_f$ | 16,500–21,500 | |
| 90 $\%\sigma_f$ | 21,500–31,500 | |
| 95 $\%\sigma_f$ | 31,500–41,500 | |
| 95 $\%\sigma_f$ | 41,500–61,500 | |

Table 7.5: Loading steps and phases

recorded signals, the damage steps were divided in three categories based on the extent of the loading level and number of cycles. These categories are illustrated in Table 7.5. A SCHENK hydraulic testing machine equipped with a 250 kN load cell was used for the test.

Four piezoelectric transducers of the same type as for the work carried out in Section 7.1, were attached on the tested surface with instant glue after the cleaning of the

surface, operating in pitch-catch mode. The arrangement of the transducers will be explained in detail in Section 7.2.2. Figure 7.16 illustrates a schematic representation of the panel along with the locations of the attached transducers. In the same figure, two photos of the front and the rear side of the panel are displayed, when the panel was mounted on the fatigue machine. As shown, the transducers were surface-bonded on the substrate, at a 5 mm distance from the closest repair ply.

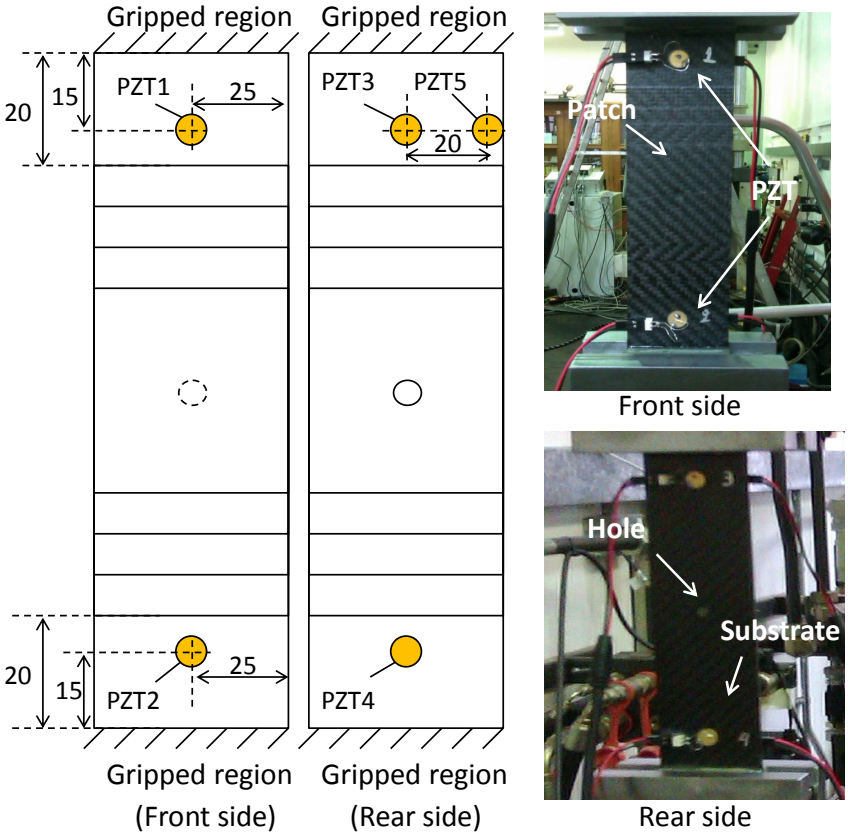


Figure 7.16: Schematic illustration and photos of the experimental set up.

A 5-cycle sine burst signal modulated by a Hanning window was selected for the excitation of the tested configuration. The peak-to-peak amplitude of the input signal was 10 V and the sampling frequency was 50 MHz. The input signal was generated by a TTi TGA1230 30 MHz wave generator. The data acquisitions were performed by a Le Croy LT224 waverunner oscilloscope. The data acquisition was performed in a stop & go mode, which means that each set of signals was recorded before and after each set of loading scenario. A set of signals was recorded before any loading was applied which was used as a baseline reference set.

The panel failed in the grips after 61,500 cycles at 95 % of the ultimate strength as a result of the damage accumulation at each different loading phase (Figure 7.17). At

(a) Failure of the panel in the grips

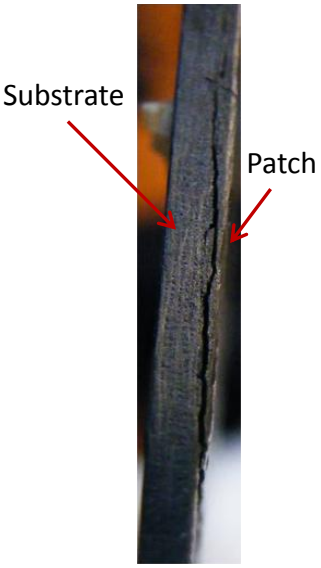


(b) Debonding of the patch

Figure 7.17: Final damage after 61,500 cycles at 95% of the ultimate strength.

this load, the panel failed prematurely due to cracks that initiated around the holes that were drilled for gripping the specimen. The reasons for this were also previously explored in Section 7.1. Along with the failure in the grips, patch debonding of a considerable extent took place. X-ray radiography and microscopic analysis were performed in order to investigate the extent and the type of the internally developed damage. These results are illustrated in Figure 7.18. X-ray radiography showed that axial splitting developed around the hole of the substrate and propagated parallel to the loading direction. The axial splitting, acts as a 'crack stopper' reducing the stress concentration factor at the hole edge, hence delaying fibre fracture at a higher applied load. At that high load though the patch debonded much further (patch debonding areas No. 1 and No. 2). A more accurate image in the microscope showed that debonding took place not only on the ply that is directly bonded on the substrate (fourth ply) but also on the direct overlapping ply (third ply). Therefore the amount of data that was collected was sufficient for reaching some useful conclusions in relation to damage monitoring.

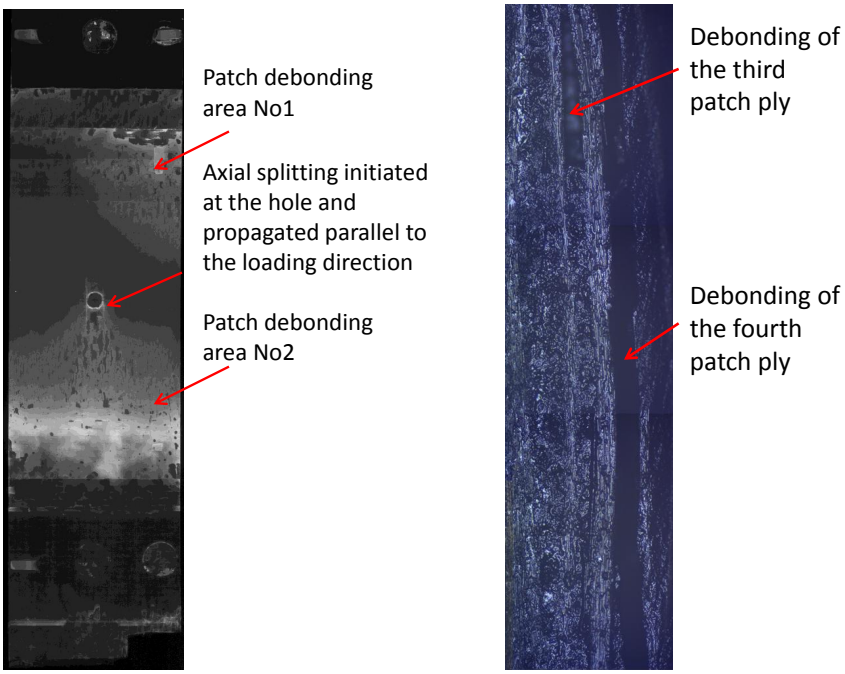


(a) X-ray radiography (b) Microscopic analysis

Figure 7.18: X-ray radiography and microscopic analysis images of the developed damage.

### 7.2.2 Excitation of the first symmetric and antisymmetric modes

In this section, the excitation of the first two fundamental Lamb wave modes in the frame of a real experimental study on a small scale configuration, which is yet representative of a real repair, is performed. This work demonstrates an alternative excitation method, for cases in which a sufficiently small wavelength is needed, therefore the excitation frequency can not be too small. This excitation method is based on the principle of the particles motion in the tested material during the wave propagation for each mode (symmetric and antisymmetric) as has been previously shown in Figure 3.4.

The applied method is illustrated in Figure 7.19. As presented, PZT1 and PZT3, operated as actuators and PZT2 and PZT4, operated as receivers. Each pair was bonded on the surface of the tested panel in an attempt for each PZT to be perfectly aligned with its respective PZT bonded at the other side of the panel. The actuators were driven in-phase for the excitation of the $S_0$ mode and out-of-phase for the excitation of the $A_0$ mode. In addition, the sensors operated in-phase during the

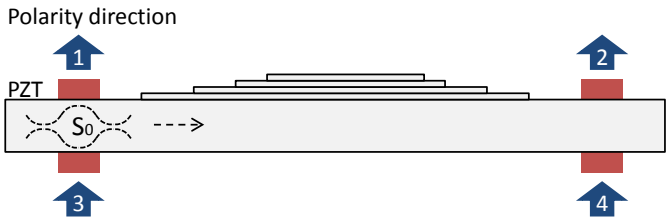


(a) Excitation of $S_0$ mode

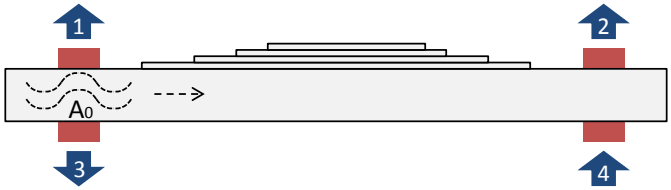


(b) Excitation of $A_0$ mode

Figure 7.19: Polling directions for the excitation of the fundamental modes during testing.

whole testing, capturing the response signals.

When Lamb waves propagate through a repaired panel of such type, they will interact with any sudden change in the thickness which in this case is the different plies of the repair patch and the hole on the substrate. Therefore every time each mode interacts with one of the layers of the patch or with the hole in the substrate, a portion of the wave will be reflected by the surface of the extra thickness and another portion will be transmitted through it as previously exhibited in Chapter 6. This means that the transmitted wave that was obtained from the receivers will be subjected to multiple mode conversions by the time it arrives at the sensors. This phenomenon has been thoroughly explored by other researchers [50], and it is not within the scope of the current work since the subsequent analysis will focus on pattern recognition. The only effect of the excitation of an appropriate mode here is the benefit of a sufficiently small wavelength and the sensitivity of the excited mode as will be later displayed.

First the dispersion curves of the substrate were plotted, in order to identify the working area for the excitation frequency. Both phase and group velocities are illustrated in Figure 7.20 where the two fundamental symmetric and antisymmetric Lamb wave modes are displayed as well as the fundamental shear horizontal mode $SH_0$ which is coupled with the Lamb wave modes. The cut-off frequency of the higher order modes in this case, allows selection of excitation frequency among a wide range, namely between 0 and 500 kHz. The aim here is the selection of as

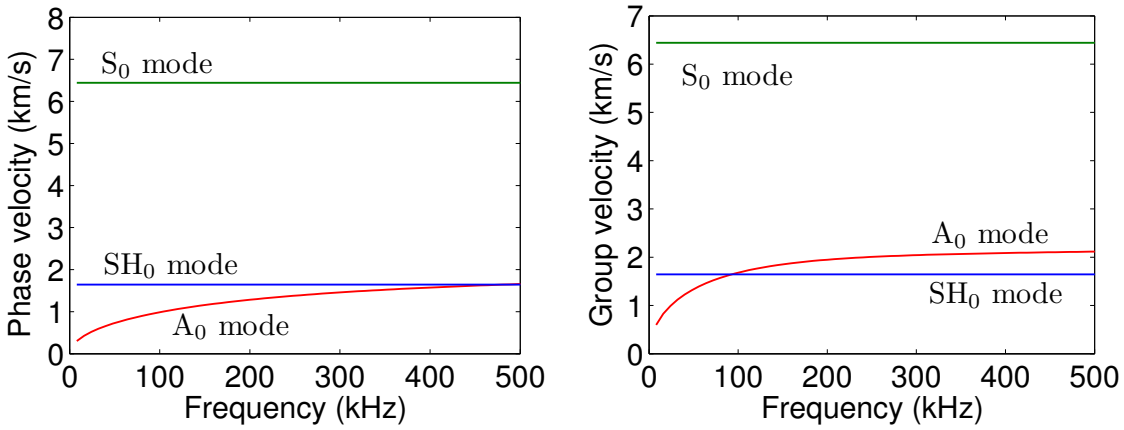


(a) Phase velocity (b) Group velocity

Figure 7.20: Dispersion curves for a $[0/90]_{8T}$ 2 mm thick plate made out of MTM56/CF0304. [48]

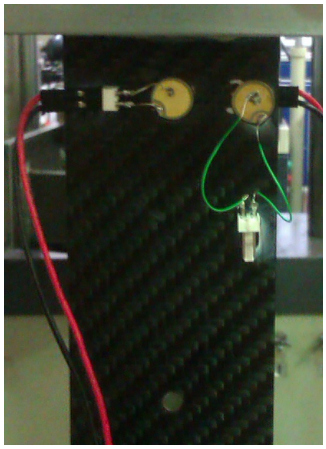

Figure 7.21: Extra PZT for the validation of the excitation of the fundamental modes.

high a frequency as possible in order to achieve a smaller wavelength and hence increase the sensitivity of the monitoring procedure. As analysed in Chapter 3, the PZTs that are widely used in similar tests, can only isolate specific modes in specific frequency ranges, posing a limitation on the required wavelength. Therefore, here the proposed excitation method was validated for a wide range of frequencies in order to conclude whether the separation of the two fundamental modes is possible or not. For that purpose, an extra PZT (PZT5) was attached next to PZT3. The distance between the centre of the transducers was equal to 20 mm, as illustrated in Figures 7.16 and 7.21. This operated as sensor when the pair of actuators operated in-phase and out-of-phase in order to record the response signal before it interacts with any discontinuities and hence undergoes mode conversion.

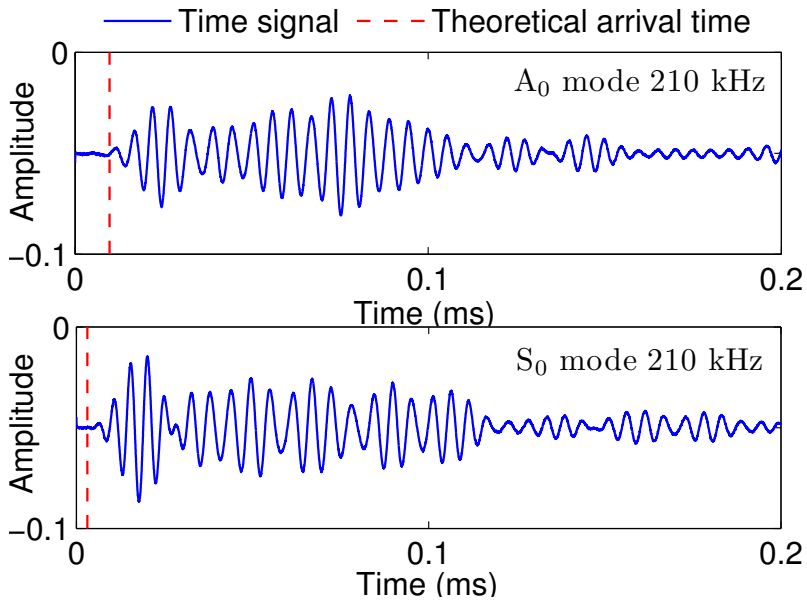


Figure 7.22: Comparison between the theoretical and the experimental arrival time for $A_0$ and $S_0$ modes at 210 kHz.

Figure 7.22 displays the response signals obtained, based on the aforementioned excitation set up, from one representative excitation frequency (210 kHz). The $A_0$ and $S_0$ mode waveforms are illustrated along with the theoretical arrival time (red line). The agreement between the theoretical and experimental arrival time seems to be relatively good for both modes.

In Figure 7.23 the two separate modes are illustrated together with the response signal when only PZT3 was excited, hence exciting both modes. In the same figure, the waveform that resulted after adding the separate $A_0$ and $S_0$ mode waveforms as well as the waveform that resulted when only PZT3 was excited are compared. It needs to be highlighted at this point that before adding the two separate $A_0$ and $S_0$ waveforms, the one that corresponded to $A_0$ mode, was multiplied by two, to account for the amount of energy that is dissipated when the transducers operate out-of-phase instead of in-phase. The two final waveforms exhibit a good agreement. This qualitative analysis was based on visual interpretation of the results and proved that the underlying principle behind the excitation of the separate modes was successful. However, a more quantitative approach has to be performed.

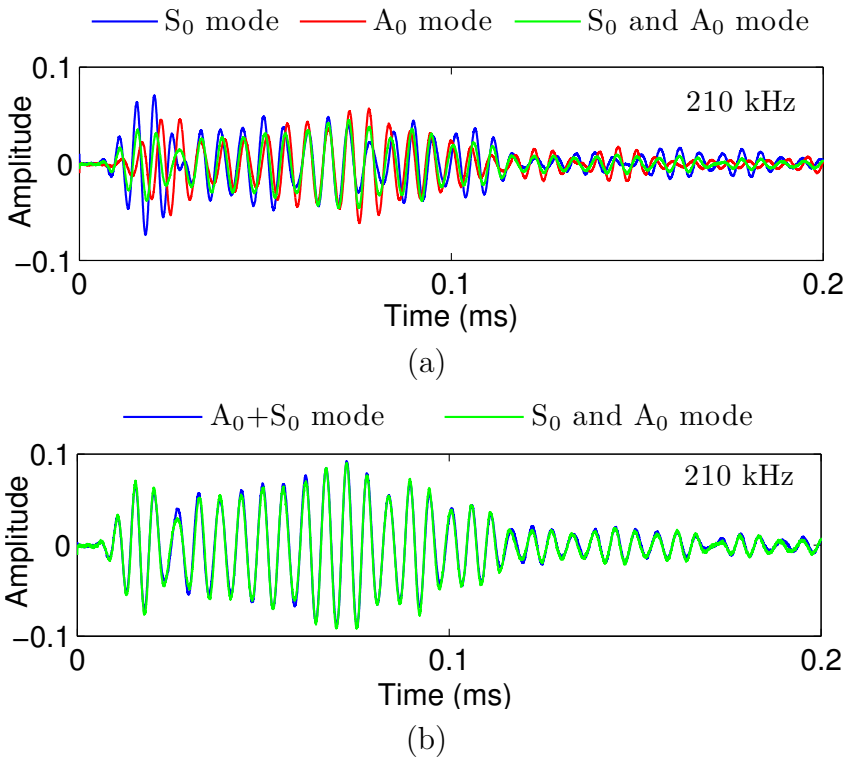


Figure 7.23: Response signals for $A_0$ and $S_0$ modes separately and waveform when both modes are excited (a), $A_0$ and $S_0$ modes added together compared with the response when both modes are experimentally excited (b) at 210 kHz.

### 7.2.3 Estimation of the group velocities through the Akaike information criterion

In Chapter 6 as well as in Section 7.2.2, the arrival time of the response signals in both cases of numerical and experimental tests, were visually estimated. This can be considered reliable in cases where the level of noise is low enough and errors due the arrival point being 'buried' in noise are negligible. However in the current work, a high level of noise was observed in the resulting signals due to the interference of the testing machine with the signals and due to the environmental conditions in the laboratory. As a consequence, an alternative approach for the estimation of the arrival time was investigated here, which is expected to minimise the errors due to noise, and which could be potentially applied in industrial applications carried out under real operating conditions and not under the idealised, controlled laboratory ones.

One of the most basic methods for determining the onset time of an ultrasound signal

apart from visual picking, is the use of an amplitude threshold picker. However in cases where the obtained signals are of very low amplitude this method might fail to distinguish between the noise and the actual signal. There have been several methods proposed for time picking following in general two main trends. The first focuses on the whole signal as a part of a global strategy and the second focuses on a preselected region which involves the onset which is called iterative strategy. A detailed review of those approaches can be found in [116].

The current work will focus on an approach that involves an autoregressive process first proposed by Akaike [117] also known as *Akaike information criterion* (AIC). According to this approach, the investigated time series is divided into two locally stationary segments after a first estimate of the onset time is performed. Each segment is modelled as an autoregressive process and represents the part of the time series mostly dominated by the noise and the original signal, respectively. Then the accurate onset point is determined as the separation point between the two segments which is the point at which the AIC is minimised. The application of the AIC-picker first needs the pre-arrangement of the onset (e.g. the point that divides the two segments). This can be performed either through the complex wavelet transform or through the Hilbert transform. In the current work the Hilbert transform was implemented.

The Hilbert transform (HT) was defined in some detail in Section 4.2. After the HT has been applied, the envelope of each signal is normalised, so that the same threshold can be applied to all signals. The threshold is defined in such a way that it picks the onset point as soon as the amplitude of the envelope has exceeded approximately 20% of its total amplitude which is equal to 0.2 for all normalised envelopes. This threshold ensured that the selected amplitude is well above the amplitude of the observed noise. Next, the selected window was defined to start from the start of the waveform and to end 200 samples after the preselected onset point. The AIC function that is further applied to the selected window is demonstrated in Equation 7.2:

$$AIC(t_w) = t_w \cdot \log(\text{var}(R_w(t_w, 1))) + (T_w - t_w - 1) \cdot \log(\text{var}(R_w(1 + t_w, T_w))) \quad (7.2)$$

where $R_w$ is the selected window, $T_w$ is the last sample of the selected window, $t_w$ ranges through all samples of $R_w$ and var is the variance function. $R_w(t_w,1)$ expresses the variance that is measured from the beginning of the window until the current

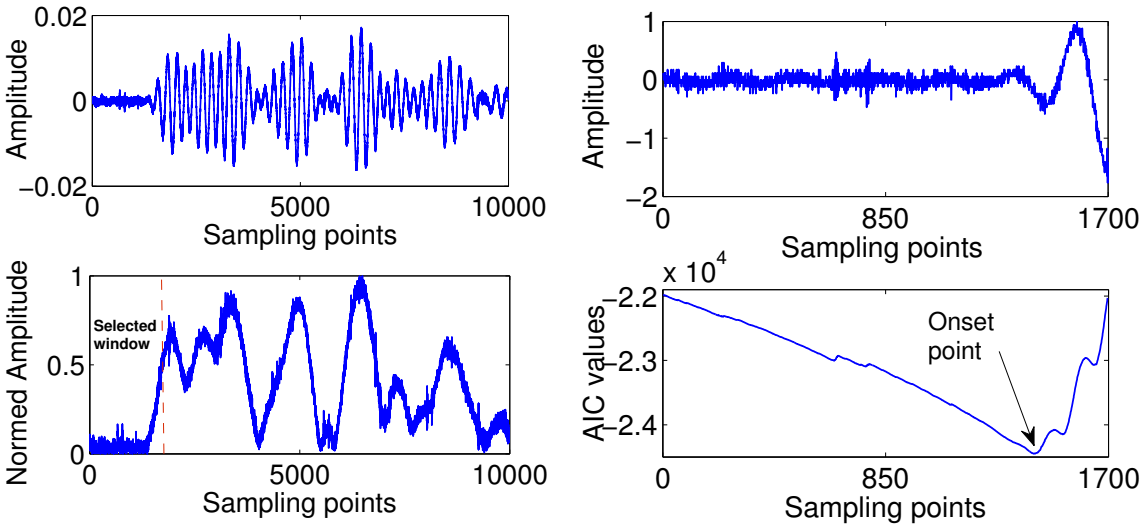


(a) Time signal; Hilbert transform (b) Selected window; AIC function

Figure 7.24: Estimation of the onset time of a Lamb wave waveform, after the application of the Hilbert transform and the application of the AIC function.

value $t_w$, while $R_w(1+t_w, T_w)$ expresses the variance that is taken for all samples ranging from $1+t_w$ to $T_w$. In Figure 7.24 an example of how the approach works is illustrated, where the global minimum of the AIC function determines the onset point of a representative Lamb wave signal recorded for the current work.

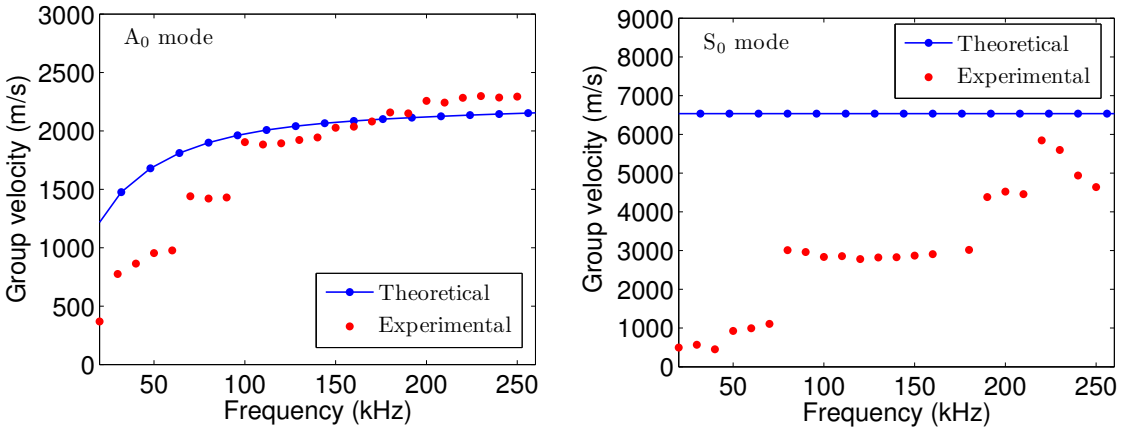


(a) $A_0$ mode (b) $S_0$ mode

Figure 7.25: Comparison between the theoretical and the experimental group velocity as extracted through the Akaike information criterion.

In Figure 7.25, the experimental and theoretical group velocity is plotted for $A_0$ and $S_0$ modes. The theoretical curves were extracted from the dispersion curves. The experimental curves were estimated after the experimental arrival time for each

waveform was measured through the AIC. Then the distance between the two transducers was divided by the arrival time and the group velocity was obtained according to the following equation.

$$c_{gr} = \frac{\Delta s}{t_{arr}} \tag{7.3}$$

where $c_{gr}$ is the group velocity, $\Delta s$ is the distance between the transducers (20 mm) and $t_{arr}$ is the arrival time of each waveform, as estimated by AIC.

The threshold defined for the AIC algorithm was 0.2 for the waveforms in the higher frequency range (40 kHz–250 kHz), and it was increased up to 0.5 for lower frequency signals since the observed level of noise in these frequencies was considerably higher. The window around the prearranged onset, was selected to be from the starting point of the waveform until 150 sampling points after the prearranged onset point providing pretty accurate results. However in the lower frequency range signals, this interval had to be adjusted starting from the beginning of the waveform until 450–650 sampling points after the prearranged onset point. This secured that the onset point would not be 'buried' in the high levels of noise.

The results show that the agreement between the experimental and the theoretical group velocities is significantly high for the $A_0$ mode and especially at the higher frequencies, namely from 100 kHz on. However, the same agreement can not be observed for the $S_0$ mode. In the second case, the experimental group velocity is considerably lower than the respective experimental, fluctuating between low and higher values. The results indicate that the excitation of $S_0$ mode was not successful, possibly due to the corruption of the pure Lamb wave mode with the respective slower shear horizontal mode, which in the case of composite materials is coupled with the Lamb wave mode. In addition, the low level of agreement between the theoretical and the experimental antisymmetric mode at frequencies below 100 kHz, could be attributed to the fact that at low frequencies, the shear horizontal mode propagates faster in the panel at a region very close to the excitation region of the $A_0$ mode exhibiting a dispersive behaviour, hence corrupting it. Therefore for the subsequent analysis, only the $A_0$ mode was selected at a frequency equal to 175 kHz where the correlation between the experimental and theoretical values was sufficient. This gives a wavelength equal to $\lambda$= 10.9 mm. Finally the current analysis highlights the advantage of the employed method for estimating the accurate arrival time of ultrasonic waves, which would lead to false results if visually implemented.

### 7.2.4 The problem of inadequate training data set

For the application of pattern recognition analysis, a strong baseline reference set is usually required. This set needs to include as many observations as possible; the bigger the training data set the more accurate the training of the algorithm will be, hence the more robust the analysis will be. However, in practical engineering cases, the recording of so many data sets might not be possible due to certain reasons. First of all, depending on the number of locations that are considered to be critical, transducers should be incorporated at all of them sometimes forming several propagation paths as has been previously illustrated, in order to capture damage that might unexpectedly occur at any direction. This means in practice, that the number of observations required for all of the paths, can be significantly high. In turn, there are certain complications that might arise in real industrial problems. First of all, the cost of pre-processing and storing all these data as well as transforming them into suitable features, can be considerably high, requiring highly trained personnel and high computational power as well as storage. Secondly, the recording of the observations at a pristine condition might be interrupted by an unexpected operational condition, or the coupling/mounting conditions might change in such a way that the original baseline reference data set might comprise of observations which have themselves been corrupted by external factors. Therefore it is important to investigate the effect of what would be considered as 'inadequate training data set' which would have an immediate consequence on the analysis proposed in Section 7.1.

In the current study, a set of 10 observations was obtained for each of the conditions summarised in Table 7.5. Although there is no general rule as to which is the optimal size for a sufficient training data set, a general rule of thumb that has been followed is that the training data set should be 10 x $n$ x $c$, where $n$ is the number of features and $c$ the number of classes in the problem [118]. From the previous analysis in Section 7.1, one could conclude that if the selected feature comprises sampling points extracted from the original time waveform, then as many sampling points as possible are required, at least 50. This leads to the conclusion that the minimum number of observations needed for a 50-dimensions and 2-classes problem, would be 100 which is not the case for the current example.

After post-processing, the obtained signals from phase II had to be discarded from the analysis, due to interference of the monitoring technique with the machine. In

addition, the mounting conditions between phase I and phase III were different, since the machine in the first case was in force mode during the acquisition of the signals and in the second case, the load was completely removed. Therefore these experimental conditions pose a certain degree of difficulty in the post processing of the obtained signals and their subsequent correlation with the observed damage in a sensible way. Within the concept of the current section, two methods will be evaluated for overcoming the aforementioned complications the level of success of which will be assessed accordingly.

The tested features obtained from the raw time signals, are 50-dimensional consisting of 50 sampling points for phase I (1,373–3,223 sampling points for PZT1 and 2,357–4,607 for PZT3) and the same for phase III (1,426–3,976 sampling points for PZT1 and 2,420–4,070 sampling points for PZT3). All features were subsampled in order to obtain the required dimensions. The captured waveform for the pristine condition for both investigated phases I and III are displayed in Figure 7.26 where the assigned features are also shown. The selection of the features was based on the isolation of the first two strong wave packages (Figure 7.26 shown with dotted red lines). In Figure 7.27, the results of the outlier analysis for phase III are displayed when $A_0$ is excited and received by PZT1. The training was performed with the first 8 observations from the baseline reference set while the rest were used for validation. The first two observations belong to the validation set, while each of the rest of the sets consists of 10 observations and corresponds to the rest of the 6 damage sets that were recorded for phase III (Table 7.5). The 1 % exclusive threshold value for an 8 observations, 50-dimensional problem was estimated after 1,000 trials.

As demonstrated, the Mahalanobis squared-distance is negative for all the test sets. This is by definition very unlikely. However, the problem seems to stem out of the definition of the covariance matrix of the training data which is required for the training of the algorithm (equation 4.1). If the training data set is insufficient, then this leads to a covariance matrix which is non-positive-definite. In turn, the resulting smallest eigenvalues are negative, which become the largest when the covariance matrix is inverted as prescribed in equation 4.1. An additional problem that can arise is the fact that the dimensions of the feature are considerably higher than the number of the observations, which does not result in a well behaved feature. Therefore other approaches need to be investigated towards two directions. First is the singular value decomposition of the covariance matrix and second is the decrease of the features. Both directions will be investigated in the following sections.

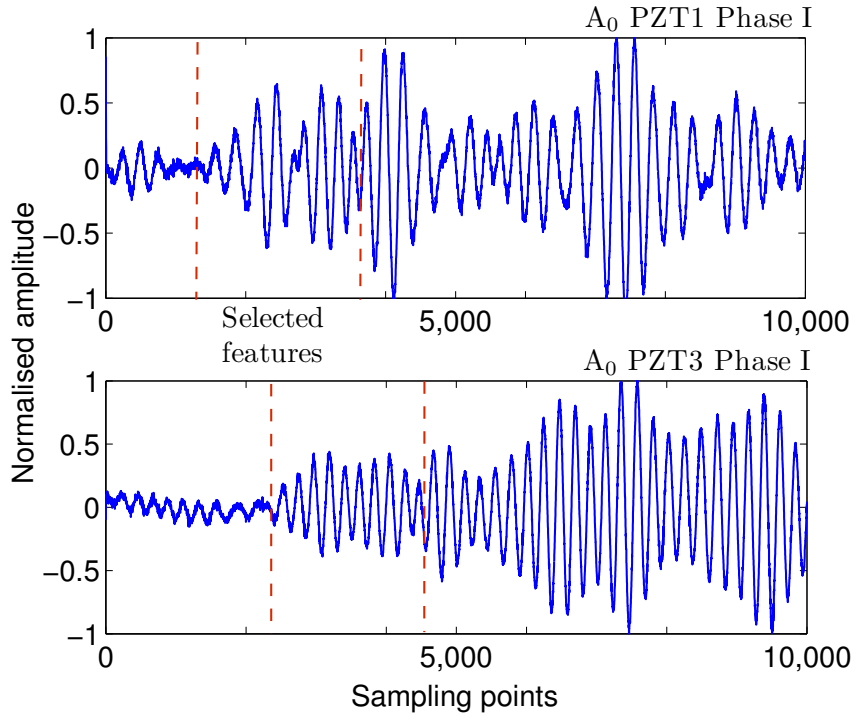


(a)Phase I

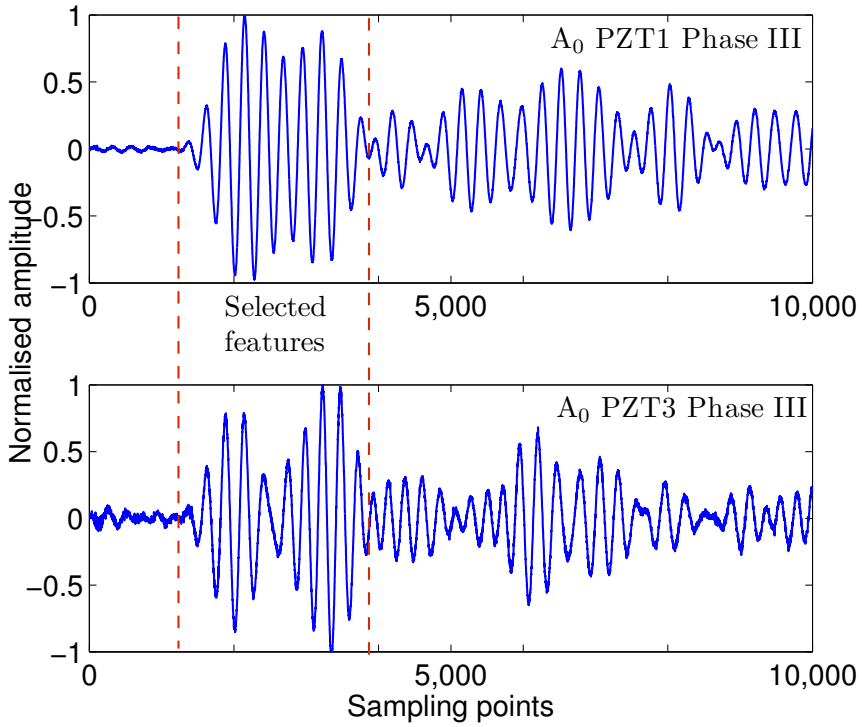


(b)Phase III

Figure 7.26: Pristine condition for phase I (a) and phase III (b) of the single patch repair configuration; dotted red lines indicate the selected features.

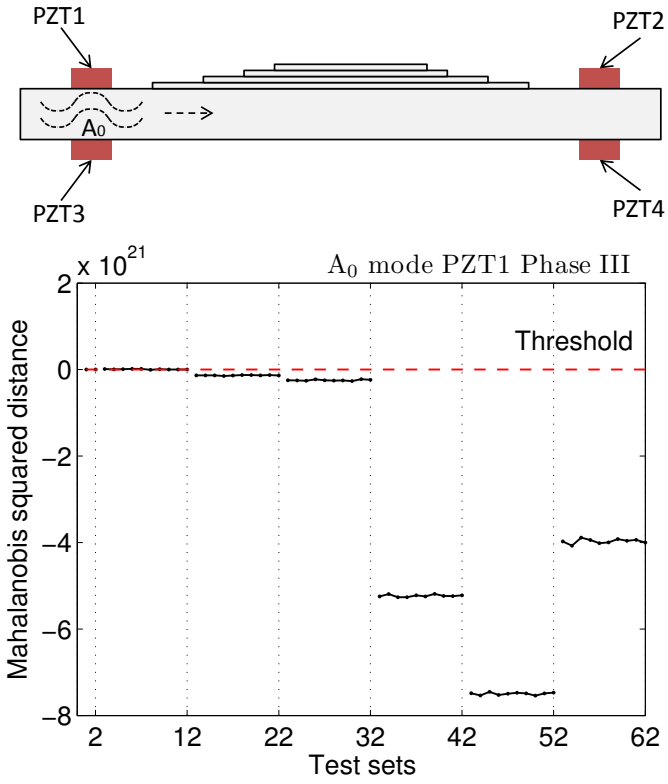


Figure 7.27: Negative Mahalanobis squared-distance due to a non positive-definite covariance matrix ($A_0$ mode received by PZT1).

### 7.2.5 Singular value decomposition and dimensional reduction for non-positive-definite covariance matrix

The problem of a non-positive-definite covariance matrix was also observed in the work carried out by Worden et al. [119] in which a reference set parametrised by an environmental variable is established in order to account for the problem of novelty detection in a changing environment. In this work, it is proposed as a possible solution, the modification of the distance measure in order to make it positive semi-definite through the singular value decomposition. According to this approach, the covariance matrix is decomposed as following:

$$[S] = [U][s][U]^T \tag{7.4}$$

where $[s]$=diag($s_1$,$s_2$,...,$s_p$) is a diagonal matrix which contains the eigenvalues in descending order of magnitude. Then the positive semi-infinite inverse of the original

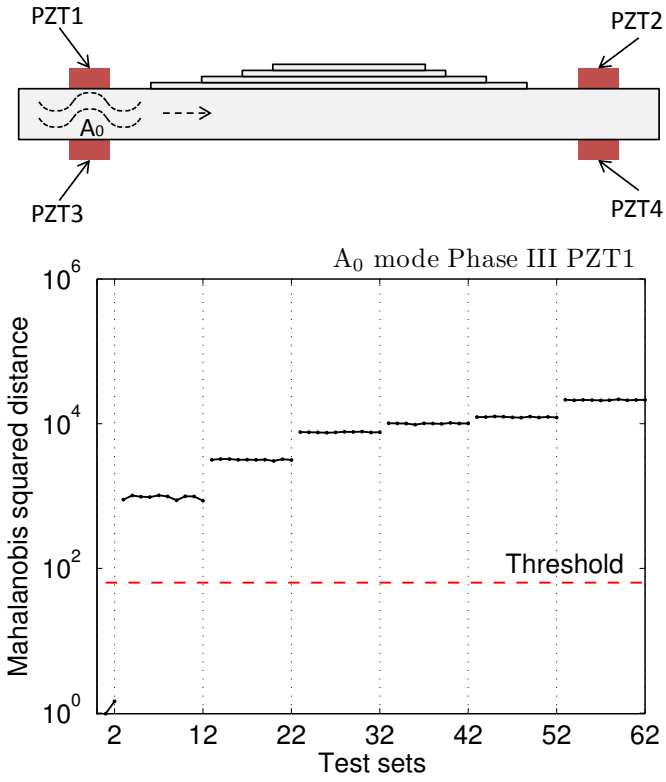


Figure 7.28: Singular value decomposition as a solution to the non-positive-definite covariance matrix for phase III ($A_0$ mode received by PZT1.)

covariance matrix $[S]^d$, $[S^d]^{-1}$ is given as:

$$[S^d]^{-1} = [U][s^d]^{-1}[U]^T \tag{7.5}$$

where $[s^d]^{-1}$=diag($s_1{}^{-1}$,$s_2{}^{-1}$,...,$s_{n-1}{}^{-1}$,0,...,0).

The result of the implemented approach is illustrated in Figure 7.28. The threshold and the test sets correspond to the same set up as the one of Figure 7.27. The problem seems to have been successfully solved, since the negative eigenvalues have been deleted. However, as mentioned in [119], the degree of accuracy of the illustrated results is subject to the percentage of the eigenvalues that were eliminated through the aforementioned approach which in this case is approximately 40 %. Moreover, the Mahalanobis squared-distance is expected to be lower due to the fact that the deleted negative eigenvalues, are the ones that would be the higher after the inverse of the covariance matrix. Therefore the level of accuracy of the employed solution to the problem of inadequate size of the training data, was evaluated through the PCA. In addition, a reduction in the dimensions of the feature is required since a 10-

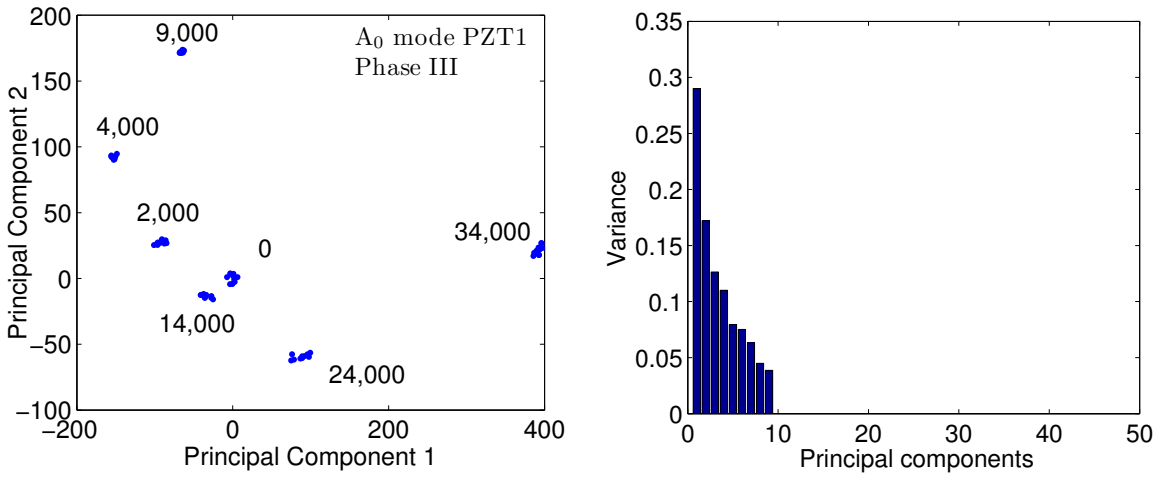


(a) PCA (b) Variance

Figure 7.29: Principal component analysis (a) and variance variation (b) for phase III ($A_0$ mode received by PZT1.)

dimensions/50-observations training set of data is not considered to be adequate for a well behaved outlier analysis. Furthermore, the reduction of the feature through the reduction of the selected sampling points would lead to significant resolution loss.

Figure 7.29, shows the PCA and the respective drop in the variance with respect to the principal components for the tested feature and phase that is illustrated in Figure 7.28. PCA shows a clear separation between the different cycles levels, while the drop in the variance shows that almost all of the variance is contained in the first ten principal components. This indicated that the data has effective dimension 10 and so the covariance matrix estimated by SVD does not lose in accuracy by deleting 40 % of the eigenvalues. This result allows an alternative feature extraction through the principal components which is equivalent to the effect of SVD to the data sets. This would enable the reduction of the features dimension to a number which is lower than the corresponding number of the observations and would lead to a well behaved outlier analysis. In order to define the appropriate number of the principal components that would serve as the new features, a convergence study was performed as illustrated in Figure 7.30 where the Mahalanobis squared distance was plotted against the test sets for phase III and for the $A_0$ mode received by PZT1 as in Figure 7.29. The figure shows that 2 principal components (PCs) are not sufficient to describe the behaviour of the monitored system while when the number of PCs increases from 3 onwards, little variation is exhibited. Some slight differences in the

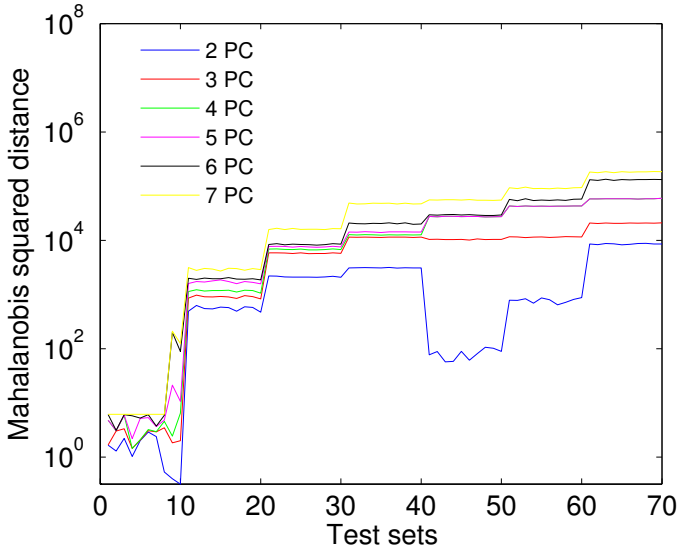


Figure 7.30: Convergence study for phase III, loadings at 80–95 % $\sigma_f$ ($A_0$ mode received by PZT1).

amplitude are not important since the assigned threshold for each considered case is not the same either. It increases as the number of principal components increases. This behaviour is reasonable since the first 3 PCs account for almost 60 % of the variance while the first 2 account for about 48 % which is less than half. Therefore the first 3 principal components were selected.

The results have been estimated without any need for SVD application for the inverse of the covariance matrix which is singular. In addition, the dimensions of the selected features are lower than the number of the observations while at the same time they contain a sufficient amount of variance of the total variance of the feature extracted from the original time waveforms (Figure 7.26). Therefore the partial solution of the problem was possible with a simple processing of the features enabling a robust analysis without any substantial loss of information. It is interesting to note that the Mahalanobis squared-distance values after the dimensional reduction, exhibits higher values than the respective values after the performance of SVD (Figure 7.28), which is an extra indication that the extracted features are well behaved and the analysis is more reliable.

After the reduction of the features' dimensions, the outlier analysis for each received waveform and for both phases I and III was assessed in order to evaluate the structural integrity of the panel and the damage sensitivity of the $A_0$ mode (Figure 7.31). The threshold, the training and validation sets and the test sets were assigned in

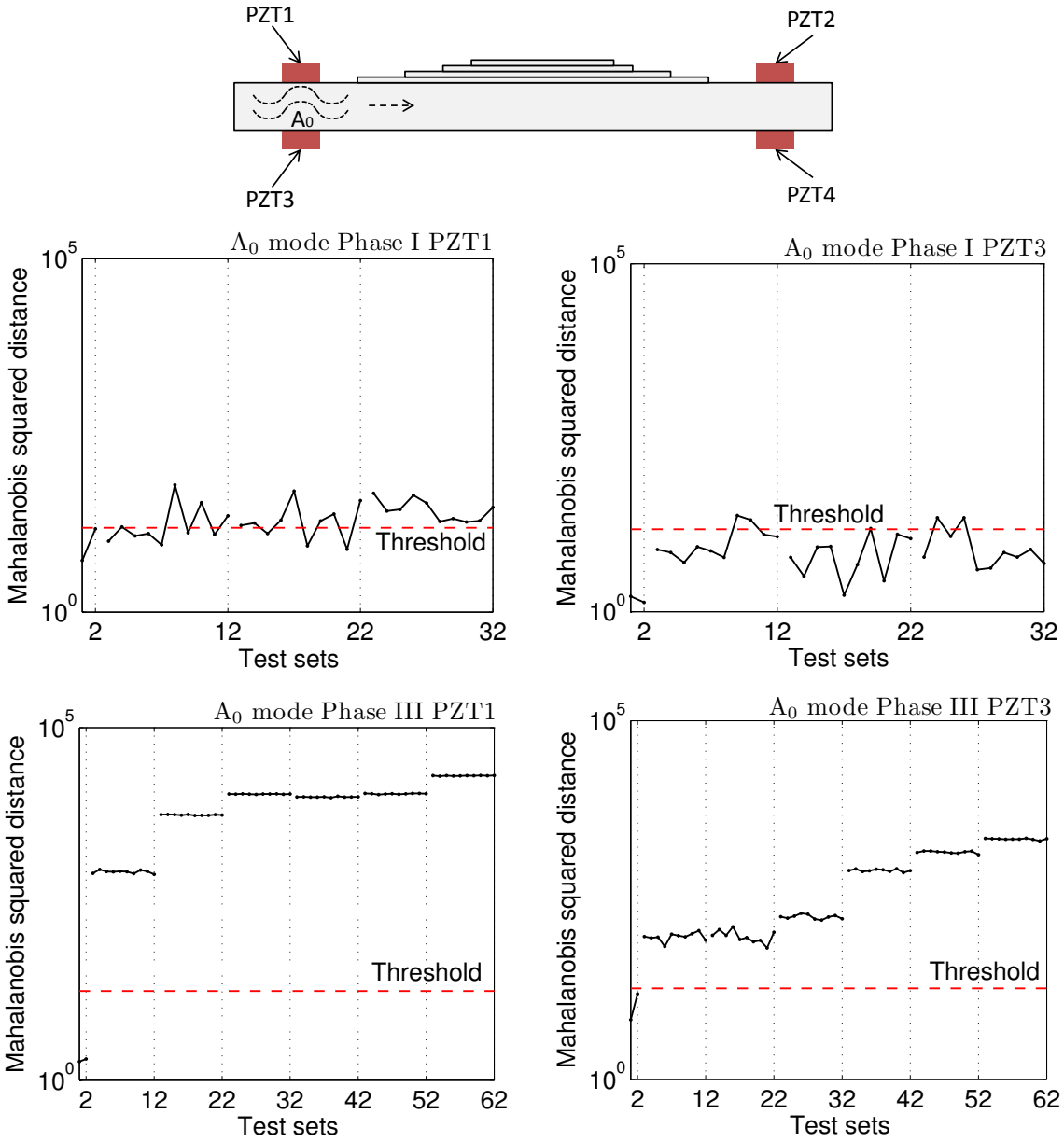


Figure 7.31: Outlier analysis results after the features reduction for phase I and phase III for both PZT1 and PZT3.

the same way as in the previous examples of the section. Only the first three principal components were selected which accounted for 80 % of the variance for phase I (PZT1), 88 % for phase I (PZT3), 60 % for phase III (PZT1) and 58 % for phase III (PZT3). The y-axis is scaled in the same way for comparative reasons for all figures. Even though the training sets of data are different for phase I and phase III, the difference with respect to the assigned threshold which is different for each phase is clear. Phase I exhibits almost no damage with only very few individual observations

being flagged as outliers except for PZT1 which shows a more distinctive deviation at the last set (after 4,500 cycles). On the other hand, phase III shows a significant deviation from the normal condition, which is more evident for PZT1 and which further accumulates as the cycling advances. At this stage extensive debonding has been developed and observed between the patch and the substrate.

## 7.3 Discussion

This chapter demonstrated different concepts of Lamb wave excitation and acquisition as well as certain signal processing scenarios aiming at the damage detection. Alternative nondestructive techniques proved the accuracy of the extracted results. More specifically, a scarf patch repair was tested under tension with Lamb waves and digital image correlation. The obtained Lamb wave signals were further processed with outlier analysis, principal component analysis (liner and nonlinear). All methods proved to be efficient, successfully representing the structural status of the monitoring system as captured by DIC, while the concept of the fitted principal curves exhibited a considerable efficiency. The only limitation of the principal curves lies in the difficulty in assigning a certain initiation and finishing point or in assigning a certain fitting path.

In addition, an external repair patch was tested under tension tension fatigue, while X-ray radiography and microscopic analysis further assessed the developed damage. Piezoelectric transducers bonded on the top and bottom of the tested surface were utilised in-phase and out-of-phase in order to excite separately the symmetric and antisymmetric fundamental Lamb wave modes. The estimation of each mode's arrival time was performed through the Akaike information criterion which indicated that only the excitation of the antisymmetric mode was successful due to the possible corruption of the symmetric mode with the shear horizontal mode. The study dealt with the problem of inadequate training data set by suggesting a pseudoinverse approach for the inverse of the covariance matrix and a reduction in the selected feature through the principal component analysis and the isolation of the most representative principal components. Finally outlier analysis was applied which successfully represented the condition of the structural integrity. The next chapter demonstrates the application of the aforementioned processing tools in a bigger scale demonstrator, namely a vertical helicopter tail stabilizer.

# Chapter 8

# Monitoring of a Repaired Helicopter Tail Stabilizer

After the investigation of the key challenges in the *in-situ* monitoring of different repaired configurations of a small scale and the examination of the applicability of certain signal processing techniques in the previous chapters, the current chapter aims to scale-up the tested configuration. Therefore, a larger scale demonstrator of a real structure was selected for testing under representative loading. The most successful methods that have been extracted by the previous chapters are chosen in order to demonstrate their efficiency in helicopter structures. The demonstrator is an aluminium helicopter tail stabilizer loaded under bending fatigue. The current work was performed within the framework of the EU project which provided the funding to the author of the thesis, the EU $7^{\text{th}}$ Framework Programme (ACP8-GA-2009-234333), IAPETUS (innovative repair of aerospace structures with curing optimization & life cycle monitoring abilities). Detailed description of the experimental set up will be given which aims to set a realisation platform for future testing while the processing approaches have been extensively explored in previous chapters.

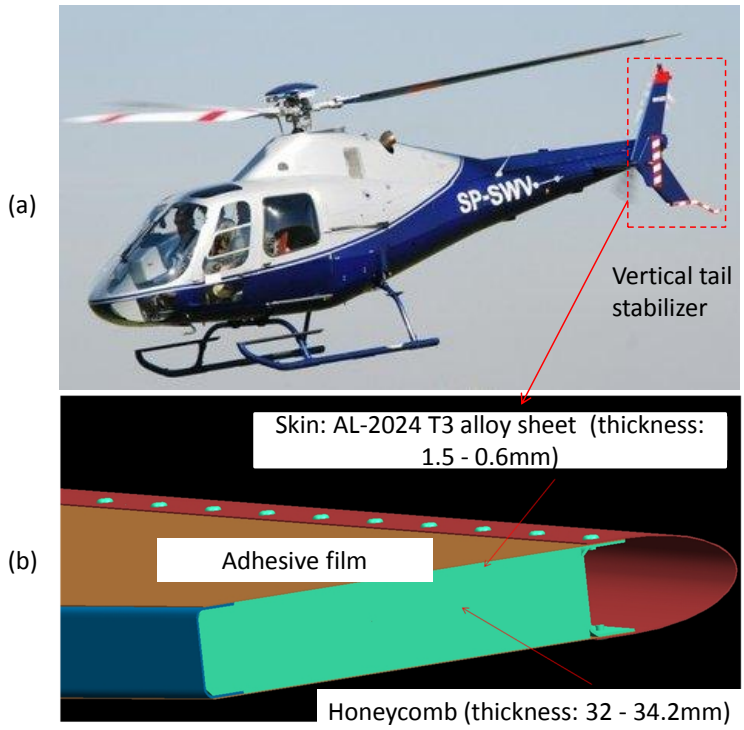


Figure 8.1: (a) SW 4 helicopter (b) schematic illustration of the cross section of the tested demonstrator.[1]

## 8.1 Repaired helicopter aluminium stabilizer

The aeronautical structure which was selected as a representative demonstrator was a vertical stabilizer of a helicopter located on the tail boom and manufactured by PZL-Swidnik/AgustaWestland (Poland). The panel was a honeycomb construction, the core of which was made of HexWeb CRIII-5/32-5052-.001N-3.8 and the skin was made of AL-2024 T3 alloy sheet, 1.5 mm to 0.6 mm thickness (Figure 8.1).

Prior to the selection of the area to be repaired, fatigue was performed and the most critical region was identified to be around the holes at the centre of the stabilizer as illustrated in Figure 8.2(a). The artificially introduced crack that would be repaired by a bonded composite patch was 35 mm long, located close to the hole as shown in Figure 8.2(b).

The repair patch consisted of 4 plies AGP 280 (Hexcel 43280S) with a stacking ply

[1]The contained data are belonging to PZL-Swidnik S.A. and any further reprinting and usage cannot be made without PZL-Swidnik S.A. written permission

[2]The contained data are belonging to PZL-Swidnik S.A. and any further reprinting and usage cannot be made without PZL-Swidnik S.A. written permission

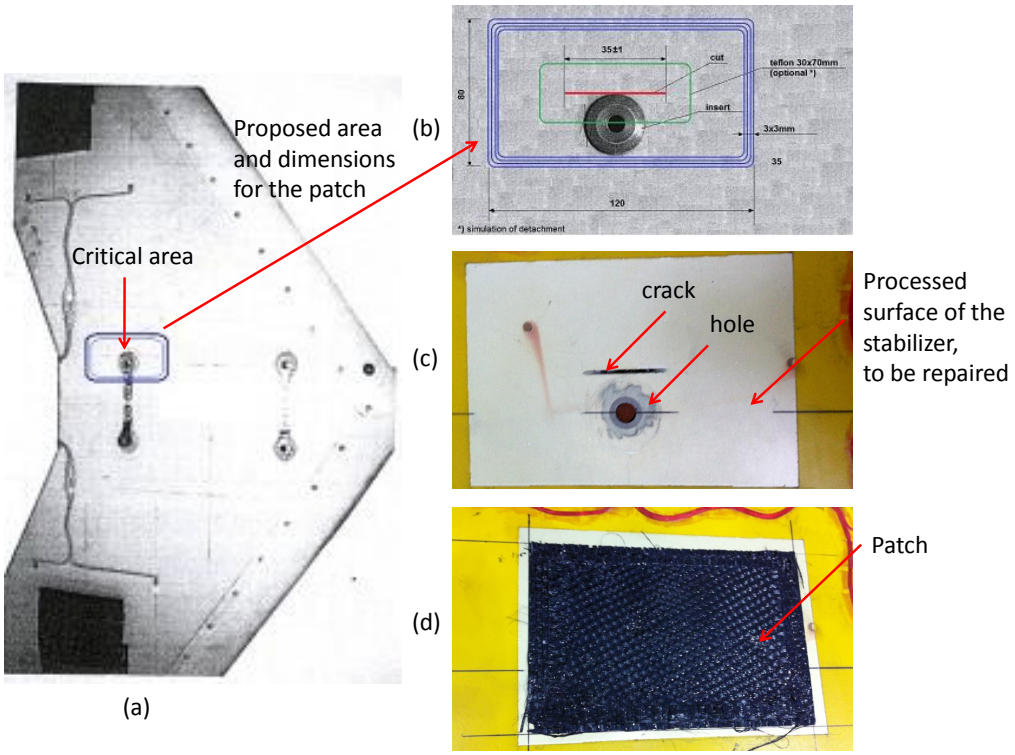


Figure 8.2: (a) Critical area and proposed location (blue line) for the attachment of the repair patch (b) schematic illustration of the repaired region (c) image of the processed surface of the stabilizer around the crack and the hole before the attachment of the patch (d) final implementation of the patch.[2]

| Number of layers | Direction | Dimension (mm) |
|---|---|---|
| L1 | 90° | 80 x 120 |
| L2 | 0° | 74 x 114 |
| L3 | 90° | 68 x 108 |
| L4 | 0° | 62 x 102 |

Table 8.1: Stepping configuration scenario for the patch (total thickness=1.16 mm).

sequence $[90/0]_2$ and total thickness equal to 1.16 mm. First the repaired surface was prepared using BR127 primer, Figure 8.2(c), and each ply was impregnated with carbon nanotubes (CNT) doped epocast which aimed to improve the electric conductivity of the patch (not used by the current method) as shown in Figure 8.2(d). Then each ply was cut to the final dimensions and laid up on the repaired region following a stepwise configuration as outlined in Table 8.1. Finally, a heating blanket was used for 2 hours at 93°C under vacuum conditions. A C-scan was performed on the demonstrator prior to testing for evaluation of the bonding quality of the composite patch which showed no uncured areas.

## 8.2 Testing and monitoring techniques

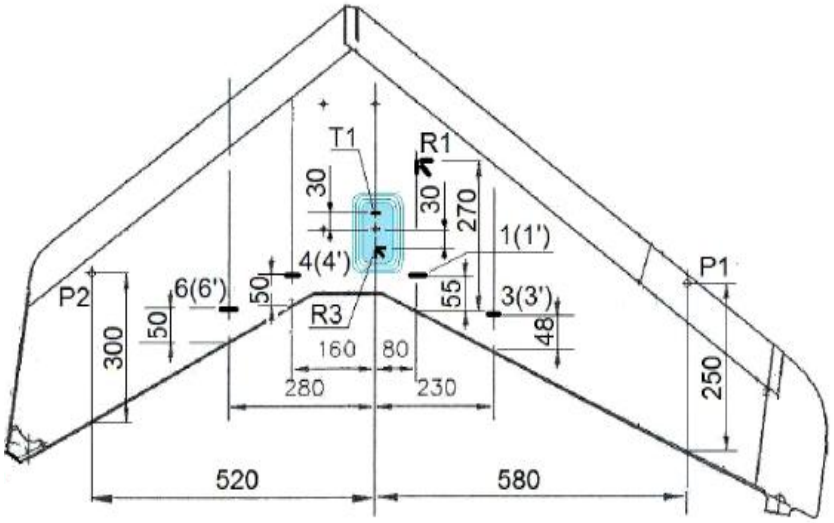


Figure 8.3: Schematic illustration of the repaired stabilizer.[3]

The testing scenario selected was representative of the kind of loading such structures are subject to, namely bending fatigue. As illustrated in Figure 8.3, there are two loading points (P1 and P2) the load of which was different in such a way that the moment about the fixed (repaired region) area, was equal both at the right and left side. The distance between the centre of the repaired region and the two loading points P1 and P2 was 580 mm and 520 mm respectively. The fatigue history is illustrated in figure 8.4. All tests were performed at a frequency equal to 20 Hz.

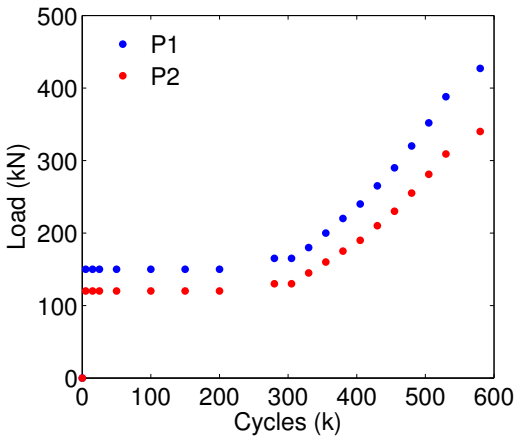


Figure 8.4: Load history of the stabilizer.

[3]The contained data are belonging to PZL-Swidnik S.A. and any further reprinting and usage cannot be made without PZL-Swidnik S.A. written permission

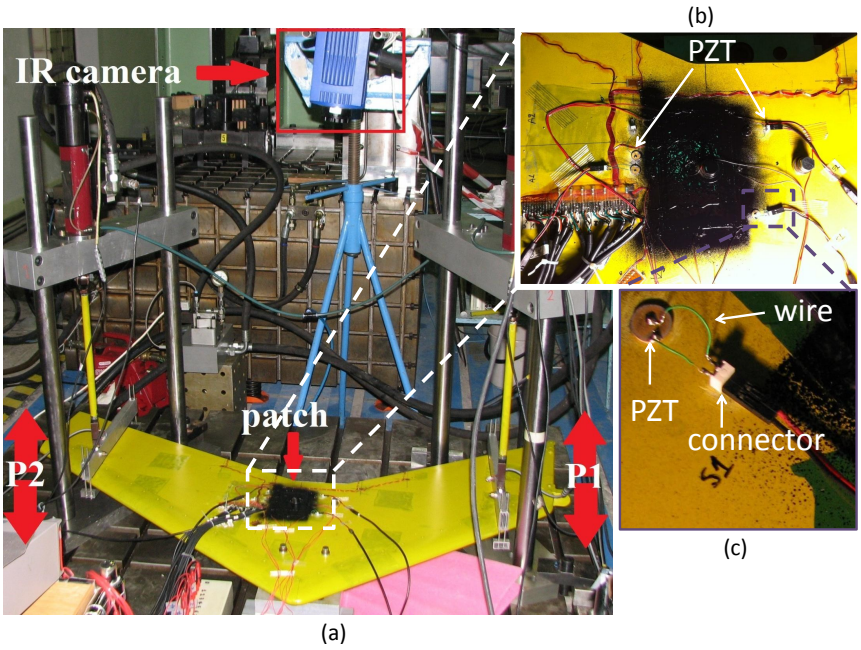


Figure 8.5: (a) Schematic illustration of the repaired stabilizer.

The aim was the monitoring of the structure through Lamb waves. In addition, lock-in thermography was implemented in order to confirm the results obtained from Lamb waves since thermography is considered to be a relatively better established technique (Appendix B). Images from an infra red (IR) camera which was positioned above the demonstrator were captured in an on-line mode during the testing. Prior to testing, 4 piezoelectric transducers were attached on the surface which would perform off-line monitoring with Lamb waves, at specific intervals. The demonstrator was first mounted on the test machine, appropriate calibrations for the monitoring techniques were performed and a baseline reference set of data was recorded for the Lamb wave testing. The final set up is illustrated in Figures 8.5(a), 8.5(b).

The first step was the surface preparation of the aluminium stabilizer prior to the bonding of the transducers. The preparation involved the use of sandpaper for obtaining a relatively rough surface which would ensure a good quality bonding of the sensors to the surface. Additionally a blade cutter was used in order to further sharpen the surface for extra security since the aluminium stabilizer would be subjected to significant deformations. Then the surface was cleaned with acetone in order to remove any excess material and dust remaining and the transducers were prepared.

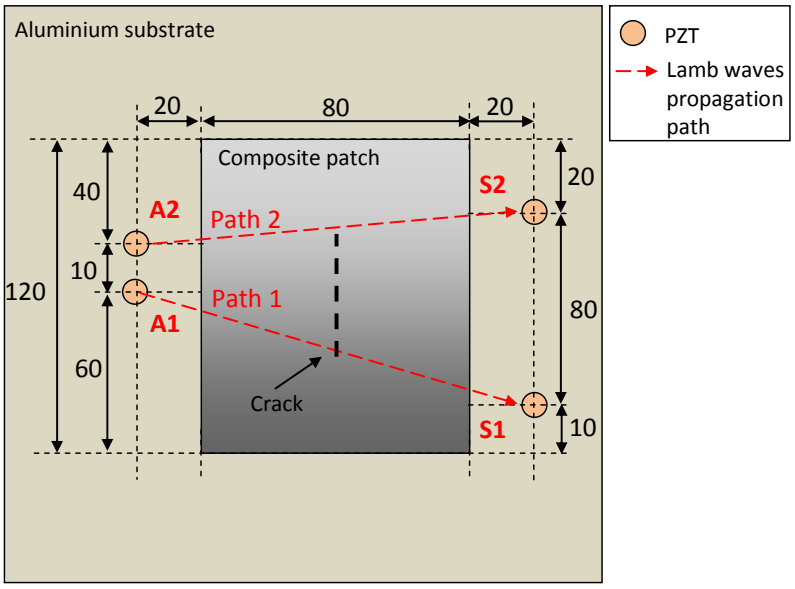


Figure 8.6: Schematic illustration of the PZTs arrangement (A=actuator, S=sensor); dimensions in mm.

The transducer set up consisted of two parts, the piezoelectric disc and the head connector. First two wires are stripped at both ends and coated with a thin layer of solder, then the piezoelectric transducer is held in a small clamp and two drops of solder are placed at the locations where the wires would be attached. Then the stripped ends of the wires are placed in contact with the soldered areas of the transducer and with the heated solder they are fixed in place. The same procedure is followed for the connector which is soldered at the other end of the stripped wires. The PZT operated in contact to the tested surface in order to excite it with stress waves. The connector is used to connect the transducer with the waveform generator which would provide the transducer with the required electric signal; this would be converted to stress signals as an effect of piezoelectricity. Finally both disc and connector were installed on the surface of the stabilizer by applying cyanoacrylate rapid bonding glue, while the application of uniform pressure ensured the effective bonding as shown in Figure 8.5(c). Four piezoelectric transducers were used (diameter=10 mm, thickness=1 mm) supplied by CeramTec, Germany.

Two of the PZTs (A1, A2) operated as actuators, exciting the tested demonstrator and the other two (S1, S2) operated as sensors receiving the output response, forming two propagation paths (Figure 8.6). This means that when actuator A1 was exciting the demonstrator only sensor S1 was recording the obtained signals, and when actuator A2 was exciting the demonstrator, only sensor S2 was recording the

resulting signals. All transducers were properly named and BNC cables which have two pins at one end were connected to each head connector, while the cables were glued with tape on the stabiliser for keeping them stable during testing.

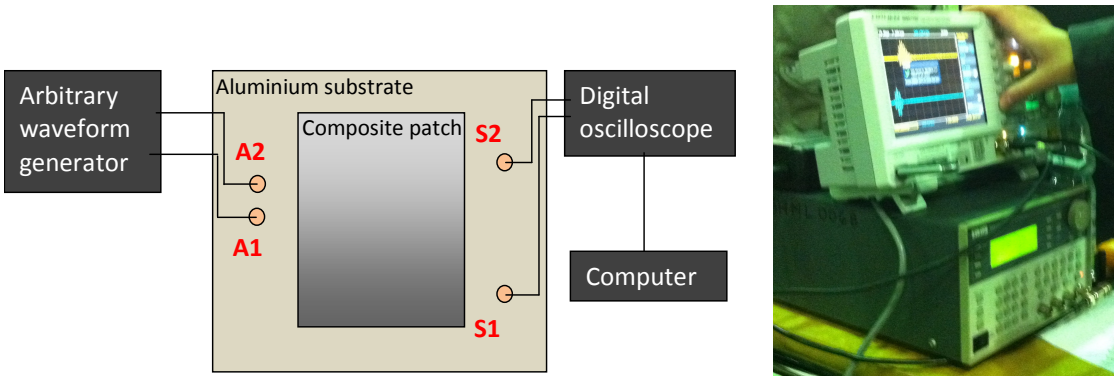


(a) (b)

Figure 8.7: A schematic (a) of the PZT excitation and a photo (b) of the data acquisition equipment; when actuator A1 was exciting the demonstrator only sensor S1 was recording the obtained signals, and when actuator A2 was exciting the demonstrator, only sensor S2 was recording the resulting signals.

The location of the employed transducers was selected in such a way that the stronger incident output signal would directly interact with the most interesting regions where damage was expected to develop, vertically to the crack's orientation. These were the edges of the patch and the crack of the stabilizer. In addition, their placement was intended to be as close to the patch as possible in order to minimise reflection of the propagating wave with other features such as strain gauges, electrodes and cables that were used for the other monitoring techniques. The placement of the PZTs was restricted in terms of space due to the prior attachment of the rest of the structural features. Finally the only suitable location for the attachment of the PZTs would be on the aluminium stabilizer and not on the repair patch, in order to avoid any loss of PZTs contact due to a potential local debonding of the patch. In addition, the PZTs would interfere with the images recorded by thermography, masking the focus of the camera.

The excitation signal was a 10-Volt peak-to-peak amplitude, 5-cycle sine pulse modulated by a Hanning window and the excitation frequency was 200 kHz. At this frequency only the two fundamental symmetric and antisymmetric modes propagate in Aluminium, enabling an easier interpretation of the acquired signals. The wave generator that was used was a TTi TGA 1230 30 MHz model and the data acquisition was performed with a HAMEG HMO 2022 digital oscilloscope at sampling

frequency equal to 25 MHz (Figure 8.7). The signals were saved at an external USB stick properly categorised in appropriate file names and they were later passed to a computer for further processing. For each set of signals, 512 averages were captured in order to minimise the effect of noise.

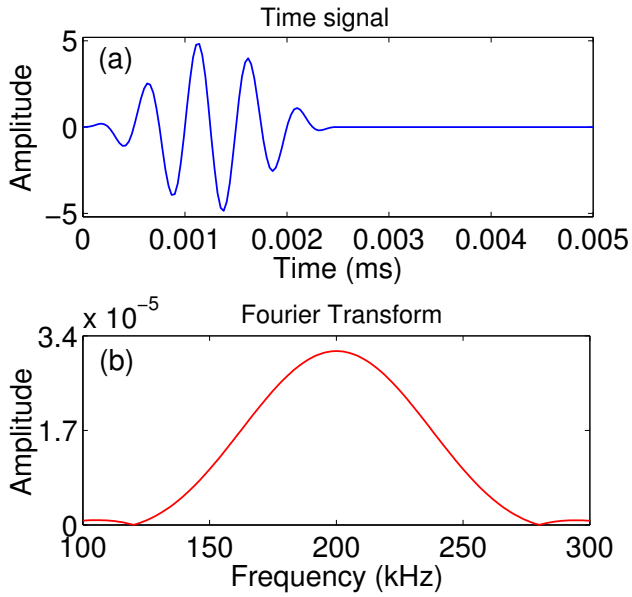


Figure 8.8: (a) Excitation signal at 200 kHz and (b) its Fourier spectrum.

The excitation signal is illustrated in Figure 8.8(a). The signal was modulated by a Hanning window in order to maximise the energy that would be 'guided' to the

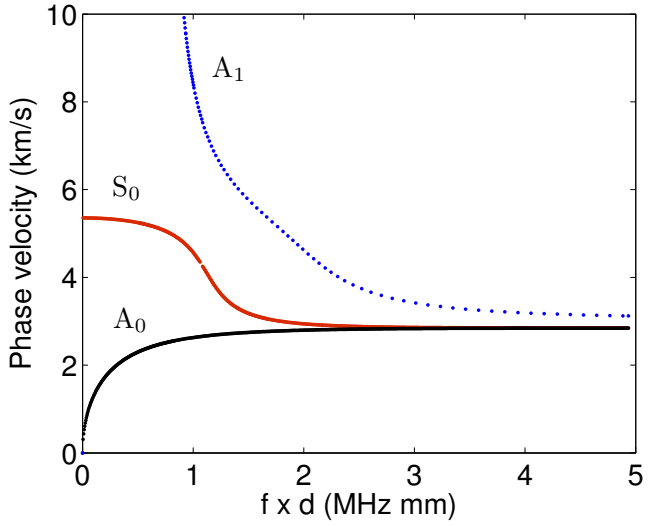


Figure 8.9: Phase dispersion diagram for Aluminium (E=70 GPa , v=0.33); phase velocity versus frequency x plate thickness product. [46]

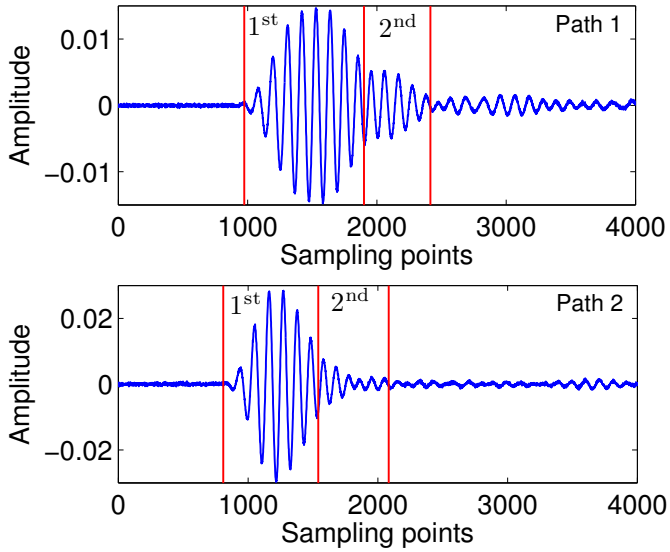


Figure 8.10: Response for the baseline reference state - 'healthy' condition along with the selected features for paths 1 and 2.

tested demonstrator. This can be verified by the Fourier spectrum of the time signal in Figure 8.8(b). The side lobes of the spectrum are almost negligible while the main lobe carries most of the energy. At this frequency, only the two fundamental modes, $S_0$ and $A_0$, propagate through the plate as illustrated in the dispersion curves in Figure 8.9. The working area is clearly below the cut-off frequency.

As part of the post-processing of the recorded waveforms, appropriate features had to be selected in order to reduce the dimensions of the data sets while isolating the regions of interest. Figure 8.10 illustrates the resulting waveforms for the baseline reference set, meaning the response prior to any loading, which is used in order to represent the 'healthy' condition. In the same figure, the selected features are illustrated for both paths considered for each demonstrator. Two features were selected for each waveform, the first corresponding to the incident wave which directly propagates through the bonded area and the edge of the crack and the second corresponding to the first reflection occurring from the edges of the patch and the crack. The rest of the captured waveform exhibits extensive attenuation as the waves undergo multiple reflections at the boundaries of the different features.

All monitoring methods started capturing failure indices at around 400– 500 kcycles. At the end of the test a clear debonding could be even visually captured as illustrated in 8.11. Thermography showed clear debonding that initiated around the hole and propagated, therefore the test was stopped. In addition, close examination of the

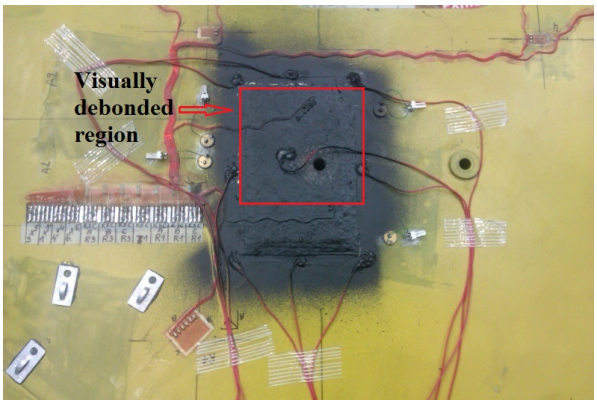


Figure 8.11: A photograph showing the final debonding after 580,000 cycles of testing.

area below the patch, showed that the length of the crack remained the same.

## 8.3 Post-processing

### 8.3.1 Outlier analysis and principal component analysis (linear and nonlinear) of the raw signals

In order to build the appropriate matrices for the subsequent analysis, 100 signals were recorded for each baseline reference set and 10 signals were recorded for each subsequent damage set; this would ensure a sufficient set of data after the observations derived by the previous chapters. After the pre-processing of the obtained signals, OA and PCA were performed in a comparative way in order to identify the agreement between the two methods and in order to explain the behaviour of the outlier analysis classes based on the orientation of the respective clusters in a 2-dimensional subspace. The aim of the analysis was the classification of the recorded waveforms and the estimation of their deviation from the baseline reference set. Based on the amount of deviation, appropriate assumptions were made for the presence of damage in the tested demonstrator.

For the illustration of the PCA results, only the first two principal components were considered, since they accounted for the highest percentage of variance. For the purpose of the outlier analysis, the 1 % exclusive threshold value for novelty for a 100-observation, 50-dimensional problem was estimated after 1,000 trials which

was found to be approximately the same for all paths, namely 100. This threshold (estimated through the Monte Carlo approach) is here denoted as Threshold 1. From the baseline reference data set, 90 observations were used as a training set in order to train the algorithm, and the remaining 10 observations were used as a validation set in order to evaluate how effectively the algorithm can identify the normal condition. This was performed for all methods. Table 8.2 illustrates the test sets of the outlier analysis and the respective cycles. It needs to be noted that the reference sets correspond to sets of data that were recorded when the test continued the next day, in which case a baseline reference set was captured prior to testing in order to ensure that the system was not affected by any possible temperature variations or other parameters.

| **Test sets** | **Cycles** |
|---|---|
| 1–10 | 0 |
| 11–20 | 500 |
| 21–30 | 5,000 |
| 31–40 | 15,000 |
| 41–50 | 25,000 |
| 51–60 | 25,000 (Reference set) |
| 61–70 | 50,000 |
| 71–80 | 100,000 |
| 81–90 | 150,000 |
| 91–100 | 200,000 |
| 101–110 | 280,000 |
| 111–120 | 305,000 |
| 121–130 | 330,000 |
| 131–140 | 3555,000 |
| 141–150 | 380,000 |
| 151–160 | 405,000 |
| 161–170 | 430,000 |
| 171–180 | 455,000 |
| 181–190 | 480,000 |
| 191–200 | 480,000 (Reference set) |
| 201—210 | 505,000 |
| 211–220 | 530,000 (Reference set) |
| 221–230 | 580,000 |

Table 8.2: Test sets and cycles for the outlier analysis.

Figures 8.12 and 8.13 illustrate the OA results and the PCA results for the selected features for propagation path 1. The OA figures have the same scale in the y-axis for comparison purposes. It needs to be reminded at this point that the Mahalanobis

squared-distance represents in this case the damage index which shows how much the monitored system has deviated from the normal condition and from a pre-assigned statistical threshold.

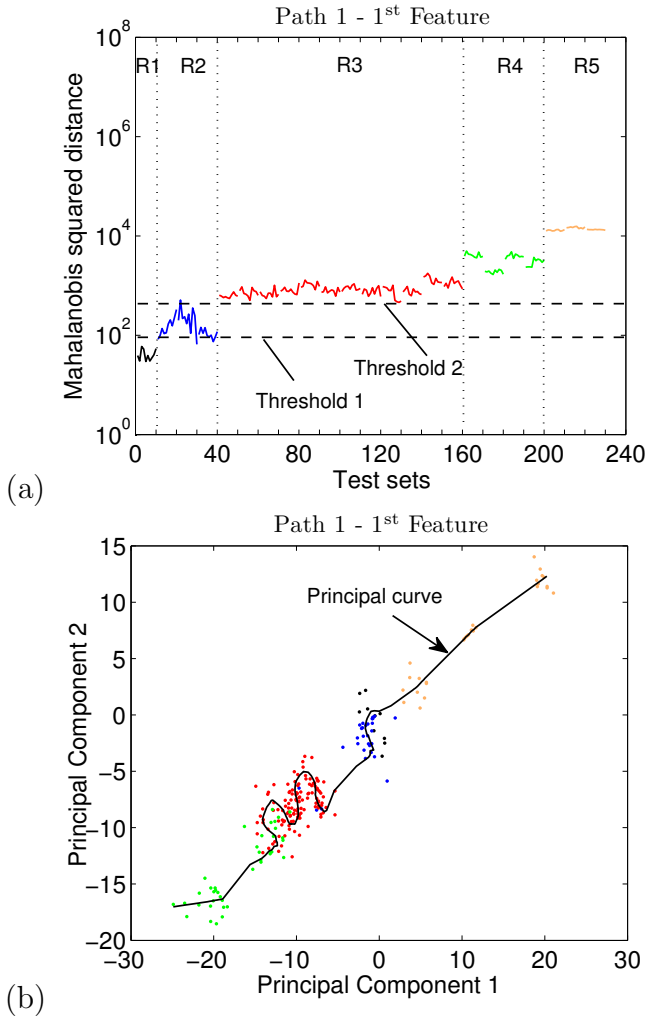


Figure 8.12: Outlier analysis (a) and principal component analysis (b) for path 1 - 1st feature.

Five areas can be distinguished based on the level of deviation from the assigned threshold (Threshold 1), noted in the figure as R1 (1st region), R2 (2nd region), R3 (3rd region), R4 (4th region) and R5 (5th region), each region corresponding to a different colour. The same colours have been assigned to the corresponding clusters in the PCA figures. 1st and 2nd regions (from 0 to 15,000 cycles) are for both features very close to the threshold, while the deviation from the normal condition is not significant. However, the 2nd region is flagged as outlier (e.g. above the threshold). At this stage, the stabilizer was loaded for just 15,000 cycles at low loads. Given the testing conditions and the little deviation of the region from the threshold, it

was assumed that no critical damage could have occurred at this stage. Nevertheless, something in the structure changed, leading to the change of the boundary conditions. An assumption of the possible reason for this behaviour is the increase in the temperature of the stabilizer after a few loading cycles, or micro-cracks at the adhesive of the transducers as soon as the testing started. These small changes could be sufficient for the observed behaviour, without necessarily notifying about

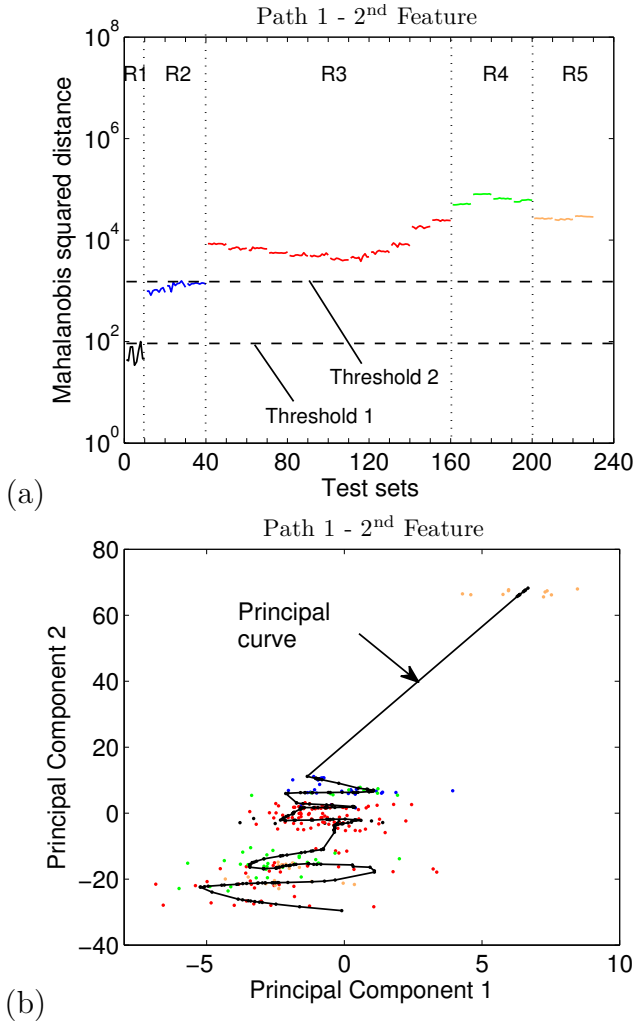


Figure 8.13: Outlier analysis (a) and principal component analysis (b) for path 1 - 2nd feature.

a critical damage. Therefore a second threshold was defined (Threshold 2). For the estimation of this threshold, the data set of the 2nd region (R2) was divided in two subsets, in the following way; Subset 1: 11-25 test sets, Subset 2: 26-40 test sets. Then the maximum value of the estimated Mahalanobis squared-distance was denoted as the threshold value for each subset. Then the final threshold 2 was estimated by taking the mean of the two aforementioned values. This method can be

expressed by:

$$\text{Threshold}\,2 = \frac{\max(\text{MSD}_{\text{Subset2}}) + \max(\text{MSD}_{\text{Subset1}})}{2} \tag{8.1}$$

where Subset 1=11–25 test sets and Subset 2=26–40 test sets and MSD is the Mahalanobis squared-distance. The test sets are summarised in Table 8.2.

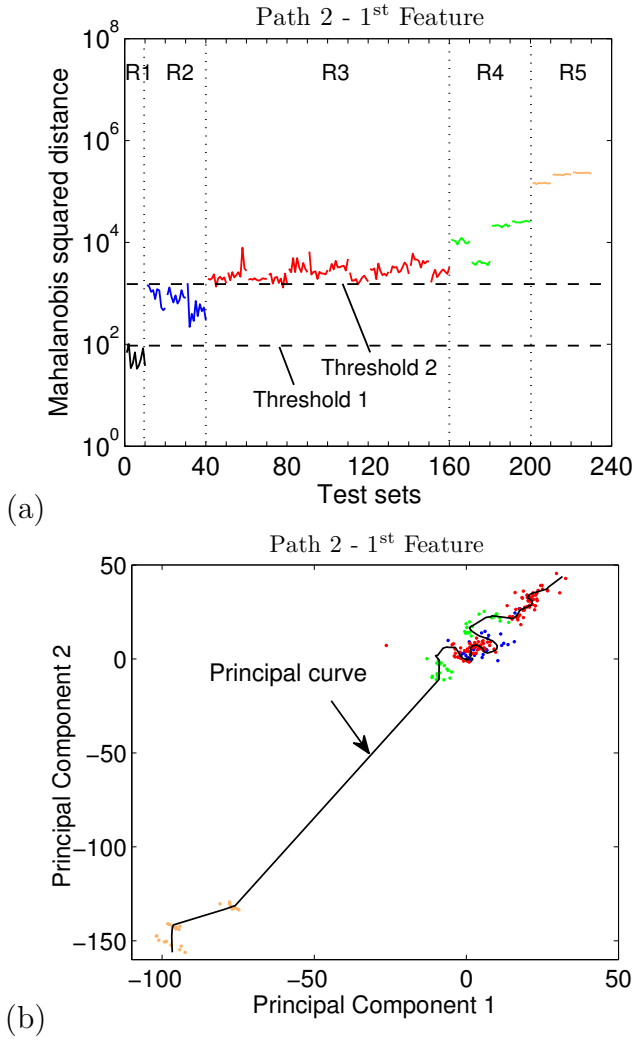


Figure 8.14: Outlier analysis (a) and principal component analysis (b) for path 2 - 1st feature.

Threshold 2 could not be estimated through the Monte Carlo technique since the data sets that correspond to this stage no longer follow a Gaussian distribution. Both thresholds have been plotted at all subsequent figures, in an attempt to demonstrate the monitored system's behaviour in a more representative way. It is worth mentioning though, that threshold 2 required a prior knowledge of the system's status, while

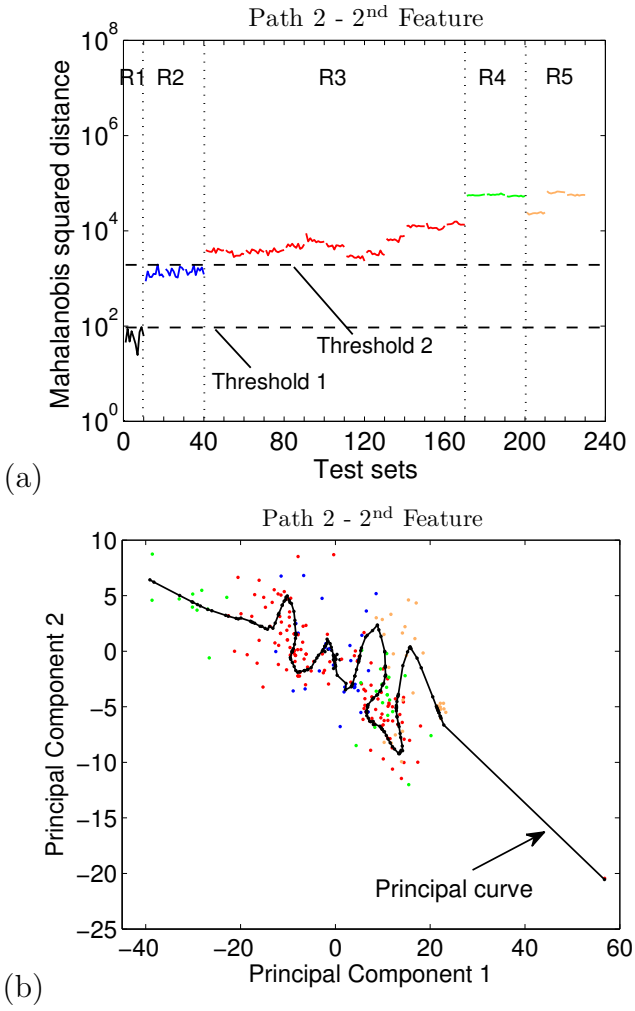


Figure 8.15: Outlier analysis (a) and principal component analysis (b) for path 2 - 2nd feature.

threshold 1 was estimated without any prior knowledge of the system's behaviour. This approach is a simple way to overcome what has been previously described. According to Tarassenko [120], in cases of on-line learning, it is important to enable the algorithm to adapt to novel data instead of simply converging to a stable model, in order to account for complex cases such as the one discussed here. This by itself is a case that needs to be further studied for future applications.

The 3rd region (15,000– 405,000 cycles) is only slightly flagged above the thresholds but without any considerable deviation. However, there is a certain increasing tendency which suggests that damage has started accumulating in the monitored area (path 1). The 4th region (405,000 – 480,000 cycles) shows a higher deviation from the thresholds than the 3rd region while the 5th region (480,000–580,000 cycles)

clearly corresponds to a stage where significant damage has developed. Feature 1 which corresponds to the part of the waveform that has been captured by the sensor without interacting with any other features/boundaries, shows more distinctive differences than feature 2. However feature 2 exhibits higher values of deviation from the two thresholds (areas R3–R5).

PCA results show how well the clusters that correspond to each region separate when they are projected on the baseline reference set. The first feature which is shown in Figure 8.12(b) exhibits a quite clear separation between the clusters, indicating the successful assignment of the regions in the OA, and verifying the deviation of the behaviour of the monitored system from the normal condition. For the second feature, even though there is a certain separation of the orange dots (R5 - $5^{th}$ region) from the rest of the clusters, in general the technique does not provide the resolution of the OA.

Figures 8.14 and 8.15 illustrate the same results but for path 2. The y-axis is scaled in the same way as for path 1 for comparison purposes. The first observation is that the same regions can be assigned in the OA figures, which indicate the level of deviation from the normal condition and from the assigned thresholds. One difference is that the $4^{th}$ (R4) region starts one set of data later (e.g. 170 test sets) for the $2^{nd}$ feature compared to the $1^{st}$ feature for the same path and both features for path 1. Furthermore, PCA exhibits quite mixed clusters, from which only the area R5 can be separated for the $1^{st}$ feature.

A comparison between the two paths shows that, their behaviour is in general similar. The area R3 is the one which mostly draws the attention, since it is the one which shows a certain deviation from the normal condition. The key requirement here is the identification of the damage sensitivity of each path with respect to an early stage damage onset detection, namely area R3. The OA for path 1 and path 2 exhibits similar results except for the $2^{nd}$ feature, which shows significantly higher levels of deviation for path 1. In addition, PCA shows a more distinctive separation between the resulting clusters for the $1^{st}$ feature of path 1 compared to the same feature for path 2. Even though this is not very clear at this stage, one could in general conclude that Path 1 exhibits a relatively higher damage sensitivity, especially at the area where the first notable damage seems to develop (e.g. R3). This observation is important since it will later verify the agreement of the tested analysis tools with the results obtained from thermography, in terms of early stage damage initiation.

In addition, the proposed technique of the principal curves based on the NLPCA is performed here, the results of which can be found in the respective figure of the PCA results (Figure 8.12– Figure 8.15). As illustrated, after 10 iterations, the principal curve fits very successfully the principal component clusters, starting from the first principal component and iteratively bending to match the required shape. The arc length of the curve is not plotted for this case study but it can be observed from the principal curves, that for all cases it would successfully describe the deviation of the clusters above 480,000 cycles from the rest which appear to be very close to each other. The same conclusion can not be derived for path 2 ($2^{nd}$ feature, Figure 8.15) where the clusters are quite mixed without a substantial separation.

### 8.3.2 Outlier analysis at the principal components

In the current section an alternative approach is attempted to assess the structural integrity of the tail stabilizer which has been previously discussed in Chapter 7. This approach focuses on the OA of the principal components that are derived from the principal component analysis. The number of the selected principal components is selected based on the drop of variance. In this case, the first 10 principal components for all steps were considered to be adequate since they accounted for approximately 80 % of the total variance of the set with some slight differences for each path/feature.

In the same way as with OA, the first 90 observations of the pristine condition were used as a training set while the rest were used for validation of the algorithm. The 1 % exclusive threshold value for novelty for a 100-observation, 10-dimensional problem was estimated after 1,000 trials which was found to be approximately the same for all paths (Threshold 1). As previously explained in Section 8.3, the Threshold 2 was defined in a similar way.

Figures 8.16(a) and 8.16(b) illustrate the variance drop that resulted from the linear PCA for propagation path 1 and for both considered features. It was decided that the first 10 principal components accurately represent the higher percentage of the data variance. Therefore they were selected for the subsequent outlier analysis. The $1^{st}$ feature shows that the results are more representative of the assumption made for the OA on the raw signals; it verifies that area R2 is not indicative of damage. This means that the $1^{st}$ (R1) and $2^{nd}$ (R2) regions are indeed labelled as inliers

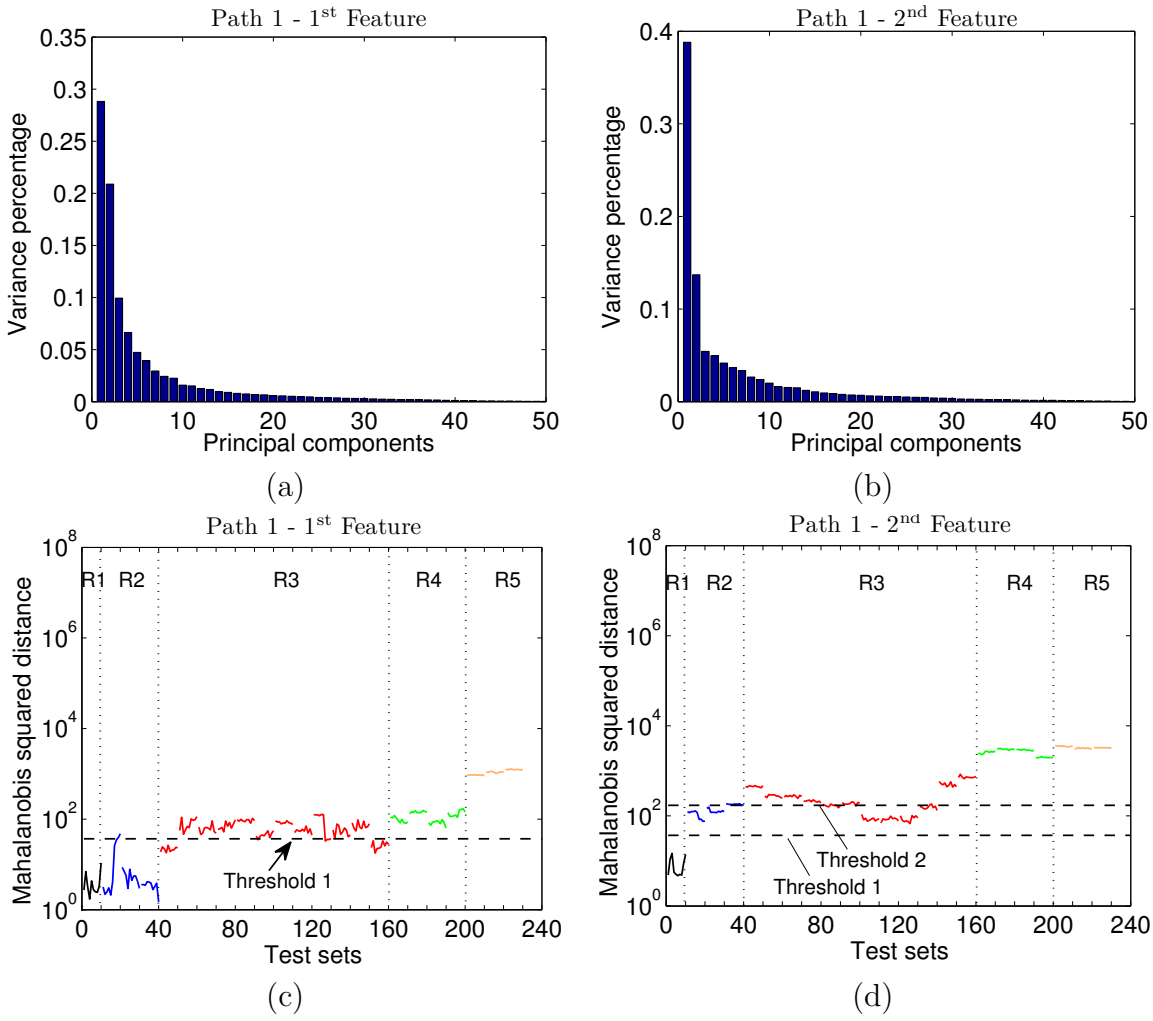


Figure 8.16: Variance drop (a), (b) and outlier analysis at the first 10 principal components (c), (d) for path 1, corresponding to 1st and 2nd features.

(below the Threshold 1) while the 3rd region (R3) is very close to the threshold only slightly flagged above it without any considerable variation. In this case there was no need to assign Threshold 2. It is only after 480,000 cycles that OA gives clear outliers (R4 and R5). On the other hand, the 2nd feature illustrates a slightly different behaviour, almost similar to the OA of the respective path/feature for the raw signals although the values of the deviation are smaller due to the change in the number of the dimensions of the feature (10-dimensional instead of 50-dimensional).

Figure 8.17 illustrates the same results for propagation path 2. The 1st feature exhibits a similar behaviour for the same feature of path 1 in Figure 8.16, exhibiting lower deviation from the normal condition and the thresholds than what the respective raw signal showed. In addition, 1st (R1) and 2nd (R2) regions are below

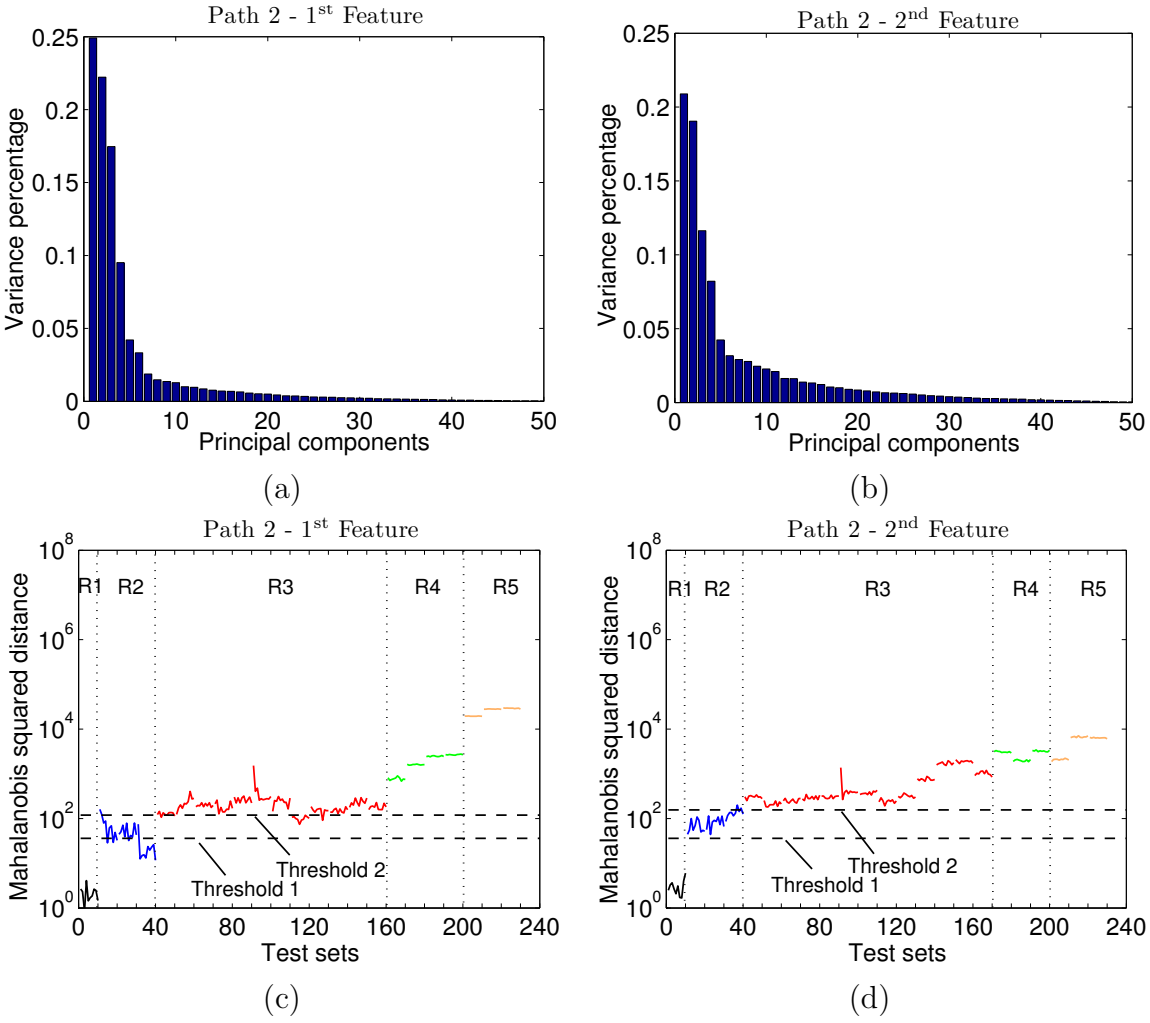


Figure 8.17: Variance drop (a), (b) and outlier analysis at the first 10 principal components (c), (d) for path 2, corresponding to 1st and 2nd features.

the threshold 1 and threshold 2 respectively, while the 3rd region (R3) is very close to threshold 2, exhibiting a relatively steady behaviour. In a similar way as with propagation path 1, R4 and R5 (above 480,000 cycles) are clearly flagged as outliers while the boundaries between the two regions are quite distinctive. On the other hand the 2nd feature exhibits a similar behaviour with the feature taken from the raw signal, without any underlying difference. The main assumption derived here is that at least the 1st feature for both paths shows an improved behaviour and represents in a more reasonable way the structural integrity of the stabilizer. This is attributed to the fact that among the whole tested data set, only the main principal components were taken into consideration, which account for the highest percentage of the variance, hence carrying most of the vital information needed, while leaving out any other parameters that could have corrupted the signals, such as noise.

## 8.4 Validation with thermography

The main objective of the current study was the verification of the relatively new monitoring technique (Lamb waves) which has not been extensively established yet with the better established lock-in thermography [121]. Therefore, on-line lock-in thermography was employed for the monitoring of patch debonding. A Jade 510 (Cedip) MWIR infrared camera was used. The camera was appropriately fixed on a stand facing perpendicularly the top (repaired) surface of the tail stabilizer after the monitored area was sprayed with black paint. Figure 8.18 illustrates the results obtained at representative loads (25, 405, 480 and 561 kcycles) while the Lamb wave propagation paths 1 and 2 are marked on the figures for illustration purposes with white arrows. Amplitude images represent the recorded temperature difference on the structure, on a pixel-by-pixel basis as depicted by the colourbars aside the images. The deterioration of the patch is reflected by the colour change on the particular images.

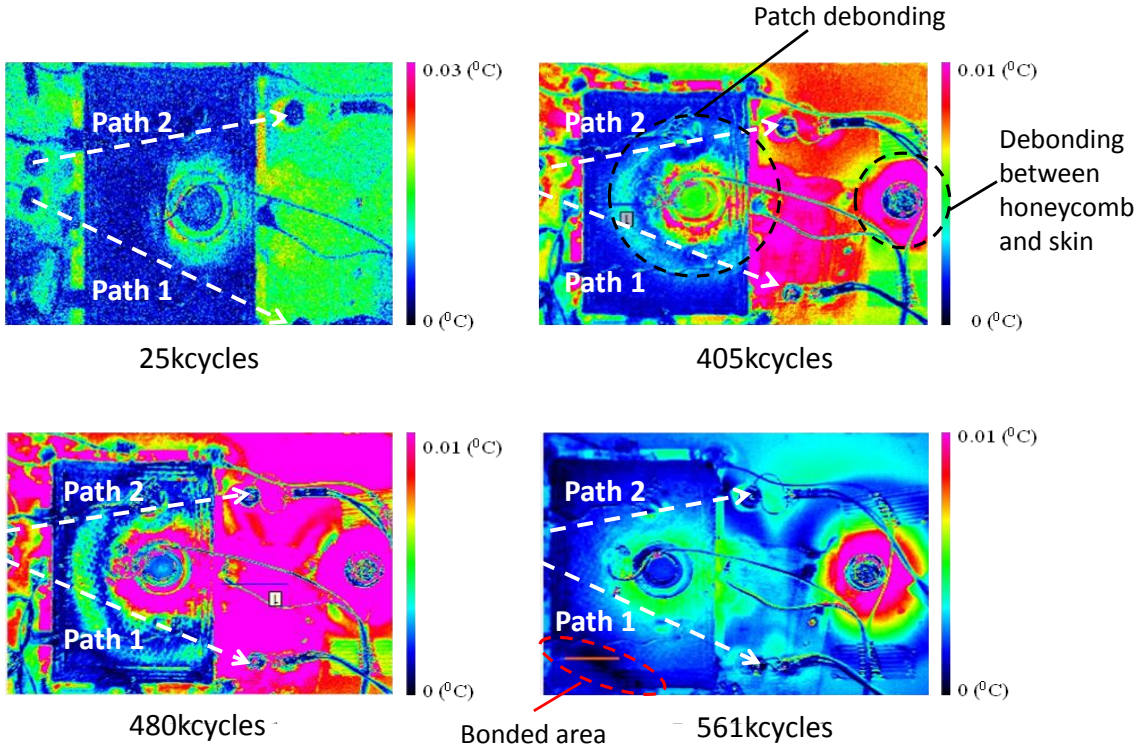


Figure 8.18: Amplitude images obtained from lock-in thermography at representative loading cycles. [122]

The debonding area initiated around the rivet and started developing around it, until it reached a stage at which only a small area maintained bonding at 561,000

cycles (Figure 8.18). The assigned areas (R1, R2, R3, R4 and R5) show a considerable consistency with the captured damage by the IR camera. Areas R1 and R2 clearly exhibit slight damage (below the assigned thresholds) and only after 25,000 cycles (R3) more significant damage started occurring around the hole accumulating throughout the loading steps until 405,000 cycles (end of R3, beginning of R4) where damage is extensive. At this stage it is clear that propagation path 1 is exhibiting higher deviation from the normal condition since the damage developed at the area covered by the respective propagation path (see Figure 8.18) is slightly higher than the respective one developed at the side of path 2. Finally at 561,000 cycles where R4 region ends the final debonding of the patch is illustrated, a level at which only a small area was maintained bonded. The results show a good agreement between the estimation of the presence and approximate location of damage performed through the Lamb waves and the images obtained with the IR thermocamera. In addition the location of the piezoelectric transducers proved to be correct since it enabled a relatively easy analysis with respect to the area of the developed damage. It needs to be highlighted though, that the images obtained from thermography, indicate that debonding between the honeycomb and skin was present, as verified by the stress concentrations observed around the rivet outside the repaired area and in between the two rivets. The internal core of the stabilizer was detached from the aluminium skin as a result of the fatigue testing, at locations that coincided with the bolted joints. However, the thermography results can distinguish between the effect of the patch debonding and the core detachments, since at loads where complete debonding took place (e.g. 561 kcycles), the stress distributions at the repaired area drop due to stress relaxation, but they increase around the other bolted joint.

Overall testing with Lamb waves proved to be an efficient technique which successfully captured the initiation and the extent of the developed damage through pattern recognition and data dimensional reduction analysis. Moreover the appropriate definition of features, that exploited certain parts of the waveform (wave packets), provided some useful information about the possible location of the damage. In addition the analysis only employed four PZTs which are cheap, light and easy to implement; the data acquisition was performed with very basic equipment and the data processing was implemented with fast and computationally efficient algorithms. These features on top of the efficiency of the technique prove the promising potentials that emerge for on-line monitoring with Lamb waves in aerospace industry. The potential effect of noise was minimised through the acquisition of 512 averages for each set of signals. In addition, the effect of temperature and other environmental

conditions was monitored through the acquisition of extra baseline reference sets throughout the test, every time the test had to stop for a considerable time period (e.g. overnight). It is worth noticing though that the characterisation of the type of damage is not possible at this stage of analysis, hence the proposed methods aim only to identify the presence of damage, while the study of the effect of each type (e.g. patch debonding or skin debonding) can be far more complicated.

## 8.5 Discussion

An aluminium helicopter tail stabilizer with an artificially introduced through-thickness crack was tested under bending fatigue. The crack was repaired with a composite patch cured with a heating blanket. The demonstrator was monitored with lock-in thermography and Lamb waves. Four PZTs were surface-bonded on the aluminium stabilizer at appropriate locations close to the patch, forming two propagation paths. Appropriate features were selected which enabled the characterisation of different part of the signals. OA and PCA were performed on the selected features for all paths. The results indicate that debonding of the patch started developing after 15,000 cycles probably in the form of resin micro cracks at the adhesive which steadily accumulated, yet no significant degradation of the structural integrity of the repaired region is observed until after 405,000 cycles. At this stage significant deviation of the system is observed which further increased until the end of the test, suggesting that extensive debonding of the patch took place. It needs to be noted though that the technique cannot distinguish between debonding of the patch and the detachment between the skin and honeycomb of the stabilizer. However, the selected features indicate that damage started propagating at the centre of each monitored area that is separated by the two paths. This suggested that the first damage occurred was debonding of the patch at the centre. In addition, comparison between the two paths showed more distinctive damage indices captured from path 1 at a level that corresponded to an early stage of damage initiation, which is an indication that the most severe damage occurred at that region. Lock-in thermography verified the aforementioned results.

# Chapter 9

# Summary and Conclusions

## 9.1 Thesis summary

The growing demand for new repair methodologies in aircraft industry, and the need for a built-in monitoring system which will enable the continuous assessment of the repaired regions, were the main motivations of the current thesis. The investigation of new repair approaches which would replace the conventional mechanical fasteners and which would exhibit high performance under critical loads with the least intrusive effect, led to the proposal of the adhesively bonded repairs. This repair method shows considerable potential due to the high performance, to its low weight, and to the flexibility in terms of shape and stiffness requirements. The risks associated with premature failure due to critical mechanical and thermal loads, highlighted the key requirement for continuous monitoring through a robust structural health monitoring system. This will eventually help towards an industrial approval. These points are explained in detail in Chapter 1.

Previous work on the nondestructive testing of such complex structures, has utilised conventional off-line methods which show little success towards the proposal of a built-in on-line monitoring scenario, while a number of the more recent structural health monitoring techniques that have been explored in the past, deal primarily with simple geometries and damage configurations. This work, aims to overcome some of the aforementioned limitation, by exploring different damage prognostic approaches for the monitoring of a variety of panels subjected to representative loads

with guided ultrasonic waves. The basic concept was the benchmarking of these approaches in small-scale configurations, before the scaling-up to real applications in aircraft industry, such as a helicopter tail stabilizer. The understanding of the underlying mechanisms was first performed through the modelling of simple models with finite elements, where the key challenges were identified. The current work was performed within the framework of the EU project which provided the funding to the author of the thesis, the EU 7$^{th}$ Framework Programme (ACP8-GA-2009-234333), IAPETUS (innovative repair of aerospace structures with curing optimization & life cycle monitoring abilities).

## 9.2 Conclusions

### Chapter 2 - Bonded repairs

In Chapter 2, an introduction to the background concerning design and structural integrity monitoring aspects of the composite adhesively patch repairs was presented. Two are the most commercially applicable types, the external patch repairs and the scarf patch repairs. Their main design characteristics and procedures were discussed for each of them, and the most notable work conducted in the area was presented. The selection criteria of the repair type lies in the design features that will match the required stiffness, weight, shape, out of mould thickness and ease of application. The risks that make the continuous monitoring of their structural integrity necessary were also outlined, supported by the relevant literature review. The most recent approach is on-line monitoring with built-in diagnostics which is expected to help towards an industrial approval and certification.

### Chapter 3 - Ultrasonic waves

In Chapter 3, the area of the employed structural health monitoring is thoroughly investigated. The propagation of ultrasonic waves has emerged as a powerful tool for several applications in a number of research fields. An introduction to the theory of wave propagation in solids, isotropic and anisotropic, is outlined. The chapter first presents the propagation of bulk waves in elastic solids, advancing with the fundamental principals of the propagation of Lamb waves in isotropic and anisotropic

plates. The characteristic equations and relevant examples are given where applicable. Significant aspects associated with the Lamb waves were demonstrated, such as the concepts of dispersion, cut-off frequencies, propagation modes, generation and detection strategies and numerical modelling techniques. Extra attention was given to the application of the Lamb waves on nondestructive studies, highlighting the benefits as well as the challenges. A relevant literature review was given based on the most representative work that has been conducted in the area.

**Chapter 4 - Signal processing techniques**

Chapter 4 demonstrated the signal processing techniques that are explored in this thesis. These techniques fall into the category of pattern recognition, dimension reduction analysis for high-dimensional, multivariate data and time-frequency analysis for nonstationary signals. Extra focus was given on the outlier analysis, linear and nonlinear principal component analysis, the Hilbert transform and the Hilbert-Huang transform. Some mathematical supporting material was presented as well as simple examples that demonstrate the applicability of the aforementioned tools on representative sets of data. The selection of the techniques was performed on the basis of novelty and damage prognostics potential. The main objective of the work was the utilisation of these techniques in order to process the obtained ultrasonic waves and attribute the processed featured to the structural integrity state of the monitored system with a certain level of confidence. Outlier analysis has been used so far for simple idealised damage detection case studies when there was an *a priori* knowledge of damage. Principal component analysis is a well established method leading to nonlinear principal component analysis which as an advanced method, has not been systematically established yet for damage detection purposes. In addition, the Hilbert-Huang transform exhibits certain advantages over the more traditional time-frequency approaches since it is an adaptive method with no need for an *a priori* defined basis.

**Chapter 5 - Time-frequency analysis of Lamb waves for feature selection**

Chapter 5 presents a time-frequency application of Lamb wave propagation on a simple system; an aluminium flat plate repaired with an aluminium one-sided external patch subjected to tension-tension fatigue loads. The selection of this system

was based on the low level of complexity in the developed failure modes compared to the composite repaired configurations. Lamb waves were excited by surface-bonded piezoelectric transducers, and the instantaneous properties of the obtained signals were further processed. The resulting instantaneous frequency exhibited considerable noisy areas due to the magnification of noise that is the effect of the differentiation of the instantaneous phase prior to the estimation of the instantaneous frequency. The EEMD was then used in order to decompose the obtained signals and clean up the observed artefacts. The EEMD in this study operated as a filtering method which removed most of the undesirable noise but not completely. This manipulation enabled the isolation of certain parts of the captured Lamb waves that were further assessed with a simple damage index. The developed damage showed a good consistency with the employed damage index, enabling the association of the wave propagation paths that were affected by damage with respective defined features that exhibited higher damage index sensitivity. In addition, a single degree of freedom system was modelled with different levels of damping, hence representing different levels of damage. This showed that the peak-to-peak amplitude of the instantaneous frequency is possibly increasing with respect to the increasing damping (e.g. increasing level of damage). This phenomenon agreed with the observed experimental behaviour. Despite the potentials of the analysis described in the chapter, there are several limitation factors that led the author to reconsider the applicability of the techniques on more complex parts of the future work. Such limitations primarily involve the few monitoring points and the limited features that could be isolated from the recorded Lamb waves, the lack of physical meaning of the resulting indices and the lack of understanding of the effect of the boundaries on the developed indices (e.g. patch). Parts of this work appear in [123], [124], [101].

**Chapter 6 - Numerical analysis of Lamb wave propagation**

In Chapter 6, a finite element model built with ABAQUS was developed in order to investigate the physics of the wave propagation mechanisms that take place in composite repaired structures. 3D solid elements were utilised to model a cross-ply carbon reinforced polymer-based laminate repaired with a one-sided external patch made out of the same material and with the same ply orientation. In addition, two configurations were considered for the repaired plate (e.g. with and without a hole). Different damage scenarios were employed, namely the debonding of the patch at representative locations, the degradation of the substrate and the simulta-

neous effect of both. The first antisymmetric mode ($A_0$ mode) was excited by means of point force excitation in pulse-echo and pitch-catch modes following an explicit analysis. A theoretical verification and an experimental validation were conducted which proved the efficiency of the built model. The experimental excitation of the $A_0$ mode was successfully performed at low frequencies through the approach of mode tuning. The objective of the current chapter was the investigation of the physics of the wave propagation mechanisms that take place in composite repaired structures and the analysis of the effect of the developed damage in order to evaluate the efficiency and applicability of the physics-based processing approaches. The study concludes on the complex phenomena in terms of wave interpretation that follow the design characteristics of the repaired structures, such as the extra thickness of the patch and the hole underneath it, which will lead to multiple mode conversions. The pitch-catch mode exhibits a higher damage sensitivity compared to the pulse-echo mode, with the second leading to considerable wave attenuation due to the multiple reflections that occur at the waves before they propagate through the repaired region. The study highlights that in real applications these phenomena are not straightforward since these mechanisms can be far more complicated with the presence of extra features such as rivets or stringers, hence underlying the existing challenges in the physics-based evaluation approaches.

**Chapter 7 - Damage detection in composite repaired structures**

In Chapter 7, two representative small-scale composite structures repaired with adhesively bonded repairs were tested under representative loads. The objective was the demonstration of different concepts towards the realisation of a damage prognosis strategy along with the identification of the level of success and the potential limitations for each of them. The chapter employed Lamb waves monitoring together with alternative nondestructive techniques in order to verify the observed phenomena. More specifically, a scarf repair patch was implemented on an impacted composite laminate and it was tested under tension and monitored with Lamb waves and on-line digital image correlation. The recorded Lamb waves were treated as multivariate data and further assessed by means of outlier analysis and principal component analysis (linear and nonlinear) after the appropriate feature selection. The principal curves were proposed as a novel damage prognosis tool through whose fitting, the damage mapping of a relatively complex system was possible with just a one-dimensional curve. The study investigated the level of success of the employed

methods through a comparative manner and managed to identify potential limitation that are associated with extreme damage loading scenarios. The effect of noise was also explored in order to locate potential effects, proving that outlier analysis can successfully detect damage even under extremely noisy conditions. All methods exhibited a considerable agreement with the results obtained from the digital image correlation, successfully validating the extent of the damage. The only limitation of the principal curves lies in the difficulty in assigning a certain initiation and finishing point or in assigning a certain fitting path.

In addition, a composite external repair patch was used to repair a composite laminate and it was further tested under tension-tension fatigue. The panel was monitored with Lamb waves while X-rays radiography and microscopic analysis were used in order to assess the internally developed damage at 95 % of the panel's ultimate strength, a step at which the panel failed. The excitation of the first antisymmetric ($A_0$) and symmetric ($S_0$) modes was attempted through the out-of-phase and in-phase operation of two surface-bonded piezoelectric transducers respectively, attached at the bottom and the top surface of the monitored panel. The estimation of the theoretical dispersion curves enabled the validation of the excitation approach, verifying the excitation of the $A_0$ mode only. The estimation of the experimental group velocity was performed through the application of the Akaike information criterion, as a more reliable way of tracking the onset time of ultrasonic waves. This mode was further processed in order to deal with the problem of inadequate training data through a pseudoinverse approach for the inverse of the covariance matrix. The reduction of the dimensions of the obtained data was proposed through the isolation of the most representative principal components, estimated through the principal component analysis. This allowed the application of the outlier analysis in a successful manner in what appeared to be a complex problem. Parts of this work appear in [125], [126], [127], [128], [129], [10].

**Chapter 8 - Monitoring of a repaired helicopter tail stabilizer**

The final chapter of the work, Chapter 8, aimed to scale up the tested configuration and to examine the applicability and efficiency of the aforementioned techniques in a helicopter structure. The demonstrator is an aluminium helicopter tail stabilizer loaded under bending fatigue. An artificially introduced crack was repaired with a composite one-sided external patch after the critical location was identified.

The demonstrator was monitored with Lamb waves and lock-in thermography. The two fundamental modes ($A_0$ and $S_0$) were excited with piezoelectric transducers surface-bonded at appropriate locations on the aluminium stabilizer, forming two propagation paths in such a way that the most critical areas of the repaired region would be covered. Appropriate features were selected which enabled the characterisation of different part of the signals. Outlier and principal component analysis were conducted in order to identify the number of cycles where damage started developing in the form of patch debonding and honeycomb detachment from the skin. Both methods proved damage sensitive, enabling a relatively good characterisation of the deviation of the monitored system from the captured baseline reference at each wave propagation path. In particular, for the outlier analysis technique, the assignment of a second threshold apart from the Monte Carlo was performed, in order to account for the irregularities introduced to a number of factors that could affect the obtained data at early normal or near-normal condition stages and potentially lead to false alarms. The observed results were further correlated with the images obtained from thermography with a remarkable agreement. However, the technique cannot distinguish between debonding of the patch and the detachment between the skin and honeycomb of the stabilizer. The principal curves were further fitted on the selected features and the reduction of the dimensions prior to the outlier analysis was possible through the isolation of appropriate principal components.

## 9.3 Contribution to knowledge

- The concept of adhesively bonded repairs has been proposed and tested for its structural and design advantages by many researchers before. However little effort has been made to investigate the damage prognostic potentials that would emerge from a structural health monitoring strategy. The thesis explored the applicability of Lamb waves for the continuous monitoring of the repaired area aiming to develop a concept that can accurately identify the initiation and growth of internal damage.

- Different repair types were tested under real testing conditions (e.g. external repair patches and scarf repair patches), which were manufactured following standard procedures used by airline companies. The testing employed different configurations, including scaled repairs to large-scale demonstrators such as

a helicopter vertical tail stabilizer. This secured that the proposed damage prognosis tools will be demonstrated under representative conditions on real structures as met in aircraft industry.

- A variety of alternative nondestructive techniques was used in order to fully support the monitoring results of the current thesis such as digital image correlation, lock-in thermography, X-ray radiography. In all cases Lamb wave monitoring proved to be consistent with the alternative techniques while its portability and cost efficiency were highlighted.

- An FE model aimed to explain the physical phenomena that take place during the propagation of Lamb waves through repaired composite panels with different types of pre-introduced damage. This step enabled a good understanding of the underlying mechanisms on how each type of damage affects the propagating waves. The realisation of the optimum excitation approach was performed (e.g. pitch-catch), and the limitations of a potential physics-based approach to the problem investigated in the current thesis were explored. This step was considered crucial since it sets a realistic basis also on future work that might aim to deal with similar problems on a physics-based approach.

- The study of the instantaneous properties of the Lamb waves along with the Hilbert-Huang transform was performed on a repaired aluminium configuration. Even though these tools have been widely explored in the past as a time-frequency approach to damage detection problems, little effort has been made on understanding the physics of the mechanisms. Although the Hilbert-Huang transform is an attractive tool due to its adaptive nature, the current thesis attempted to show the limitations in a potential use with Lamb waves due to the lack of sufficient theoretical background.

- The outlier analysis was successfully applied for damage detection, which accurately identified the initiation and propagation of damage for the tested configurations. The effect of noise was tested which showed that outlier analysis can detect damage even under extremely noisy environments. Along with the principal component analysis which is a well established technique, the possibility of the drop in the Mahalanobis squared-distance was explored although damage propagated. This phenomenon was attributed to the extreme deviation of the monitored system from the baseline reference which was pictured in the two-dimensional space captured from the principal component

analysis.

- The concept of nonlinear principal component analysis was utilised in order to extract the principal curves as a potential damage prognosis tool. These were further applied on the estimated clusters of the linear principal component analysis. The proposed approach is based on the interpretation of the variation of the arc length of the curves with respect to the loads. The motivation of this proposal lay in the attempt to reduce the dimensionality of the multivariate data sets and depict the structural integrity of a complex system with simply a curve.

- Two proposed ideas for the excitation of the two fundamental Lamb wave modes ($A_0$ and $S_0$) were experimentally validated. More specifically, the modes tuning that was initially proposed by Giurgiutiu [112] was validated on a unidirectional carbon fibre laminate for the validation of the finite element model. The $A_0$ mode was successfully excited at low frequencies (e.g. below 30 kHz). Additionally, the excitation of both $A_0$ and $S_0$ modes was explored through the exploitation of the polarity of piezoelectric transducers attached at the top and bottom surface of a woven carbon fibre laminate (external repair patch). The excitation of the $A_0$ mode was successful while the excitation of the $S_0$ mode was corrupted possibly due to the coupled shear horizontal mode.

- The problem of inadequate training data for the outlier analysis was studied for the experimental investigation of the external repair patch and two methods were explored in order to overcome the problem. The one was based on the pseudoinverse approach for the inverse of the covariance matrix. The second was based on the reduction of the dimensions of the obtained data through the isolation of the most representative principal components, estimated through the principal component analysis.

- The use of Akaike information criterion was employed in order to estimate the onset time of the recorded Lamb waves for the damage detection of the external repair patch, in order to accurately estimate the experimental group velocity. This method aimed to overcome the problem of identifying the arrival time under noisy conditions, which was successfully demonstrated.

## 9.4 Recommendations for future work

The future work could be divided into three main categories following the main areas this thesis deals with, namely the numerical modelling, the signal processing and the experimental testing.

### Numerical modelling

Future work could potentially explore how the different design parameters of the repairs can affect the propagation mechanisms such as different shapes, ply orientation, double-sided external repairs and scarf repairs. Additionally, more work could be carried out on optimising the excitation of the Lamb waves by accurately modelling the piezoelectric transducers through the use of sub-routines in ABAQUS, in order to better approximate the experimental conditions. Towards that direction, the meshing approach could also be investigated, in order to better represent the shape of the hole under the patch. Extra cases can be taken into consideration, such as repaired cracks that further propagate under the patch, a case that was experimentally tested for the stabilizer. With respect to the model's validation, the identification of those features that affect the accuracy can be made, such as the mode tuning with the piezoelectric transducers. Moreover, the phenomenon of mode conversion at the boundaries of the repair patch could be further examined. All these points could probably enable a better understanding of how a physics-based approach could be exploited for the damage detection and location on composite repaired structures.

### Signal processing

First of all, the optimisation of the principal curves code could be conducted in order to account for cases where the arc length does not connect data sets with increasing order of damage. This would provide extra confidence with respect to the use of this proposal as a damage prognosis tool. Furthermore, the training approach for the outlier analysis, could be modified in such a way that it would take into consideration data sets that come from the normal condition, and which do not follow a Gaussian distribution. This case was met in the analysis of the stabilizer, where a second threshold had to be assigned in order to account for the data sets that appeared to have a near-normal condition but no longer followed a Gaussian distribution. In

terms of the time-frequency analysis tools, although the author would not directly suggest the use of the Hilbert-Huang transform for damage detection with Lamb waves, nevertheless a better understanding of the effect of damage on the obtained results could probably improve the applicability of this approach. It should then be further tested in experimental conditions that would consider a large number of testing steps. Analysis on signals obtained from validated finite elements models could be potentially easier, since the conditions would be under control with no noise or interference by any experimental set up. Finally, the training of the presented pattern recognition methods could be attempted with data obtained from a finite element model. In this case a test could determine whether experimental data could be accurately flagged as inliers or outliers. In this case all the complications associated with obtaining a strong baseline reference would be minimised.

**Experimental testing**

Even though the experimental testing conducted within the framework of this thesis is considered to be quite representative, taking into consideration the most common repair types and quite representative loading conditions regularly met in aircraft industry, some further work could potentially be of interest. For instance, different kind of loads could be investigated such as 4-point bending and impact in order to produce more localised and more controllable kinds of damage. Then in this case, the employed damage prognosis strategy could focus on ways to identify the location and the type of the developed damage.

# Bibliography


[1] A. A. Baker, L. F. Rose, and R. Jones, *Advances in the bonded composite repair of metallic aircraft structure*, vol. 1. Elsevier Science, 2003.

[2] J. B. Avram, "Fatigue response of thin stiffened alumminum cracked panels repaired with bonded composite patches," tech. rep., DTIC Document, 2001.

[3] W. Staszewski, C. Boller, and G. Tomlinson, *Health Monitoring of Aerospace Structures: Smart Sensor Technologies and Signal Processing*. Wiley, 2004.

[4] A. Rytter, "Vibration based inspection of civil engineering structures," in *PhD disertation, department of building technology and structural enginnering, Aalborg University*, 1993.

[5] Y. Bar-Cohen, "Emerging NDE Technologies and Challenges at the Beginning of the 3rd Millennium - Part I," *Materials Evaluation*, vol. 58, no. 1, pp. 17–30, 2000.

[6] Y. Bar-Cohen, "Emerging NDE Technologies and Challenges at the Beginning of the 3rd Millennium - Part II," *Materials Evaluation*, vol. 58, no. 2, pp. 141–150, 2000.

[7] J. Liaw, S. Chu, C. Yeh, and M. Kuo, "Analysis of eddy currents in a bar containing an embedded defect," *NDT and E International*, vol. 32, no. 5, pp. 293–303, 1999.

[8] S. Barre and M. Benzeggagh, "On the use of acoustic emission to investigate damage mechanisms in glass-fibre-reinforced polypropylene," *Composites Science and Technology*, vol. 52, no. 3, pp. 369 – 376, 1994.

[9] S. Pavlopoulou, "Non destructive inspection of a repaired aluminium structure with lamb waves," Master's thesis, Mechanical Engineering department, The University of Sheffield, 2009.

[10] M. Caminero, S. Pavlopoulou, M. Lopez-Pedrosa, B. Nicolaisson, C. Pinna, and C. Soutis, "Analysis of adhesively bonded repairs in composites: Damage detection and prognosis," *Composite Structures*, vol. 95, pp. 500 – 517, 2013.

[11] T. Hua, H. Xie, S. Wang, Z. Hu, P. Chen, and Q. Zhang, "Evaluation of the quality of a speckle pattern in the digital image correlation method by mean subset fluctuation," *Optics & Laser Technology*, vol. 43, no. 1, pp. 9 – 13, 2011.

[12] B. Pan, H. Xie, Z. Wang, K. Qian, and Z. Wang, "Study on subset size selection in digital image correlation for speckle patterns," *Opt. Express*, vol. 16, pp. 7037–7048, May 2008.

[13] C. Farrar and K. Worden, "An introduction to structural health monitoring," *Philosophical Transactions of the Royal Society A: Mathematical, Physical and Engineering Sciences*, vol. 365, no. 1851, pp. 303–315, 2007.

[14] D. Adams, *Health Monitoring of Structural Materials and Components: Methods with Applications*. Wiley, 2007.

[15] C. Boller and W. J. Staszewski, *Aircraft Structural Health and Usage Monitoring*, pp. 29–73. John Wiley & Sons, Ltd, 2004.

[16] H. Hosseini-Toudeshky, "Effects of composite patches on fatigue crack propagation of single-side repaired aluminum panels," *Composite Structures*, vol. 76, no. 3, pp. 243 – 251, 2006.

[17] A. A. Baker, "Repair efficiency in fatigue-cracked aluminum components reinforced with boron/epoxy patches," *Fatigue & Fracture of Engineering Materials & Structures*, vol. 16, no. 7, pp. 753–765, 1993.

[18] A. A. Baker and R. Jones, *Bonded repair of aircraft structures*. Martinus-Nijhoff, 1988.

[19] J. Xiong and R. Shenoi, "Integrated experimental screening of bonded composites patch repair schemes to notched aluminum-alloy panels based on static and fatigue strength concepts," *Composite Structures*, vol. 83, no. 3, pp. 266

– 272, 2008.

[20] T. V. Umamaheswar and R. Singh, "Modelling of a patch repair to a thin cracked sheet," *Engineering Fracture Mechanics*, vol. 62, no. 23, pp. 267 – 289, 1999.

[21] F. Hu and C. Soutis, "Strength prediction of patch-repaired cfrp laminates loaded in compression," *Composites Science and Technology*, vol. 60, no. 7, pp. 1103 – 1114, 2000.

[22] L. J. Hart-Smith, "An engineer's viewpoint on design and analysis of aircraft structural joints," *Proceedings of the Institution of Mechanical Engineers, Part G: Journal of Aerospace Engineering*, vol. 209, no. 2, pp. 105–129, 1995.

[23] A. Baker and P. R Jones, *Bonded Repair of Aircraft Structures*. Engineering Applications of Fracture Mechanics, Springer, 1988.

[24] L. Hart-Smith, "Further developments in the design and analysis of adhesive-bonded structural joints," *Joining of Composite Materials, ASTM STP*, vol. 749, pp. 3–31, 1981.

[25] L. Hart-Smith, "An engineer's viewpoint on design and analysis of aircraft structural joints," *Proc. Instn Mech. Engrs, Part G*, vol. 209(G2), pp. 105–129, 1995.

[26] P. Papanikos, K. Tserpes, G. Labeas, and S. Pantelakis, "Progressive damage modelling of bonded composite repairs," *Theoretical and Applied Fracture Mechanics*, vol. 43, no. 2, pp. 189 – 198, 2005.

[27] A. Albedah, B. B. Bouiadjra, R. Mhamdia, F. Benyahia, and M. Es-Saheb, "Comparison between double and single sided bonded composite repair with circular shape," *Materials & Design*, vol. 32, no. 2, pp. 996 – 1000, 2011.

[28] C. Soutis and F. Z. Hu, "Design and performance of bonded patch repairs of composite structures," *Proceedings of the Institution of Mechanical Engineers, Part G: Journal of Aerospace Engineering*, vol. 211, no. 4, pp. 263–271, 1997.

[29] B. Whittingham, A. Baker, A. Harman, and D. Bitton, "Micrographic studies on adhesively bonded scarf repairs to thick composite aircraft structure," *Composites Part A: Applied Science and Manufacturing*, vol. 40, no. 9, pp. 1419 – 1432, 2009.

[30] H. Hosseini-Toudeshky and B. Mohammadi, "Thermal residual stresses effects on fatigue crack growth of repaired panels bounded with various composite materials," *Composite Structures*, vol. 89, no. 2, pp. 216–223, 2009.

[31] S. Pavlopoulou, C. Soutis, and G. Manson, "Non-destructive inspection of adhesively bonded patch repairs using lamb waves," *Plastics, Rubber and Composites*, vol. 41, no. 2, pp. 61–68, 2012.

[32] A. Bulavinov, M. Dalichow, M. Krning, J. Kurz, F. Walte, and K. Reddy, "Quantitative ultrasonic testing of pressurized components using sampling phased array," Proc. National Seminar on Non-Destructive Evaluation, Indian Society for Non-Destructive Testing Hyberabad Chapter, Dec. 7-9 2006.

[33] Y. Koh, N. Rajic, W. Chiu, and S. Galea, "Smart structure for composite repair," *Composite Structures*, vol. 47, no. 14, pp. 745 – 752, 1999.

[34] A. Baker, "Bonded composite repair of fatigue-cracked primary aircraft structure," *Composite Structures*, vol. 47, no. 14, pp. 431 – 443, 1999.

[35] M. Lin, X. Qing, A. Kumar, and S. J. Beard, "Smart layer and smart suitcase for structural health monitoring applications," in *Society of Photo-Optical Instrumentation Engineers (SPIE) Conference Series*, vol. 4332, pp. 98–106, 2001.

[36] R. Jones and S. Galea, "Health monitoring of composite repairs and joints using optical fibres," *Composite Structures*, vol. 58, no. 3, pp. 397 – 403, 2002.

[37] C. Soutis and J. Ihn, "Design, analysis, and shm of bonded composite repair and substructure," *Encyclopedia of Structural Health Monitoring*.

[38] X. P. Qing, S. J. Beard, A. Kumar, and R. Hannum, "A real-time active smart patch system for monitoring the integrity of bonded repair on an aircraft structure," *Smart Materials and Structures*, vol. 15, no. 3, p. N66, 2006.

[39] H. Kolsky, *Stress Waves in Solids*. Dover Phoenix Editions, Dover Publ., 2003.

[40] I. Viktorov, *Rayleigh and Lamb waves: physical theory and applications*. Ultrasonic technology, Plenum Press, 1970.

[41] J. Rose, *Ultrasonic Waves in Solid Media*. Cambridge University Press, v.10, 1999.

[42] J. Achenbach, *Wave Propagation in Elastic Solids*. North-Holland series in applied mathematics and mechanics, v. 16, North-Holland Pub., 1987.

[43] L. P. Solie and B. A. Auld, "Elastic waves in free anisotropic plates," *The Journal of the Acoustical Society of America*, vol. 54, no. 1, pp. 50–65, 1973.

[44] G. Stokes, "Corrected reprint of the smith's prize exam taken by james clerk maxwell at cambridge, feb 1854: Question 8 on stokes' theorem," in *Antennas and Propagation, 2007. EuCAP 2007. The Second European Conference on*, pp. 1 –3, 2007.

[45] K. Graff, *Wave Motion in Elastic Solids*. Dover Books on Engineering Series, Dover Publ., 1975.

[46] Y. Hayashi, H. Suzuki, and T. Kinjo, "Vallen wavelet and dispersion programme," Retrieved in March 2010, http://www.vallen.de/products/software/wavelet.

[47] B. Pavlakovic and M. Lowe, "Disperse," Last visited on 20 Feb. 2013, http://www3.imperial.ac.uk/nde/products

[48] Z. A. B. Ahmad, *Numerical Simulation of Lamb Waves in Plates Using a Semi-Analytical Finite Element Method*. VDI Fortschritt-Berichte Reihe 20 Nr. 437, 2011.

[49] Z. A. B. Ahmad and U. Gabbert, "Simulation of Lamb wave reflections at plate edges using the semi-analytical finite element method," *Ultrasonics*, vol. 52, pp. 815–820, 2012.

[50] Y. Cho, "Estimation of ultrasonic guided wave mode conversion in a plate with thickness variation," *Ultrasonics, Ferroelectrics and Frequency Control, IEEE Transactions on*, vol. 47, pp. 591 –603, may 2000.

[51] D. Alleyne and P. Cawley, "The interaction of lamb waves with defects," *Ultrasonics, Ferroelectrics and Frequency Control, IEEE Transactions on Ultrasonics, Ferroelectrics, and Frequency Control*, vol. 39, pp. 381 –397, may 1992.

[52] Z. Su and L. Ye, *Identification of Damage Using Lamb Waves: From Fundamentals to Applications*. Springer, 2009.

[53] D. N. Alleyne and P. Cawley, "Optimization of lamb wave inspection techniques," *NDT & E International*, vol. 25, no. 1, pp. 11 – 22, 1992.

[54] Z. Guo, J. Achenbach, and S. Krishnaswamy, "Emat generation and laser detection of single lamb wave modes," *Ultrasonics*, vol. 35, no. 6, pp. 423 – 429, 1997.

[55] W. Staszewski, B. Lee, L. Mallet, and F. Scarpa, "Structural health monitoring using scanning laser vibrometry: I. lamb wave sensing," *Smart Materials and Structures*, vol. 13, no. 2, p. 251, 2004.

[56] R. Monkhouse, P. Wilcox, and P. Cawley, "Flexible interdigital pvdf transducers for the generation of lamb waves in structures," *Ultrasonics*, vol. 35, no. 7, pp. 489 – 498, 1997.

[57] J. Fraden, *Handbook of Modern Sensors: Physics, Designs, and Applications*. Springer New York, 2011.

[58] V. Giurgiutiu and A. Zagrai, "Characterization of piezoelectric wafer active sensors," *Journal of Intelligent Material Systems and Structures*, vol. 11, no. 12, pp. 959–976, 2000.

[59] P. Wilcox, M. Lowe, and P. Cawley, "The effect of dispersion on long-range inspection using ultrasonic guided waves," *NDT & E International*, vol. 34, no. 1, pp. 1 – 9, 2001.

[60] S. S. Kessler, S. M. Spearing, and C. Soutis, "Damage detection in composite materials using lamb wave methods," *Smart Materials and Structures*, vol. 11, no. 2, p. 269, 2002.

[61] K. Worden, C. R. Farrar, G. Manson, and G. Park, "The fundamental axioms of structural health monitoring," *Proceedings of the Royal Society A: Mathematical, Physical and Engineering Science*, vol. 463, no. 2082, pp. 1639–1664, 2007.

[62] Y. Lu, L. Ye, Z. Su, and C. Yang, "Quantitative assessment of through-thickness crack size based on lamb wave scattering in aluminium plates," *NDT & E International*, vol. 41, no. 1, pp. 59 – 68, 2008.

[63] M. J. S. Lowe and O. Diligent, "Low-frequency reflection characteristics of the s0 lamb wave from a rectangular notch in a plate," *The Journal of the*

*Acoustical Society of America*, vol. 111, no. 1, pp. 64–74, 2002.

[64] J. Strikwerda, *Finite difference schemes and partial differential equations*. Society for Industrial Mathematics, 2004.

[65] O. Zienkiewicz, R. Taylor, and J. Zhu, *The finite element method: its basis and fundamentals*, vol. 1. Butterworth-Heinemann, 2005.

[66] Y. Cho and J. L. Rose, "A boundary element solution for a mode conversion study on the edge reflection of lamb waves," *The Journal of the Acoustical Society of America*, vol. 99, no. 4, pp. 2097–2109, 1996.

[67] J. Jin, S. T. Quek, and Q. Wang, "Wave boundary element to study lamb wave propagation in plates," *Journal of Sound and Vibration*, vol. 288, no. 12, pp. 195 – 213, 2005.

[68] W. M. Ostachowicz, "Damage detection of structures using spectral finite element method," *Computers & Structures*, vol. 86, no. 35, pp. 454 – 462, 2008.

[69] B. C. Lee and W. J. Staszewski, "Modelling of lamb waves for damage detection in metallic structures: Part i. wave propagation," *Smart Materials and Structures*, vol. 12, no. 5, p. 804, 2003.

[70] P. P. Delsanto and M. Scalerandi, "A spring model for the simulation of the propagation of ultrasonic pulses through imperfect contact interfaces," *The Journal of the Acoustical Society of America*, vol. 104, no. 5, pp. 2584–2591, 1998.

[71] P. Delsanto, A. Gliozzi, M. Hirsekorn, and M. Nobili, "A 2d spring model for the simulation of ultrasonic wave propagation in nonlinear hysteretic media," *Ultrasonics*, vol. 44, no. 3, pp. 279 – 286, 2006.

[72] U. Dassault Systemes Simulia Corp. Providence RI, *ABAQUS Users Manual. 6.10-2.*

[73] P. Fromme and C. Rouge, "Directivity of guided ultrasonic wave scattering at notches and cracks," *Journal of Physics: Conference Series*, vol. 269, no. 1, p. 012018, 2011.

[74] P. Wilcox, "Modeling the excitation of lamb and sh waves by point and line

sources," *AIP Conference Proceedings*, vol. 700, no. 1, pp. 206–213, 2004.

[75] C. Yang, L. Ye, Z. Su, and M. Bannister, "Some aspects of numerical simulation for lamb wave propagation in composite laminates," *Composite Structures*, vol. 75, no. 14, pp. 267 – 275, 2006.

[76] K. Diamanti, C. Soutis, and J. Hodgkinson, "Piezoelectric transducer arrangement for the inspection of large composite structures," *Composites Part A: Applied Science and Manufacturing*, vol. 38, no. 4, pp. 1121 – 1130, 2007.

[77] K. Diamanti, C. Soutis, and J. Hodgkinson, "Non-destructive inspection of sandwich and repaired composite laminated structures," *Composites Science and Technology*, vol. 65, no. 13, pp. 2059 – 2067, 2005.

[78] Y. Koh, W. Chiu, and N. Rajic, "Integrity assessment of composite repair patch using propagating lamb waves," *Composite structures*, vol. 58, no. 3, pp. 363–371, 2002.

[79] K. Worden, G. Manson, and N. R. J. Fieler, "Damage detection using outlier analysis," *Journal of Sound and Vibration*, vol. 229, no. 3, pp. 647 – 667, 2000.

[80] K. Worden, S. G. Pierce, G. Manson, W. R. Philp, W. J. Staszewski, and B. Culshaw, "Detection of defects in composite plates using lamb waves and novelty detection," *International Journal of Systems Science*, vol. 31, no. 11, pp. 1397–1409, 2000.

[81] D. Chetwynd, J. A. Rongong, S. G. Pierce, and K. Worden, "Damage detection in an aluminium plate using outlier analysis," *Fatigue & Fracture of Engineering Materials & Structures*, vol. 31, no. 8, pp. 629–643, 2008.

[82] A. Yan, G. Kerschen, P. D. Boe, and J. Golinval, "Structural damage diagnosis under varying environmental conditions. part i: A linear analysis," *Mechanical Systems and Signal Processing*, vol. 19, no. 4, pp. 847 – 864, 2005.

[83] K. Worden, "Inferential parametrisation using principal curves," *Proceedings of 3rd International Conference on Identification of Engineering Systems, Swansea, UK*, pp. 341–352, 2002.

[84] T. Y. Hsu and C. H. Loh, "Damage detection accommodating nonlinear environmental effects by nonlinear principal component analysis," *Structural Control and Health Monitoring*, vol. 17, no. 3, pp. 338–354, 2010.

[85] T. Hastie and W. Stuetzle, "Principal curves," *Journal of the American Statistical Association*, vol. 84, pp. 502–516, June 1989.

[86] L. Cohen, "Time-frequency distributions-a review," *Proceedings of the IEEE*, vol. 77, pp. 941 –981, jul 1989.

[87] W. Staszewski, "Wavelet based compression and feature selection for vibration analysis," *Journal of sound and vibration*, vol. 211, no. 5, pp. 735–760, 1998.

[88] W. Yang, "Interpretation of mechanical signals using an improved hilbert–huang transform," *Mechanical Systems and Signal Processing*, vol. 22, no. 5, pp. 1061–1071, 2008.

[89] W. Staszewski, K. Worden, and G. Tomlinson, "Time–frequency analysis in gearbox fault detection using the wigner–ville distribution and pattern recognition," *Mechanical systems and signal processing*, vol. 11, no. 5, pp. 673–692, 1997.

[90] B. Boashash, "Estimating and interpreting the instantaneous frequency of a signal-part 1: Fundamentals," *Proceedings of the IEEE*, vol. 80, no. 4, pp. 520–538, 1992.

[91] B. Boashash, "Estimating and interpreting the instantaneous frequency of a signal. ii. algorithms and applications," *Proceedings of the IEEE*, vol. 80, no. 4, pp. 540–568, 1992.

[92] N. Huang, Z. Wu, S. Long, K. Arnold, X. Chen, and K. Blank, "On instantaneous frequency," *Adv. Adapt. Data Anal*, vol. 1, no. 2, pp. 177–229, 2009.

[93] D. Gabor, "Theory of communication. part 1: The analysis of information," *Proceedings of the IEEE*, vol. 93, no. 26, pp. 429 –441, 1946.

[94] W. Ville, "Theorie et applications de la notion de signal analytique," *Cables et Transmission*, vol. 2a, pp. 61–74, 1948.

[95] S. Saliu, "Definition of instantaneous frequency on real signals.," *Proceedings of European Signal Processing Conference, Tampere, Finland*, pp. 343–346, 2000.

[96] N. Huang, Z. Shen, S. Long, M. Wu, H. Shih, Q. Zheng, N. Yen, C. Tung, and H. Liu, "The empirical mode decomposition and the hilbert spectrum for

nonlinear and non-stationary time series analysis," *Proceedings of the Royal Society of London. Series A: Mathematical, Physical and Engineering Sciences*, vol. 454, no. 1971, pp. 903–995, 1998.

[97] Z. Wu and E. Norden, "Ensemble empirical mode decomposition: A noise-assisted data analysis method," *Advances in Adaptive Data Analysis*, vol. 1, no. 01, pp. 1–41, 2009.

[98] G. Rilling, P. Flandrin, P. Gonçalvés, *et al.*, "On empirical mode decomposition and its algorithms," in *IEEE-EURASIP workshop on Nonlinear Signal and Image Processing, NSIP-03, Grado (I)*, 2003.

[99] N. Huang, M. Wu, S. Long, S. Shen, W. Qu, P. Gloersen, and K. Fan, "A confidence limit for the empirical mode decomposition and hilbert spectral analysis," *Proceedings of the Royal Society of London. Series A: Mathematical, Physical and Engineering Sciences*, vol. 459, no. 2037, pp. 2317–2345, 2003.

[100] Z. Wu and N. Huang, "A study of the characteristics of white noise using the empirical mode decomposition method," *Proceedings of the Royal Society of London. Series A: Mathematical, Physical and Engineering Sciences*, vol. 460, no. 2046, pp. 1597–1611, 2004.

[101] S. Pavlopoulou, W. J. Staszewski, and C. Soutis, "Evaluation of instantaneous characteristics of guided ultrasonic waves for structural quality and health monitoring," *Structural Control and Health Monitoring*, vol. 20, no. 6, pp. 937–955, 2013.

[102] M. F. Ghazali, W. J. Staszewski, J. Shucksmith, J. B. Boxall, and S. B. Beck, "Instantaneous phase and frequency for the detection of leaks and features in a pipeline system," *Structural Health Monitoring*, 2010.

[103] R. Yan and R. Gao, "Hilbert-huang transform-based vibration signal analysis for machine health monitoring," *Instrumentation and Measurement, IEEE Transactions on*, vol. 55, pp. 2320 –2329, dec. 2006.

[104] B. Liu, S. Riemenschneider, and Y. Xu, "Gearbox fault diagnosis using empirical mode decomposition and hilbert spectrum," *Mechanical Systems and Signal Processing*, vol. 20, no. 3, pp. 718 – 734, 2006.

[105] H. Chen, Y. Yan, W. Chen, J. Jiang, L. Yu, and Z. Wu, "Early damage

detection in composite wingbox structures using hilbert-huang transform and genetic algorithm," *Structural Health Monitoring*, vol. 6, no. 4, pp. 281–297, 2007.

[106] S. T. Quek, P. S. Tua, and Q. Wang, "Detecting anomalies in beams and plate based on the hilberthuang transform of real signals," *Smart Materials and Structures*, vol. 12, no. 3, p. 447, 2003.

[107] *Abaqus User's Manual, Version 6.10.*

[108] I. Bartoli, F. L. di Scalea, M. Fateh, and E. Viola, "Modeling guided wave propagation with application to the long-range defect detection in railroad tracks," *NDT & E International*, vol. 38, no. 5, pp. 325 – 334, 2005.

[109] F. Moser, L. J. Jacobs, and J. Qu, "Modeling elastic wave propagation in waveguides with the finite element method," *Ndt & E International*, vol. 32, no. 4, pp. 225–234, 1999.

[110] D. Alleyne and P. Cawley, "A two-dimensional fourier transform method for the measurement of propagating multimode signals," *The Journal of the Acoustical Society of America*, vol. 89, no. 3, pp. 1159–1168, 1991.

[111] P. Fromme, *Defect detection in plates using guided waves.* PhD thesis, Diss ETH No. 14397, 2001.

[112] V. Giurgiutiu, "Tuned lamb wave excitation and detection with piezoelectric wafer active sensors for structural health monitoring," *Journal of Intelligent Material Systems and Structures*, vol. 16, no. 4, pp. 291–305, 2005.

[113] M. Found and J. Lamb, "Damage assessment of impacted thin cfrp panels," *Composites Part A: Applied Science and Manufacturing*, vol. 35, no. 9, pp. 1039 – 1047, 2004.

[114] Boeing, Seattle, USA, *767-300 Structural Repair Manual*, 2011.

[115] B. Nicolaisson, "Analysis of adhesively bonded repairs in composite structures," *MSc Dissertation, The University of Sheffield, Mechanical Engineering department*, September 2011.

[116] J. H. Kurz, C. U. Grosse, and H.-W. Reinhardt, "Strategies for reliable automatic onset time picking of acoustic emissions and of ultrasound signals in

concrete," *Ultrasonics*, vol. 43, no. 7, pp. 538 – 546, 2005.

[117] H. Akaike, "Markovian representation of stochastic processes and its application to the analysis of autoregressive moving average processes," *Annals of the Institute of Statistical Mathematics*, vol. 26, pp. 363–387, 1974.

[118] G. Nagy, "Classifiers that improve with use," *Proceedings of the Conference on Pattern Recognition and Multimedia (IECE), Tokyo, Japan*, pp. 79–86, 2004.

[119] K. Worden, H. Sohn, and C. Farrar, "Novelty detection in a changin environment: Regression and interpolation approaches," *Journal of Sound and Vibration*, vol. 258, no. 4, pp. 741 – 761, 2002.

[120] L. Tarassenko, *Guide to Neural Computing Applications*. Hodder Arnold Publication, Elsevier Science, 1998.

[121] S. A. Grammatikos, E. Z. Kordatos, N.-M. Barkoula, T. E. Matikas, and A. S. Paipetis, "Innovative non-destructive evaluation and damage characterisation of composite aerostructures using thermography," *Plastics, Rubber and Composites*, vol. 40, no. 6-7, pp. 342–348, 2011.

[122] S. Grammatikos, *Structural integrity assessment of aerostructures using innovative Non-Destructive Techniques*. PhD thesis, Materials Science & Eng. Dept., University of Ioannina, 2013.

[123] S. Pavlopoulou, W. J. Staszewski, and C. Soutis, "A comparative study on novelty detection and frequency analysis of lamb waves for the monitoring of metallic repaired structures.," *5th International Conference on Emerging Technologies in Non-Destructive Testing (ETNDT5)*, 19-21 September, 2011, Ioannina, Greece.

[124] S. Pavlopoulou, W. J. Staszewski, C. Soutis, and G. Manson, "Analysis of instantaneous characteristics of guided ultrasonic waves in metallic structures with aluminium repair patches," *Proc. SPIE 7984, 79842Y*, 6-8 March 2011, San Diego, California, USA.

[125] S. Pavlopoulou, C. Soutis, and W. Staszewski, "Structural health monitoring of composite scarf repairs with guided waves," *Key Engineering Materials*, vol. 518, pp. 328–337, 2011.

[126] S. Pavlopoulou, C. Soutis, and K. Worden, "Application of pattern recogni-

tion for damage classification in scarf repairs," *International Conference on Noise and Vibration Engineering (ISMA12)*, 17-19 September, 2012, Leuven, Belgium.

[127] M. Caminero, S. Pavlopoulou, M. Lopez-Pedrosa, and B. Nicolaisson, "Digital image correlation analysis applied to monitor damage evolution of composite plates with stress concentrations and bonded patch repairs," *Proceedings of the 15th European Conference on Composite Materials, 2012, Venice, Italy, ISBN 978-88-88785-33-2.*

[128] S. Pavlopoulou, K. Worden, and C. Soutis, "Structural health monitoring and prognosis in composite repaired structures through the excitation of guided ultrasonic waves," *SPIE*, 11-14 March 2013, San Diego, California.

[129] M. A. Caminero, S. Pavlopoulou, M. Lopez-Pedrosa, B. G. Nicolaisson, C. Pinna, and C. Soutis, "Using digital image correlation techniques for damage detection on adhesively bonded composite repairs," *Advanced Composites Letters*, vol. 21, no. 2, pp. 51–57, 2012.

[130] M. Sutton, W. Wolters, W. Peters, W. Ranson, and S. McNeill, "Determination of displacements using an improved digital correlation method," *Image and Vision Computing*, vol. 1, no. 3, pp. 133 – 139, 1983.

[131] H. Lu and P. Cary, "Deformation measurements by digital image correlation: Implementation of a second-order displacement gradient," *Experimental Mechanics*, vol. 40, pp. 393–400, 2000.

[132] G. Vendroux and W. Knauss, "Submicron deformation field measurements: Part 2. improved digital image correlation," *Experimental Mechanics*, vol. 38, pp. 86–92, 1998.

[133] B. Pan, H. Xie, Z. Wang, K. Qian, and Z. Wang, "Study on subset size selection in digital image correlation for speckle patterns," *Optics express*, vol. 16, no. 10, pp. 7037–7048, 2008.

[134] X. Maldague and P. Moore, *Nondestructive Testing Handbook: Infrared and Thermal Testing*. Nondestructive testing handbook, Amer Society for Nondestructive, 2001.

[135] D. Wu and G. Busse, "Lock-in thermography for nondestructive evaluation of

materials," *Revue Gnrale de Thermique*, vol. 37, no. 8, pp. 693 – 703, 1998.

[136] G. M. Carlomagno and C. Meola, "Comparison between thermographic techniques for frescoes ndt," *NDT & E International*, vol. 35, no. 8, pp. 559 – 565, 2002.

[137] G. Giorleo and C. Meola, "Comparison between pulsed and modulated thermography in glassepoxy laminates," *NDT & E International*, vol. 35, no. 5, pp. 287 – 292, 2002.

# Appendix A

# Digital Image Correlation

Digital image correlation (DIC) is a non-contact optical techniques which was first introduced to experimental mechanics by Peter and Ramson in 1981 who first proposed the use of computer-based image acquisition and deformation measurements in materials systems [130]. This technique has been lately used for nondestructive purposes, where 2-dimensional (2D) and 3-dimensional (3D) surface displacements and strain fields are estimated for the tested object.

One properly calibrated camera for the 2D and two cameras for the 3D DIC, record images of the object before (reference image) and after loading. The cameras employed, have CCD (charge couple device-sensor) arrays which are photosensitive cells of thousand or more pixels. These record the intensity of the light that targets a specific pixel. The recorded signal from each array is digitized in order to provide a reading in terms of the intensity of the light. A calibration grid is required for the establishment of the working parameters of the cameras. The surface of the object is sprayed with paint in order to create a speckle pattern that will provide a random texture (grey-scale pattern). This will guarantee that each signature taken from the surface is unique, hence the surface should have a non repetitive, high contrast pattern. The speckles size should be of a few pixels. The readings are then processed by means of matching sub-images of the images that are recorded before and after the loading.

In Figure A.1 illustrates a simplified approach on the correlation between the baseline image and the deformed image during the 2D DIC. In the figure, the baseline

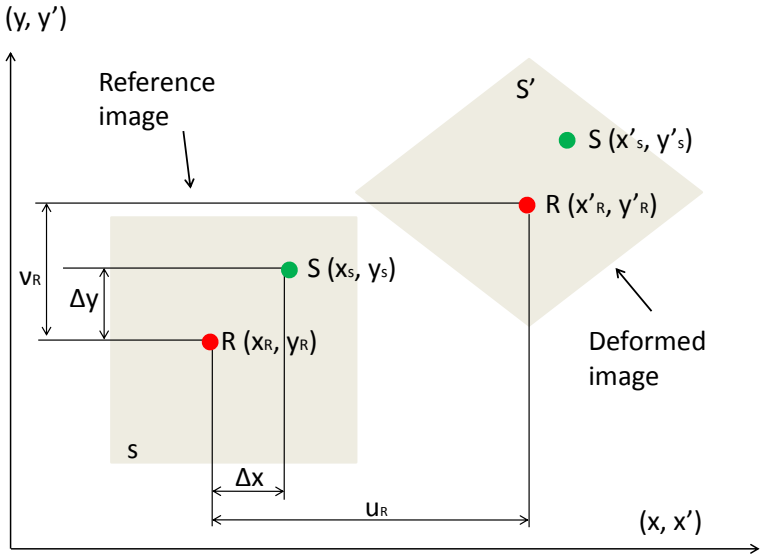


Figure A.1: Schematic illustration of the basic principle of DIC technique.

image and the deformed image are illustrated. The principal will be explained on the basis of the points R and S. Assuming that the set of neighbouring points R and S will remain neighbouring points even after the deformation, the estimation of the deformation of the point R is performed by taking into consideration the point S. If the coordinates of the two points are R:($x_R$,$y_R$), S:($x_S$,$y_S$) before the deformation and R:($x'_R$,$y'_R$), S:($x'_S$,$y'_S$) after the deformation, then the in-plane displacements of the point R ($u_R$, $\nu_R$) can be found through the approximation of the first-order Taylor expansion [131],[132]:

$$x'_S = x_R + u_R + \frac{\partial u_R}{\partial x}\Delta x + \frac{\partial u_R}{\partial y}\Delta y \tag{A.1}$$

$$y'_S = y_R + \nu_R + \frac{\partial \nu_R}{\partial x}\Delta x + \frac{\partial \nu_R}{\partial y}\Delta y \tag{A.2}$$

where Δx and Δy are the sub-image from the point R. Then the displacement vector is expressed by:

$$\vec{V_R} = [u_R, \nu_R, \frac{\partial u_R}{\partial x}, \frac{\partial \nu_R}{\partial y}, \frac{\partial u_R}{\partial y}, \frac{\partial \nu_R}{\partial x}]^T \tag{A.3}$$

The basic mechanism behind DIC is the correlation of the recorded sub-images in order to determine the displacement vector. The correlation of the sub-images is performed with certain commercial codes which are based on well established algorithms that utilise either criteria based on the cross-correlation coefficient or on the least-square correlation coefficient [133]. If f($x_R$,$y_R$) is the light intensity

value of the the point R, then $f(x'_R,y'_R)$, is the intensity value of the point R after the deformation. Then the least squares correlation coefficient can be expressed as [131],[132]:

$$C = \frac{\sum_S [f(x_R, y_R) - f(x'_R, y'_R)]^2}{\sum_S f(x_R, y_R)^2} \tag{A.4}$$

where $(x_R,y_R)$ belongs to the subset S in the baseline image and $(x'_R,y'_R)$ belongs to the subset S' which is the deformed image (7.4). The cross correlation coefficient can be expressed by:

$$C = 1 - \frac{\sum_S [f(x_R, y_R) f(x'_R, y'_R)]}{\sum_S f^2(x_R, y_R)] \sum_S f^2(x'_R, y'_R)]^{\frac{1}{2}}} \tag{A.5}$$

In comparison with other experimental techniques such as Moiré interferometry and electric speckle interferometry, DIC is simple and robust because complicated surface treatment is not needed and its requirement for testing environment is low. On the other hand, the subset size accuracy and the quality of a speckle pattern are of vital importance [133], [10].

# Appendix B

# Lock-in Thermography

Infrared thermography (IrT) has been widely used for nondestructive techniques, in order to detect subsurface defects and features, by monitoring their thermal gradient at the near surface regions, following a thermal stimulation. The defects result to a delay in the cooling process since they act as heat traps within the material [121]. There are two main categories for IrT, based on the stimulation method, namely the active and passive thermography. For the passive approach, the temperature of the material is exploited without any external stimulation source, if the material's temperature is naturally higher than the surrounding area. On the other hand, the active thermography requires a thermal stimulation, in order to enable the characterisation of the defects based on the thermal differences of the surface [121]. There is a wide range of external excitations such as optical, mechanical or inductive. Optical excitations (e.g. infrared lamps) are externally stimulated, and the energy is transferred to the tested material in the form of light which is transformed into heat. Then these thermal waves, interact with the defects, and depending on the thermal properties of the material, they either slow down or speed up. Mechanical excitations (also known as vibro-thermography) are usually performed through a mechanical oscillation that utilises waves. These mechanical waves propagate through the material and they produce dissipated heat waves as they interact with the discontinuities. The inductive excitation, can only applied to electro-conductive materials, where eddy currents heat the specimen [134].

The most popular active IrT approaches are the pulse thermography (PT), the pulsed phased thermography (PPT) and the lock-in thermography (LT). The first

employs an excitation source that follows a square pulse, enabling two possible modes, the transmission and the reflection modes. This approach allows for the duration of the pulse to be modified (from milliseconds to a few seconds) in order to account for materials with different conductivity. The second method, employs the same principals as with the PT, only in this case the Fourier transform is utilised to provide both phase and amplitude images of the tested object. This work focused on an active thermography approach (i.e. the lock-in thermography) [135].

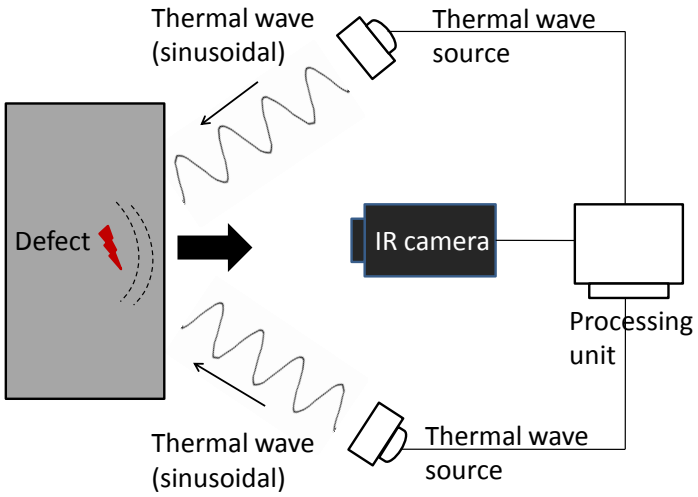


Figure B.1: Schematic illustration of the lock-in thermography experimental set up.

In the lock-in thermography (IrT) also known as modulated thermography (MT), the external source is periodic, more usually sinusoidal. A typical experimental set-up that is followed for this case is illustrated in Figure B.1. The monitored system needs to be coupled to a thermal wave source, which can result to a sinusoidal temperature modulation. These waves can be generated, if the acquisition device and the source of heating are synchronised. Therefore the heat source needs to be properly calibrated for each frequency in order to achieve a constant sinusoidal temperature waveform. The equation that expressed the thermal wave in the case of lock-in thermography is given by [136]:

$$T(t,z) = T_0 e^{-\frac{z}{\mu}} \cos(\omega t - \frac{2\pi x}{\lambda}) \tag{B.1}$$

where  is the temperature, $z$ is the depth, $t$ is the time and $\lambda$ is the thermal wavelength ($\lambda$=$2\pi\mu$).

The signals are then recorded by the lock-in amplifier at each time instant and local changes in the amplitude and phase provide information about the presence

and location of internal defects as a response to the modulated thermal input. The depth the can be monitored depends on a variety of factors, such as the wave cycle time, the heat conductivity and capacity of the material and its density. For the thermal wave to penetrate into the object, it needs to attenuate. The inverse of the thermal diffusion length $\mu$, can be defined by [136], [137]:

$$\mu = \sqrt{\frac{\alpha}{\pi f}} \tag{B.2}$$

where $\alpha$ is the thermal diffusivity and $f$ is the wave frequency. The inverse of the thermal diffusion expresses the real and imaginary parts of the complex wave number of a heavily damped wave. This is associated with the modulated heat transport. The depth range for the amplitude image that can be monitored is given by $\mu$ while the maximum depth that can be inspected for the phase image is 1.8 $\mu$. The wave frequencies can get a wide range [137]. However at lower frequencies, higher depths values can be achieved while at high frequencies, only surface or near-surface defects can be detected.

# Appendix C

# ABAQUS input files

This Appendix contains a representative input file that was used for the ABAQUS FE analysis that was demonstrated throughout this work. Due to space restriction, the respective file does not include all the elements and the nodes of the model and only the model of the damage scenario 4 (D2) is displayed as a more representative example.

```
*Heading
** Job name: SC4_D2 Model name: D2
** Generated by: Abaqus/CAE 6.10-2
*Preprint, echo=NO, model=NO, history=NO, contact=NO
**
** PARTS
**
*Part, name=Patch
*Node
      1, 0.0160000008, 0.00499999989, 0.00200000009
      2, 0.0160000008, 0.00600000005, 0.00200000009
      3, 0.0149999997, 0.00600000005, 0.00200000009....
*Element, type=C3D8R
1, 128, 142, 141, 127,   1,   2,   3,   4
2, 129, 143, 140, 126, 128, 142, 141, 127
3, 130, 144, 139, 125, 129, 143, 140, 126....
*Nset, nset=_PickedSet12, internal, generate
     1,  15129,      1
*Elset, elset=_PickedSet12, internal, generate
     1,  12800,      1
*Elset, elset=Patch1
     1,     9,    10,    11,    12,    13,    14,    15,    16,    17,    18,...
*Elset, elset=Patch2
     2,    23,    24,    25,    26,    27,    28,    29,    30,    31,    32,...
*Elset, elset=Patch3
     3,    37,    38,    39,    40,    41,    42,    43,    44,    45,    46,...
*Elset, elset=Patch4
```

```
     4,    51,    52,    53,    54,    55,    56,    57,    58,    59,    60,...
*Elset, elset=Patch5
     5,    65,    66,    67,    68,    69,    70,    71,    72,    73,    74,...
*Elset, elset=Patch6
     6,    79,    80,    81,    82,    83,    84,    85,    86,    87,    88,...
*Elset, elset=Patch7
     7,    93,    94,    95,    96,    97,    98,    99,   100,   101,   102,...
*Elset, elset=Patch8
     8,   107,   108,   109,   110,   111,   112,   113,   114,   115,   116,...
*Orientation, name=Ori-1
1., 0., 0., 0., 1., 0.
3, 0.
** Region: (CFRP 997/2:Picked), (Material Orientation:Patch1)
*Elset, elset=_I1, internal
     1,     9,    10,    11,    12,    13,    14,    15,    16,    17,    18,...
** Section: CFRP 997/2
*Solid Section, elset=_I1, orientation=Ori-1, material="CFRP 997/2"
,
*Orientation, name=Ori-2
1., 0., 0., 0., 1., 0.
3, 90.
** Region: (CFRP 997/2:Picked), (Material Orientation:Patch2)
*Elset, elset=_I2, internal
     2,    23,    24,    25,    26,    27,    28,    29,    30,    31,    32,...
** Section: CFRP 997/2
*Solid Section, elset=_I2, orientation=Ori-2, material="CFRP 997/2"
,
*Orientation, name=Ori-3
1., 0., 0., 0., 1., 0.
3, 90.
** Region: (CFRP 997/2:Picked), (Material Orientation:Patch3)
*Elset, elset=_I3, internal
     3,    37,    38,    39,    40,    41,    42,    43,    44,    45,    46,...
*Solid Section, elset=_I3, orientation=Ori-3, material="CFRP 997/2"
,
*Orientation, name=Ori-4
1., 0., 0., 0., 1., 0.
3, 0.
** Region: (CFRP 997/2:Picked), (Material Orientation:Patch4)
*Elset, elset=_I4, internal
     4,    51,    52,    53,    54,    55,    56,    57,    58,    59,    60,...
** Section: CFRP 997/2
*Solid Section, elset=_I4, orientation=Ori-4, material="CFRP 997/2"
,
*Orientation, name=Ori-5
1., 0., 0., 0., 1., 0.
3, 0.
** Region: (CFRP 997/2:Picked), (Material Orientation:Patch5)
*Elset, elset=_I5, internal
     5,    65,    66,    67,    68,    69,    70,    71,    72,    73,    74,...
** Section: CFRP 997/2
*Solid Section, elset=_I5, orientation=Ori-5, material="CFRP 997/2"
,
*Orientation, name=Ori-6
1., 0., 0., 0., 1., 0.
```

```
3, 90.
** Region: (CFRP 997/2:Picked), (Material Orientation:Patch6)
*Elset, elset=_I6, internal
     6,    79,    80,    81,    82,    83,    84,    85,    86,    87,    88,...
** Section: CFRP 997/2
*Solid Section, elset=_I6, orientation=Ori-6, material="CFRP 997/2"
,
*Orientation, name=Ori-7
1., 0., 0., 0., 1., 0.
3, 90.
** Region: (CFRP 997/2:Picked), (Material Orientation:Patch7)
*Elset, elset=_I7, internal
     7,    93,    94,    95,    96,    97,    98,    99,   100,   101,   102,...
** Section: CFRP 997/2
*Solid Section, elset=_I7, orientation=Ori-7, material="CFRP 997/2"
,
*Orientation, name=Ori-8
1., 0., 0., 0., 1., 0.
3, 0.
** Region: (CFRP 997/2:Picked), (Material Orientation:Patch8)
*Elset, elset=_I8, internal
     8,   107,   108,   109,   110,   111,   112,   113,   114,   115,   116,...
** Section: CFRP 997/2
*Solid Section, elset=_I8, orientation=Ori-8, material="CFRP 997/2"
,
*End Part
**
*Part, name=Substrate
*Node
      1, 0.0199999996, -0.0649999976, 0.00200000009
      2, 0.0199999996, -0.0199999996, 0.00200000009
      3, 0.0160000008, -0.0199999996, 0.00200000009 ...
*Element, type=C3D8R
   1,   394,  6027, 51991,  5985,     1,   193,  5721,   286
   2,  6027,  6028, 51992, 51991,   193,   194,  5722,  5721
   3,  6028,  6029, 51993, 51992,   194,   195,  5723,  5722 ...
*Nset, nset=_PickedSet329, internal
      1,      2,      3,      4,      5,      6,      7,      8,      9,     10,...
*Elset, elset=_PickedSet329, internal
      1,      2,      3,      4,      5,      6,      7,      8,      9,     10,...
*Nset, nset=_PickedSet330, internal
     80,     83,     85,     86,     96,     98,    117,    120,   2399,   2400,...
*Elset, elset=_PickedSet330, internal, generate
 67961,  68760,      1
*Elset, elset=Substrate1
      1,      2,      3,      4,      5,      6,      7,      8,      9,     10,...
*Elset, elset=Substrate2
    181,    182,    183,    184,    185,    186,    187,    188,    189,    190,...
*Elset, elset=Substrate3
    361,    362,    363,    364,    365,    366,    367,    368,    369,    370,...
*Elset, elset=Substrate4
    541,    542,    543,    544,    545,    546,    547,    548,    549,    550,...
*Elset, elset=Substrate5
    721,    722,    723,    724,    725,    726,    727,    728,    729,    730,...
*Elset, elset=Substrate6
```

```
    901,    902,    903,    904,    905,    906,    907,    908,    909,    910,...
*Elset, elset=Substrate7
   1081,   1082,   1083,   1084,   1085,   1086,   1087,   1088,   1089,   1090,...
*Elset, elset=Substrate8
   1261,   1262,   1263,   1264,   1265,   1266,   1267,   1268,   1269,   1270,...
*Orientation, name=Ori-1
1., 0., 0., 0., 1., 0.
3, 0.
** Region: (CFRP 997/2:Picked), (Material Orientation:Substrate1)
*Elset, elset=_I1, internal
      1,      2,      3,      4,      5,      6,      7,      8,      9,     10,...
** Section: CFRP 997/2
*Solid Section, elset=_I1, orientation=Ori-1, material="CFRP 997/2"
,
*Orientation, name=Ori-2
1., 0., 0., 0., 1., 0.
3, 90.
** Region: (CFRP 997/2:Picked), (Material Orientation:Substrate2)
*Elset, elset=_I2, internal
    181,    182,    183,    184,    185,    186,    187,    188,    189,    190,...
** Section: CFRP 997/2
*Solid Section, elset=_I2, orientation=Ori-2, material="CFRP 997/2"
,
*Orientation, name=Ori-3
1., 0., 0., 0., 1., 0.
3, 90.
** Region: (CFRP 997/2:Picked), (Material Orientation:Substrate3)
*Elset, elset=_I3, internal
    361,    362,    363,    364,    365,    366,    367,    368,    369,    370,...
** Section: CFRP 997/2
*Solid Section, elset=_I3, orientation=Ori-3, material="CFRP 997/2"
,
*Orientation, name=Ori-4
1., 0., 0., 0., 1., 0.
3, 0.
** Region: (CFRP 997/2:Picked), (Material Orientation:Substrate4)
*Elset, elset=_I4, internal
    541,    542,    543,    544,    545,    546,    547,    548,    549,    550,...
** Section: CFRP 997/2
*Solid Section, elset=_I4, orientation=Ori-4, material="CFRP 997/2"
,
*Orientation, name=Ori-5
1., 0., 0., 0., 1., 0.
3, 0.
** Region: (CFRP 997/2:Picked), (Material Orientation:Substrate5)
*Elset, elset=_I5, internal
    721,    722,    723,    724,    725,    726,    727,    728,    729,    730,...
** Section: CFRP 997/2
*Solid Section, elset=_I5, orientation=Ori-5, material="CFRP 997/2"
,
*Orientation, name=Ori-6
1., 0., 0., 0., 1., 0.
3, 90.
** Region: (CFRP 997/2:Picked), (Material Orientation:Substrate6)
*Elset, elset=_I6, internal
```

```
    901,    902,    903,    904,    905,    906,    907,    908,    909,    910,...
** Section: CFRP 997/2
*Solid Section, elset=_I6, orientation=Ori-6, material="CFRP 997/2"
,
*Orientation, name=Ori-7
1., 0., 0., 0., 1., 0.
3, 90.
** Region: (CFRP 997/2:Picked), (Material Orientation:Substrate7)
*Elset, elset=_I7, internal
   1081,   1082,   1083,   1084,   1085,   1086,   1087,   1088,   1089,   1090,...
** Section: CFRP 997/2
*Solid Section, elset=_I7, orientation=Ori-7, material="CFRP 997/2"
,
*Orientation, name=Ori-8
1., 0., 0., 0., 1., 0.
3, 0.
** Region: (CFRP 997/2:Picked), (Material Orientation:Substrate8)
*Elset, elset=_I8, internal
   1261,   1262,   1263,   1264,   1265,   1266,   1267,   1268,   1269,   1270,...
** Section: CFRP 997/2
*Solid Section, elset=_I8, orientation=Ori-8, material="CFRP 997/2"
,
** Region: (Damage:Picked), (Material Orientation:Substrate8)
*Elset, elset=_I9, internal, generate
 67961,  68060,      1
** Section: Damage
*Solid Section, elset=_I9, orientation=Ori-8, material="Damage 10% off"
,
** Region: (Damage:Picked), (Material Orientation:Substrate7)
*Elset, elset=_I10, internal, generate
 68061,  68160,      1
** Section: Damage
*Solid Section, elset=_I10, orientation=Ori-7, material="Damage 10% off"
,
** Region: (Damage:Picked), (Material Orientation:Substrate6)
*Elset, elset=_I11, internal, generate
 68161,  68260,      1
** Section: Damage
*Solid Section, elset=_I11, orientation=Ori-6, material="Damage 10% off"
,
** Region: (Damage:Picked), (Material Orientation:Substrate5)
*Elset, elset=_I12, internal, generate
 68261,  68360,      1
** Section: Damage
*Solid Section, elset=_I12, orientation=Ori-5, material="Damage 10% off"
,
** Region: (Damage:Picked), (Material Orientation:Substrate4)
*Elset, elset=_I13, internal, generate
 68361,  68460,      1
** Section: Damage
*Solid Section, elset=_I13, orientation=Ori-4, material="Damage 10% off"
,
** Region: (Damage:Picked), (Material Orientation:Substrate3)
*Elset, elset=_I14, internal, generate
 68461,  68560,      1
```

```
** Section: Damage
*Solid Section, elset=_I14, orientation=Ori-3, material="Damage 10% off"
,
** Region: (Damage:Picked), (Material Orientation:Substrate2)
*Elset, elset=_I15, internal, generate
 68561,  68660,      1
** Section: Damage
*Solid Section, elset=_I15, orientation=Ori-2, material="Damage 10% off"
,
** Region: (Damage:Picked), (Material Orientation:Substrate1)
*Elset, elset=_I16, internal, generate
 68661,  68760,      1
** Section: Damage
*Solid Section, elset=_I16, orientation=Ori-1, material="Damage 10% off"
,
*End Part
**
**
** ASSEMBLY
**
*Assembly, name=Assembly
**
*Instance, name=Substrate-1, part=Substrate
*End Instance
**
*Instance, name=Patch-1, part=Patch
          0.,           0.,        0.002
*End Instance
**
*Nset, nset=_PickedSet307, internal, instance=Patch-1
   95,   96,   97,  101,  102,  104,  105,  106,  110,  116,  119,...
*Elset, elset=_PickedSet307, internal, instance=Patch-1
 10961, 10962, 10963, 10964, 11465, 11466, 11467, 11468, 11469, 11470,...
*Nset, nset=_PickedSet309, internal, instance=Patch-1
    5,    8,   11,   13,   14,   15,   16,   21,   22,   25,  112,...
*Elset, elset=_PickedSet309, internal, instance=Patch-1
   121,   122,   123,   124,   153,   154,   155,   156,   157,   158,...
*Nset, nset=_PickedSet311, internal, instance=Patch-1
   45,   54,   59,   60,  723,  724,  725,  726,  727,  728,  729,...
*Elset, elset=_PickedSet311, internal, instance=Patch-1, generate
 6021,  6120,     1
*Nset, nset=_PickedSet312, internal, instance=Substrate-1
    44,    46,    49,    50,    53,    54,    65,    69,    70,    75,...
*Elset, elset=_PickedSet312, internal, instance=Substrate-1
 54873, 54874, 54875, 54876, 54877, 54878, 54879, 54880, 54881, 55411,...
*Nset, nset=_PickedSet313, internal, instance=Patch-1
    6,    7,   12,   29,   30,   32,   37,   38,   39,   40,   43,   44,...
*Elset, elset=_PickedSet313, internal, instance=Patch-1
   984,   985,   986,   987,   988,   989,   990,   991,   992,  1875, ...
*Nset, nset=A(bel), instance=Substrate-1
 38358,
*Nset, nset=A(up), instance=Substrate-1
 38754,
*Nset, nset=S1, instance=Substrate-1
 16340,
```

```
*Nset, nset=S2, instance=Substrate-1
 38753,
*Elset, elset=__PickedSurf306_S4, internal, instance=Substrate-1
 93728, 93736, 93744, 93752, 98800, 98808, 98816, 98824, 98832, 98840, 98848,...
*Elset, elset=__PickedSurf306_S1, internal, instance=Substrate-1, generate
 83637,  83640,      1
*Elset, elset=__PickedSurf306_S2, internal, instance=Substrate-1, generate
 77649,  77704,      1
*Surface, type=ELEMENT, name=_PickedSurf306, internal
__PickedSurf306_S4, S4
__PickedSurf306_S1, S1
__PickedSurf306_S2, S2
*Elset, elset=__PickedSurf308_S2, internal, instance=Substrate-1
 1441, 1442, 1443, 1444, 1445, 1446, 1447, 1448, 1449, 1450, 1451, 1452, 1453,...
*Elset, elset=__PickedSurf308_S1, internal, instance=Substrate-1, generate
 20717,  20720,      1
*Surface, type=ELEMENT, name=_PickedSurf308, internal
__PickedSurf308_S2, S2
__PickedSurf308_S1, S1
*Elset, elset=__PickedSurf310_S1, internal, instance=Substrate-1, generate
 68661,  68760,      1
*Surface, type=ELEMENT, name=_PickedSurf310, internal
__PickedSurf310_S1, S1
*Surface, type=NODE, name=_PickedSet307_CNS_, internal
_PickedSet307, 1.
*Surface, type=NODE, name=_PickedSet309_CNS_, internal
_PickedSet309, 1.
*Surface, type=NODE, name=_PickedSet311_CNS_, internal
_PickedSet311, 1.
*Surface, type=NODE, name=_PickedSet312_CNS_, internal
_PickedSet312, 1.
*Surface, type=NODE, name=_PickedSet313_CNS_, internal
_PickedSet313, 1.
** Constraint: Constraint-1
*Tie, name=Constraint-1, adjust=yes
_PickedSet313_CNS_, _PickedSet312_CNS_
*End Assembly
*Amplitude, name=Hanning
          0.,           0.,      3.8e-07, 0.00523585711,      7.6e-07,
             0.0371164798,     1.14e-06,  0.100940171
    1.52e-06,   0.16994021,      1.9e-06,  0.191439676,     2.28e-06,  0.109000677,
             2.66e-06, -0.107477371
    3.04e-06, -0.436166895,     3.42e-06, -0.794460923,      3.8e-06,  -1.05398433,
             4.18e-06,  -1.07813585
    4.56e-06, -0.771892574,     4.94e-06, -0.127429809,     5.32e-06,  0.751816998,
             5.7e-06,      1.66086
    6.08e-06,     2.338816,     6.46e-06,   2.54077407,     6.84e-06,   2.11618394,
             7.22e-06,   1.06958203
     7.6e-06, -0.417616458,     7.98e-06,  -2.01554313,     8.36e-06,  -3.32136963,
             8.74e-06,  -3.96406228
    9.12e-06,  -3.71026587,      9.5e-06,  -2.54065565,     9.88e-06, -0.672606754,
            1.026e-05,   1.48089154
   1.064e-05,   3.40834328,    1.102e-05,   4.62873797,     1.14e-05,   4.81818692,
            1.178e-05,   3.89934614
```

```
   1.216e-05,   2.06809803,    1.254e-05, -0.251215244,    1.292e-05,  -2.51110806,
            1.33e-05,  -4.17911727
   1.368e-05,  -4.87195393,    1.406e-05,  -4.44989842,    1.444e-05,  -3.04677857,
           1.482e-05,  -1.02871372
    1.52e-05,   1.10571397,    1.558e-05,   2.85562341,    1.596e-05,    3.8427494,
            1.634e-05,   3.89827728
   1.672e-05,   3.09053753,     1.71e-05,   1.68963832,    1.748e-05, 0.0825393965,
           1.786e-05,  -1.33519284
   1.824e-05,   -2.2600708,    1.862e-05,  -2.54729442,      1.9e-05,  -2.22834796,
           1.938e-05,   -1.4796482
   1.976e-05, -0.556118714,    2.014e-05,  0.287789304,    2.052e-05,  0.865811214,
            2.09e-05,   1.09837061
   2.128e-05,   1.01460775,    2.166e-05,  0.722503746,    2.204e-05,  0.360875034,
           2.242e-05,  0.050924501
    2.28e-05, -0.137131474,    2.318e-05, -0.193848799,    2.356e-05, -0.157351505,
            2.394e-05, -0.0856905724
   2.432e-05, -0.0274704866,     2.47e-05, -0.00261469643,    2.508e-05,
       0.,    2.546e-05,           0.
   2.584e-05,           0.,    2.622e-05,           0.,     2.66e-05,           0.,
           2.698e-05,           0.
   2.736e-05,           0.,    2.774e-05,           0.,    2.812e-05,           0.,
            2.85e-05,           0.
   2.888e-05,           0.,    2.926e-05,           0.,    2.964e-05,           0.,
           3.002e-05,           0.
    3.04e-05,           0.,    3.078e-05,           0.,    3.116e-05,           0.,
            3.154e-05,           0.

**
** MATERIALS
**
*Material, name="CFRP 997/2"
*Density
1600.,
*Elastic, type=ENGINEERING CONSTANTS
 1.53e+11, 1.03e+10, 1.03e+10,      0.3,      0.3,      0.4,    6e+09,    6e+09
  3.7e+09,
*Material, name="Damage 10% off"
*Density
1600.,
*Elastic, type=ENGINEERING CONSTANTS
 1.37e+11, 9.27e+09, 9.27e+09,     0.27,     0.27,     0.36,  5.4e+09,  5.4e+09
 3.33e+09,
**
** INTERACTION PROPERTIES
**
*Surface Interaction, name=IntProp-1
*Friction
0.,
*Surface Behavior, no separation, pressure-overclosure=HARD
** ----------------------------------------------------------------
**
** STEP: Step-1
**
*Step, name=Step-1, nlgeom=NO
*Dynamic, Explicit
```

```
, 0.0002
*Bulk Viscosity
0.06, 1.2
**
** BOUNDARY CONDITIONS
**
** Name: A(bel) Type: Displacement/Rotation
*Boundary, amplitude=Hanning
A(bel), 3, 3, 1e-09
** Name: A(up) Type: Displacement/Rotation
*Boundary, amplitude=Hanning
A(up), 3, 3, 1e-09
**
** INTERACTIONS
**
** Interaction: Int-1
*Contact Pair, interaction=IntProp-1, mechanical constraint=PENALTY, cpset=Int-1
_PickedSurf306, _PickedSet307_CNS_
** Interaction: Int-2
*Contact Pair, interaction=IntProp-1, mechanical constraint=PENALTY, cpset=Int-2
_PickedSurf308, _PickedSet309_CNS_
** Interaction: Int-3
*Contact Pair, interaction=IntProp-1, mechanical constraint=PENALTY, cpset=Int-3
_PickedSurf310, _PickedSet311_CNS_
**
** OUTPUT REQUESTS
**
*Restart, write, number interval=1, time marks=NO
**
** FIELD OUTPUT: F-Output-1
**
*Output, field, number interval=400
*Node Output
U,
**
** HISTORY OUTPUT: A(bel)
**
*Output, history, time interval=1e-07
*Node Output, nset=A(bel)
U3,
**
** HISTORY OUTPUT: A(up)
**
*Node Output, nset=A(up)
U3,
**
** HISTORY OUTPUT: S1
**
*Node Output, nset=S1
U3,
**
** HISTORY OUTPUT: S2
**
*Node Output, nset=S2
U3,
```

*End Step